

LHCb 上质子-铅核对撞中显粲的产
生和冷核物质效应研究

**Study of Open Charm Production and
Cold Nuclear Matter Effects in
Proton-Lead Collisions at LHCb**

(申请清华大学理学博士学位论文)

培 养 单 位： 工程物理系

学 科： 物理学

研 究 生： 罗 毅 恒

指 导 教 师： 朱 相 雷 副 教 授

二〇二二年五月

**Study of Open Charm Production and
Cold Nuclear Matter Effects in
Proton-Lead Collisions at LHCb**

Dissertation Submitted to

Tsinghua University

in partial fulfillment of the requirement

for the degree of

Doctor of Philosophy

in

Physics

by

Luo Yiheng

Dissertation Supervisor: Associate Professor Zhu Xianglei

May, 2022

学位论文公开评阅人和答辩委员会名单

公开评阅人名单

无（全隐名评阅）

答辩委员会名单

| | | | |
|----|--------------|-------|------|
| 主席 | 高原宁 | 教授 | 北京大学 |
| 委员 | 杨振伟 | 教授 | 北京大学 |
| | 王青 | 教授 | 清华大学 |
| | CHEN SHAOMIN | 教授 | 清华大学 |
| | 朱相雷 | 副教授 | 清华大学 |
| 秘书 | 屈三强 | 助理研究员 | 清华大学 |

关于学位论文使用授权的说明

本人完全了解清华大学有关保留、使用学位论文的规定，即：

清华大学拥有在著作权法规定范围内学位论文的使用权，其中包括：（1）已获学位的研究生必须按学校规定提交学位论文，学校可以采用影印、缩印或其他复制手段保存研究生上交的学位论文；（2）为教学和科研目的，学校可以将公开的学位论文作为资料在图书馆、资料室等场所供校内师生阅读，或在校园网上供校内师生浏览部分内容；（3）根据《中华人民共和国学位条例暂行实施办法》及上级教育主管部门具体要求，向国家图书馆报送相应的学位论文。

本人保证遵守上述规定。

作者签名：罗毅恒

导师签名：朱世宏

日期：2022年4月1日

日期：2022年4月1日

摘要

夸克胶子等离子体 (QGP) 是以解除囚禁的夸克和胶子为基本组分的新物质形态。高能重离子碰撞实验的重要目标是产生 QGP 并定量研究其性质。各种实验探针除了对 QGP 产生的热核物质效应敏感外, 还会受到与 QGP 产生无关的冷核物质 (CNM) 效应的影响。质子-重核碰撞由于时空尺度小, 不能产生 QGP, 对这一碰撞中相关实验探针进行精确测量可以对核部分子分布函数 (nPDF) 和色玻璃凝聚 (CGC) 等 CNM 效应进行有效限定, 为重离子碰撞中研究 QGP 特性提供参考。

粲夸克由于质量较大, 只能在重离子碰撞的早期通过硬散射成对产生, 在强子化之前会经历火球的整个演化过程, 是 QGP 的有效探针。目前 RHIC 和 LHC 的重离子碰撞中对粲强子核修正因子测量发现了粲夸克在 QGP 介质中的较大能量损失, 对 D_s^+ 和 D^0 粒子比的测量也发现了奇异性产额增强。但是 nPDF 和 CGC 等冷核物质效应也会造成粲强子核修正因子的压低, 质子-重核等小碰撞系统中也存在奇异性产额增强。目前需要在质子-重核碰撞中对相应粲强子观测量进行精确测量限定这些粲强子探针中的 CNM 效应。

大型强子对撞机 LHC 上的 LHCb 探测器于 2013 年初采集了积分亮度为 $1.58 \pm 0.02 \text{ nb}^{-1}$, 核子-核子质心系能量为 $\sqrt{s_{\text{NN}}} = 5.02 \text{ TeV}$ 的质子-铅核 ($p\text{Pb}$) 对撞数据。本论文利用这些数据首次测量了 $p\text{Pb}$ 对撞中前向瞬发 D^+ 和 D_s^+ 的微分截面, 运动学区间覆盖前向快度区 $1.5 < y < 4.0$ 与后向快度区 $-5.0 < y < -2.5$, 横动量范围为 $0 < p_{\text{T}} < 14 \text{ GeV}/c$ 。利用这些结果, 本论文计算了两种粒子的核修正因子 $R_{p\text{Pb}}$ 与前后向截面比 R_{FB} , 研究影响粲强子产生的 CNM 效应。本论文还测量了 D_s^+ 、 D^+ 和 D^0 间的截面比值, 研究碰撞中的粲夸克强子化机制和奇异性增强。

$R_{p\text{Pb}}$ 和 R_{FB} 的测量表明在 5.02 TeV $p\text{Pb}$ 对撞中存在明显的 CNM 效应。 D^+ 和 D_s^+ 的截面在前向快度区都存在明显的压低, 在误差范围内与之前的 D^0 测量以及 nPDF 和 CGC 的理论预言符合较好, 暗示在小动量分数 x 存在核遮蔽效应。在后向快度区, D_s^+ 的压低效应不明显且与 nPDF 计算符合较好, 暗示存在核的反遮蔽效应, 而 D^+ 的 $R_{p\text{Pb}}$ 小于理论预言, 尤其是高横动量的 R_{FB} 显著大于 nPDF 理论计算, 预示 $p\text{Pb}$ 碰撞中可能存在其它的核物质效应。截面比值 R_{D^+/D^0} , $R_{D_s^+/D^0}$ 和 $R_{D_s^+/D^+}$ 显示后向快度区 D^+ 截面相对 D^0 和 D_s^+ 存在少量压低, 但在前向和后向均未见 D_s^+ 相对 D^0 产生截面的增强。

关键词: 夸克胶子等离子体; 显粲; 产生截面; 冷核物质效应; 奇异性增强

ABSTRACT

Quark-gluon plasma (QGP) is a new state of matter with deconfined quarks and gluons as fundamental constituents. An essential goal of high-energy heavy-ion collision experiments is to create QGP and investigate its properties quantitatively. Various experimental probes, which are sensitive to the hot nuclear matter effects induced by QGP, may also be affected by the cold nuclear matter (CNM) effects irrelevant to the QGP formation. Precise measurements of these experimental probes in proton-nucleus collisions, which cannot produce QGP due to their small time-space scales, can effectively quantify the CNM effects such as nuclear parton distribution function (nPDF) and color glass condensate (CGC), and provide a reference for the study of QGP properties in heavy-ion collisions.

Due to their large mass, charm quarks are pair-produced in the early stage of heavy-ion collisions by hard scatterings and will undergo the whole evolution of the fireball before hadronization, and are sensitive probes to the QGP medium properties. The present measurements on charm hadron nuclear modification factors in heavy-ion collisions at RHIC and LHC reveal a large energy loss of charm quarks in the QGP medium, and the measurement of D_s^+ to D^0 yield ratios also exhibits the effect of enhanced strangeness production in charm hadronization. However, cold nuclear matter effects such as nPDF and CGC may also suppress the charm hadron nuclear modification factor, and the strangeness enhancement also exists in small collision systems such as proton-nucleus. Currently, the precise measurements of these charm hadron observables in proton-nucleus collisions become essential to constrain the CNM effects in these QGP probes.

In early 2013, the LHCb detector at the Large Hadron Collider (LHC) has collected the data of proton-lead (p Pb) collisions with an integrated luminosity of $1.58 \pm 0.02 \text{ nb}^{-1}$ at nucleon-nucleon centre-of-mass energy of $\sqrt{s_{\text{NN}}} = 5.02 \text{ TeV}$. This thesis utilizes these data to measure for the first time the differential cross-sections of prompt D^+ and D_s^+ in p Pb collisions at forward region, with the measured kinematic intervals covering the forward rapidity region of $1.5 < y < 4.0$ and the backward rapidity region of $-5.0 < y < -2.5$ and the transverse momentum range of $0 < p_T < 14 \text{ GeV}/c$. Using these cross-section results, this thesis calculates the nuclear modification factor $R_{p\text{Pb}}$ and the forward-backward cross-section ratio R_{FB} for both particles. CNM effects that influence the production of

charm hadrons are studied. The cross-section ratios between D_s^+ , D^+ and D^0 are also measured in this thesis to explore the charm quark hadronization mechanism and strangeness enhancement in $p\text{Pb}$ collisions.

The $R_{p\text{Pb}}$ and R_{FB} measurements indicate significant CNM effects in $p\text{Pb}$ collisions at 5.02 TeV. The cross-sections of both D^+ and D_s^+ are obviously suppressed in the forward rapidity region, which are in good agreement with the previous D^0 measurements and the theoretical predictions of nPDF and CGC within uncertainties, indicating the existence of nuclear shadowing effects in the small momentum fraction x . In the backward rapidity region, the suppression of D_s^+ production is insignificant and in good agreement with the nPDF calculations, suggesting the existence of nuclear anti-shadowing effects, while D^+ 's $R_{p\text{Pb}}$ are slightly smaller than the nPDF predictions. In particular, D^+ 's R_{FB} at high transverse momentum are significantly larger than the nPDF calculations, implying the possible existence of other nuclear matter effects in $p\text{Pb}$ collisions. The cross-section ratios R_{D^+/D^0} , $R_{D_s^+/D^0}$ and $R_{D_s^+/D^+}$ demonstrate a small suppression of the D^+ cross-section relative to D^0 and D_s^+ in the backward rapidity region, but no evidence of D_s^+ enhancement relative to D^0 production is observed in both forward and backward rapidities.

Keywords: quark-gluon plasma; open charm; production cross-section; cold nuclear matter effects; strangeness enhancement

TABLE OF CONTENTS

| | |
|--|-----|
| 摘要..... | I |
| ABSTRACT | II |
| TABLE OF CONTENTS | IV |
| LIST OF FIGURES AND TABLES | VII |
| CHAPTER 1 INTRODUCTION | 1 |
| 1.1 Standard Model and Quantum Chromodynamics | 1 |
| 1.2 QGP and heavy-ion collisions | 5 |
| 1.3 Charmed hadrons in heavy-ion collisions | 7 |
| 1.3.1 Charmed hadrons as a sensitive probe to QGP..... | 7 |
| 1.3.2 Charm production in pp collisions | 8 |
| 1.3.3 Charm production in pA and AB collisions | 11 |
| 1.3.4 Nuclear matter effects in pA and AA collisions..... | 14 |
| 1.3.5 CNM effects on open charm production | 16 |
| 1.3.6 Recent results on production and CNM effects of open charm at LHC..... | 24 |
| 1.4 Thesis motivation and structure | 31 |
| 1.4.1 Thesis motivation | 31 |
| 1.4.2 Thesis structure | 31 |
| CHAPTER 2 LHCb EXPERIMENT | 32 |
| 2.1 Large Hadron Collider | 32 |
| 2.2 LHCb Detector..... | 35 |
| 2.2.1 Magnet System | 36 |
| 2.2.2 Tracking System..... | 37 |
| 2.2.3 PID System..... | 43 |
| 2.2.4 Trigger | 48 |
| 2.2.5 LHCb Data Flow | 50 |
| CHAPTER 3 ANALYSIS STRATEGY | 52 |
| 3.1 Data and simulation samples..... | 52 |
| 3.2 Strategy to measure the production cross-sections..... | 56 |

TABLE OF CONTENTS

| | |
|---|-----|
| 3.3 Strategy to study cold nuclear matter effects..... | 57 |
| 3.4 Strategy to study the cross-section ratios..... | 58 |
| CHAPTER 4 MEASUREMENT OF D^+ AND D_s^+ PRODUCTIONS IN p Pb COLLISIONS | 59 |
| 4.1 Event selections..... | 59 |
| 4.1.1 Stripping..... | 59 |
| 4.1.2 Offline selections | 61 |
| 4.2 Prompt yield extraction | 64 |
| 4.2.1 Inclusive yield determination | 64 |
| 4.2.2 Prompt yield determination | 68 |
| 4.3 Acceptance | 74 |
| 4.4 Reconstruction and selection efficiency | 76 |
| 4.4.1 Truth matching efficiency | 76 |
| 4.4.2 Tracking efficiency | 78 |
| 4.4.3 Dependence on multiplicity..... | 78 |
| 4.5 Particle identification efficiency | 85 |
| 4.6 Total efficiency..... | 89 |
| 4.7 Systematic uncertainties | 91 |
| 4.7.1 Signal yield systematic uncertainty | 91 |
| 4.7.2 Simulation sample size uncertainty..... | 95 |
| 4.7.3 Kinematic distribution..... | 95 |
| 4.7.4 Tracking and multiplicity correction..... | 96 |
| 4.7.5 PID calibration table | 100 |
| 4.7.6 Other systematic uncertainties..... | 101 |
| 4.7.7 Summary of systematic uncertainties..... | 101 |
| CHAPTER 5 RESULTS | 102 |
| 5.1 Open charm production cross-sections | 102 |
| 5.2 Nuclear modification factors | 107 |
| 5.3 Forward-backward ratio | 111 |
| 5.4 Cross-section ratios between D mesons | 114 |
| CHAPTER 6 SUMMARY AND OUTLOOK | 119 |
| 6.1 Summary..... | 119 |

TABLE OF CONTENTS

6.2 Outlook 121

REFERENCES 125

APPENDIX A SUPPLEMENTARY MATERIAL..... 136

ACKNOWLEDGEMENTS..... 152

声 明..... 153

RESUME..... 154

COMMENTS FROM THESIS SUPERVISOR..... 155

RESOLUTION OF THESIS DEFENSE COMMITTEE 156

LIST OF FIGURES AND TABLES

| | | |
|-------------|---|----|
| Figure 1.1 | Categories of elementary particles in SM. This figure is taken from Ref. [5]. | 1 |
| Figure 1.2 | Summary of experimentally measured running coupling constants α_s as a function of the energy scale, Q . This figure is taken from Ref. [8]. | 3 |
| Figure 1.3 | Schematic QCD phase diagram at finite temperature and baryon number density. This figure is taken from Ref. [13]. | 4 |
| Figure 1.4 | Space-time evolution of relativistic heavy-ion collisions. | 6 |
| Figure 1.5 | Charm quark pair production diagrams. This figure is taken from Ref. [22]. | 8 |
| Figure 1.6 | The pQCD factorization approach in high-energy collisions. This figure is taken from Ref. [32]. | 9 |
| Figure 1.7 | PDFs of protons, at the energy scales of $Q^2 = 10 \text{ GeV}^2$ (left) and $Q^2 = 10^4 \text{ GeV}^2$ (right), respectively. This figure is taken from Ref. [33]. | 10 |
| Figure 1.8 | Schematic geometry of proton-nucleus (pA) collisions and nucleus-nucleus (AB) collisions. | 12 |
| Figure 1.9 | Elastic and inelastic cross-section of pp collisions at different energies. This figure is taken from Ref. [20]. | 13 |
| Figure 1.10 | R_{pPb} for heavy-flavor electron jets with the jet radii $R = 0.3, 0.4$ and 0.6 at ALICE. The figure is taken from Ref. [42]. | 15 |
| Figure 1.11 | Nuclear modification factors R_{AA} and R_{pPb} for D^0 -tagged jets (left) and R_{AA} for D^0 -tagged jets, charge particles jets and D mesons (right). These figures are taken from Ref. [42]. | 15 |
| Figure 1.12 | Enhanced yield of strange hadrons as a function of multiplicity $\langle dN_{ch}/d\eta \rangle$ in ALICE pp , pPb and $PbPb$ experiments (left); D_s^+/D^0 ratio in AuAu collisions compared with pp simulation Pythia and data as a function of transverse momentum p_T (right). The figures are taken from Ref. [45] and Ref. [47], respectively. | 17 |
| Figure 1.13 | $R_i^A(x, Q^2)$ calculated by EPS09, EPPS16 and DSSZ at $Q^2 = 10 \text{ GeV}^2$. Figure (a), figure (b), and figure (c) represent the results for valence quarks, sea quarks, and gluons, respectively. These figures are taken from Ref. [59]. | 19 |

LIST OF FIGURES AND TABLES

| | | |
|-------------|--|----|
| Figure 1.14 | PDF evolution with x and Q (left); the evolution of the saturation energy scale Q_s with $A^{1/3}$ and x^λ (right). The figures are taken from Ref. [69] and Ref. [70], respectively..... | 21 |
| Figure 1.15 | Production process of heavy quark pairs at LO. Here, $k_{1\perp}$, $k_{2\perp}$ and k_\perp represents the transverse momentum of different gluons, and p_\perp and q_\perp represents the transverse momentum of quarks (c) and antiquarks (\bar{c}). The figure is taken from Ref. [59]..... | 22 |
| Figure 1.16 | Nuclear modification factor of J/ψ and D as a function of rapidity based on the CGC framework. The figure is taken from Ref. [72-73]..... | 22 |
| Figure 1.17 | Prompt D mesons cross-sections in pp collisions at 5.02 TeV from LHCb (top, middle) and ALICE (bottom) compared with the predictions in collinear factorization frameworks (POWHEG+NNPDF3.0L, FONLL or GMVFNS). The figures are taken from Ref. [30] and Ref. [31], respectively. | 25 |
| Figure 1.18 | Ratios of different D mesons cross-sections in pp collisions from LHCb (left) and in pPb collisions from ALICE (right) at 5.02 TeV. The figures are taken from Ref. [30] and Ref. [90], respectively. | 26 |
| Figure 1.19 | Nuclear modification factor R_{pPb} of average D^0 , D^+ , D^{*+} (left) and μ^\pm from heavy-flavor decay (right) as a function of p_T . The figures are taken from Ref. [90] and Ref. [99], respectively. | 26 |
| Figure 1.20 | Nuclear modification factor R_{pPb} (left) and the forward-backward ratio R_{FB} (right) of D^0 as a function of the rapidity y^* . The figures are taken from Ref. [97]. | 28 |
| Figure 1.21 | Phase space coverage of charged hadrons in pPb collisions at $\sqrt{s_{NN}} = 5.02$ TeV from LHC and other experiments, including CMS ^[111] , ATLAS ^[112] , ALICE ^[113] , PHENIX ^[114] and PHOBOS ^[115] . The saturation region of Pb is taken from Ref. [116-117]. The figure is taken from Ref. [118]. | 29 |
| Figure 1.22 | Results of $R_i^A(x, Q^2)$ computed by nNNPDF3.0 set with and without D^0 cross-section at LHCb as input. The figure is taken from Ref. [125]..... | 30 |
| Figure 2.1 | Schematic diagram of the LHC and its accessories. | 33 |
| Figure 2.2 | Integrated luminosities of pPb and $PbPb$ collisions collected during the LHCb Run 1 and Run 2 periods..... | 34 |

LIST OF FIGURES AND TABLES

| | | |
|-------------|---|----|
| Figure 2.3 | Outgoing angles of b and \bar{b} hadrons in pp collisions at LHC (from Pythia simulation). | 35 |
| Figure 2.4 | Layout of the LHCb detector: the z-axis is in parallel with the beam direction, the y-axis is vertically upward, and the x-, y- and z-axes form the right-hand coordinate system. | 35 |
| Figure 2.5 | Magnet system of LHCb (left) and the magnetic field strength B_y along the z axis for both polarities (right). These figures are taken from Ref. [126]. | 36 |
| Figure 2.6 | Cross-section at $y = 0$ of the VELO silicon sensors in the fully closed status. The bottom left and right figures show the front faces of the most upstream VELO station in the closed and open status, respectively. The figure is taken from Ref. [132]. | 37 |
| Figure 2.7 | Structure of the third TT layer. Different readout sectors are indicated with different colors. | 38 |
| Figure 2.8 | LHCb tracking system(TT, T1-T3). The purple part is TT and IT, which are made of silicon microstrip sensors, and the green part is the OT. | 39 |
| Figure 2.9 | Structure of the second IT layer along the x-axis (left); and cross section of a OT straw-tube module (right). | 39 |
| Figure 2.10 | Different types of reconstructed tracks and the corresponding magnetic field strength B_y along the z-axis. | 40 |
| Figure 2.11 | Relative momentum resolution of the 2011 data. This figure is taken from Ref. [137]. | 42 |
| Figure 2.12 | Long track reconstruction efficiency as a function of momentum p (left) and pseudo-rapidity η (right). | 42 |
| Figure 2.13 | Variations of the Cherenkov angle θ_c with momentum for various charged particles in three different materials used in LHCb RICH detectors. | 44 |
| Figure 2.14 | Schematic layout of the RICH1 detector in the y-z plane (left); schematic layout of the RICH2 detector in the x-z plane (right). | 45 |
| Figure 2.15 | Side view of the LHCb muon system. | 47 |
| Figure 2.16 | LHCb trigger diagram in pp collisions during Run 1. | 48 |
| Figure 2.17 | LHCb data flow and the corresponding applications. | 49 |
| Figure 3.1 | The nVeloClusters distributions from the original and multiplicity-fixed D^+ (top) and D_s^+ (bottom) simulation samples, and compared to those from real data. | 55 |

LIST OF FIGURES AND TABLES

| | | |
|-------------|---|----|
| Figure 4.1 | Definition of the $K^- K^+$ mass windows ΔM used by the CLEO collaboration (top) and their corresponding branching ratios (bottom). The figure is taken from Ref. [159]. | 63 |
| Figure 4.2 | $M(K^- \pi^+ \pi^+)$ distribution fit results in the kinematic range of $2 < p_T < 3 \text{ GeV}/c$, $2.5 < y^* < 3.0$ for the forward (left) data sample and $2 < p_T < 3 \text{ GeV}/c$, $-4.0 < y^* < -3.5$ for the backward (right) data sample. | 65 |
| Figure 4.3 | $M(K^- K^+ \pi^+)$ distribution fit results in the kinematic range of $2 < p_T < 3 \text{ GeV}/c$, $2.5 < y^* < 3.0$ for the forward (left) data sample and $2 < p_T < 3 \text{ GeV}/c$, $-4.0 < y^* < -3.5$ for the backward (right) data sample. | 66 |
| Figure 4.4 | Inclusive D^+ signal yields as a function of p_T and y^* in the forward (left) and backward (right) rapidity regions. | 67 |
| Figure 4.5 | Inclusive D_s^+ signal yields as a function of p_T and y^* in the forward (left) and backward (right) rapidity regions. | 67 |
| Figure 4.6 | Topology of the decay $D^+ \rightarrow K^- \pi^+ \pi^+$ from a B hadron. | 68 |
| Figure 4.7 | Difference of μ between the non-prompt and prompt simulated samples of D^+ in the forward (left) and backward (right) configurations. | 70 |
| Figure 4.8 | Difference of μ between the non-prompt and prompt simulated samples of D_s^+ in the forward (left) and backward (right) configurations. | 70 |
| Figure 4.9 | The $\log_{10} \chi_{\text{IP}}^2(D^+)$ distribution fit results in bin of $2 < p_T < 3 \text{ GeV}/c$, $2.5 < y^* < 3.0$ in the forward (left) data sample and $2 < p_T < 3 \text{ GeV}/c$, $-4.0 < y^* < -3.5$ in the backward (right) data sample. | 71 |
| Figure 4.10 | The $\log_{10} \chi_{\text{IP}}^2(D_s^+)$ distribution fit results in bin of $2 < p_T < 3 \text{ GeV}/c$, $2.5 < y^* < 3.0$ in the forward (left) data sample and $2 < p_T < 3 \text{ GeV}/c$, $-4.0 < y^* < -3.5$ in the backward (right) data sample. | 71 |
| Figure 4.11 | Prompt signal yields obtained from the $\log_{10} \chi_{\text{IP}}^2(D^+)$ fit in the forward (left) and backward (right) rapidity regions. Statistical uncertainties only. | 72 |
| Figure 4.12 | Prompt signal yields obtained from the $\log_{10} \chi_{\text{IP}}^2(D_s^+)$ fit in the forward (left) and backward (right) rapidity regions. Statistical uncertainties only. | 72 |
| Figure 4.13 | Prompt fractions of D^+ as a function of p_T and y^* in the forward (left) and backward (right) configurations. | 73 |

LIST OF FIGURES AND TABLES

| | | |
|-------------|--|----|
| Figure 4.14 | Prompt fractions of D_s^+ as a function of p_T and y^* in the forward (left) and backward (right) configurations. | 73 |
| Figure 4.15 | Geometrical acceptance efficiency ϵ_{acc} of prompt D^+ as a function of p_T and y^* in the forward (left) and backward (right) configurations. Statistical uncertainties only. | 75 |
| Figure 4.16 | Geometrical acceptance efficiency ϵ_{acc} of prompt D_s^+ as a function of p_T and y^* in the forward (left) and backward (right) configurations. Statistical uncertainties only. | 75 |
| Figure 4.17 | Invariant mass distributions of $D^+ \rightarrow K^- \pi^+ \pi^+$ decays that are not truth matched for the forward (left) and backward (right) simulation samples, respectively. | 77 |
| Figure 4.18 | Invariant mass distributions of $D_s^+ \rightarrow K^- K^+ \pi^+$ decays that are not truth matched for the forward (left) and backward (right) simulation samples, respectively. | 77 |
| Figure 4.19 | Tracking efficiency table (2012) as a function of p and η | 79 |
| Figure 4.20 | Distributions of nTracks, nVeloClusters, nTstations, nTTClusters and nLongTracks in forward (left) or backward (right) sWeighted data and simulated samples for D^+ . Both the distributions of sWeighted data and simulated samples are displayed. For simulated events, the raw distributions and reweighted distributions are shown. | 80 |
| Figure 4.21 | Distributions of nTracks, nVeloClusters, nTstations, nTTClusters and nLongTracks in forward (left) or backward (right) sWeighted data and simulated samples for D_s^+ . Both the distributions of sWeighted data and simulated samples are displayed. For simulated events, the raw distributions and reweighted distributions are shown. | 81 |
| Figure 4.22 | The D^+ reconstruction and selection efficiencies $\epsilon(x)$ and their fit results as a function of multiplicity (nTracks, nVeloClusters and nTstations) for the backward configuration. | 82 |
| Figure 4.23 | Correction factors α_{corr} of D^+ reconstruction and selection efficiencies in each p_T and y^* bin in the forward (left) and backward (right) rapidity regions. | 83 |

LIST OF FIGURES AND TABLES

| | | |
|-------------|--|----|
| Figure 4.24 | Correction factors α_{corr} of D_s^+ reconstruction and selection efficiencies in each p_T and y^* bin in the forward (left) and backward (right) rapidity regions..... | 84 |
| Figure 4.25 | Corrected reconstruction and selection efficiency of prompt D^+ as a function of p_T and y^* in forward (left) and backward (right). Only statistical uncertainties are shown. | 84 |
| Figure 4.26 | Corrected reconstruction and selection efficiency of prompt D_s^+ as a function of p_T and y^* in forward (left) and backward (right) configurations. Only statistical uncertainties are shown. | 84 |
| Figure 4.27 | The $D_{(s)}^+$ nVeloClusters distributions of simulation, sWeighted data and D^0 calibration sample in the forward (left) and backward (right) rapidity regions..... | 86 |
| Figure 4.28 | The reweighted $D_{(s)}^+$ nVeloClusters distributions of simulation, D^0 calibration sample and sWeighted data in the forward (left) and backward (right) rapidity regions. | 87 |
| Figure 4.29 | The D^+ single-track PID efficiency for K and π in bins of (p, η) for $p\text{Pb}$ forward (left) and backward (right) collisions. Statistical uncertainties only. | 87 |
| Figure 4.30 | The D_s^+ single-track PID efficiency for K and π in bins of (p, η) for $p\text{Pb}$ forward (left) and backward (right) collisions. Statistical uncertainties only. | 88 |
| Figure 4.31 | Particle identification efficiency ϵ_{PID} of prompt D^+ , as a function of p_T and y^* in the forward (left) and backward (right) collision samples. Statistical uncertainties only. | 88 |
| Figure 4.32 | Particle identification efficiency ϵ_{PID} of prompt D_s^+ , as a function of p_T and y^* of prompt D_s^+ in the forward (left) and backward (right) collision samples. Statistical uncertainties only. | 89 |
| Figure 4.33 | Total efficiency ϵ_{tot} of prompt D^+ as a function of p_T and y^* for both forward (left) and backward (right) configurations. | 89 |
| Figure 4.34 | Total efficiency ϵ_{tot} of prompt D_s^+ as a function of p_T and y^* for both forward (left) and backward (right) configurations. | 90 |
| Figure 4.35 | Relative systematic uncertainty (%) related to invariant mass fit of D^+ in bins of p_T and y^* in the forward (left) and backward (right) configurations. | 92 |

LIST OF FIGURES AND TABLES

| | | |
|-------------|---|-----|
| Figure 4.36 | Relative systematic uncertainty (%) related to invariant mass fit of D_s^+ in bins of p_T and y^* in the forward (left) and backward (right) configurations.92 | 92 |
| Figure 4.37 | Relative systematic uncertainties (%) due to $\log_{10} \chi_{\text{IP}}^2 (D^+)$ fit in bins of p_T and y^* in the forward (left) and backward (right) configurations. | 93 |
| Figure 4.38 | Relative systematic uncertainties (%) due to $\log_{10} \chi_{\text{IP}}^2 (D_s^+)$ fit in bins of p_T and y^* in the forward (left) and backward (right) configurations. | 94 |
| Figure 4.39 | Relative systematic uncertainties (%) due to the limited simulation sample size of D^+ as a function of p_T and y^* in the forward (left) and backward (right) configurations..... | 95 |
| Figure 4.40 | Relative systematic uncertainties (%) due to the limited simulation sample size of D_s^+ as a function of p_T and y^* in the forward (left) and backward (right) configurations..... | 95 |
| Figure 4.41 | Comparisons of p_T and y^* distributions between D^+ data and MC samples in the forward (left) and backward (right) configurations..... | 96 |
| Figure 4.42 | The D^+ reconstruction and selection efficiencies in each p_T and y^* bin corrected by five multiplicities (nTracks, nVeloClusters, nTstations, nTTClusters and nLongTracks) in the forward configuration, respectively. | 97 |
| Figure 4.43 | The D^+ reconstruction and selection efficiencies in each p_T and y^* bin corrected by five multiplicities (nTracks, nVeloClusters, nTstations, nTTClusters and nLongTracks) in the backward configuration, respectively. | 98 |
| Figure 4.44 | The D_s^+ reconstruction and selection efficiencies in each p_T and y^* bin corrected by five multiplicities (nTracks, nVeloClusters, nTstations, nTTClusters and nLongTracks) in the forward configuration, respectively. | 98 |
| Figure 4.45 | The D_s^+ reconstruction and selection efficiencies in each p_T and y^* bin corrected by five multiplicities (nTracks, nVeloClusters, nTstations, nTTClusters and nLongTracks) in the backward configuration, respectively. | 99 |
| Figure 5.1 | Double-differential cross-section of prompt D^+ mesons in proton-lead collisions at $\sqrt{s_{\text{NN}}} = 5.02$ TeV for the forward (left) and backward (right) rapidities. The error bar is the statistical uncertainty and the box represents the systematic uncertainty..... | 102 |

LIST OF FIGURES AND TABLES

| | | |
|-------------|---|-----|
| Figure 5.2 | Double-differential cross-section of prompt D_s^+ mesons in proton-lead collisions at $\sqrt{s_{\text{NN}}} = 5.02$ TeV for the forward (left) and backward (right) rapidities. The error bar is the statistical uncertainty and the box represents the systematic uncertainty. | 103 |
| Figure 5.3 | One-dimensional cross-section of prompt D^+ as a function of p_T (left) or y^* (right) in the forward and backward configurations. | 105 |
| Figure 5.4 | One-dimensional cross-section of prompt D_s^+ as a function of p_T (left) or y^* (right) in the forward and backward configurations. | 105 |
| Figure 5.5 | Prompt D^+ nuclear modification factors as a function of p_T in the forward (left) and backward (right) rapidity bins. The error bar on each data point denotes the statistical uncertainty, whereas the box represents the systematic uncertainty. | 107 |
| Figure 5.6 | Prompt D_s^+ nuclear modification factors as a function of p_T in the forward (left) and backward (right) rapidity bins. The error bar on each data point denotes the statistical uncertainty, whereas the box represents the systematic uncertainty. | 107 |
| Figure 5.7 | Nuclear modification factor $R_{p\text{Pb}}$ for prompt D^+ and D_s^+ as a function of p_T for the forward (left) and backward (right) data samples, integrated over the common rapidity range of $2.0 < y^* < 4.0$ (left) and $-4.5 < y^* < -2.5$ (right), respectively. Previous LHCb D^0 results and various model calculations are shown for comparison. | 108 |
| Figure 5.8 | Nuclear modification factor $R_{p\text{Pb}}$ for prompt D^+ and D_s^+ as a function of y^* , integrated over the p_T range of $p_T < 10$ GeV/c. Previous LHCb D^0 results and various model calculations are shown for comparison. | 108 |
| Figure 5.9 | Forward-backward production ratios for prompt D^+ (left) and D_s^+ (right) as a function of p_T in different $ y^* $ bins in $p\text{Pb}$ collisions. | 111 |
| Figure 5.10 | Forward-backward production ratio R_{FB} of $D_{(s)}^+$ as a function of (left) p_T integrated over $2.5 < y^* < 4.0$, (right) as a function of $ y^* $ integrated over $0 < p_T < 14$ GeV/c. Previous D^0 and Λ_c^+ results and various model calculations are shown for comparison. | 112 |
| Figure 5.11 | Cross-section ratio of D^+ to D^0 , R_{D^+/D^0} , as a function of p_T in different y^* bins for the forward (left) and backward (right) $p\text{Pb}$ configurations at 5.02 TeV. | 114 |

LIST OF FIGURES AND TABLES

| | | |
|-------------|--|-----|
| Figure 5.12 | Cross-section ratio of D_s^+ to D^0 , $R_{D_s^+/D^0}$, as a function of p_T in different y^* bins for the forward (left) and backward (right) pPb configurations at 5.02 TeV..... | 114 |
| Figure 5.13 | Cross-section ratio of D_s^+ to D^+ , $R_{D_s^+/D^+}$, as a function of p_T in different y^* bins for the forward (left) and backward (right) pPb configurations at 5.02 TeV..... | 115 |
| Figure 5.14 | R_{D^+/D^0} , $R_{D_s^+/D^0}$ and $R_{D_s^+/D^+}$ ratio as a function of p_T , integrated over the full measured rapidity range in the forward and backward pPb configurations. The previous measurements in pp collisions from LHCb ^[30] and in pp and pPb collisions from ALICE ^[31,90] at 5.02 TeV are also shown for comparisons. | 117 |
| Figure 5.15 | R_{D^+/D^0} , $R_{D_s^+/D^0}$ and $R_{D_s^+/D^+}$ ratio as a function of $ y^* $, integrated over the measured p_T ranges in the forward and backward pPb configurations. The previous measurements in pp collisions from LHCb ^[30] at 5.02 TeV are also shown for comparisons. | 118 |
| Figure 6.1 | Open charm cross-section ratios of $R_{13/7}(D^+)+m$ and $R_{13/5}(D_s^+)+m$ in 5 TeV pp collisions at LHCb, where m represents a 10^{-m} scaling of the result. Then figures are taken from Ref. [30] and Ref. [79], respectively..... | 122 |
| Figure 6.2 | Phase space range covered by fixed-target experiments (left); the nCTEQ15 nPDFs before (red) and after (green, blue and yellow) the reweighting are predicted by AFTER Group using D^0 production with different factorization scales μ_F (right). These figures are taken from Ref. [169] and Ref. [170], respectively..... | 124 |
| Table 1.1 | Examples of open charm (D^0 , D^+ , D^{*+} or D_s^+) cross-sections in pp collisions at LHC..... | 23 |
| Table 1.2 | Nuclear modification factors R_{pPb} of charm hadrons in pPb collisions at LHC. 27 | |
| Table 1.3 | Phase space cover regions in terms of Bjorken x_F at some fixed-target experiments..... | 29 |
| Table 2.1 | Number of muon stations needed to trigger "IsMuon" in different momentum intervals. The table is taken from Ref. [143]. | 46 |
| Table 3.1 | Simulation samples for the decay mode $D^+ \rightarrow K^- \pi^+ \pi^+$ | 53 |

LIST OF FIGURES AND TABLES

| | | |
|-----------|---|-----|
| Table 3.2 | Simulation samples for the decay mode $D_s^+ \rightarrow K^- K^+ \pi^+$ | 54 |
| Table 4.1 | Stripping selections of $D_{(s)}^+$ candidates..... | 61 |
| Table 4.2 | Offline selections of $D_{(s)}^+$ candidates..... | 63 |
| Table 4.3 | Fixed parameter values and their errors when fitting an invariant mass distribution of data sample. | 65 |
| Table 4.4 | Fixed parameter values and their errors when fitting a $\log_{10} \chi_{\text{IP}}^2(D_{(s)}^+)$ distribution of background-subtracted data. A parameter with the indicator “1” belongs to the Bukin function of the prompt component; a parameter with the indicator “2” belongs to the Bukin function of the non-prompt component..... | 69 |
| Table 4.5 | Summary of systematic and statistical uncertainties (%). | 101 |
| Table 5.1 | Data values of the double-differential cross-section (mb) of prompt D^+ in proton-lead collisions at $\sqrt{s_{\text{NN}}} = 5.02$ TeV in each (p_{T}, y^*) bin for forward and backward rapidities. The first uncertainty reflects statistical uncertainty, the second represents uncorrelated systematic uncertainty between bins, and the third represents correlated uncertainty. | 103 |
| Table 5.2 | Data values of the double-differential cross-section (mb) of prompt D_s^+ in proton-lead collisions at $\sqrt{s_{\text{NN}}} = 5.02$ TeV in each (p_{T}, y^*) bin for forward and backward rapidities. The first uncertainty reflects statistical uncertainty, the second represents uncorrelated systematic uncertainty between bins, and the third represents correlated uncertainty. | 104 |
| Table 5.3 | Nuclear modification factor of D^+ in different p_{T} range, integrated over the rapidity range of $2.0 < y^* < 4.0$ in the forward (left) configuration and $-4.5 < y^* < -2.5$ in the backward (right) configuration. The first and second uncertainties are statistical and systematic, respectively. | 110 |
| Table 5.4 | Nuclear modification factor of D_s^+ in different p_{T} range, integrated over the rapidity range of $2.0 < y^* < 4.0$ in the forward (left) configuration and $-4.5 < y^* < -2.5$ in the backward (right) configuration. The first and second uncertainties are statistical and systematic, respectively. | 110 |
| Table 5.5 | Forward-backward production ratio R_{FB} for D^+ in different p_{T} range (top), integrated over the common rapidity range of $2.5 < y^* < 4.0$; in different $ y^* $ range (bottom) integrated over $0 < p_{\text{T}} < 14$ GeV/c. The first error is statistical, while the second is systematic..... | 112 |

LIST OF FIGURES AND TABLES

| | | |
|-----------|---|-----|
| Table 5.6 | Forward-backward production ratio R_{FB} for D_s^+ in different p_{T} range (top), integrated over the common rapidity range of $2.5 < y^* < 4.0$; in different $ y^* $ range (bottom) integrated over $0 < p_{\text{T}} < 14 \text{ GeV}/c$. The first error is statistical, while the second is systematic..... | 113 |
| Table 6.1 | Integrated luminosities in $p\text{Pb}$ collisions and the corresponding pp reference at LHCb from Run 2 to Run 4. | 121 |

CHAPTER 1 INTRODUCTION

1.1 Standard Model and Quantum Chromodynamics

The dynamics of the universe is governed by four (known) fundamental forces including strong, weak, electromagnetic interactions and gravitation^[1]. Originated in the 1970s, the Standard Model (SM) has turned into a precise theory that describes the strong and electroweak interactions between the elementary constituents of matter, and serves as the cornerstone of understanding the microscopic world.

The elementary particles in SM, as summarized in Fig. 1.1, include three generations of quarks and leptons, gauge bosons, and scalar bosons. Quarks and leptons with their antiparticles are the essential components of matter or antimatter, and gauge bosons mediate the strong and electroweak interactions. The Higgs boson, first predicted by Peter Higgs and François Englert in 1964^[2] and discovered at the LHC of CERN in 2012^[3-4], is an essential piece of the SM jigsaw that leads to spontaneous breaking of electroweak symmetry and endows elementary particles with mass.

Based on group theory, SM is mathematically described by gauge field theory satisfying the local gauge symmetry of $U(1) \otimes SU(2) \otimes SU(3)_C$. In 1968, Glashow, Salam, and Weinberg unified quantum electrodynamics (QED) and weak interactions with the electroweak theory^[6], which uses $U(1) \otimes SU(2)$ as the gauge group. Quantum chromodynamics (QCD) is a non-Abelian quantum gauge field theory with the gauge group

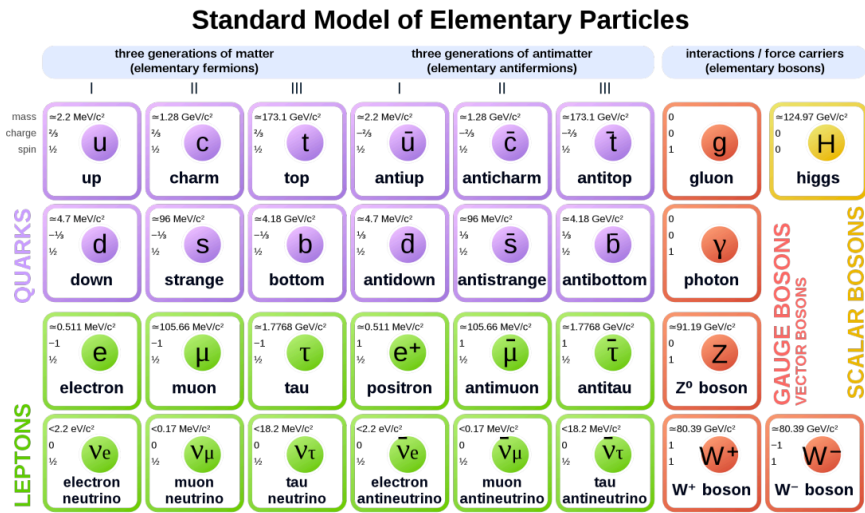


Figure 1.1 Categories of elementary particles in SM. This figure is taken from Ref. [5].

of $SU(3)_C$, where C denotes color, the basic charge of strong interaction. Quarks, together with gluons, are the fundamental degrees of freedom in QCD. The basic representation of the $SU(3)_C$ symmetry group is formed by quarks carrying three different color charges. Quark also has a flavor degree of freedom, which is separated into three generations, namely (u, d) , (c, s) and (t, b) . Different flavors have different masses but the same color interactions. Gluons are gauge bosons that mediate color interactions, and they themselves carry eight different color charges, which form an adjoint representation of the color $SU(3)_C$ symmetry group.

The Lagrangian of QCD is

$$\mathcal{L}_{QCD} = \bar{\psi}_q^i (i\gamma^\mu) (D_\mu)_{ij} \psi_q^j - m_q \bar{\psi}_q^i \psi_q^i - \frac{1}{4} F_{\mu\nu}^A F^{A\mu\nu}, \quad (1.1)$$

where γ^μ is the Dirac matrix, and ψ_q^i denotes the Dirac spinor field of a quark with color i and flavor q . $F_{\mu\nu}^A$ ($A = 1, 2, \dots, 8$) is the gluon field strength tensor with

$$F_{\mu\nu}^A = \partial_\mu \mathcal{A}_\nu^A - \partial_\nu \mathcal{A}_\mu^A - g_s f_{ABC} \mathcal{A}_\mu^B \mathcal{A}_\nu^C, \quad (1.2)$$

where \mathcal{A}_μ^A is the gluon field, g_s is the color coupling (analogous to e in QED) and f_{ABC} is the structural constant of the $SU(3)_C$ group. The covariant derivation D_μ connects the quark field to the gluon field, which is defined as

$$(D_\mu)_{ij} = \delta_{ij} \partial_\mu - i g_s \lambda_{ij}^a / 2 \mathcal{A}_\mu^a, \quad (1.3)$$

with λ^a denoting the Gell-Mann matrices^[7].

QED is an Abelian gauge field theory based on $U(1)$ gauge symmetry. The photon which mediates the electromagnetic force is electrically neutral. Hence there are no direct photon-photon coupling in QED Lagrangian. However, gluons, as the mediators of strong interactions, carry color charges, hence interact strongly with each other. This is reflected as the non-Abelian nature of QCD in the direct self-coupling of the gluon field in $F_{\mu\nu}^A$.

As in other renormalizable field theory like QED, the ‘‘running coupling constant’’ α_s ($\equiv g_s^2/(4\pi)$) in QCD, describing the strong interaction’s strength, does not remain fixed but instead moves with the momentum transfer, Q^2 . As Q^2 increases, α in QED increases. But due to self-interaction of gluons in QCD, the variation of α_s with Q^2 is quite different from that of α ,

$$\alpha_s(Q^2) \approx \frac{12\pi}{\beta_0 \ln(Q^2/\Lambda_{QCD}^2)}, \quad (1.4)$$

where Λ_{QCD} (~ 200 MeV) is the energy scale of QCD, and $\beta_0 = 33 - 2N_f$ is a constant larger than 0 with N_f indicating the number of quark flavors.

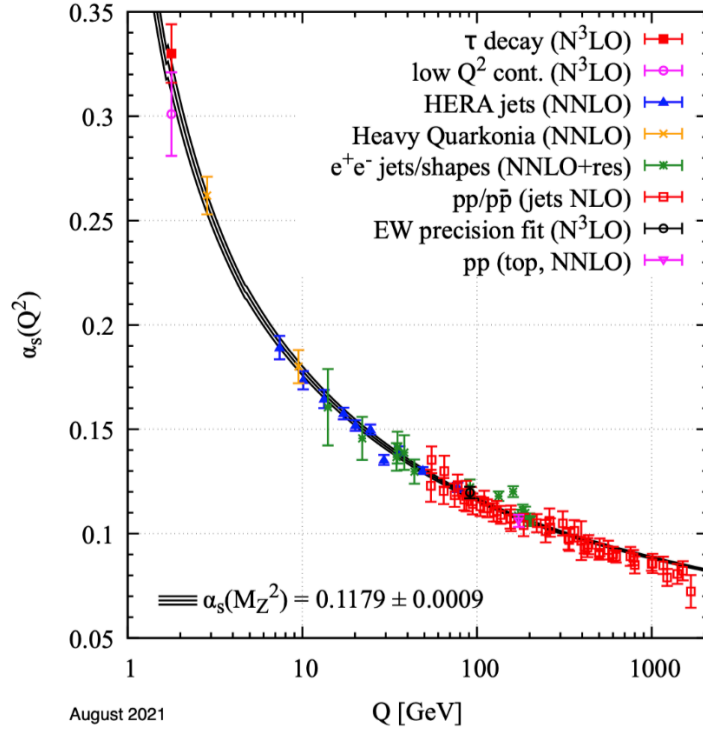


Figure 1.2 Summary of experimentally measured running coupling constants α_s as a function of the energy scale, Q . This figure is taken from Ref. [8].

As shown in Fig. 1.2, α_s depends strongly on Q^2 . When the energy scale Q^2 is small (or the distance scale is large, the corresponding QCD process is called the “soft process”), $\alpha_s(Q^2)$ is large (close to unity) and perturbation expansion cannot be used. On the contrary, in “hard process” where the energy scale Q^2 is large (or the distance scale is small), $\alpha_s(Q^2)$ gets small, and the interaction between quarks and gluons becomes weak. This is the “asymptotically free” property of QCD which was discovered by Gross, Politzer^[9], and Wilczek^[10] in 1973. Due to the “asymptotic freedom”, hard processes at large energy scales can be calculated using perturbative QCD (pQCD). However, the soft processes at small energy scales can only be solved by non-perturbative methods such as lattice QCD^[11] (LQCD).

In QCD, color (or quark) confinement refers to the phenomenon that quarks/gluons (that carry color charges) cannot be isolated and thus cannot be detected under normal experimental situations^[12]. In other words, quarks/gluons must be bounded together to form hadrons. The interactions between quarks/gluons inside hadrons are soft processes, hence there is not yet a strict proof of confinement from QCD. However, LQCD predicts that the deconfinement would occur at high temperature (under zero baryon number density). In this circumstance, quarks and gluons will be liberated from hadrons and form directly

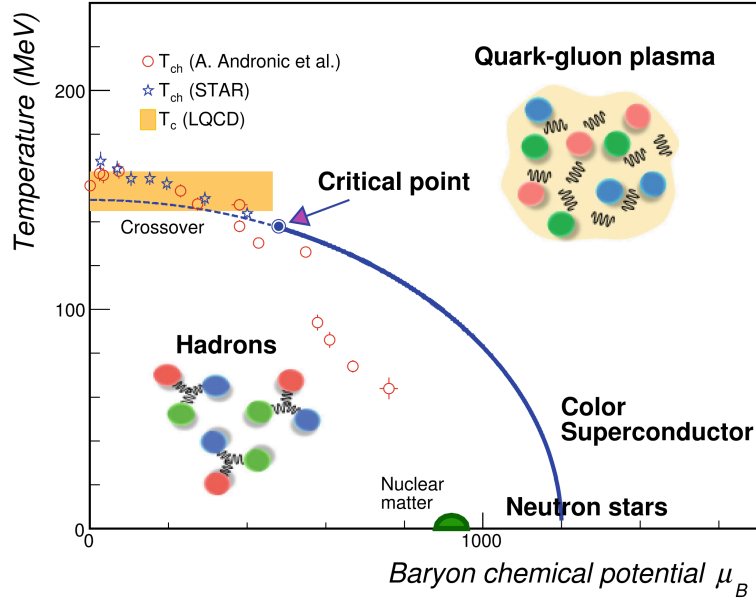


Figure 1.3 Schematic QCD phase diagram at finite temperature and baryon number density. This figure is taken from Ref. [13].

a new state of matter, called Quark-Gluon Plasma (QGP)^[14]. The critical temperature for the phase transition (or smooth crossover) from hadron gas to QGP is approximately 170 MeV, and the chiral symmetry restoration phase transition also occurs at roughly the same temperature^[15-17].

In considering also the case at finite baryon number density (or baryon chemical potential, μ_B), the phase diagram of QCD is shown in Fig. 1.3, which can be roughly divided into three regions:

- (1) low-temperature and low-density region: the system is in the “color confinement” phase, where only hadronic matter exists.
- (2) high-temperature region: the system is in the QGP phase, with quarks and gluons as the basic degrees of freedom.
- (3) low-temperature and high-density region: the system may be in the color superconducting phase or other phases with light quarks as the basic degrees of freedom.

LQCD calculations predict the existence of a critical point in QCD phase diagram at $\mu_B \approx 360$ MeV and temperature $T \approx 162$ MeV. The phase transition is of second order at this point, and long wavelength fluctuations occur, leading specific experimental results analogous to critical opalescence^[13].

At higher μ_B , the QCD models predict a first-order phase transition^[18]. However the transition from hadronic gas to QGP at lower μ_B seems to be a continuous or smooth crossover^[19]. The exploration of QCD phase diagram and the search for QCD critical

point at finite density are currently hot topics in theoretical and experimental studies.

1.2 QGP and heavy-ion collisions

According to the Big Bang theory, the cosmos might be in the state of QGP with nearly zero baryon chemical potential during a short period of 10^{-11} to 10^{-6} s after its formation. It eventually evolved into the current universe after a protracted period of expansion and cooling. On the other hand, the deconfinement at high baryon density may happen in the interior of compact celestial bodies such as neutron stars. The quantitative studies on QCD phase transition and QGP properties will certainly lead to better understandings in these fields.

In line with the QCD phase diagram, there are two ways to induce the transition from hadronic phase to QGP:

(1) To compress the normal nuclear matter and keep increasing μ_B . The nucleon wave functions will be gradually overlapped and a quark-gluon color-deconfined state of matter will be produced eventually when the μ_B reaches a critical value.

(2) To modify the vacuum's characteristics by keep increasing the system's temperature T such that more and more quark-antiquark pairs (or hadrons) are excited from the quantum fields. Due to the overlapping of hadron wave functions, quarks and gluons will eventually appear as the fundamental constituents.

Heavy-ion (or heavy nucleus-nucleus) collision experiments are the only opportunity on Earth to achieve deconfinement and chiral symmetry restoration phase transitions. In high-energy (or relativistic) heavy-ion collisions at LHC or top RHIC energies, a large fraction of the kinetic energy carried by the nuclei will be deposited in a small volume (similar size to the nucleus) around the collision point, the vacuum in this volume will be heated up to create QGP with nearly zero baryon number density. However, in heavy-ion collisions at lower energies, a large fraction of the baryon number carried by the nuclei will be stopped in this volume, and this may create a deconfined phase with large baryon chemical potential but at lower temperature. Therefore, heavy-ion collisions at different energies can probe a large region of the QCD phase diagram. This thesis will focus on the high energy collisions at LHC only.

As depicted in Fig. 1.4, the five stages in the space-time evolution of relativistic heavy-ion collisions are:

(1) Initial state: The accelerator accelerates the nucleus to near the speed of light.

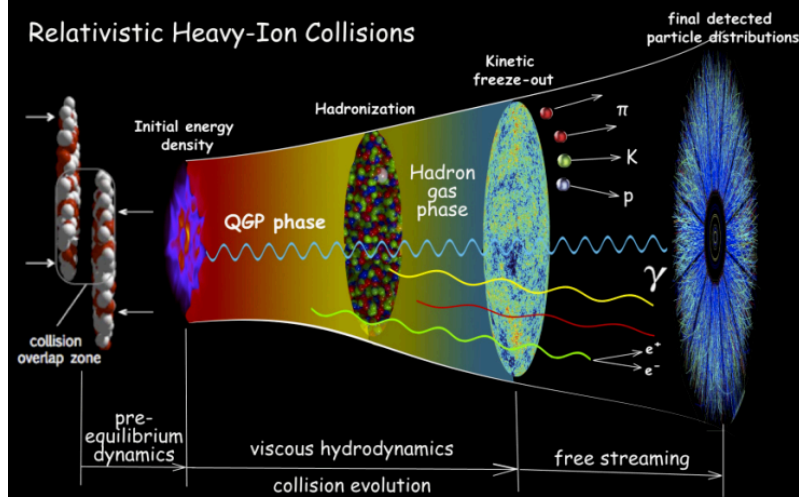


Figure 1.4 Space-time evolution of relativistic heavy-ion collisions.

The nucleus looks like a thin disc in the center of the mass system due to the Lorentz contraction, and the nucleons in the overlapping regions will most likely participate in the subsequent violent reactions. Usually, the Glauber model^[20] can be used to describe the initial collision geometries.

(2) Pre-equilibrium: A large number of quarks and gluons excited by the initial collision will frequently interact through hard or semi-hard processes, causing the quick energy deposition in the fireball and also driving the fireball to attain local thermal equilibrium at a time scale of ~ 1 fm/ c . The degree of freedom and entropy of the system will quickly increase throughout this process. Heavy-flavor quarks are produced at this stage in hard processes.

(3) QGP evolution: When the fireball reaches local thermal equilibrium, it is then in the QGP phase. The partons (quarks and gluons) inside QGP have two types of motions: thermal motions inside a local volume and collective motion along with this volume which is driven by the large pressure gradient between different local volumes. The QGP fireball quickly expand due to collective motion and then cool down. Relativistic viscous hydrodynamics can describe the evolution in this stage.

(4) Hadronization: The fireball continues to expand and cool down. Its temperature decreases gradually to the critical temperature T_c , and the system will undergo a phase transition from quark-gluon plasma to hadron gas.

(5) Freeze-out: The fireball keeps expanding and cooling down after the hadronization. Then chemical freeze-out occurs when inelastic scatterings between hadrons finish, and subsequent collisions between particles will no longer change the particle composition in the hadron gas phase. Thermal or kinetic freeze-out occurs when elastic scatterings

stop, and the momentum of the hadrons will no longer vary and will be measured by detectors.

1.3 Charmed hadrons in heavy-ion collisions

1.3.1 Charmed hadrons as a sensitive probe to QGP

The fireball created in high-energy heavy-ion collision is not a static system. It has an extraordinarily high temperature (about 10^{12} K), a tiny spatial scale (about 10 fm), and survives for just about $10 \text{ fm}/c$ ($\approx 3 \times 10^{-23}$ s) after the collision, making it impossible to study directly. Therefore, in the measured final state, one need to find some specific observables which are sensitive to the early stage of the collisions, and to determine whether the QGP phase has been created there. These observables are called the signatures of QGP, and may be classified into three types.

The first type, which is usually called “hard probe”, is related to the observations about high transverse momentum or heavy flavor hadrons which are produced during the initial hard scattering collisions. The second type is called “soft probe”, and is related to the observations about low transverse momentum hadrons produced by “soft processes” throughout the whole evolution of the fireball. Global features of the strongly-interacting medium can be studied using “soft probes” such as the collective flow^[21]. The third type of signatures is called “electroweak probe”, such as dileptons (directly produced in collisions or decay products of gauge bosons, Z^0 and photons), which can pass through QGP with being negligibly affected by strong interactions.

Charmed hadrons are sensitive hard probes to the properties of QGP created in heavy-ion collisions. At zero temperature, the majority of the mass of light quarks (u, d, s) is due to the spontaneous breaking of QCD’s chiral symmetry, while the mass of heavy quarks is mainly due to electroweak interaction with the Higgs field. Therefore, unlike light quarks, the mass of c quark in QGP (where chiral symmetry is restored) is still substantially larger than the temperature of the medium ($m_c \approx 1.275 \text{ GeV} \gg T \approx (0.3 - 0.5) \text{ GeV}$) created in heavy-ion collisions at RHIC and LHC energies, the thermal production of c quarks in QGP can be ignored. Furthermore, since c quark has a mass significantly larger than the QCD energy scale ($m_c \gg \Lambda_{QCD} \approx 200 \text{ MeV}$), its production by hard scatterings in the early stage can be calculated reliably with pQCD. Because the formation time of the c quarks ($\Delta\tau \approx 1/(2m_c) \approx 0.07 \text{ fm}$) is significantly shorter than that of the QGP, it can go through the entire evolution of the fireball, lose energy due to the frequent and strong

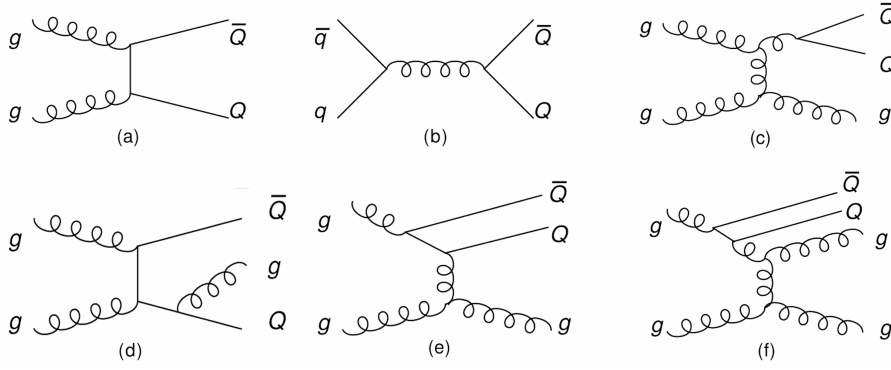


Figure 1.5 Charm quark pair production diagrams. This figure is taken from Ref. [22].

interactions with the medium, and even participate in the collective motion. Therefore, the measurements of charmed hadrons in heavy-ion collisions can provide us valuable information about the properties of QGP.

1.3.2 Charm production in pp collisions

In order to extract the QGP properties with open charm measurements in heavy-ion collisions, it is essential to understand first the open charm production in pp collisions at the same energy, where QGP is not expected due to small system size. The mass of the charm quark works as a long-distance cut-off, allowing the calculation of charm production in the context of pQCD down to very low p_T . Moreover, due to the availability of numerous hard scales (m_c, p_T), the perturbation series could be investigated in various kinematic areas ($p_T < m_c$ or $p_T \gg m_c$).

The primary mechanisms for charm pair production, as described in Fig. 1.5, are as follows: (a) gluon fusion, (b) quark-antiquark annihilation, (c) gluon splitting, (d) quark pair production with gluon emission, (e) flavor excitation, and (f) gluon splitting in combination with flavor excitation.

In pp collisions, charm production at LHC energies can be predicted with the QCD factorization approaches including k_T ^[23] and collinear^[24] factorization.

In k_T factorization framework, charm production can be calculated to the Leading Order (LO) precision with a perturbative expansion of α_s . At LO, charm production is dominated by two sub-processes displayed in Fig. 1.5: (1) $g + g \rightarrow Q + \bar{Q}$, (2) $q + \bar{q} \rightarrow Q + \bar{Q}$. The theoretical prediction of collinear factorization calculates charm production up to the Next-to-Leading Order (NLO) precision. The models of collinear factorization mainly consist of General-Mass Variable-Flavour-Number Scheme (GMVFNS)^[25-26], Positive Weight Hardest Emission Generator (POWHEG)^[27] and “Fixed Order + Next-to-Leading

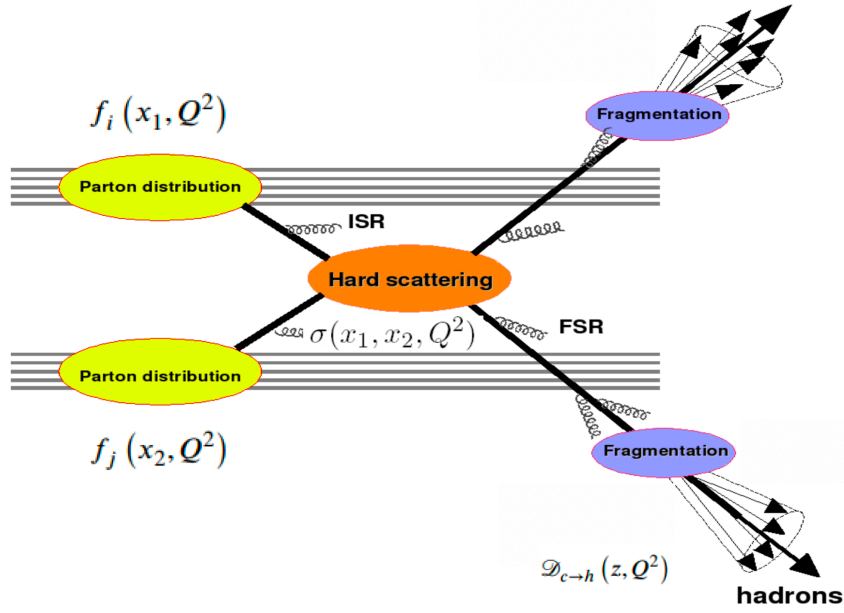


Figure 1.6 The pQCD factorization approach in high-energy collisions. This figure is taken from Ref. [32].

Logarithms” (FONLL)^[28]. The sub-processes in NLO contain the virtual one-loop modification to the LO sub-processes, and the $2 \rightarrow 3$ processes: (1) $g + g \rightarrow Q + \bar{Q} + g$, (2) $q + \bar{q} \rightarrow Q + \bar{Q} + g$, (3) $g + q \rightarrow q + Q + \bar{Q}$ and (4) $g + \bar{q} \rightarrow \bar{q} + Q + \bar{Q}$.

Models based on k_T and collinear factorization describe charm production well within uncertainties in different kinematic regions at LHC. For example, at intermediate to high p_T , k_T factorization calculations show agreement with production for heavy-flavor decay electrons in mid-rapidity at 7 TeV from ALICE^[29]. As shown in Fig. 1.17, the GMVFNS+NNPDF3.0L, FONLL and POWHEG predictions agree with data in pp collisions at 5.02 TeV from LHCb^[30] and ALICE^[31].

As shown in Fig. 1.6, in pp collisions, the single inclusive charm production with transverse momentum and rapidity distributions can be written as a three-term convolution with the pQCD factorization method,

$$d\sigma_{pp \rightarrow h} = f_i(x_1, Q^2) \otimes f_j(x_2, Q^2) \otimes d\sigma_{ij \rightarrow c\bar{c}}(x_1, x_2; Q^2, \alpha_s) \otimes \mathcal{D}_{c \rightarrow h}(z). \quad (1.5)$$

The above three terms are discussed separately below:

- f_i (f_j) is the parton i (j) distribution functions (PDFs) of nucleons, as shown in Fig. 1.7.

Protons are assumed to be composed of many point-like objects, namely partons, which can be either quarks or gluons. Essentially, hadron-hadron collision is a process in which partons interact with each other to produce a large number of

MSTW 2008 NLO PDFs (68% C.L.)

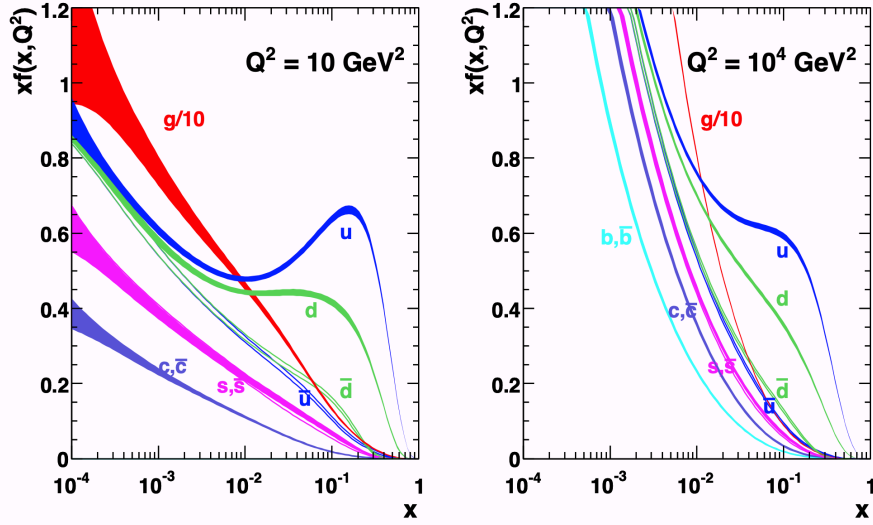


Figure 1.7 PDFs of protons, at the energy scales of $Q^2 = 10 \text{ GeV}^2$ (left) and $Q^2 = 10^4 \text{ GeV}^2$ (right), respectively. This figure is taken from Ref. [33].

new particles. Parton will carry part of the longitudinal momentum of the nucleon, and PDFs represent the probability density function of the parton i with the 4-momentum percentage $x_i = p_{\text{parton}}/p_{\text{nucleon}}$ in the nucleon. Since partons are trapped inside hadrons, PDFs should be related to non-perturbative dynamics inside hadrons, which QCD cannot calculate. PDF is process-independent and needs to be obtained through a series of Deep Inelastic Scattering (DIS) experiments such as electron-proton scattering at HERA [34].

- $\sigma_{ij \rightarrow c\bar{c}}(x_1, x_2, Q^2)$ is the parton-parton hard scattering cross-section, which can be calculated by perturbative expansion with respect to α_s to LO or NLO.
- $\mathcal{D}_{c \rightarrow h}(z)$ is the fragmentation function (FF), it denotes the transition from the charm quark with momentum p_c to the charm flavored hadron h , with momentum $p_h = zp_c$.

There are generally two types of FFs, scale-dependent and scale-independent. The Binnewise-Kniehl-Kramer (BKK) [35] method-based fragmentation function used in GMVFNS [25-26] and the perturbative fragmentation function (PFF) used in the FONLL [28] framework are both scale-dependent FFs. The DGLAP equation [36,36] based on pQCD can describe both the evolution processes of PDFs and FFs with the energy scale Q^2 . Scale-independent FFs, *e.g.* the Peterson fragmentation function [37] and the Lund string fragmentation function [38-39], are applied in Pythia [40]. The scale-independent FF is universal. Once the scale-independent FF is deter-

mined by DIS experiments or e^+e^- collisions, it can also be used to characterize the charm production in other “hard processes”.

1.3.3 Charm production in pA and AB collisions

The heavy nucleus is composed of many nucleons, and the proton-nucleus (pA) or nucleus-nucleus (AB) collisions have much larger multiplicities and hence are more complicated than the pp collisions. In pA and AB collisions, a variable called “centrality” is required to describe the geometric configuration of proton-nucleus or nucleus-nucleus. The femtometer-scale impact parameter b , the number of binary nucleon-nucleon collisions N_{coll} , together with the number of participating (wounded) nucleons N_{part} , are closely related to “centrality”. However, N_{coll} and N_{part} cannot be directly measured in experiments. Instead, the Glauber model^[20] is used to estimate the N_{coll} and N_{part} of a collision. The assumptions used in the Glauber model are: the trajectory of the nucleon is straight line; the nucleon motions inside the nucleus are independent of each other; the size of the heavy nuclei is much larger than the force range of nucleon-nucleon interaction.

According to the approximation of the Glauber model, the production of charm hadrons in proton-proton collisions (Eq. (1.5)) can be extrapolated to AB or pA (set $B=1$) collisions as

$$d\sigma_{AB \rightarrow h} \approx A \cdot B \cdot f_i(x_1, Q^2) \otimes f_j(x_2, Q^2) \otimes d\sigma_{ij \rightarrow c\bar{c}} \otimes \mathcal{D}_{c \rightarrow h}(z). \quad (1.6)$$

Since for AB collisions, one typically measures the invariant yields N under a particular b or N_{part} , the following formula is usually used instead of Eq. (1.6),

$$dN_{AB \rightarrow h}(b) = \langle N_{\text{coll}}(b) \rangle \cdot dN_{pp \rightarrow h}. \quad (1.7)$$

where the impact b and the number of binary collisions N_{coll} are determined by the Glauber model.

Here is a brief description of the Glauber model framework^[20]. The two input conditions of the Glauber model are the nucleon number density distribution function and the nucleon-nucleon inelastic scattering cross-section. The Woods-Saxon distribution^[41] is usually used to describe the nucleon density distribution function,

$$\rho(r) = \frac{\rho_0(1 + \omega(r/R)^2)}{1 + e^{(r-R)/a}} \quad (1.8)$$

where the distance from the nucleus’s centre is denoted by r , R is the radius of the nucleus, a is the edge width of the nucleus, ω describes how far the nucleus deviates from a spherical shape, and ρ_0 is the density of nucleons in the middle of the nucleus^[20]. The

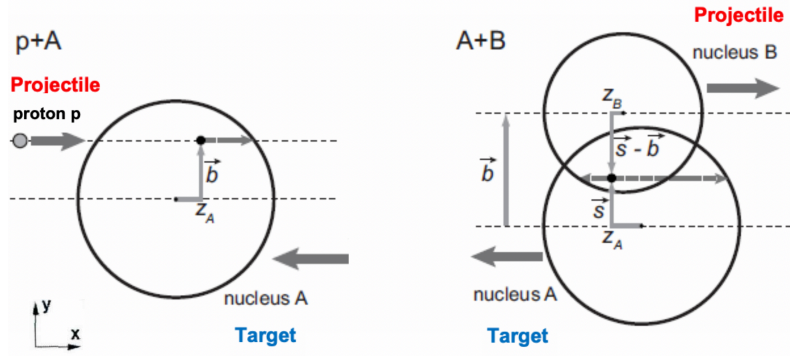


Figure 1.8 Schematic geometry of proton-nucleus (pA) collisions and nucleus-nucleus (AB) collisions.

difference between protons and neutrons is usually ignored, and the parameters in Woods-Saxon distribution are derived from electron-nucleus scattering measurements.

The longitudinal direction is defined as the direction of the colliding beam (x -direction). From the view of x -direction, the right side of Fig. 1.8 shows the schematic geometrical diagram of the nucleus-nucleus (AB) collision, in which the nucleus with mass number B is called the “projectile” nucleus, and the nucleus with mass number A is used as the “target” nucleus. The left side shows the geometric diagram of the pA collision, in which the proton p (mass number equals to 1) is used as the projectile, and the atomic nucleus with mass number A is used as the target. The probability of finding a nucleon per unit volume in target A is $\hat{\rho}_A(\vec{s}, z_A) (\equiv \rho(\vec{s}, z_A)/A)$, satisfying the normalization condition $\int \hat{\rho}_A d\vec{s} dz = 1$. After integrating its longitudinal z_A , the probability of finding a nucleon per unit area of the flow tube of the target nucleus A can be obtained as $\hat{T}_A(\vec{s}) = \int \hat{\rho}_A(\vec{s}, z_A) dz_A$. The “nuclear overlap function” is defined as

$$\hat{T}_{AB}(\vec{b}) = \int \hat{T}_A(\vec{s}) \hat{T}_B(\vec{s} - \vec{b}) d^2\vec{s}. \quad (1.9)$$

$\hat{T}_{AB}(\vec{b})$ has unit of reciprocal area, depicting the “effective overlap region” of interactions between nucleus in A and B separated by b . The nucleon-nucleon elastic collisions have slight energy loss, therefore they can be ignored in the Glauber-type model. The probability of one nucleon-nucleon reaction during the nucleus-nucleus collision is approximately equal to $\hat{T}(\vec{b})\sigma_{\text{inel}}^{\text{NN}}$. As shown in Fig. 1.9, $\sigma_{\text{inel}}^{\text{NN}}$ represents the cross-section of the nucleon-nucleon inelastic collision which can be measured experimentally. For pp collisions at $\sqrt{s} = 5.02$ TeV at the LHC and $\sqrt{s} = 200$ GeV at RHIC, the inelastic cross-section is 64 mb and 42 mb, respectively. In AB collision, if n pairs of nucleons are selected, there are C_{AB}^n options, the probability of each pair of nucleons having inelastic

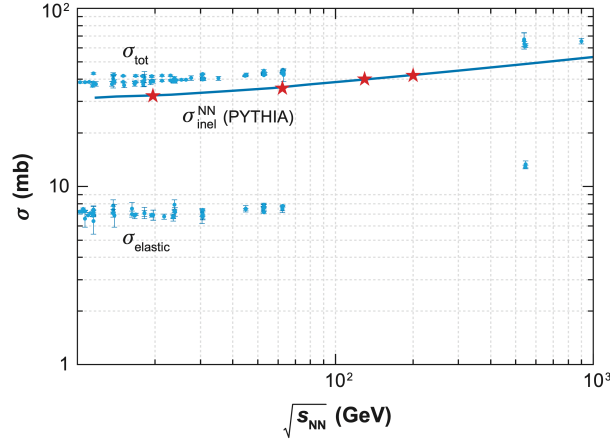


Figure 1.9 Elastic and inelastic cross-section of pp collisions at different energies. This figure is taken from Ref. [20].

collision is $[\hat{T}_{AB}(\vec{b})\sigma_{\text{inel}}^{\text{NN}}]^n$, while $[1 - \hat{T}_{AB}(\vec{b})\sigma_{\text{inel}}^{\text{NN}}]^{AB-n}$ is the probability that the remaining $(AB - n)$ inelastic collisions do not occur. Then the probability of n inelastic collisions between target A and projectile B is

$$P(n, \vec{b}) = (C_{AB}^n) [\hat{T}_{AB}(\vec{b})\sigma_{\text{inel}}^{\text{NN}}]^n [1 - \hat{T}_{AB}(\vec{b})\sigma_{\text{inel}}^{\text{NN}}]^{AB-n}. \quad (1.10)$$

The total cross-section of inelastic scattering for AB collisions can be obtained from the inelastic scattering cross-section of nucleon-nucleon and the “nuclear overlap function” as

$$\sigma_{\text{inel}}^{A+B} = \int_0^\infty 2\pi b db \left\{ 1 - [1 - \hat{T}_{AB}(b)\sigma_{\text{inel}}^{\text{NN}}]^{AB} \right\}. \quad (1.11)$$

As for pA collisions, it can be treated as a special case of AB collision with the nucleon density distribution function inside B (proton) set to $\delta(\vec{s}, z_A)$ and the mass number of B set to 1. The total number of nucleons participating in AB collision (also known as the number of “wounded” nucleons) N_{part} and the number of binary nucleon-nucleon collisions N_{coll} are closely related to the total number of final state hadrons produced in this AB collision (i.e., the multiplicity). In general, the multiplicity contributed by the “soft processes” is related to N_{part} , which can be expressed as

$$N_{\text{part}}(\mathbf{b}) = A \int \hat{T}_A(s) \left\{ 1 - [1 - \hat{T}_B(s-b)\sigma_{\text{inel}}^{\text{NN}}]^B \right\} d^2s + B \int \hat{T}_B(s-b) \left\{ 1 - [1 - \hat{T}_A(s)\sigma_{\text{inel}}^{\text{NN}}]^A \right\} d^2s, \quad (1.12)$$

while the contribution from the “hard processes” is determined by N_{coll} , which is

$$N_{\text{coll}}(b) = \sum_{n=1}^{AB} nP(n, b) = AB\hat{T}_{AB}(b)\sigma_{\text{inel}}^{\text{NN}}. \quad (1.13)$$

1.3.4 Nuclear matter effects in pA and AA collisions

The production of charm hadrons (and other particles) in pA and AA collisions are affected by many nuclear matter effects, and usually cannot be simply treated as the superposition of nucleon-nucleon collisions. For example, in pA collisions, cold nuclear matter (CNM) effects exist, such as the rectification of the PDFs inside a nucleus. In order to quantify the nuclear matter effects in AA collisions, an observable called the nuclear modification factor R_{AA} is introduced, defined as

$$R_{AA}(p_T, y; b) = \frac{d^2 N_{AA}/dp_T dy}{\langle T_{AA}(b) \rangle \times d^2 \sigma_{pp}/dp_T dy}, \quad (1.14)$$

where b is the impact parameter, $T_{AA} = A^2 \hat{T}_{AA} = N_{\text{coll}}/\sigma_{\text{inel}}^{\text{NN}}$ is the “nuclear overlap function”, y and p_T denote the rapidity in nucleon-nucleon centre-of-mass system and the transverse momentum of particles, respectively. R_{AA} will be equal to unity if AA collisions are just incoherent superpositions of pp collisions as assumed in the Glauber model, without any nuclear matter effects. The deviation of the experimentally measured R_{AA} value from unity will reveal the existence of nuclear matter effects.

In AA collisions, the possible presence of QGP in early stage will affect charm and other particle productions significantly, these effects are often called hot nuclear matter (HNM) effects. These effects which can be reflected in the R_{AA} and other experimental observables, could provide valuable information about the presence and properties of QGP and hence serve as excellent QGP signatures, as stated in 1.3.1. As these observables could also be affected by CNM effects, it is essential to quantify their contributions with the corresponding measurements in pA collisions where QGP is not likely to be produced.

The following are some of the currently known QGP signatures related to charm production in high-energy heavy-ion collisions.

- *Jet quenching*

When a jet traverses QGP, elastic and inelastic scattering occurs between the jet and the partons in QGP medium, resulting in collisional and radiative energy losses. This HNM effect is called “jet quenching”.

Many experiments have confirmed jet quenching, one of which is to measure the nuclear modification factor R_{AA} of heavy-flavor or charged-particle jets in AA collisions. R_{AA} is expected to be less than unity at high p_T in AA collisions if there exists “jet quenching” in the QGP medium. Heavy-flavor jets contain D mesons, heavy-flavor electrons or B hadrons. In order to distinguish the final-state effects

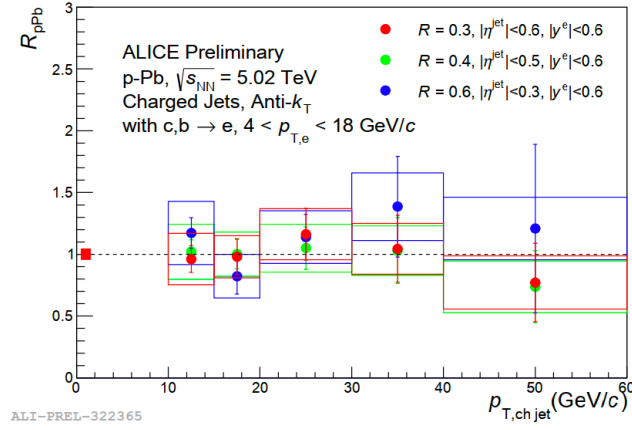


Figure 1.10 R_{pPb} for heavy-flavor electron jets with the jet radii $R = 0.3, 0.4$ and 0.6 at ALICE. The figure is taken from Ref. [42].

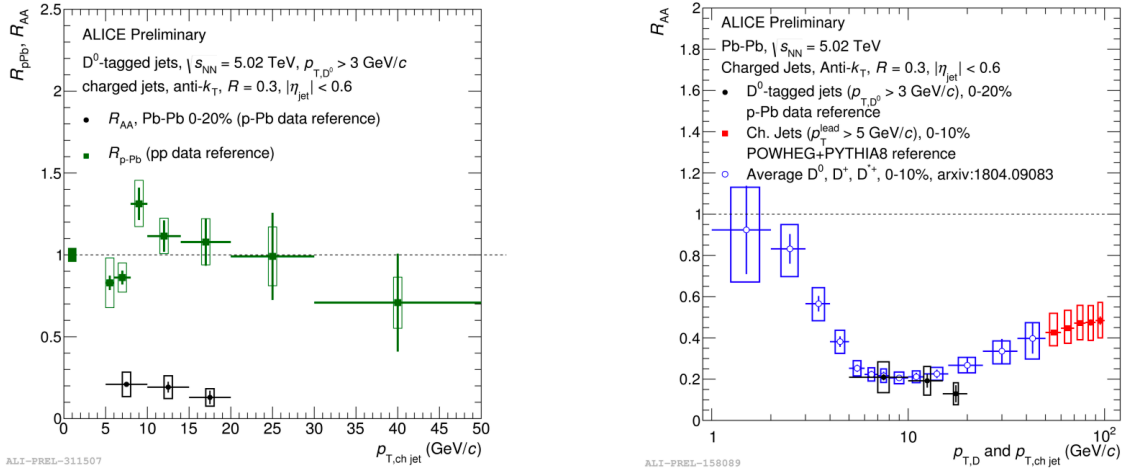


Figure 1.11 Nuclear modification factors R_{AA} and R_{pPb} for D^0 -tagged jets (left) and R_{AA} for D^0 -tagged jets, charge particles jets and D mesons (right). These figures are taken from Ref. [42].

caused by a QGP and CNM effects, a comparison of heavy-flavor jet nuclear modification factor measurements in pPb and $PbPb$ is required. In $\sqrt{s_{NN}} = 5.02$ TeV pPb collisions at ALICE, the nuclear modification factor R_{pPb} for heavy-flavor electron jets with different jet radius R is shown in Fig. 1.10. R_{pPb} is consistent with unity within uncertainties as p_T increases. Figure 1.11 shows the nuclear modification factors R_{AA} and R_{pPb} for D^0 -tagged jet in pPb and $PbPb$ collisions at LHC. The $PbPb$ results indicate a strong suppression at high p_T and a similar trend for D^0 -tagged jets and D mesons in central $PbPb$ collisions. While the ALICE pPb results show no obvious CNM effects are found in both heavy-flavor electron and D^0 -tagged jets at high p_T at mid-rapidity, although the uncertainties are large.

- *Strangeness enhancement*

Strangeness enhancement, i.e. the enhanced production of strange hadrons (in particular hyperons) in AA collisions, first observed by the CERN SPS experiment, is a vital QGP signature^[43]. In hadron-hadron rescatterings, strange hadrons have large masses and have to be pair produced due to the requirement of strangeness conservation, with a threshold energy of above 500 MeV. While the mass of s quark (~ 100 MeV) in QGP medium where chiral symmetry is restored is smaller than the QGP temperature, hence the threshold of strange quark and anti-quark pair production is much lower in QGP (dominated by the $gg \rightarrow s\bar{s}$ mechanism) than in hadronic gas. Besides, because the parton density in QGP is substantial, multiple partonic scatterings would certainly result in a significant increase in the “abundance” of strange quarks.

The ratio of strange-hadron yields to π^\pm after integrating p_T as a function of multiplicity $\langle dN_{\text{ch}}/d\eta \rangle$ is shown in Fig. 1.12 (left) for the ALICE pp ^[44], $p\text{Pb}$ ^[45] and PbPb ^[46] collisions. $\langle dN_{\text{ch}}/d\eta \rangle$ is the average charged particle multiplicity, which is closely related to the initial energy density of the fireball. The data shows a significant strangeness enhancement in PbPb , and even in high multiplicity $pp/p\text{Pb}$ events, especially for multi-strange hyperons. As shown in Fig. 1.12 (right), the D_s^+/D^0 yield (or cross-section) ratios as a function of p_T in 200 GeV AuAu collisions from STAR^[47] and 5.02 TeV PbPb collisions from ALICE^[45] are much higher than those in pp collisions at LHC from ALICE and from the Pythia pp simulations. These results first imply that extra pairs of strange quarks and anti-strange quarks are produced in QGP in heavy-ion collisions at RHIC and LHC. Moreover, the charmed mesons D_s^+ and D^0 could be produced at the QGP hadronization stage via the coalescence of charm quarks, which are produced in the initial hard scatterings, and the light quarks. These measurements reveal how the enhanced production of strange quarks in QGP affects charm hadronization.

1.3.5 CNM effects on open charm production

CNM effects on open charm production in AA collisions should be precisely constrained in order to study quantitatively the HNM effects in PbPb collisions. This can be experimentally achieved by open charm measurements in pA collisions. Similar to Eq. (1.14), in a particular centrality C of $p\text{Pb}$ collisions, the nuclear modification factor

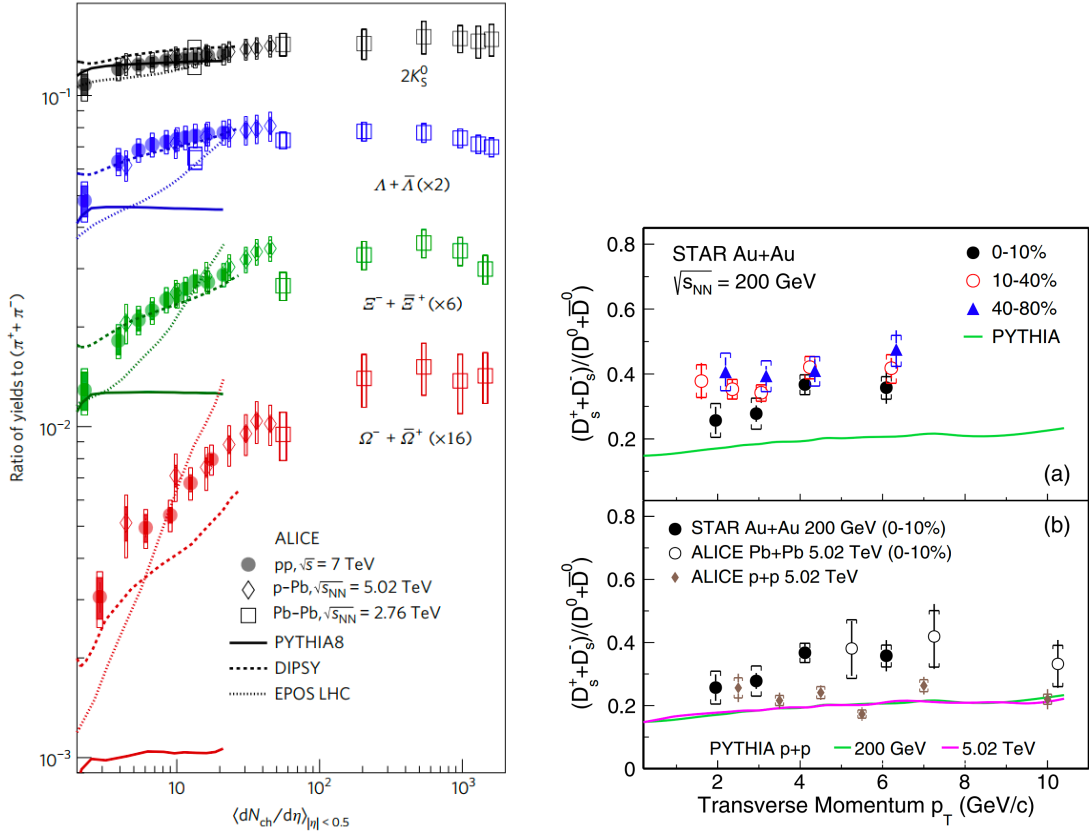


Figure 1.12 Enhanced yield of strange hadrons as a function of multiplicity $\langle dN_{ch}/d\eta \rangle$ in ALICE pp , pPb and $PbPb$ experiments (left); D_s^+/D^0 ratio in AuAu collisions compared with pp simulation Pythia and data as a function of transverse momentum p_T (right). The figures are taken from Ref. [45] and Ref. [47], respectively.

R_{pPb}^C can be defined as the ratio of the yield N_{pPb}^C in pPb collisions scaled by $\langle T_{pPb}^C(b) \rangle$ to the cross-section of pp collisions,

$$R_{pPb}^C(p_T, y; b) = \frac{d^2 N_{pPb}^C / dp_T dy}{\langle T_{pPb}^C(b) \rangle \times d^2 \sigma_{pp} / dp_T dy}, \quad (1.15)$$

where $T_{pPb}^C(b)$ is the “nuclear overlap function” of pPb collisions. For minimum bias collisions (without any centrality selections), the nuclear modification factor can be rewritten as

$$R_{pPb}(p_T, y) = \frac{d^2 \sigma_{pPb} / dp_T dy}{A \times d^2 \sigma_{pp} / dp_T dy}, \quad (1.16)$$

where A is the mass number of the ^{208}Pb nucleus. Since pA collisions are asymmetric in rapidities, the CNM effect can also be measured by the ratio of the cross-sections at forward and backward rapidities, R_{FB} , which is defined as,

$$R_{FB}(p_T, y) \equiv \frac{d^2 \sigma_{pPb}(p_T, +|y|) / dp_T dy}{d^2 \sigma_{pPb}(p_T, -|y|) / dp_T dy}. \quad (1.17)$$

Here “forward” ($p\text{Pb}$) represents the proton-going direction, the rapidity y is defined to be positive; the “backward” ($\text{Pb}p$) denotes the opposite direction, and the rapidity y is negative. The measurement of R_{FB} in $p\text{Pb}$ collisions does not require the cross-sections in pp collisions as reference. Some uncertainties in the forward and backward cross-sections also cancel out in R_{FB} . The CNM effects can be revealed by the deviation of $R_{p\text{Pb}}$ (or R_{FB}) from unity.

Initial state effects, final state effects, and other effects that are neither initial state nor final state are the three types of CNM effects that affect charm hadrons production. Initial state effects include, for example, nuclear shadowing^[48], gluon saturation^[49], initial-state energy loss^[50], and Cronin effect^[51]. The hadronic rescatterings^[52] are the instances of final state effects. The coherent energy loss^[53] is an effect that is neither the initial nor the final state.

The following initial CNM effects will be briefly discussed: nuclear shadowing, gluon saturation, Cronin effect and initial-state energy loss, all are closely related to the production of open charm mesons in this thesis.

- *Modification of parton distribution function (nuclear shadowing)*

The nucleus is composed of many bounded nucleons (protons and neutrons), that of the nucleus (nPDF) will be different from the parton distribution function of free nucleons (PDF). With the increasing mass number A of nucleus, this CNM effects become more significant. A shadowing function $R_i^A(x, Q^2)$ is often introduced to evaluate the effect of initial nuclear environment on the parton density distribution in the nucleus,

$$R_i^A(x, Q^2) = f_i^A(x, Q^2) / f_i^p(x, Q^2). \quad (1.18)$$

$R_i^A(x, Q^2)$ is also referred as the nuclear modification of parton distribution function, and f_i^p and f_i^A denote the PDF and nPDF for the parton type i , respectively. Many theoretical models have extracted specific $R_i^A(x, Q^2)$, such as EPS09^[54], EKS^[55], HKN^[56], DSSZ^[57], nCTEQ15^[58] and EPPS16^[59].

These values are obtained by fitting the cross-section data from DIS experiments. The nPDF evolution at various scales Q^2 could be derived by the DGLAP^[36,36] equation. EPS09 is the most widely used among the above theoretical calculations, and EPPS16 is an upgraded version of EPS09. EPPS16 includes more data in the fit, such as the Drell-Yan process in pion-nucleus scatterings and the neutrino-nucleus DIS experiments. The EPPS16 parameterization is also the first model to employ

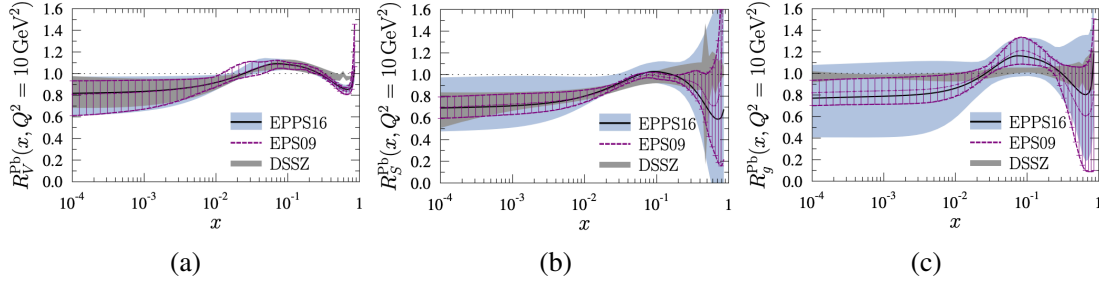


Figure 1.13 $R_i^A(x, Q^2)$ calculated by EPS09, EPPS16 and DSSZ at $Q^2 = 10 \text{ GeV}^2$. Figure (a), figure (b), and figure (c) represent the results for valence quarks, sea quarks, and gluons, respectively. These figures are taken from Ref. [59].

the $p\text{Pb}$ collisions data at LHC for NLO fitting.

As shown in Fig. 1.13, EPS09, EPPS16, and DSSZ models have calculated the $R_i^A(x, Q^2)$ at the energy scale $Q^2 = 10 \text{ GeV}^2$ as a function of x , where x is the momentum fraction carried by probed partons. It is essential to constrain the large uncertainty of $R_i^A(x, Q^2)$ with the data.

According to different values of $R_i^A(x, Q^2)$, nPDF could be separated into four x regions:

- (1) the nuclear shadowing region: $0 \lesssim x \lesssim 0.1$, and $R_i^A(x, Q^2)$ is less than unity. The shadowing effect results from quantum mechanical interferences between partons and numerous nucleons. The coherence length of the interaction between partons and nucleons is $l_c = (2m_N x)^{-1}$, where m_N is the mass of nucleons. When the momentum of partons is small enough, and l_c is much larger than the distance between nucleons, interferences between partons and multiple nucleons will take place.
- (2) the anti-shadowing region: $0.1 \lesssim x \lesssim 0.3$, and $R_i^A(x, Q^2)$ is slightly larger than unity. The anti-shadowing effect is associated with multiple-scatterings between partons and the nucleus^[60].
- (3) the EMC region: $0.3 \lesssim x \lesssim 0.8$, $R_i^A(x, Q^2)$ is slightly smaller than unity, reaches the lowest point at $x \approx 0.6$, and rises to unity. Discovered by the European Muon Collaboration (EMC)^[61], the EMC effect observes that the muon cross-section at the DIS experiment from a nucleus is different from that of the same number of nucleons^[62].
- (4) the Fermi Motion region: in the vicinity of x close to 1. The Fermi Motion effect describes the modification of the nuclear structure-function of DIS experiments at large x according to the nucleon momentum distribution in a nucleus^[63-64].

- *The gluon saturation (CGC)*

As shown in Fig. 1.7, the densities of gluons and sea quarks rise relative to valence quarks with the decreasing Bjorken x , due to the relativistic effect, many gluons will be accumulated in the disc-shaped Pb nucleus and interfere with each other; when recombination and bremsstrahlung processes of gluons approach dynamic equilibrium, their density tends to a saturation state. The Pb nucleus at this time are thought to be a dense system mainly composed of saturated gluons, known as the “color glass condensate” (CGC):

(1) “Color”: in the CGC state, quarks and gluons carry color charges, and strong interactions dominate.

(2) “Glass”: the gluon behavior is analogous to a glass system in the real world. The glass is a system of disordered molecules in the actual world. Under gluon saturation, the gluon field evolution is very sluggish compared to the natural time scale. The CGC takes the shape of an ordered state in a short period, with gluon locations are relatively fixed, similar to a solid; as time dilates, it becomes more disorganized, like a fluid.

(3) “Condensate”: with the collision energy rises or at smaller x , gluons become denser and congregate in vast numbers at the same high-energy level Q_s^2 , saturating the phase space in a manner analogous to Bose-Einstein condensation in multiple particle systems. The saturation energy scale Q_s is referred as the characteristic momentum of gluons in the saturated state.

Fig. 1.14 (left) depicts the PDF variation in hadrons with x and the energy scale Q^2 :

(1) When x is taken as a relatively large fixed value, the DGLAP equation^[36,36] may be used to explain the PDF evolution with the energy scale Q^2 , and the concentration of partons rises as Q^2 rises.

(2) With a decrease in x , the quantity of partons in hadrons increases quickly due to effects like bremsstrahlung. The Balitsky-Fadin-Kuraev-Lipatov (BFKL) evolution equation^[65] describes this procedure.

(3) When x is smaller than unity, the recombination mechanism (*e.g.*, $gg \rightarrow g$) will work to slow down the growth of gluons until gluons reach saturation, and the densities of saturated gluons are on the order of α_s^{-1} . Balitsky-Kovchegov (BK)^[66-67] and Jalilian-Marian-Iancu-McLerran-Weigert-Leonidov-Kovner (JIMWLK)^[68] evolution equations describe this non-linear process. According to the BK evolution

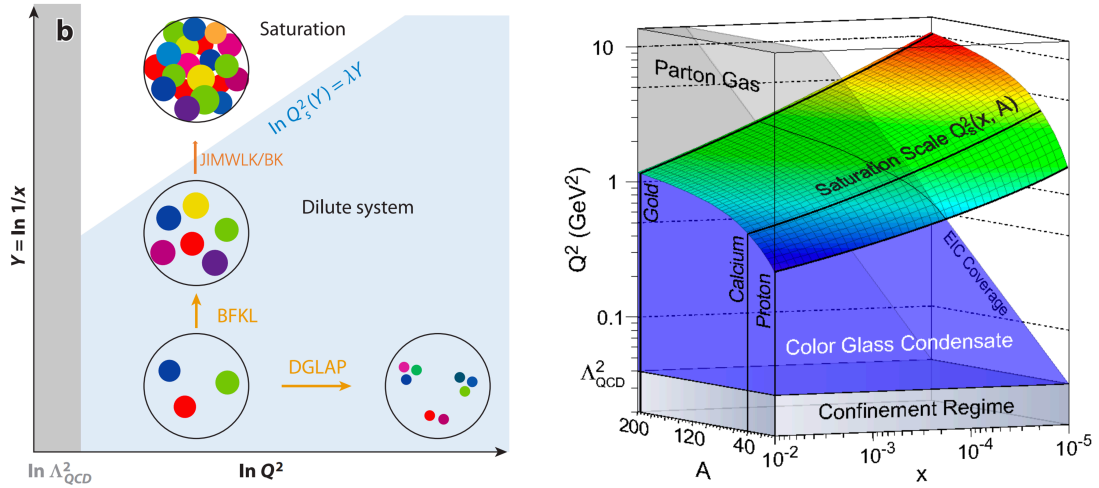


Figure 1.14 PDF evolution with x and Q (left); the evolution of the saturation energy scale Q_s with with $A^{1/3}$ and x^λ (right). The figures are taken from Ref. [69] and Ref. [70], respectively.

equation^[69], the Q_s^2 distribution satisfies

$$Q_s^2(Y) \simeq Q_0^2 e^{\lambda Y}. \quad (1.19)$$

Here, $Y = \ln 1/x$, $\lambda \approx 4.9\alpha_s$; in the nucleus, the non-perturbative initial scale Q_0^2 is $A^{1/3}$ (the third power of the mass number A).

As presented in Fig. 1.14 (right), the magnitude of the saturation energy scale Q_s is proportional to $A^{1/3}$ and x^λ . The gluon saturation may be observed in the larger x region in $p\text{Pb}$ collisions when compared to pp collisions. The open charm production is highly affected by the gluon saturation effect at smaller x . Therefore, the measurement of open charm cross-section in $p\text{Pb}$ collisions is more appropriate than in pp collisions to investigate the CGC theory.

As shown in Fig. 1.15, the CGC theory considers the LO process of $c\bar{c}$ pairs production in $p\text{Pb}$ collisions^[71]: in one case, incoming gluons form $c\bar{c}$ pairs before multiple scatterings with the Pb nucleus; in another case, incoming gluons first undergo multiple scatterings with the Pb nucleus before generating $c\bar{c}$ pairs. The $c\bar{c}$ pairs production in $p\text{Pb}$ collisions based on the CGC theory^[72-73] is

$$d\sigma_D = D_c^D \otimes \varphi_p \otimes \phi_A \otimes \Xi_c, \quad (1.20)$$

where D_c^D stands for the probability of c quark fragmenting into open charm mesons; φ_p is the unintegrated-gluon-distribution-function (UGDF) of protons; ϕ_A is the propagator of the $c\bar{c}$ pair passing through the color field of the Pb nucleus; Ξ_c is the matrix element of the hard-scattering part;

The nuclear modification factor of charm mesons (J/ψ and D) in $p\text{Pb}$ collisions

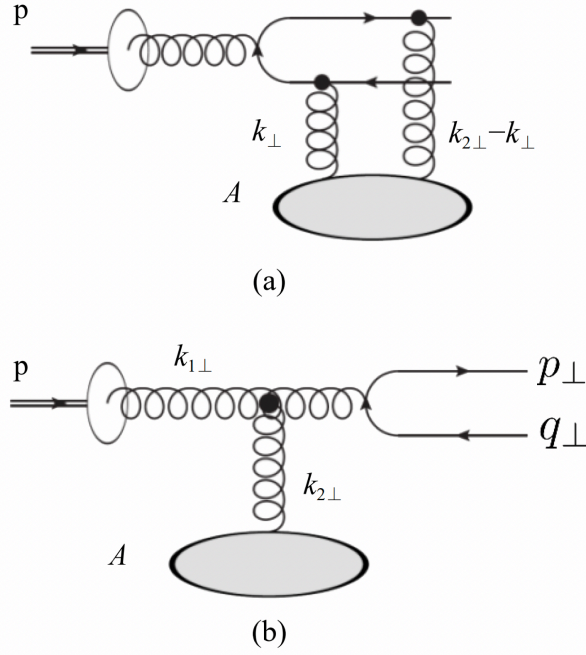


Figure 1.15 Production process of heavy quark pairs at LO. Here, $k_{1\perp}$, $k_{2\perp}$ and k_{\perp} represents the transverse momentum of different gluons, and p_{\perp} and q_{\perp} represents the transverse momentum of quarks (c) and antiquarks (\bar{c}). The figure is taken from Ref. [59].

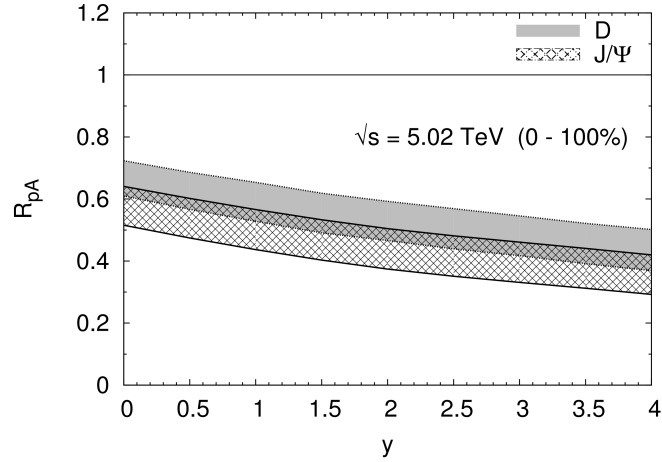


Figure 1.16 Nuclear modification factor of J/ψ and D as a function of rapidity based on the CGC framework. The figure is taken from Ref. [72-73].

at 5.02 TeV from LHCb was calculated by Fujii and Watanabe using the CGC theory^[72-73], as displayed in Fig 1.16. Within the uncertainty range, the CGC predictions are compatible with the data.

- *The Cronin effect*

In fact, unlike the first nucleon-nucleon collision process described by the Glauber model, the wounded nucleons that participated in the collision for the first time may continue to collide inelastically with other nucleons in heavy-ion collisions. The

Table 1.1 Examples of open charm (D^0 , D^+ , D^{*+} or D_s^+) cross-sections in $p\bar{p}$ collisions at LHC.

| phase space | $\sqrt{s_{\text{NN}}}$ (TeV) | reference |
|---|------------------------------|-----------|
| LHCb | | |
| $0 < p_T < 10 \text{ GeV}/c, 2.0 < y < 4.5$ | 5.02 | [30] |
| $0 < p_T < 8 \text{ GeV}/c, 2.0 < y < 4.5$ | 7 | [78] |
| $0 < p_T < 15 \text{ GeV}/c, 2.0 < y < 4.5$ | 13 | [79] |
| ALICE | | |
| $p_T > 1 \text{ GeV}/c, y < 0.5$ | 2.76 | [80] |
| $p_T > 0 \text{ GeV}/c, y < 0.5$ | 5.02 | [31] |
| $p_T > 1 \text{ GeV}/c, y < 0.5$ | 7 | [81-83] |
| ATLAS | | |
| $3.5 < p_T < 100 \text{ GeV}/c, \eta < 2.1$ | 2.76 | [84] |

transverse momentum k_T spectrum of partons also affects the PDF. In the initial stage, inelastic multiple scatterings of partons bring about the Cronin effect in $p\bar{p}$ collisions, resulting in the k_T spectrum broaden compared to pp collisions^[74-75],

$$\left\langle k_{T,i}^2 \right\rangle_{p\bar{p}} = \left\langle k_{T,i}^2 \right\rangle_{pp} + \left\langle k_{T,i}^2 \right\rangle_{\text{IS}}, \quad \left\langle k_{T,i}^2 \right\rangle_{\text{IS}} = \left\langle \frac{2\mu^2 L}{\lambda_i} \right\rangle \quad (1.21)$$

Here, $\left\langle k_{T,i}^2 \right\rangle_{\text{IS}}$ is the average square of the k_T -broadening due to the involvement in multiple scatterings of partons in the initial state (IS), μ refers to the momentum transfer of inelastic scattering between the parton i and the nucleon, L describes the size of the nucleon, and λ_i is the average free path of the parton i . Studies^[76] reveal that particles yields are enhanced because of the Cronin effect compared to results scaled by the “nuclear overlap function” in the intermediate p_T interval.

- *Initial – state energy loss*

Incident partons i and j will lose part of their energy by radiation at early stages in $p\bar{p}$ collisions before the “hard process” ($i + j \rightarrow k + l$) with large momentum transfer. This initial state effect is reflected in correcting the PDF as below^[77],

$$\left[\phi_{i,j}(x_{i,j}) \right]_{p\bar{p}} = \left[\phi_{i,j} \left(\frac{x_{i,j}}{1 - \epsilon_{i,j}} \right) \right]_{pp}, \quad \epsilon_{i,j} = \frac{\Delta E_{i,j}}{E_{i,j}}. \quad (1.22)$$

Here, $\epsilon_{i,j}$ is the percentage of energy lost through radiation before parton hard scatterings, which rises linearly with medium opacity in a given Q^2 range.

1.3.6 Recent results on production and CNM effects of open charm at LHC

Due to short lifetimes, the productions of charm hadrons may be explored in the following techniques or probes^[85], according to classifications of their decays:

- Fully reconstructed exclusive decays modes. For example, in this analysis D^+ and D_s^+ are reconstructed by decay modes of $D^\pm \rightarrow K^\mp \pi^\pm \pi^\pm$ and $D_s^\pm \rightarrow K^\mp K^\pm \pi^\pm$, respectively.
- Non-photonic leptons from charm flavor decays. In 200 GeV d Au collisions at PHENIX, the forward yield from heavy-flavor muons is suppressed compared to the backward yield^[86]. The STAR experiment also measured the leptons production from heavy-flavor decays at the same center-of-mass energy^[87].
- Azimuth correlation between heavy-flavor hadrons, elliptic flow v_2 ^[88].
- Search for charm-tagged jets among reconstructed jets^[89].
- Leptons or charm hadrons (*e.g.* J/ψ) from b decay.

The charm production in pp collisions is taken as a reference for p Pb and PbPb collisions, either determined directly by experiments or acquired by theoretical extrapolations or interpolations. Open charm (D^0 , D^+ , D^{*+} or D_s^+) cross-sections in pp collisions have been measured at LHC energies, as listed in Table. 1.1. The left and right panels in Fig. 1.17 show the cross-sections of prompt D mesons in 5.02 TeV pp collisions at LHCb and ALICE, respectively. Prompt D mesons include those produced directly from pp collisions and those from the decays of excited charmed resonances. Within uncertainties, the data from pp collisions and the theoretical predictions based on pQCD framework are consistent; central values predicted by FONLL^[28] and POWHEG^[27] models are somewhat lower than the data, while central values predicted by GMVFNS^[25-26] is slightly higher.

Strangeness enhancement in charm hadronization can be studied by the yield ratios of D_s^+ and non-strange D mesons with the transverse momentum p_T in AuAu and PbPb collisions.

In small systems like pp and p Pb collisions, the cross-section ratios of different D mesons can provide an important reference. The cross-section values of different D mesons in pp collisions from LHCb (left) and in pp and p Pb collisions from ALICE (right) at 5.02 TeV are shown in Fig 1.18. The measured ratios indicate its slight dependence on p_T . Moreover, the ratios of D_s^+/D^0 in p Pb collisions are consistent with pp within uncer-

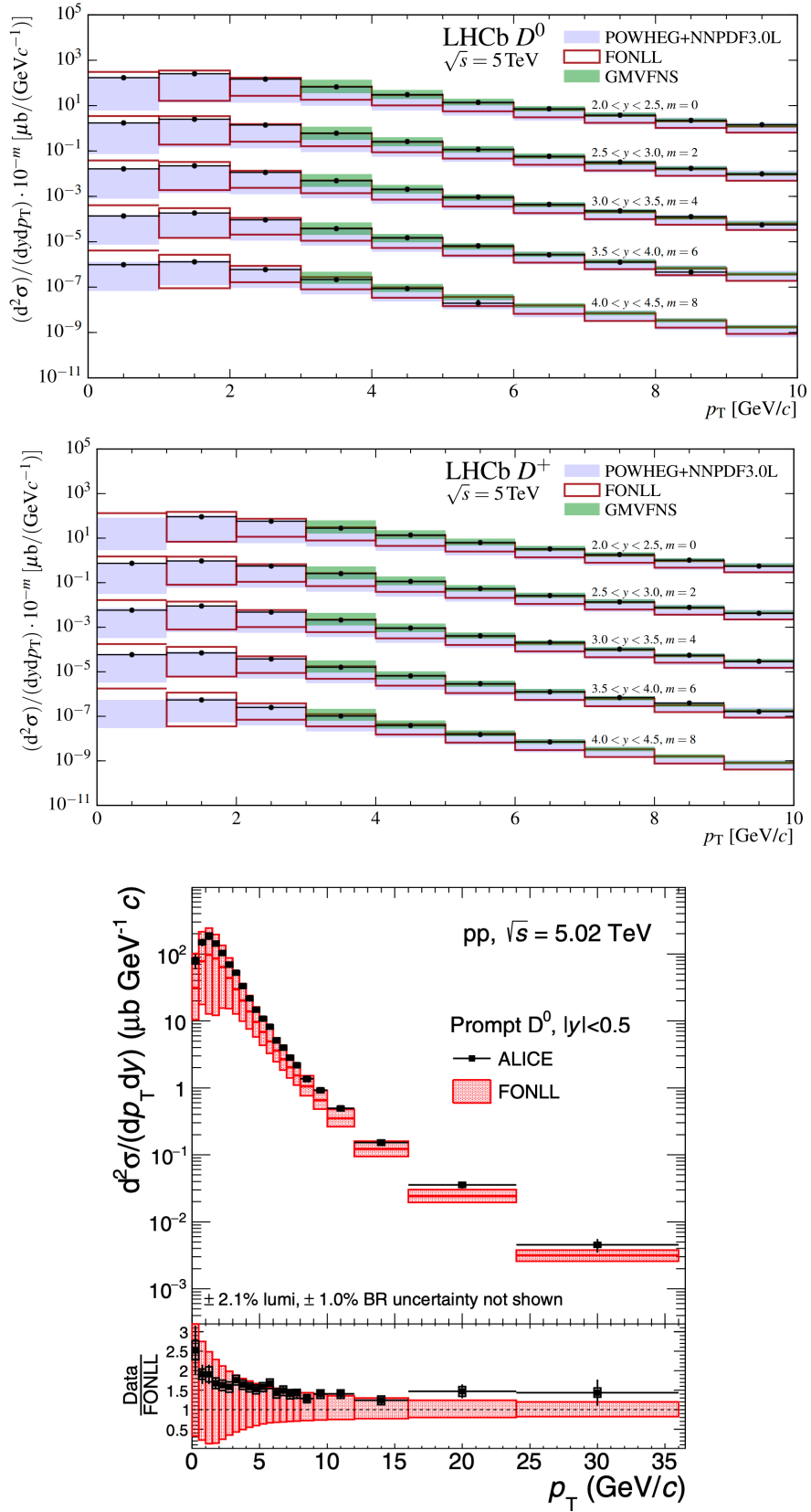


Figure 1.17 Prompt D mesons cross-sections in pp collisions at 5.02 TeV from LHCb (top, middle) and ALICE (bottom) compared with the predictions in collinear factorization frameworks (POWHEG+NNPDF3.0L, FONLL or GMVFNS). The figures are taken from Ref. [30] and Ref. [31], respectively.

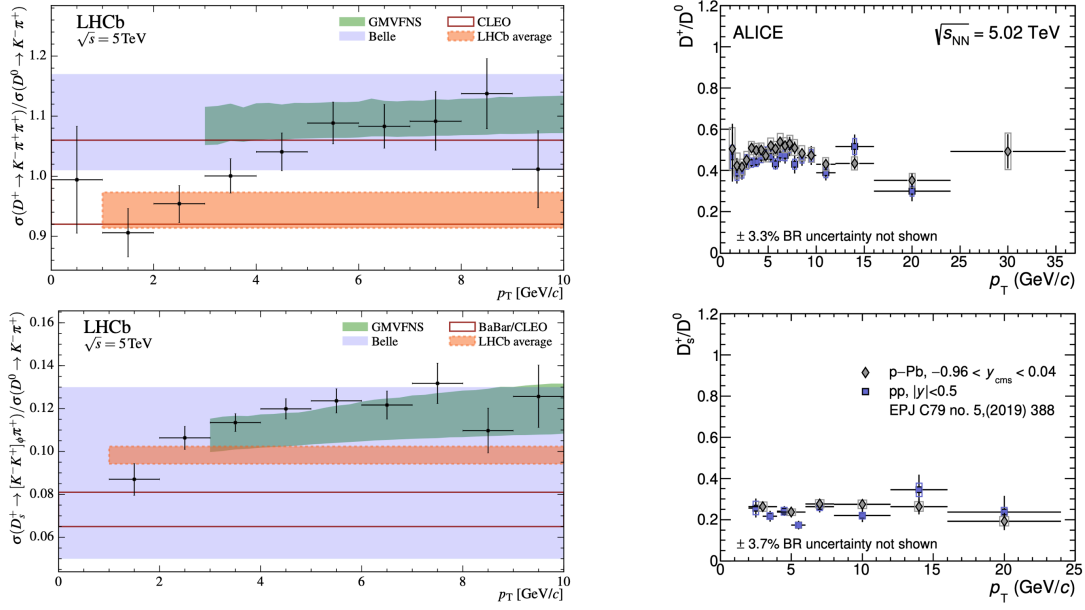


Figure 1.18 Ratios of different D mesons cross-sections in pp collisions from LHCb (left) and in pPb collisions from ALICE (right) at 5.02 TeV. The figures are taken from Ref. [30] and Ref. [90], respectively.

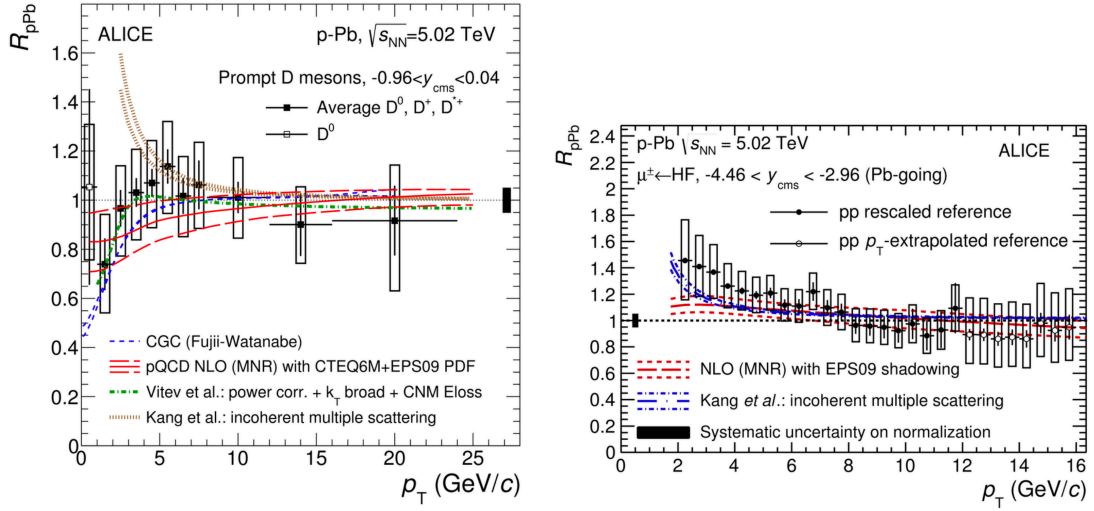


Figure 1.19 Nuclear modification factor R_{pPb} of average D^0 , D^+ , D^{*+} (left) and μ^\pm from heavy-flavor decay (right) as a function of p_T . The figures are taken from Ref. [90] and Ref. [99], respectively.

tainties which indicates no obvious strangeness enhancement.

Recent experimental results about charm hadrons (open and hidden charm) nuclear modification factor R_{pPb} in pPb collisions at $\sqrt{s_{NN}} = 2.76, 5.02$ and 8.16 TeV at LHC are summarized in Table. 1.2.

Table 1.2 Nuclear modification factors R_{pPb} of charm hadrons in pPb collisions at LHC.

| probe | $\sqrt{s_{NN}}$ (TeV) | reference |
|---------------------------|-----------------------|-----------|
| LHCb | | |
| D^0 | 5.02 | [91] |
| Λ_c^+ | 5.02 | [92] |
| J/ψ | 5.02 | [93] |
| $\psi(2S)$ | 5.02 | [94] |
| J/ψ | 8.16 | [95] |
| $\chi_{c1,2}$ | 8.16 | [96] |
| D^0 | 8.16 | [97] |
| ALICE | | |
| heavy-flavor electrons | 5.02 | [98] |
| heavy-flavor muons | 5.02 | [99] |
| D^0, D^+, D^{*+}, D_s^+ | 5.02 | [90] |
| J/ψ | 5.02 | [100-101] |
| J/ψ | 8.16 | [102] |
| $\psi(2S)$ | 2.76 | [103-104] |
| ATLAS | | |
| J/ψ | 5.02 | [105] |
| CMS | | |
| charm-tagged jet | 5.02 | [89] |
| J/ψ | 5.02 | [106] |
| $\psi(2S)$ | 5.02 | [107] |

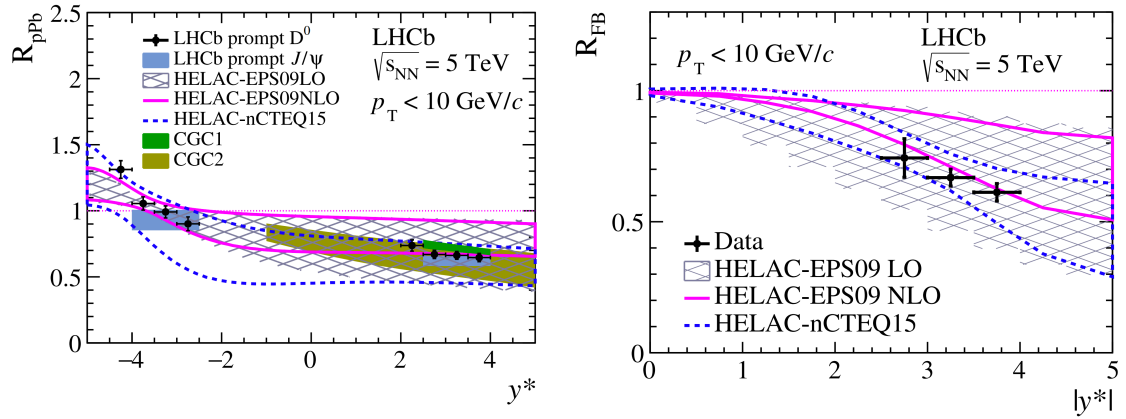


Figure 1.20 Nuclear modification factor R_{pPb} (left) and the forward-backward ratio R_{FB} (right) of D^0 as a function of the rapidity y^* . The figures are taken from Ref. [97].

ALICE experiments measure the nuclear modification factors of non-strange D mesons (D^0 , D^+ , D^{*+})^[90] and heavy-flavored muons^[99] in 5.02 TeV pPb collisions, as shown in Fig. 1.19. The data are well described by several models that solely incorporate CNM effects (e.g. CGC^[72-73], FONLL^[28]), but the systematic uncertainties are large (nearly 20%).

As a beauty/charm quark factory, the LHCb detector has an excellent resolution of the impact parameter (IP). It is very good at distinguishing prompt D mesons from b hadrons' decay. Compared with the ALICE experiment, the nuclear modification factor of D^0 in Fig. 1.20 (left) obtained in pPb collisions from LHCb at the same center-of-mass energy has much smaller uncertainties. As shown in Fig. 1.20, R_{pPb} (left) and R_{FB} (right) of D^0 are calculated by a heavy-flavored automated matrix element generator call HELAC-Onia^[108-110] with nuclear PDFs of EPS09LO, EPS09NLO^[54] and nCTEQ15^[58], respectively. The measurements of D^0 with smaller uncertainties are comparable to predictions based on several nPDF (HELAC-EPS09LO, HELAC-EPS09NLO and HELAC-nCTEQ15) or CGC^[72-73] models. Moreover, the nuclear modification factors of open charm D^0 and hidden charm J/ψ are consistent within uncertainties in pPb collisions at $\sqrt{s_{NN}} = 5.02$ TeV. According to results of R_{pPb} and R_{FB} at LHCb, the forward cross-section of D^0 is obviously suppressed relative to the backward, indicating strong CNM effects in pPb collisions.

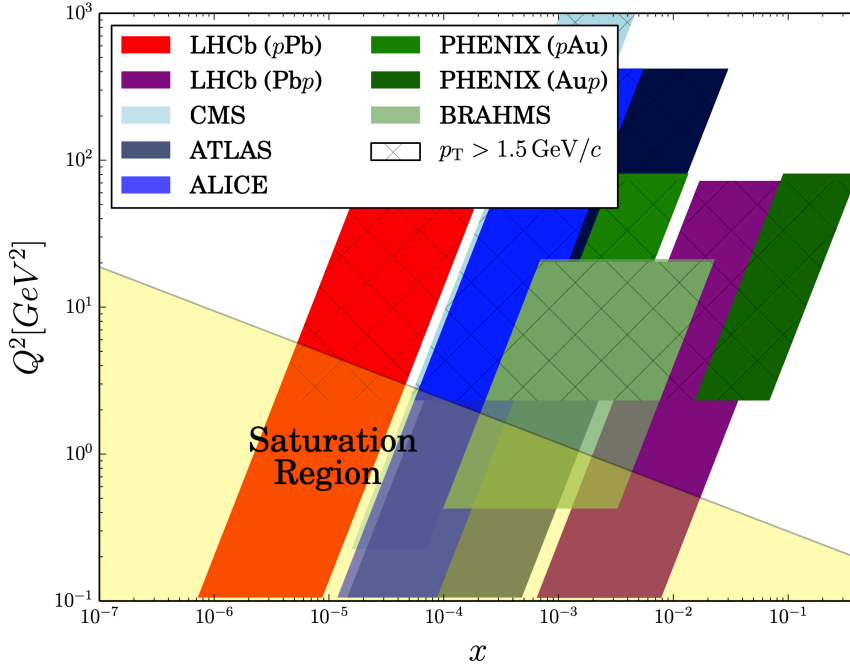


Figure 1.21 Phase space coverage of charged hadrons in $p\text{Pb}$ collisions at $\sqrt{s_{\text{NN}}} = 5.02 \text{ TeV}$ from LHC and other experiments, including CMS^[111], ATLAS^[112], ALICE^[113], PHENIX^[114] and PHOBOS^[115]. The saturation region of Pb is taken from Ref. [116-117]. The figure is taken from Ref. [118].

Table 1.3 Phase space cover regions in terms of Bejorken x_F at some fixed-target experiments.

| Experiments | Collision systems | E_{lab} [GeV] | Phase space |
|---------------------------|-------------------------------------|-----------------|----------------------|
| HERA-B ^[119] | $p\text{-C, W, Ti}$ | 920 | $-0.34 < x_F < 0.14$ |
| E866 ^[120] | $p\text{-Be, W, Fe,}$ | 800 | $-0.1 < x_F < 0.93$ |
| NA50 ^[121-122] | $p\text{-Be, Pb, W, Al, Cu, Ag}$ | 400/450 | $-0.1 < x_F < 0.1$ |
| NA60 ^[123] | $p\text{-Be, Pb, W, Al, Cu, U, In}$ | 158/400 | $-0.1 < x_F < 0.35$ |
| NA3 ^[124] | $p\text{-H, Pt}$ | 200 | $0.0 < x_F < 0.7$ |

Fig. 1.21 depicts the phase space coverage of charged particles in 5.02 TeV $p\text{Pb}$ collisions at LHC and in $d\text{Au}$ 200 GeV collisions at RHIC in terms of Q^2 and x ,

$$Q^2 \approx m_T^2 = m^2 + p_T^2, \quad (1.23)$$

$$x \sim Q^2 \cdot e^{-\eta} / \sqrt{s_{\text{NN}}}, \quad (1.24)$$

Here, $m = 0.255 \text{ GeV}/c^2$, is the average mass of charged particles. With respect to the polar angle θ made with the beamline, pseudo-rapidity η , is “ $-\ln\left(\tan\frac{\theta}{2}\right)$ ”.

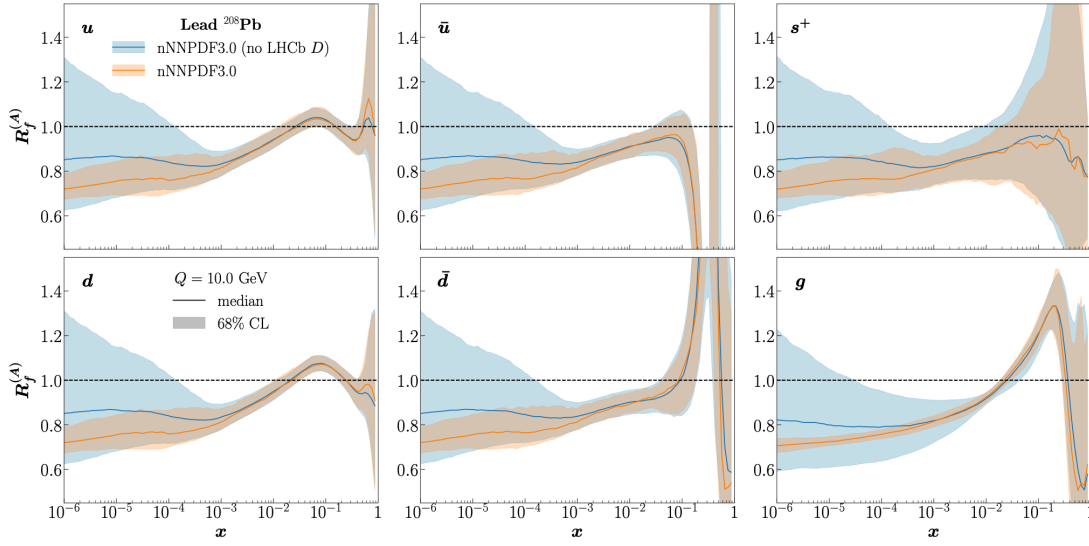


Figure 1.22 Results of $R_i^A(x, Q^2)$ computed by nNNPDF3.0 set with and without D^0 cross-section at LHCb as input. The figure is taken from Ref. [125].

As shown in Fig. 1.21 and Table. 1.3, compared with pA collisions at RHIC (PHENIX^[114], PHOBOS^[115]), LHC (CMS^[111], ATLAS^[112], ALICE^[113]) and other fixed-target experiments (HERA-B^[119], E866^[120], NA50^[121-122], NA60^[123], NA3^[124]), the forward rapidity region at LHCb can explore the small x region of $R_i^A(x, Q^2)$ corresponding to the nuclear shadowing effect until 10^{-6} , which cannot be probed by other experiments; the backward rapidity region can detect the mid- x region of $R_i^A(x, Q^2)$ that corresponds to the anti-shadowing effect. In the (x, Q^2) plane, the unique coverage of pPb collisions at LHCb complement other experiments well when investigating CNM effects.

As illustrated in Fig. 1.22, recently Khalek and Rhorry et al. employed the constrains from D^0 cross-section in 5.02 TeV pPb collisions at LHCb in the nNNPDF3.0^[125] calculations of the nuclear modification $R_i^A(x, Q^2)$. The uncertainty of $R_i^A(x, Q^2)$ with the D^0 constraints is significantly reduced compared to previous results without the D^0 constraints. In this study, open charm (D^+ , D_s^+) cross-sections are determined in same experimental configurations as D^0 , and their cross-sections are expected to improve the $R_i^A(x, Q^2)$ result at both small and mid x regions.

1.4 Thesis motivation and structure

1.4.1 Thesis motivation

Although D^+ and D_s^+ cross-sections have been measured in 5.02 TeV p Pb collisions covering the mid-rapidity from ALICE down to $p_T = 1$ GeV/ c and $p_T = 2$ GeV/ c ^[90]. In this thesis, the first measurement of D^+ and D_s^+ productions approaches $p_T = 0$ GeV/ c in forward and backward rapidity regions at LHCb, which provides a precise constraint to the small x nPDF and CGC predictions. With D^+ and D_s^+ cross-sections for forward and backward configurations at 5.02 TeV, CNM effects in p Pb collisions can be probed by the forward-backward cross-section ratio. The nuclear modification factor R_{pPb} is determined using D^+ and D_s^+ cross-sections in pp collisions is another good observable to investigate CNM effects and constrain pQCD calculations in nPDF and CGC frameworks. The cross-section ratios between strange D_s^+ and non-strange D^+ , D^0 in p Pb collisions can be compared with that in pp collisions. The ratios in small systems can study the strangeness enhancement and provide a baseline for nucleus-nucleus collisions.

1.4.2 Thesis structure

The thesis is organized as follows: In Chapter 2, the LHC experiment and the LHCb detector are introduced. The specific process of the analysis is introduced in Chapter 3 and Chapter 4. First, the inclusive D^+ and D_s^+ yields are determined by applying unbinned maximum likelihood fit to the invariant mass distribution, and then the *sPlot* method is used to remove combinatorial backgrounds. Since the LHCb vertex detector has the best IP resolution at LHC, the method of fitting the $\log_{10} \chi_{IP}^2(D_{(s)}^+)$ is used to obtain prompt D^+ and D_s^+ signal yields. Then a series of efficiencies are calculated to correct them. In each analysis step, various systematic uncertainties are taken into account. In Chapter 5, the production cross-sections of D^+ and D_s^+ in the unique forward rapidity region at LHCb are determined, and the physical quantities such as R_{FB} , R_{pPb} and particle cross-section ratios are systematically studied with transverse momentum and rapidity. Chapter 6 summarizes the main results and provides the prospects for measuring open charm cross-sections in p Pb collisions and fixed-target experiments during the LHCb Run 2-4 periods.

CHAPTER 2 LHCb EXPERIMENT

The prompt D mesons of interest in this study are produced in high-energy proton-lead collisions, which were collected by the LHCb detector. The Large Hadron Collider beauty (LHCb) experiment^[126] is one of the four major experiments at the Large Hadron Collider (LHC)^[127]. Its primary scientific goal is to look for indirect evidence of New Physics in CP violation and rare decays of beauty and charm hadrons. Therefore, the LHCb detector was designed particularly for heavy flavor measurements, and it has an outstanding vertex detection and particle identification system for the reconstruction of beauty and charm hadrons.

Section. 2.1 of this chapter briefly introduces the LHC collider, while Section. 2.2 introduces the LHCb detector and its tracking system, particle identification system, trigger system and data flow.

2.1 Large Hadron Collider

With a tunnel circumference of about 27 kilometres and a depth of about 50 to 175 meters underground, LHC is a ring-shaped particle collider built to replace the Large Electron-Positron Collider (LEP) at CERN. ATLAS^[128], CMS^[129], ALICE^[130], and LHCb^[126] are the four major experiments at the LHC. ATLAS and CMS are dedicated to the studies of the origin of mass, the unification of fundamental forces, and the dark matter and dark energy, and have made significant contributions to the discovery of the Higgs boson. ALICE studies the properties of strongly interacting matter at extremely high energy densities with heavy-ion collisions at LHC. Besides measuring the CKM matrix and studying CP violations (CPV) and rare decays in b physics, LHCb, as a general purpose detector at forward rapidities, can also explore a wide range of other physics topics, such as hadron spectroscopy and heavy-ion physics.

Fig. 2.1 shows the accelerator complex at CERN and the locations of ATLAS^[128], CMS^[129], ALICE^[130] and LHCb^[126] experiments at the LHC. In this complex, protons are first accelerated to 50 MeV by a linear accelerator (LINAC2) and then to 1.4 GeV and 25 GeV by the Proton Synchrotron Booster (PSB) and the Proton Synchrotron (PS), respectively. The protons are subsequently accelerated to 450 GeV in the third ring accelerator, the Super Proton Synchrotron (SPS). Finally, in the LHC, the protons are accelerated

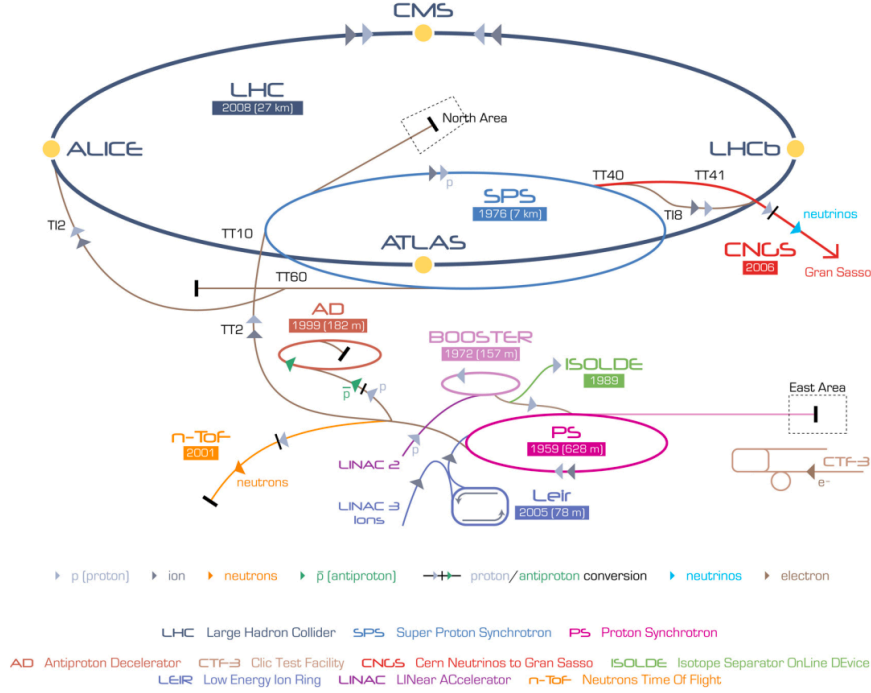


Figure 2.1 Schematic diagram of the LHC and its accessories.

to 7 TeV in two distinct beam tubes where the proton beams circulate in opposite directions. Protons are filled into the LHC in bunches, which are separated by multiples of nearly 25 ns in time (or 7 meters in distance).

Protons are filled into the LHC in bunches separated by time intervals of 25 ns (or about 7 metres in distance)^[131]. Protons from the two beams collide during the bunch crossing, the upper limit of designed centre-of-mass energy for proton-proton collisions is $\sqrt{s} = 14$ TeV. Slightly different from protons, the Pb beams are first accelerated with a linear accelerator (LINAC3) and a Low-Energy Ion Ring (LEIR), then enter the PS. During this period, the Pb beams are stripped into heavy-ions by passing through the metal foil twice. The Pb ions are further accelerated in SPS and finally filled into LHC to reach the designed energy, which is 2.76 TeV per nucleon. To control the direction of the particle beam and ensure that the beam travels safely in the collider, the LHC uses 1232 super Nb-Ti electromagnets, which are cooled to nearly 1.9 K by a liquid helium circulation system to make them reach a superconducting state. A strong magnetic field of about 8.33 T is generated. Additionally, 392 quadrupole magnets were also installed to focus the beam and increase the rate of collisions.

The number of certain events per second in the collision point of the LHC is given by Eq. (2.1)

$$N_{\text{event}} = \sigma_{\text{event}} \times \mathcal{L}, \quad (2.1)$$

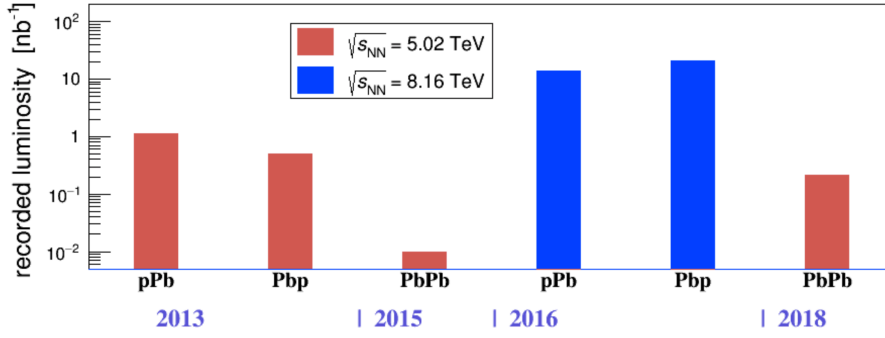


Figure 2.2 Integrated luminosities of $p\text{Pb}$ and PbPb collisions collected during the LHCb Run 1 and Run 2 periods.

where σ_{event} is the cross-section of event studied, and \mathcal{L} is the instantaneous luminosity of the collider. In pp collisions, the luminosity is defined as

$$\mathcal{L} = \frac{k N_p^2 f}{4\pi \sigma_x^* \sigma_y^*} \quad (2.2)$$

where k represents the number of bunches in the beam (2802), N_p is the number of protons in each bunch (1.5×10^{11}), f is the revolution frequency (11.245 kHz), and σ_x^* , σ_y^* represent the beam size in transverse directions (the values are $16.7 \mu\text{m}$ for ATLAS and CMS and $70.9 \mu\text{m}$ for ALICE and LHCb) at the collision point. The designed luminosity of LHC is $10^{34} \text{ cm}^{-2} \text{ s}^{-1}$, which is also peak of ATLAS and CMS. However, the problems of high detector response, high occupancy, and multiple vertices brought by high luminosity make the reconstruction of tracks difficult; the detector radiation damage under high luminosity is also more severe. Therefore, LHCb typically has a luminosity of $2 \times 10^{32} \text{ cm}^{-2} \text{ s}^{-1}$ and can reach a maximum of $5 \times 10^{32} \text{ cm}^{-2} \text{ s}^{-1}$. In this way, the number of proton-proton interactions in each bunch crossing is kept around 1 – 2. The integrated luminosity collected by LHCb in $p\text{Pb}$ and PbPb collisions are shown in Fig. 2.2. In the Run 1 period, LHCb collected about 1.5 nb^{-1} of $p\text{Pb}$ collisions data at $\sqrt{s_{\text{NN}}} = 5.02 \text{ TeV}$ in 2013; in the Run 2 period, LHCb collected about 30 nb^{-1} of $p\text{Pb}$ collisions data at $\sqrt{s_{\text{NN}}} = 8.16 \text{ TeV}$ in 2016, and nearly $210 \mu\text{b}^{-1}$ of PbPb collisions data at $\sqrt{s_{\text{NN}}} = 5.02 \text{ TeV}$ were collected in 2015 and 2018. During the Long-Shutdown2 of the LHC in 2020, LHCb will undergo a substantial detector upgrade, with the goal of collecting nearly 14 fb^{-1} of data in Run 3 (from 2022 to 2024).

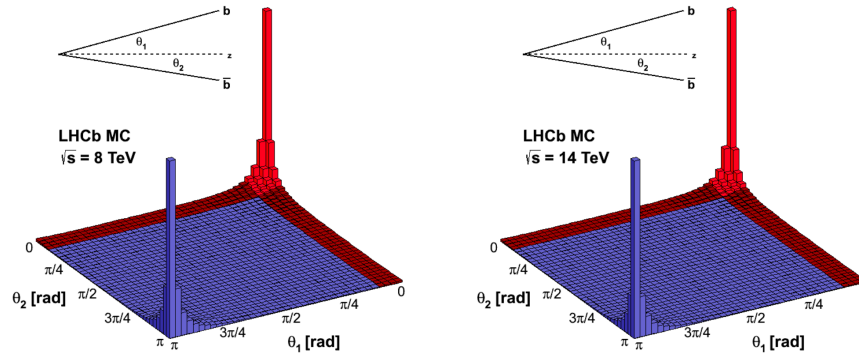


Figure 2.3 Outgoing angles of b and \bar{b} hadrons in pp collisions at LHC (from Pythia simulation).

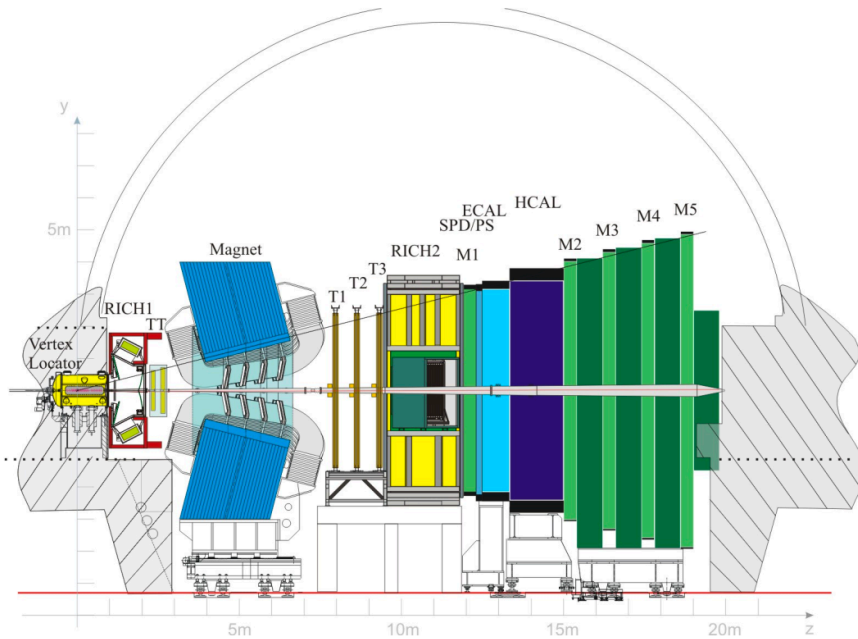


Figure 2.4 Layout of the LHCb detector: the z -axis is in parallel with the beam direction, the y -axis is vertically upward, and the x -, y - and z -axes form the right-hand coordinate system.

2.2 LHCb Detector

The LHCb is a single-arm forward detector, with an angular acceptance covering 10 to 300 mrad horizontally and 10 to 250 mrad vertically. This design is based on the fact that the b and \bar{b} hadron pairs produced in pp collisions at LHC are highly concentrated in a small cone in either forward or backward directions, as shown in Fig. 2.3. The middle 0-10 mrad region is the beam tube of the LHC, therefore, the 10 mrad cone in the centre is not within the LHCb acceptance. Even though LHCb occupies only 4% of the solid angle, the Pythia simulation shows that it can collect 27% of the b or \bar{b} hadrons.

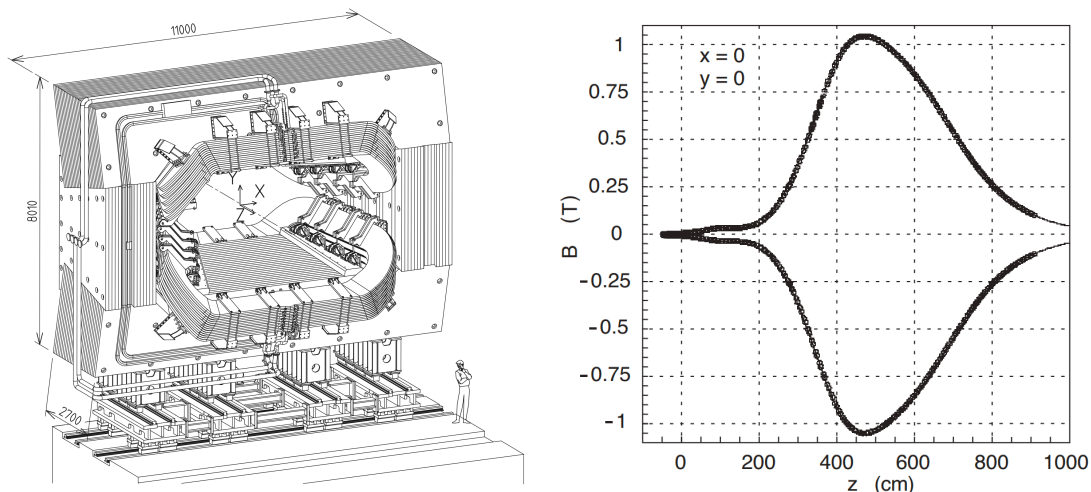


Figure 2.5 Magnet system of LHCb (left) and the magnetic field strength B , along the z axis for both polarities (right). These figures are taken from Ref. [126].

The layout of the LHCb detector is shown in Fig. 2.4. There are several components of the LHCb spectrometer: a Vertex Locator (VELO)^[132], two Ring Imaging Cherenkov detectors (RICH1, RICH2), four planar tracking stations (TT, T1, T2 and T3), a Scintillation-Pad detector (SPD), a pre-shower detector (PS), a hadron calorimeter (HCAL), an electromagnetic calorimeter (ECAL), the muon detector (M1-M5), and other sub-detectors. The following describes each sub-detector in details.

2.2.1 Magnet System

The normal temperature dipole magnet installed on the LHCb detector can produce a deflection magnetic field with an integrated magnetic field strength of 3.6 Tm. By deflecting the trajectory of charged particles in a magnetic field, momentum p can be calculated. As shown in Fig. 2.5 (left), the entire magnet system is composed of a 1500-ton magnet yoke and two coils with a total weight of 54 tons. Two identical coils are placed mirror-symmetrically in a pheasant-shaped magnet yoke. This design is suitable for a geometric acceptance requirement of $2 < \eta < 5$. Fig. 2.5 (right) shows the variation of magnetic field strength B in the beam direction. To measure the momentum with an accuracy of $\delta p/p = 0.5\%$ in a large momentum range (0 – 100 GeV/c), the location of the peak magnetic field strength is accurate to the order of millimeters. Magnetic fields are periodically reversed to reduce the impact of left-right asymmetry on some measurements such as CPV.

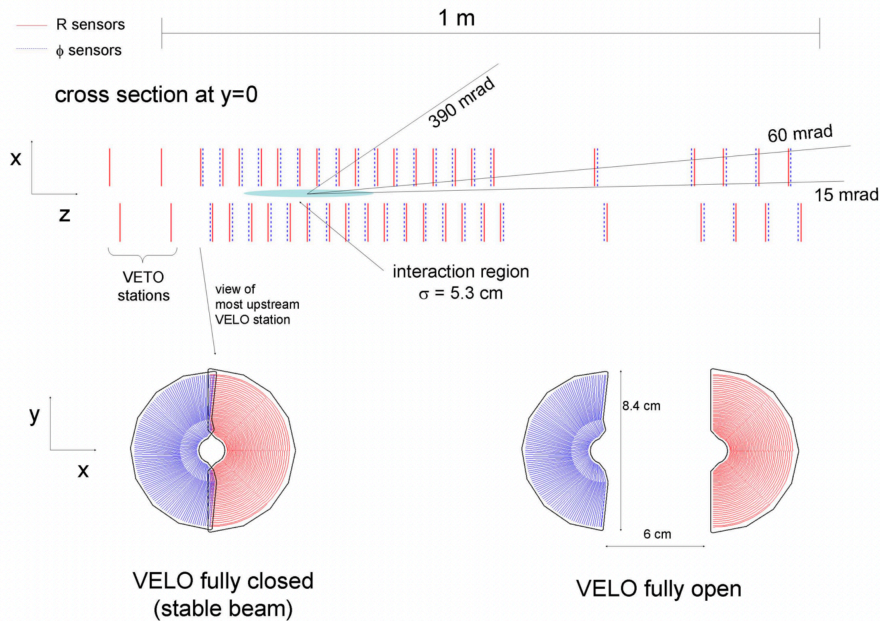


Figure 2.6 Cross-section at $y = 0$ of the VELO silicon sensors in the fully closed status. The bottom left and right figures show the front faces of the most upstream VELO station in the closed and open status, respectively. The figures are taken from Ref. [132].

2.2.2 Tracking System

The tracking system^[132] of the LHCb detector consists of a VELO detector and four tracking stations (TT, T1–T3). The tracking system reconstructs the track of a charged particle using the hits left by this particle when passing through the detectors.

2.2.2.1 Vertex Locator

As shown in Fig. 2.6, the VELO consists of 21 silicon stations distributed along the z -axis; each station contains two partially overlapping silicon sensors, which can measure the particle radial coordinate r and deflection angle coordinate ϕ . Upstream of the VELO, two extra stations (also known as the pile-up system) that only detect radial position information are used to measure charged-track multiplicity of some backward events and assist in the reconstruction of primary vertices. The VELO stations can be opened or closed, as shown in Fig. 2.6. It is opened during beam injection for protection, and the VELO halves can retract by 3 cm from the beam axis. After the beam is stable, the VELO stations are closed to get a better primary vertex (PV) resolution. The minimum distance of the VELO sensors to the beam axis can be about 8 mm. The resolution of the primary vertex along the z -axis (x - or y - axis) is about 60 μm (10 μm), and the exact values depend on the number of tracks used in vertex reconstruction. The impact parameter (IP) defined

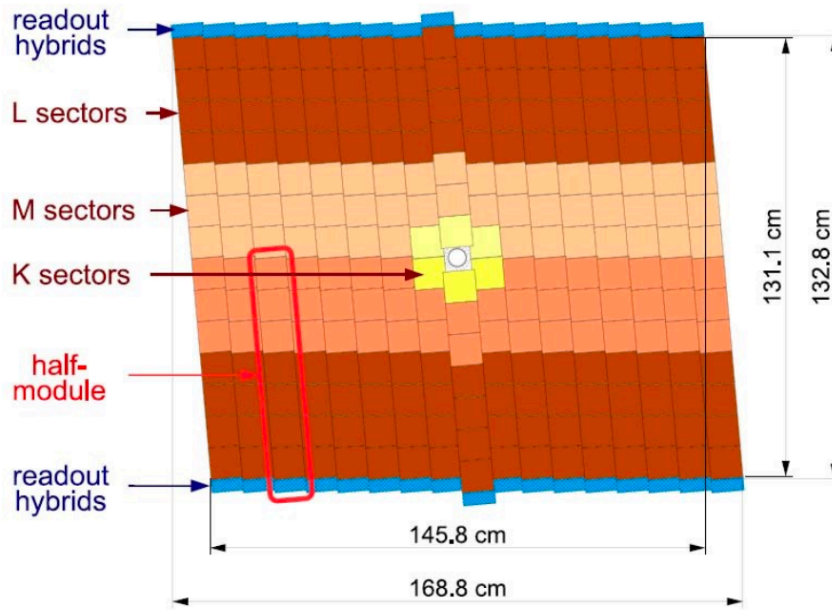


Figure 2.7 Structure of the third TT layer. Different readout sectors are indicated with different colors.

as the distance between a track and the PV at its closest approach, is very effective for identifying those tracks originating from secondary vertices. The resolution of IP is also below $20\ \mu\text{m}$ for very high transverse momentum tracks, ignoring the uncertainty in the primary vertex.

2.2.2.2 Trigger Tracker

The Trigger Tracker^[133] (TT) is a silicon microstrip detector located between the RICH1 and the dipole magnet. The magnetic field in TT allows quick measurement of particle momentum for trigger decisions.

The TT is composed of four rectangular detection layers with a width of 150 cm and a height of 130 cm. It can completely cover the acceptance of LHCb. These detection layers are arranged in an $x - u - v - x$ geometry. The first and fourth layers are called x -layers, have vertical read-out strips (pitch is about $200\ \mu\text{m}$). While the second and third layers are rotated by $+5^\circ$ (u -layers) and -5° (v -layers) respectively. The four layers are divided into two groups (x, u) and (v, x), and each group contains two layers. These two groups, (x, u) and (v, x), are called “TTa” and “TTb”, respectively. The distance between TTa and TTb is about 27 cm. The structure of the third layer is shown in Fig. 2.7.

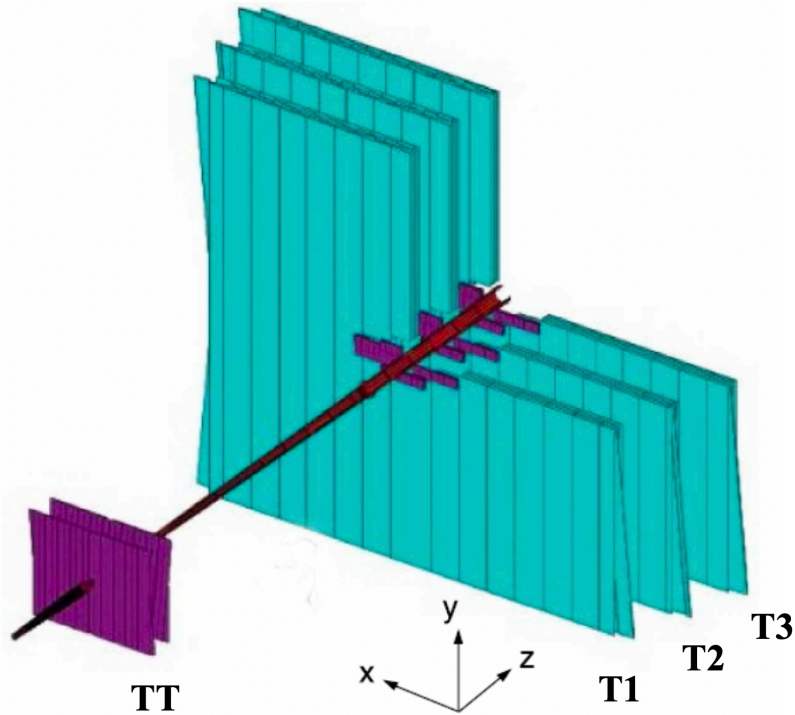


Figure 2.8 LHCb tracking system(TT, T1-T3). The purple part is TT and IT, which are made of silicon microstrip sensors, and the green part is the OT.

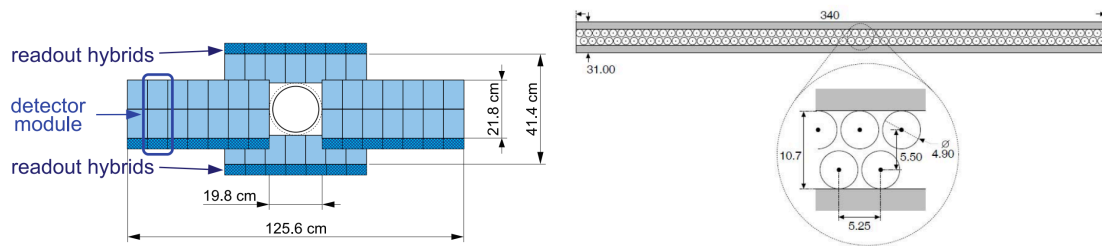


Figure 2.9 Structure of the second IT layer along the x-axis (left); and cross section of a OT straw-tube module (right).

2.2.2.3 Tracking Station

The three tracking stations T1-T3 are depicted in Fig. 2.8, and charged particles can only be detected by them if their momentum is greater than 5 GeV. In considering the inhomogeneous particle densities on tracking stations, each track station is divided into the inner tracker system (IT) and the outer tracker system (OT). The IT^[134] consists of four layers of silicon microstrip sensors; the IT is about 120 cm in width and 40 cm in height, and the total area of the sensitive area is about 4 m². The structure of the second IT layer along the x-axis is shown in Fig. 2.9 (left). The IT occupies only 2% of the solid angle of the LHCb detector, but about 20% of tracks passes through it.

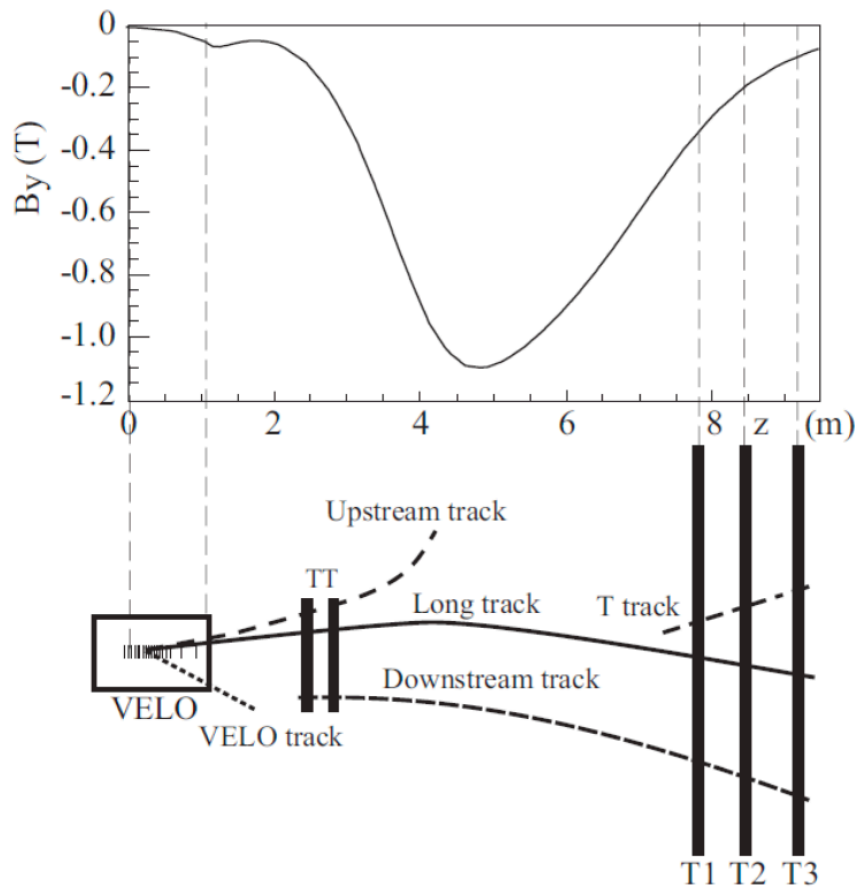


Figure 2.10 Different types of reconstructed tracks and the corresponding magnetic field strength B_y along the z -axis.

The OT is a straw-tube drift-chamber detector, and is also composed of four detection layers. Each detection layer has several air-tight straw-tube modules containing two staggered layers of drift-tubes, as shown in Fig. 2.9 (right). The working gas of OT^[135] is a mixture of 70% argon, 28.5% carbon dioxide and 1.5% oxygen, which can guarantee a spatial resolution of less than 200 μm and a temporal resolution of fewer than 50 ns.

2.2.2.4 Track Reconstruction

The tracking software combines the hits generated by charged particles in the tracking detectors to reconstruct particle trajectories. As displayed in Fig. 2.10, based on the location of their hits in tracking stations, the tracks can be classified into the following types: long track, upstream track, downstream track, vertex detector track, and T-track^[136].

- The long tracks, traverse through all tracking detectors, from the vertex detector VELO to the tracking T stations. They include their hits from all tracking detectors in track reconstruction, and hence have the best track quality (good IP and excellent

momentum resolution). Therefore, they are the essential type of tracks for reconstructing charm hadron decay.

- The upstream tracks, have hits only in the VELO and the TT detectors. These tracks usually have lower momentum and are deflected by the magnetic field, hence cannot reach the T-stations.
- The downstream tracks, have hits only in the TT and the tracking stations T1-T3. These tracks also have good momentum resolution. As Λ and K_s^0 could decay outside of the vertex detector acceptance, the downstream tracks are usually needed for reconstructing Λ and K_s^0 .
- The VELO tracks, have hits only in the VELO. These tracks could have large outgoing angle or even point backwards (called backward tracks), and are very helpful for the PV reconstruction.
- The T tracks, have hits only in the T stations. They are mainly generated during the secondary interactions, and are helpful for particle identification in RICH2.

The following is the track reconstruction procedure: The first step is to search for track seeds. It begins with the regions with low magnetic field, such as VELO and T stations, so that the tracks there can be considered as straight lines. Then the forward tracking algorithm will extrapolate the VELO seeds to the correct T and TT hits, resulting in the finding of long tracks. Once a track is found, it is fitted with a Kalman filter to get its parameters, such as χ^2 . In order to increase the efficiency in reconstructing long tracks, the track matching algorithm will try to match the T seeds with the VELO seeds that failed in forward tracking extrapolation. Once a good match is found, the resulted long track will be fitted with Kalman filter as well. After that, the upstream (downstream) tracking start to match the left VELO (T) tracks with TT hits for finding the upstream (downstream) tracks. The VELO (T) seeds that have not been associated with any long tracks and upstream (downstream) tracks will be considered as VELO (T) tracks.

The performance of track reconstruction is usually evaluated by the track reconstruction efficiency and momentum resolution. The relative long track momentum resolution of the 2011 data (shown in Fig. 2.11) and the long track reconstruction efficiency of the 2012 data and simulation (shown in Fig. 2.12) were determined using a tag-and-probe method with the $J/\psi \rightarrow \mu^+ \mu^-$ decay channel. The relative momentum resolution is more than 0.4% and increases with the increasing p . When $p_T > 10 \text{ GeV}/c$ or $\eta > 2$, the reconstruction efficiency for the long track is larger than 95%. The difference between the long

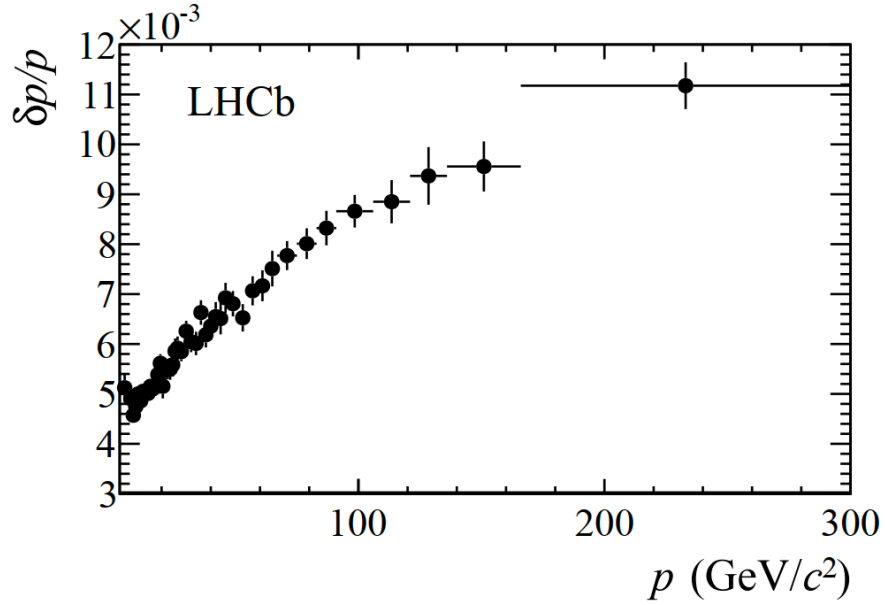


Figure 2.11 Relative momentum resolution of the 2011 data. This figure is taken from Ref. [137].

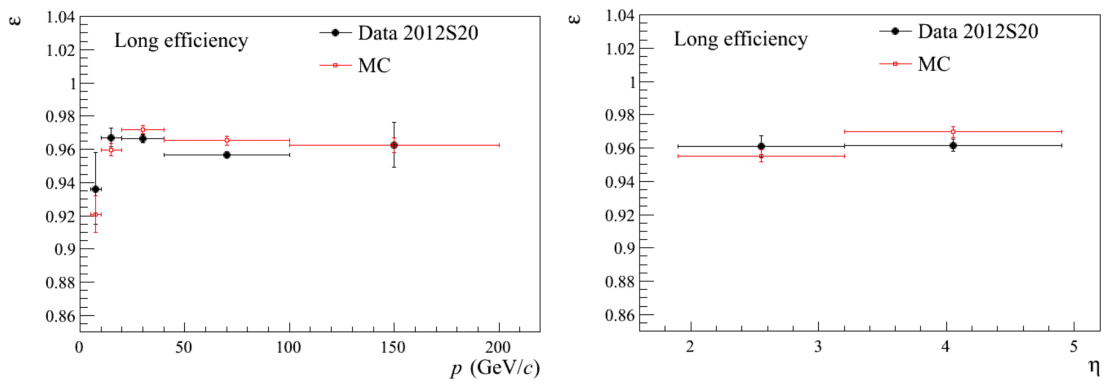


Figure 2.12 Long track reconstruction efficiency as a function of momentum p (left) and pseudo-rapidity η (right).

track efficiencies calculated with the simulation and with the data has been accounted for in the tracking efficiency tables, more details are provided in Section. 4.4.2.

2.2.3 PID System

The RICH1 and RICH2, the electromagnetic and hadron calorimeters, and the muon system are the primary sub-detectors of the LHCb particle identification system. RICH1 and RICH2 are used to distinguish K from π , which is important for the measurements of open charm mesons. Electromagnetic calorimeters can help to identify electrons and photons, and the muon system are explicitly dedicated to muon identification.

2.2.3.1 RICH

If the speed v of a charge particle is larger than that of light in an insulating medium, the particle continuously emits light on a cone about its moving direction and loses energy, which is also known as the Cherenkov radiation. The cone angle θ_c is given by

$$\cos(\theta_c) = \frac{c}{nv} = \frac{1}{n\beta}, \quad (2.3)$$

where n is the refractive index of the medium. RICH detects the Cherenkov radiation angle θ_c , which is used with the momentum p acquired by the tracking detectors to determine the mass of a charged particle for particle identification. The relations between the Cherenkov angle θ_c and the momentum for different particles in different materials (with different refractive indices) are depicted in Fig. 2.13.

RICH1^[138] employs C_4F_{10} ($n = 1.0014$ at $\lambda = 400$ nm) gas and aerogel ($n = 1.03$ at $\lambda = 400$ nm) as radiators and has a wide Cherenkov radiation angle acceptance range: from ± 25 mrad to ± 300 mrad in the horizontal direction and ± 250 mrad in the vertical direction^[139]. It covers the low momentum charged particles from ~ 1 to 60 GeV/ c . RICH2^[140] employs CF_4 ($n = 1.0005$ at $\lambda = 400$ nm) gas as radiators and has a smaller Cherenkov radiation angle acceptance range: from ± 15 mrad to ± 120 mrad in the horizontal direction and ± 100 mrad in the vertical direction. It covers the high momentum charged particles from 15 to 100 GeV/ c .

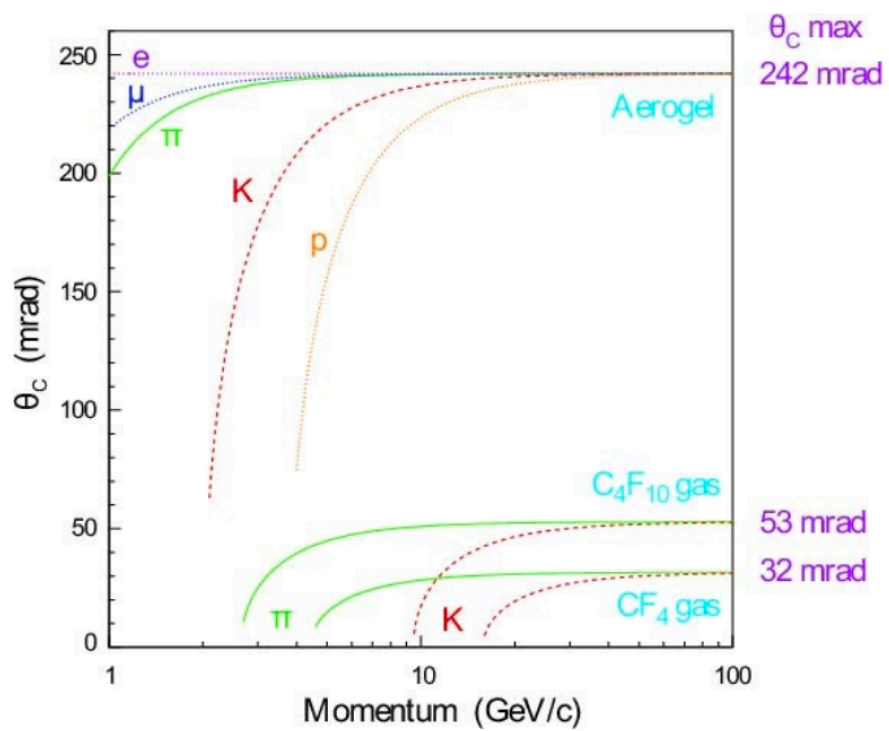


Figure 2.13 Variations of the Cherenkov angle θ_c with momentum for various charged particles in three different materials used in LHCb RICH detectors.

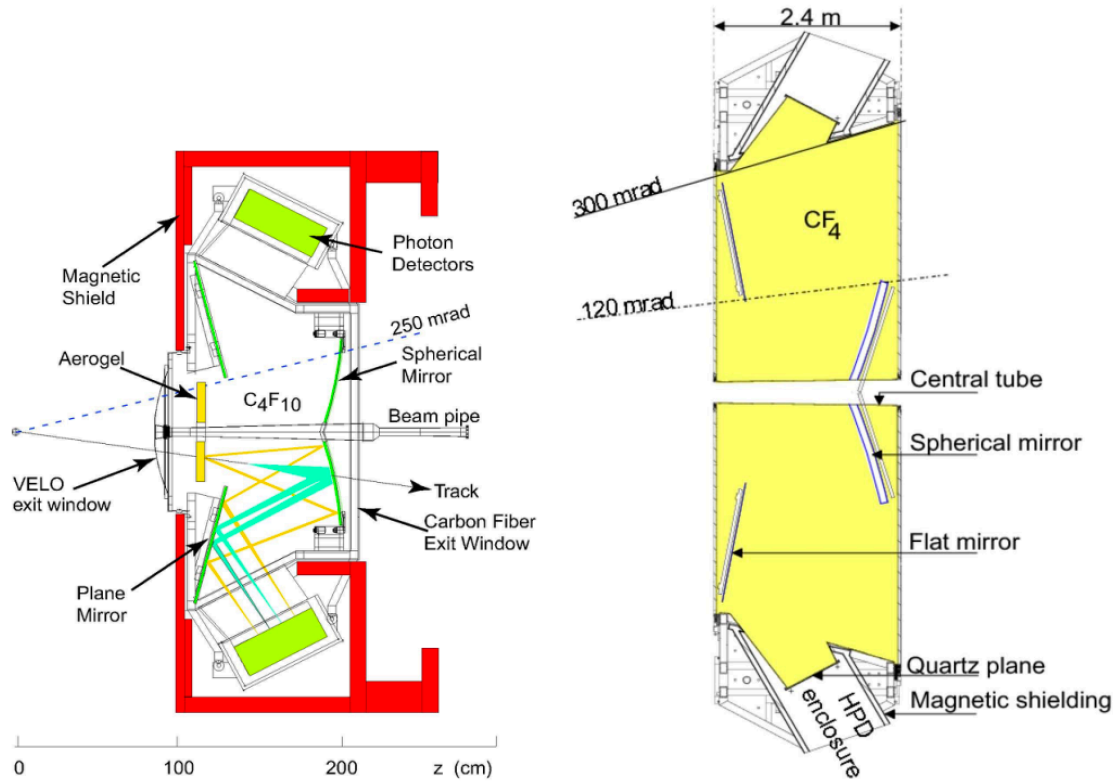


Figure 2.14 Schematic layout of the RICH1 detector in the y - z plane (left); schematic layout of the RICH2 detector in the x - z plane (right).

Hybrid photon detectors (HPDs) situated outside of the LHCb acceptance, spherical mirrors, and flat mirrors together constitute the optical system of both RICH detectors. As shown in Fig. 2.14, these devices are arranged vertically in RICH1 and horizontally in RICH2. The Cherenkov photons are focused by spherical mirrors and the resulting ring images are reflected by flat mirrors to the HPDs, which detect the photons with wavelength ranging from 200 to 600 nm.

2.2.3.2 Calorimeters

The calorimeters are used to identify hadrons, electrons, and photons, and measure their position and energy, and also to select candidates with large transverse energy in the hardware trigger (L0). The LHCb calorimeter system^[137] is made up of four components: the SPD, the PS, the ECAL, and the HCAL^[141].

The SPD is located in front of the ECAL. As only charged particles can interact with scintillator, the SPD identifies charged particles and allows electrons to be separated from photons. Through the 12 mm thick lead layer behind the SPD, electrons and photons create EM showers, which can then be measured in the subsequent second layer of scintillator pads to determine the particles electromagnetic properties (i.e., whether it is an electron if

it is charged, or a photon if it is neutral.). At the trigger level, the SPD and PS are utilized in conjunction with the ECAL to identify the existence of electrons, photons, and neutral pions.^[136] The ECAL comes before the HCAL. With a total thickness of 25 radiation lengths (X_0), it is a sampling scintillator/lead “shashlik” structure detector composed of 2 mm-thick lead absorber layers and 4 mm-thick polystyrene scintillator layers. The ECAL is designed with an energy resolution of $\delta(E)/E = 10\%/\sqrt{E} \oplus 1\%$, with E in the unit of GeV and \oplus expressing quadratic sum. The HACL is another sampling calorimeter with iron and scintillator as absorption layer and detection layer respectively. HACL is used mostly for hardware triggering. The energy of incident hadrons is derived from the hadron shower. The energy resolution of the hadron calorimeter is $\delta(E)/E = 69\%/\sqrt{E} \oplus 9\%$.

2.2.3.3 Muon System

As shown in Fig. 2.15, the muon^[142] system consists of five stations (M1-M5), which perform muons identification and provide the first-level hardware trigger (L0).

The M1 is installed before the calorimeters, and is used to determine the momentum of muons in L0. Behind the calorimeter, M2-M5 are arranged in parallel and are separated by 80 cm thick iron absorbers, which select the traversing muons. As listed in Table 2.1, “IsMuon” is a Boolean quantity commonly used in physical analysis to identify muons, and is defined by the number of detection stations the candidate muon has passed through, where the number of stations it can cross is dependent on the momentum^[143]. The momentum of muons traversing the five stations should exceed 6 GeV/c, and the total absorption length reaches 20 times the nuclear interaction length (λ_i).

Table 2.1 Number of muon stations needed to trigger “IsMuon” in different momentum intervals. The table is taken from Ref. [143].

| Momentum interval | Muon stations |
|-------------------------------|--------------------------|
| $p \in (3, 6) \text{ GeV}/c$ | M2 and M3 |
| $p \in (6, 10) \text{ GeV}/c$ | M2 and M3 and (M4 or M5) |
| $p > 10 \text{ GeV}/c$ | M2 and M3 and M4 and M5 |

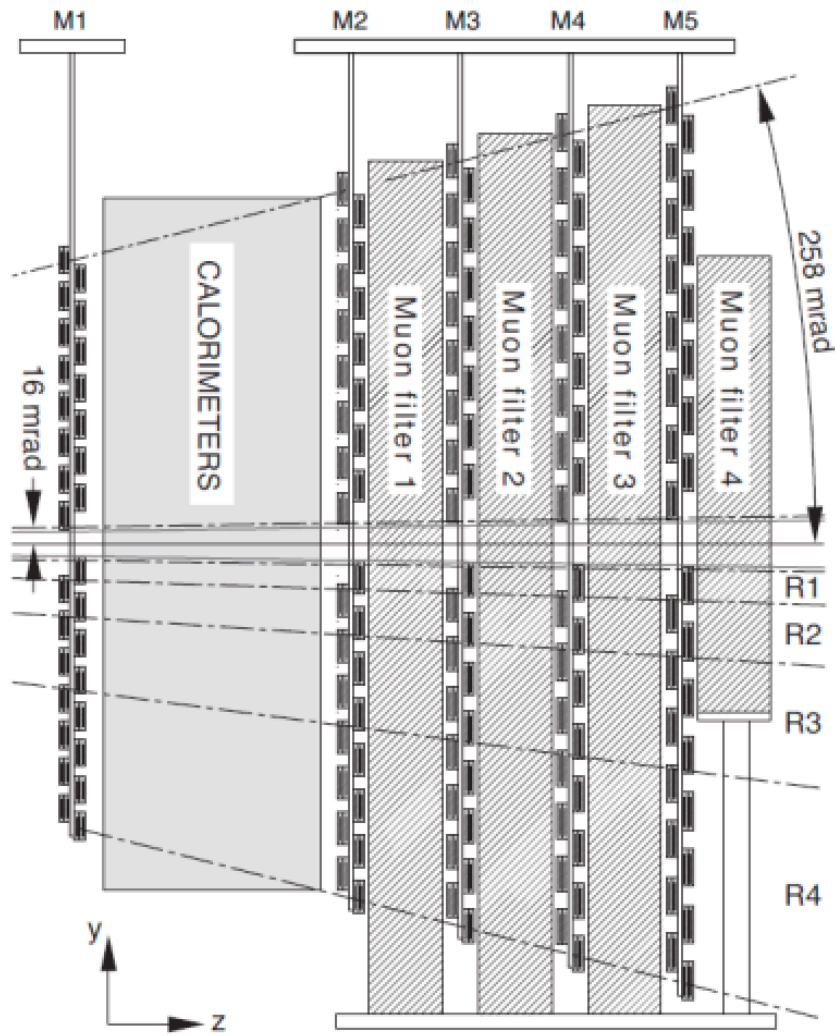


Figure 2.15 Side view of the LHCb muon system.

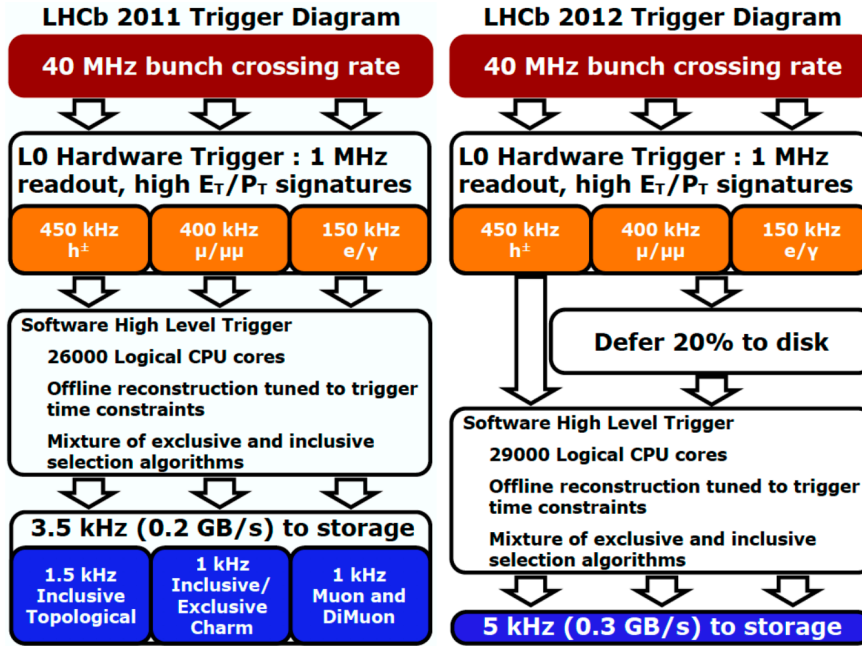


Figure 2.16 LHCb trigger diagram in pp collisions during Run 1.

2.2.4 Trigger

The nominal LHC bunch crossing frequency is 40 MHz. Due to the limitation of the detector electronics and data bandwidth of the storage, this frequency must be reduced to no more than 2 kHz by the trigger before events are written into storage for the offline analysis. As shown in Fig. 2.16, the LHCb experiment has the first-level trigger (L0) and the high-level trigger (HLT)^[144]. The L0 is a hardware trigger that works synchronously with the bunch crossing. The HLT is a software trigger that runs on the computer clusters.

2.2.4.1 L0 System

The purpose of L0 is to reduce the 40 MHz bunch crossing rate to a 1.1 MHz events rate so that the whole detector can be read out^[145]. The pile-up system, the calorimeter trigger system, the muon trigger system, and the decision-making unit are the four sub-trigger systems that constitute the L0 system. The pile-up system is used to exclude events with multiple primary vertices. The L0 calorimeter system (SPD, PS, ECAL, HCAL) aims to search for particles with high transverse energy E_T , which are identified as electrons, photons or hadrons based on their energy deposited in the calorimeter system. The goal of the muon system is to filter out muons with high transverse momentum. After obtaining the information of the above three trigger systems, the decision-making unit adds filtering conditions to multiple tracks and thresholds, and makes a comprehensive decision for

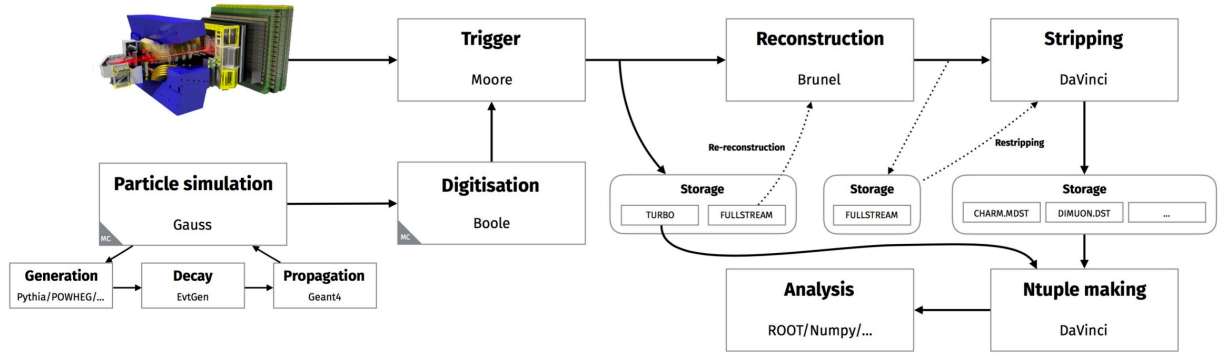


Figure 2.17 LHCb data flow and the corresponding applications.

each event. This decision will be passed to the data acquisition system and front-end electronics.

2.2.4.2 HLT System

In Run 1, the HLT computer system consists of almost 3000 logical CPU cores, which are utilized to confirm the L0 system decision and implement a series of online reconstruction procedures. The HLT is divided into two stages: HLT1 and HLT2. The HLT1^[146] reconstructs the particles corresponding to the L0 selections in the VELO and T stations, reduces the event rate to around 30kHz, and the total decision time per event is roughly 10~15 ms. The HLT2 provides for a full reconstruction of the events selected by HLT1 to further reduce the trigger rate to a few kHz.

According to different physics goals, different trigger lines are set in L0, HLT1, and HLT2 triggers, and they run in parallel. If an event triggers at least one of the trigger lines, it will be recorded to offline storage. A unique trigger configuration key (TCK) is formed by all trigger lines on the user-interested events and their corresponding specific filter settings, which can be saved in files for offline analysis.

This thesis focuses on the open charm data analysis in $p\text{Pb}$ collisions. Both the number of bunches (~ 340) and the bunch crossing frequency (~ 420 kHz) in $p\text{Pb}$ collisions are much smaller than those in pp collisions in 2013. Therefore, no strict selections have been applied in the triggers in order to keep as many open charm candidates as possible. The trigger efficiency is considered to be 100%, which will be discussed in details in Section. 3.1.

2.2.5 LHCb Data Flow

The whole process of data reconstruction, selection, and storage at LHCb is shown in Fig. 2.17. The LHCb software^[147], which is based on the Gaudi framework^[148], is used to process the data step by step. The specific procedure is given in the following:

- The LHCb data are filtered using the trigger, which includes the L0 and HLT. The L0 is carried out in hardware. The HLT is carried out in software via the Moore application.
- The reconstruction process of triggered data is implemented to convert detector hits into objects like tracks. The Brunel application is responsible for this process. Reconstructed data is then stored in Data Summary Tape (DST) format.
- The DST data can be used directly for physics analysis. Due to the limited computing resources, further central filtering on the data is required. The data is filtered with a series of central preselections with the DaVinci program^[149], also called the Stripping process, then stored in mDST or micro-DST format. The output data with similar selection criteria is saved in the same data stream (Full stream) to improve analysis performance and save storage space. After 2016, only the information relevant to the events required for reconstruction is preserved, processed by the Tesla software project, and used for physical measurements for reconstructed events through the HLT. This data storage is referred to as the Turbo stream^[150] to separate it from the Full stream in Run 1.
- DST files are filtered and analysed in the DaVinci framework. DaVinci contains tools for processing physics event objects with respect to vertices and particles, as well as tools for accessing the Monte Carlo (MC) truth match information.

Simulation samples or called MC events are crucial in designing event selection criteria, calculating efficiency, and estimating the shape distribution of the signal for open charm production measurement. The processing flow of MC is analogous to that of data, except that the pp collision is simulated by the Gauss application^[151], and the detector digitization is controlled by the Boole application^[152]:

- The D mesons simulation process in pp and pPb collisions goes as follows: first, the Gauss application calls NL Pythia^[153] or NLO POWHEG^[154] generator to simulate the $c\bar{c}$ pairs production and hadronization to D mesons in pp collisions; if pPb simulation samples are required, D mesons are embedded into the minimum bias pPb events generated by the EPOS^[155] generator and calibrate the samples

using LHCb data^[151]; after that, the decay of the hadrons was simulated with Evt-Gen^[156], and the QED radiation effect was described using Photos^[157]; at last, all particles propagate through a simulation of the detector geometry, and the detector response is recorded using the Geant4 software package^[158].

- The Boole application converts the simulated hits generated in the virtual detector into signals that reflect the actual sensor^[151]. The file format of the simulation samples is the same as the data after the detector digitization process. Then the simulation samples pass through the standard data processing step, starting with the trigger.

CHAPTER 3 ANALYSIS STRATEGY

Based on the $p\text{Pb}$ data collected at LHCb, the cross-sections, the cold nuclear matter effects and the cross-section ratios for open charm mesons (D^+ , D_s^+ and D^0) are measured. This chapter first describes the data and simulation samples used in this measurement in Section. 3.1. Then Section. 3.2 presents the method for determining open charm production cross-sections. Section. 3.3 outlines a strategy for studying the cold nuclear matter effects on open charm production. Finally, the method for assessing the cross-section ratios of D^+ , D_s^+ and D^0 will be detailed in Section. 3.4.

3.1 Data and simulation samples

The data of $p\text{Pb}$ collisions at $\sqrt{s_{NN}} = 5.02$ TeV collected by the LHCb detector in early 2013 is used in this analysis. During the data taking, two beam configurations were used. In the forward (Fwd) configuration, the proton beam traverses the LHCb detector from the VELO to the muon system and intersects with the lead beam in the interaction point. While in the backward (Bwd) configuration, the proton beam enters the LHCb detector in the opposite direction, i.e. from the muon system. Both magnetic polarities were used to for the data-taking in those two configurations.

The integrated luminosities of the forward and backward data are $(1.06 \pm 0.02) \text{ nb}^{-1}$ and $(0.52 \pm 0.01) \text{ nb}^{-1}$, respectively. The relatively low luminosity of about $5 \times 10^{27} \text{ cm}^{-2} \text{ s}^{-1}$ results in a three-order-of-magnitude lower $p\text{Pb}$ event rate than the nominal LHCb pp runs, hence the trigger line settings for 2013 $p\text{Pb}$ run are relatively loose compared to pp collisions in 2011 and 2012. Both L0 and HLT2 are in pass-through mode in 2013 $p\text{Pb}$ run, i.e. all events are kept in these two levels. In HLT1, at least one VELO track is required in the Hlt1MBMicroBiasVelo line, which is used in this analysis. This trigger requirement is very loose, hence the corresponding trigger efficiency is 100%.

Among the six TCKs (0x6a1710, 0x6d0048, 0x6e0048, 0x6e0049, 0x6e004a, and 0x6f004a) used in $p\text{Pb}$ collisions at 5.02 TeV, only the data samples recorded with TCKs 0x6d0048, 0x6e0048, and 0x6e004a are used in this open charm cross-section analysis^[131]. The runs with conditions significantly different from the bulk of the data are ignored, including those with TCK 0x6A1710, and run indexes (135700, 135800, 135901) because of muons inefficiency, those with TCK 0x6E0049 because they have a higher

Table 3.1 Simulation samples for the decay mode $D^+ \rightarrow K^- \pi^+ \pi^+$

| $D^+ \rightarrow K^- \pi^+ \pi^+$ | | | |
|-----------------------------------|-----------------|------------------------------|------------------------------|
| Configuration | Magnet polarity | $\sqrt{s_{\text{NN}}}$ (TeV) | Statistics ($\times 10^6$) |
| forward | magnet-up | 5.02 | 2 |
| forward | magnet-down | 5.02 | 2 |
| backward | magnet-up | 5.02 | 2 |
| backward | magnet-down | 5.02 | 2 |
| forward (multiplicity-fixed) | magnet-up | 5.02 | 6 |
| forward (multiplicity-fixed) | magnet-down | 5.02 | 6 |
| backward (multiplicity-fixed) | magnet-up | 5.02 | 6 |
| backward (multiplicity-fixed) | magnet-down | 5.02 | 6 |
| pp | magnet-up | 8.16 | 5 |
| pp | magnet-down | 8.16 | 5 |

SumEt threshold, and those with TCK 0x6F004A since the Hlt1MBMicroBiasVelo line was obviously prescaled.

Both pp and $p\text{Pb}$ simulation samples of $D^+ \rightarrow K^- \pi^+ \pi^+$ and $D_s^+ \rightarrow K^- K^+ \pi^+$ decays are used for this analysis. The generation of $D_{(s)}^+$ pp and $p\text{Pb}$ simulation samples are implemented by Gauss^[151] and Boole^[152] applications, as discuss in Section. 2.2.5. The $p\text{Pb}$ simulation samples with and without multiplicity-fixed at $\sqrt{s} = 5.02$ TeV are used to obtain information of prompt D mesons and for calculating reconstruction and selection efficiency, and PID efficiency. Here, "multiplicity-fixed" means that the multiplicity distribution of the $p\text{Pb}$ simulation is modified to be closer to the data than the original simulation. The reason and method of modification to simulation samples will be discussed later. pp simulation samples $\sqrt{s} = 8.16$ TeV are used to obtain information of D mesons from b decay. For both pp and $p\text{Pb}$ simulation samples, their detailed configurations of the decay modes, the magnet polarity, the corresponding centre-of-mass energies and the number of generated events saved to disk are listed in Tab. 3.1 and Tab. 3.2.

The open charm reconstruction and selection efficiency strongly depends on the event multiplicity, since the LHCb tracking detector occupancy increases quickly at high multiplicity, for example VELO will start to saturate in peripheral PbPb collisions. Since there is difference in multiplicity distribution between simulation samples and the real

Table 3.2 Simulation samples for the decay mode $D_s^+ \rightarrow K^- K^+ \pi^+$

| $D_s^+ \rightarrow K^- K^+ \pi^+$ | | | |
|-----------------------------------|-----------------|------------------------------|------------------------------|
| Configuration | Magnet polarity | $\sqrt{s_{\text{NN}}}$ (TeV) | Statistics ($\times 10^6$) |
| forward | magnet-up | 5.02 | 1.5 |
| forward | magnet-down | 5.02 | 1.5 |
| backward | magnet-up | 5.02 | 1.5 |
| backward | magnet-down | 5.02 | 1.5 |
| forward (multiplicity-fixed) | magnet-up | 5.02 | 6 |
| forward (multiplicity-fixed) | magnet-down | 5.02 | 6 |
| backward (multiplicity-fixed) | magnet-up | 5.02 | 6 |
| backward (multiplicity-fixed) | magnet-down | 5.02 | 6 |
| pp | magnet-up | 8.16 | 2.6 |
| pp | magnet-down | 8.16 | 2.6 |

data, reweighting the multiplicity distribution of the simulation samples is essential for calculating the reconstruction and selection efficiency accurately. Unfortunately, the high multiplicity events in the original $p\text{Pb}$ simulation sample (with two EPOS events) is too few compared to the actual data to apply the weighting. Thus, “multiplicity-fixed” simulations are introduced by changing FixedNInteractions (the number of EPOS events) in the Gauss step. In the forward configuration, FixedNInteractions is set to 2 for the original simulation samples and to 3 for the multiplicity-fixed simulation samples. In the backward configuration, FixedNInteractions is set to 2 for the original simulation samples, and to 4 for the multiplicity-fixed simulation samples.

As can be seen in Fig. 3.1, multiplicity-fixed simulation samples have fewer low-multiplicity events and more high-multiplicity events than the original simulation samples, which are closer to the multiplicity distribution of the actual data. There is still a significant difference between the multiplicity distribution of the multiplicity-fixed simulated samples and the data, which affects the accurate calculation of the reconstruction selection efficiency and the particle identification efficiency, and the impact of this difference on the subsequent physical analysis and the correction methods are discussed in Section. 4.4.3 and Section. 4.5.

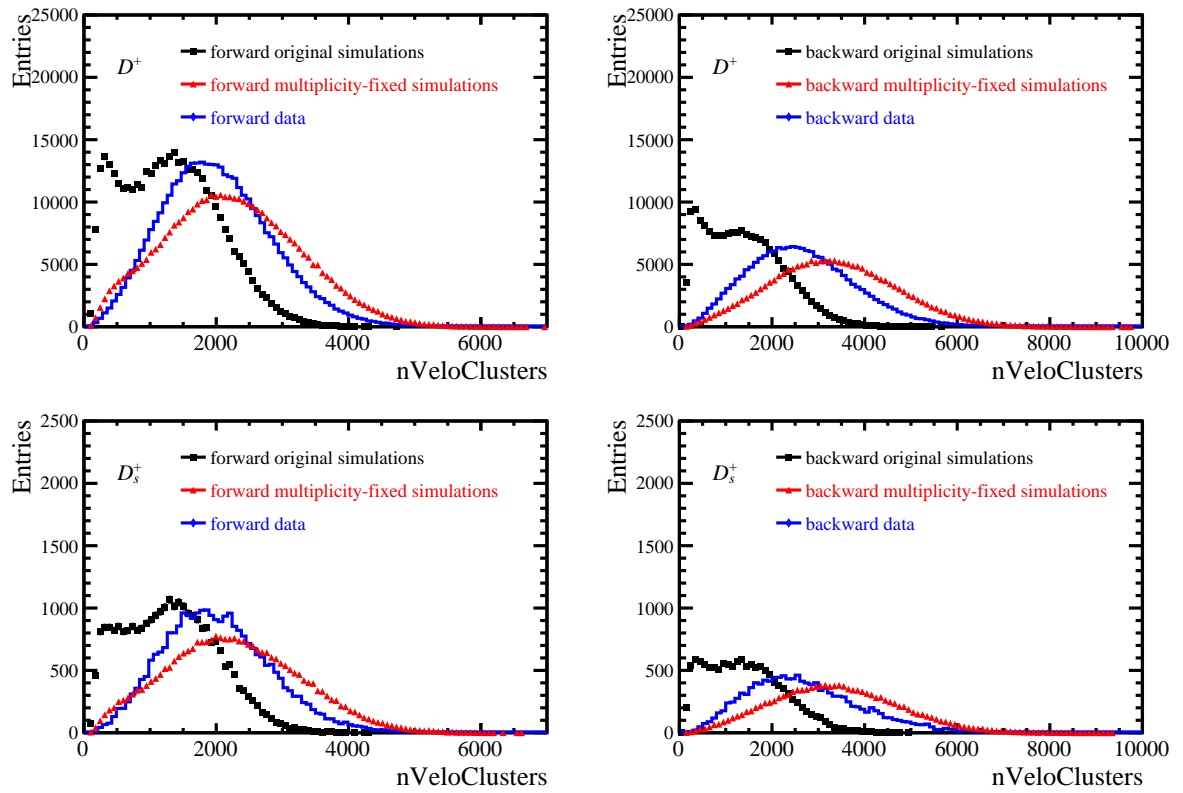


Figure 3.1 The nVeloClusters distributions from the original and multiplicity-fixed D^+ (top) and D_s^+ (bottom) simulation samples, and compared to those from real data.

3.2 Strategy to measure the production cross-sections

With the current statistics, the open charm cross-section measurements can be done for $p_T(D_{(s)}^+) < 14 \text{ GeV}/c$. The rapidity acceptance in the laboratory frame for $D_{(s)}^+$ is roughly $2.0 < y < 4.5$ for the forward configuration, and $-4.5 < y < -2.0$ for the backward configuration. The laboratory frame does not coincide with the proton-nucleon center-of-mass frame, which has a rapidity of ± 0.4645 in the laboratory frame in forward/backward configuration. Therefore the rapidity in the pN rest frame, y^* , is shifted by a constant value with respect to the rapidity in the laboratory frame, $y = y^* \pm 0.4645$. We thus define the rapidity acceptance in the pN center-of-mass frame to be $1.5 < y^* < 4.0$ ($-5.0 < y^* < -2.5$) for the forward (backward) configurations ^①.

To measure the prompt $D_{(s)}^+$ mesons, one must remove the contributions of the $D_{(s)}^+$ from b -hadrons decay. This can be done statistically at LHCb thanks to its excellent vertex and IP resolutions. In practice, the prompt signals can be determined by fitting the invariant mass and $\log_{10} \chi_{\text{IP}}^2(D_{(s)}^+)$ distributions simultaneously in each kinematic bin. Additionally, the detector efficiency needs to be corrected. The double-differential cross-section for prompt $D_{(s)}^+$ production in a given (p_T, y^*) bin is defined as below:

$$\frac{d^2\sigma}{dp_T dy^*} = \frac{N(p_T, y^*)}{\mathcal{L} \times \epsilon_{\text{tot}} \times \mathcal{B} \times \Delta p_T \times \Delta y^*}. \quad (3.1)$$

- $N(p_T, y^*)$ is the number of prompt $D_{(s)}^+$ signals reconstructed through the $D^+ \rightarrow K^- \pi^+ \pi^+$ or $D_s^+ \rightarrow K^- K^+ \pi^+$ decay channel. It is obtained by the fit described in details in Section. 4.2.
- \mathcal{L} is the integrated luminosity.
- ϵ_{tot} is the total efficiency determined in each (p_T, y^*) bin. It consists of three parts: geometrical acceptance efficiency, reconstruction and selection efficiency, and PID efficiency. Simulations can be used to estimate these efficiencies, a more detailed discussion is provided in Section. 4.3-Section. 4.6;

^① More precisely, the rapidity region is $1.9645 < |y| < 4.4645$ ($2.0355 < |y| < 4.5355$) for forward (backward) $p\text{Pb}$ collisions in the laboratory frame; the backward collision corresponds to a more forward range (+0.07) in the LHCb acceptance.

- \mathcal{B} is the branching fraction. Including charge conjugate, the branching fraction for the decay $D^+ \rightarrow K^- \pi^+ \pi^+$ is $9.38 \pm 0.16\%$ obtained from the PDG review^[8], while the branching fraction for the decay $D_s^+ \rightarrow K^- K^+ \pi^+$ is $2.24 \pm 0.13\%$ with a $K^+ K^-$ invariant mass in the range $1000 < m(K^+ K^-) < 1040 \text{ MeV}/c$, measured by CLEO collaboration^[159].

- Δp_T is the bin width of the $D_{(s)}^+$ transverse momentum.

The p_T binning scheme of this study

- $p_T [\text{GeV}/c]$: [0, 1, 2, 3, 4, 5, 6, 7, 8, 9, 10, 11, 12, 13, 14] for D^+ in forward and backward configurations;
- $p_T [\text{GeV}/c]$: [0, 1, 2, 3, 4, 5, 6, 7, 8, 9, 10, 12, 14] for D_s^+ in forward configuration;
- $p_T [\text{GeV}/c]$: [0, 1, 2, 3, 4, 5, 6, 7, 8, 9, 10, 14] for D_s^+ in backward configuration;
- $\Delta y^* = 0.5$ is the bin width of the $D_{(s)}^+$ rapidity.

The y^* binning scheme of this study

- y^* : [1.5, 2.0, 2.5, 3.0, 3.5, 4.0] for $D_{(s)}^+$ in forward configuration;
- y^* : [-5.0, -4.5, -4.0, -3.5, -3.0, -2.5] for $D_{(s)}^+$ in backward configuration;

The efficiency of each small kinematics interval is the average value in the interval; since the widths of Δp_T and Δy^* are small enough, the simulation well reproduces the data in this condition, which means the simulated sample distributions of p_T and y^* are highly comparable to those of the data. In a specific kinematic range, the single differential and total cross-section is calculated by integrating the double-differential cross-section.

3.3 Strategy to study cold nuclear matter effects

CNM effects are studied by the measurements of nuclear modification factors $R_{p\text{Pb}}$ and forward-to-backward cross-section ratios R_{FB} , which have been defined by Eq. (1.16) and Eq. (1.17), respectively.

The reference for $R_{p\text{Pb}}$ is the corresponding cross-sections in pp collisions at the same center-of-mass energy^[30]. According to the measured kinematic range of pp , the transverse momentum intervals of $R_{p\text{Pb}}$ are $0 < p_T < 10 \text{ GeV}/c$ and $1 < p_T < 10 \text{ GeV}/c$ for D^+ and D_s^+ , respectively; the positive rapidity region is $2.0 < y^* < 4.0$, and the negative rapidity region is $-4.5 < y^* < -2.5$.

The relative nuclear modification factors between the proton-going and lead-going directions were quantitated by R_{FB} . When determining R_{FB} , one must ensure that the cross-sections are defined in the common transverse momentum and rapidity range of the forward and backward configurations, which is $0 < p_{\text{T}} < 14 \text{ GeV}/c$, $2.5 < |y^*| < 4.0$ in this thesis.

3.4 Strategy to study the cross-section ratios

The production ratios between different charm hadrons are sensitive probes to the charm hadronization mechanism^[83,160]. In particular, strangeness enhancement can be studied by comparing the cross-section ratios between strange D mesons with those of non-strange D mesons as a function of transverse momentum and rapidity. With the previous measurement of D^0 cross-section in $p\text{Pb}$ collisions at $\sqrt{s_{\text{NN}}} = 5.02 \text{ TeV}$ from LHCb^[30], one can calculate the ratio of D^+ to D^0 , D_s^+ to D^0 , and D_s^+ to D^+ . Within the same kinematic interval, the cross-section ratio of D_s^+ to D^0 is defined as

$$R_{D_s^+/D^0}(p_{\text{T}}, y^*) \equiv \frac{d^2\sigma_{D_s^+}(p_{\text{T}}, y^*)/dp_{\text{T}}dy^*}{d^2\sigma_{D^0}(p_{\text{T}}, y^*)/dp_{\text{T}}dy^*}. \quad (3.2)$$

Similarly, the cross-section ratio between D_s^+ and D^+ is defined as

$$R_{D_s^+/D^+}(p_{\text{T}}, y^*) \equiv \frac{d^2\sigma_{D_s^+}(p_{\text{T}}, y^*)/dp_{\text{T}}dy^*}{d^2\sigma_{D^+}(p_{\text{T}}, y^*)/dp_{\text{T}}dy^*}. \quad (3.3)$$

The ratio R_{D^+/D^0} between non-strange D mesons can be used as a reference for $R_{D_s^+/D^0}$ and $R_{D_s^+/D^+}$, and in a given kinematic region, it is defined as

$$R_{D^+/D^0}(p_{\text{T}}, y^*) \equiv \frac{d^2\sigma_{D^+}(p_{\text{T}}, y^*)/dp_{\text{T}}dy^*}{d^2\sigma_{D^0}(p_{\text{T}}, y^*)/dp_{\text{T}}dy^*}. \quad (3.4)$$

CHAPTER 4 MEASUREMENT OF D^+ AND D_s^+ PRODUCTIONS IN $p\text{Pb}$ COLLISIONS

4.1 Event selections

There are a large number of background events in the open charm data samples of $p\text{Pb}$ collisions. It is expected that the physical information of the signal events will be different from the background, such as the lifetime of the charm hadron, its invariant mass and the decay topology. Reasonable constraints on these variables can separate the signal from the background. Event selections include stripping and offline selections. The stripping selection criteria removes most of the background and also reduces file size, saves storage space and reduces analysis time. Afterwards, the offline selection criteria will be tighter to improve the purity of the data samples, i.e., to further reduce the background while retaining as much of the signal as possible.

4.1.1 Stripping

The D^+ candidate is fully reconstructed from two pion and one kaon tracks according to the decay ^① $D^+ \rightarrow K^- \pi^+ \pi^+$ at LHCb with the stripping line D2HHHForXSecD2KPPLine. The D_s^+ candidate is fully reconstructed from two kaon and one pion tracks according to the decay $D_s^+ \rightarrow K^- K^+ \pi^+$ with the stripping line D2HHHForXSecD2KKPLine.

Following previous LHCb analyses of the open charm production measurements in pp collisions at $\sqrt{s} = 7 \text{ TeV}$ ^[78] and $\sqrt{s} = 13 \text{ TeV}$ ^[79], the physical variables used for the stripping selection criteria and their specific conditions are as follows:

- p_T : transverse momentum, that is, the momentum in $p\text{Pb}$ collisions perpendicular to the z-axis.

On average, the transverse momentum of $D_{(s)}^+$ decay product is larger than that of the prompt background. Due to the large uncertainty when measuring the parameters of particles with low transverse momentum, The tracks of the three “daughters”^② are required to have large transverse momentum, which implies that the transverse momentum of the three tracks at least satisfy $p_T > 400 \text{ MeV}/c$, and the tracks with

^① If not stated otherwise, charge conjugation is assumed throughout this thesis.

^② The “daughter” refers to the decay product of $D_{(s)}^+$, i.e. kaon or pion.

the largest transverse momentum should satisfy $p_T(\text{max}) > 600 \text{ MeV}/c$.

- χ_{IP}^2 : the difference in χ^2 between a particular PV reconstructed with and without the $D_{(s)}^+$ candidate's track in consideration^[92].

IP refers to the shortest distance from the PV to the extrapolation of a track. The “ χ^2 ” is computed as $\Delta^T \Sigma^{-1} \Delta$, where Δ is the vector from the closest point on the extrapolated track to the PV, and Σ is the sum of the covariance matrices of the track and vertex fits. The larger χ_{IP}^2 is, the more likely the $D_{(s)}^+$ candidate's track is not from the PV.

The tracks of the three daughters do not come from the PV, which requires that their χ_{IP}^2 are all larger than 4 and that their maximum χ_{IP}^2 should be larger than 9.

- DLL: Delta Log Likelihood, derived by particle identification (PID) logarithm likelihood.

The variable $\text{DLL}_{K\pi}$ is used to indicate particle identification information at LHCb. It is generally acquired by combining signals from multiple detectors using multivariate analysis. This variable can be used to represent the possibility that a particle is a kaon. The larger the value of the variable, the more likely it is to be a kaon, while the smaller the value, the more likely it is to be a pion. The kaon tracks are required to be more kaon-like by requiring $\text{DLL}_{K\pi} > 3$, and the pion tracks more pion-like by requiring $\text{DLL}_{K\pi} < 0$.

- DoCA: the distance of closest approach.

The maximum distance between any two tracks (DoCA) for a collection of tracks physically coming from the same vertex should be small. As the setting $\text{DoCA} < 0.5 \text{ mm}$, tracks are well constrained to a common vertex.

- Direction angle: the angle formed by the vector from the PV to reconstructed vertex and the reconstructed momentum.

The measured momentum of $D_{(s)}^+$ mesons should coincide with the vector between the decay vertex and the PV. Therefore, the angle between the two vectors should be less than 35 mrad (2° or about 10% of the LHCb acceptance range).

- $\chi^2/\text{ndf}(\text{vtx})$: the ratio of the fit goodness to the fit degrees of freedom for the decay point of the mother particle.

The $D_{(s)}^+$ candidate is expected to have a good vertex fit quality, requiring $\chi^2/\text{ndf}(\text{vtx}) < 25$.

- τ : decay time of the candidates.

- $\chi^2(\text{VD})$: the quality difference of the PV fit with and without adding tracks from the reconstructed decay vertex.

When the candidate decays far away from the PV, the particle lifetime is longer and $\chi^2(\text{VD})$ is larger, which means the decay tracks are unable to rebuild a good vertex with the tracks from the PV. The vertex should be displaced from the PV by requiring the $D_{(s)}^+$ to have either a significant vertex displacement (VD), $\chi^2(\text{VD}) > 16$ or a large measured proper decay time $\tau > 0.15$ ps ^①.

These selection conditions reduce the $D_{(s)}^+$ candidates from b -hadron decays, and combinatorial backgrounds with tracks of daughters coming from secondary decays. The stripping selections are summarized in Table. 4.1.

Table 4.1 Stripping selections of $D_{(s)}^+$ candidates.

| Quantity | Selections |
|---------------------------------|--|
| p_T (track) | $p_T(\text{max}) > 600 \text{ MeV}/c$ |
| χ_{IP}^2 (track) | $\chi_{\text{IP}}^2(\text{max}) > 9$ |
| p_T (track) | $> 400 \text{ MeV}/c$ |
| χ_{IP}^2 (track) | > 4 |
| $\text{DLL}_{K\pi}(K^-)$ | > 3 |
| $\text{DLL}_{K\pi}(\pi^+)$ | < 0 |
| DoCA | $< 0.5 \text{ mm}$ |
| Direction angle | $< 35 \text{ mrad}$ |
| $\chi^2/\text{ndf}(\text{vtx})$ | < 25 |
| Lifetime ($D_{(s)}^+$) | $\chi^2(\text{VD}) > 16$ or $\tau > 0.15 \text{ ps}$ |

4.1.2 Offline selections

The offline selections focus on reducing the background, especially in backward rapidly regions with higher multiplicity where more random combinations of backgrounds exist.

Momentum p and η must fall within the PID calibration kinematic spectrum and the acceptable PID performance range, requiring $3.2 < p < 100 \text{ GeV}/c$, $2 < \eta < 5$.

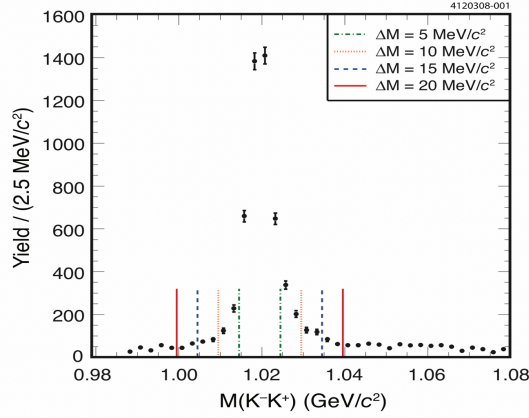
^① The lifetime of D^+ is $1.040 \pm 0.007 \text{ ps}$, the lifetime of D_s^+ is $0.504 \pm 0.004 \text{ ps}$.

Ghost tracks are suppressed by requiring the ghost probability to be less than 0.3. The χ^2 per degree of freedom of the kaon and pion tracks is returned by the Kalman fit. This variable is less than 4 to distinguish between real and ghost tracks. The requirements on the impact parameter significance of the child tracks are tightened to be $\chi_{\text{IP}}^2 > 6$, and the direction angle should be less than 0.0035 mrad.

The PID selections are tightened to $\text{DLL}_{K\pi} > 5$ for the kaon, and $\text{DLL}_{K\pi} < 0$ for the pion. The $D_{(s)}^+$ candidate is expected to have a vertex fit quality requirement $\chi^2/\text{ndf}(\text{vtx}) < 6$ and the flight-distance significance $\chi^2(\text{FD})$ between the PV and the $D_{(s)}^+$ decay vertex should be larger than 50. When studying the weak decay, a longer lifetime is needed and a loose upper limit to exclude the component from b -hadron decays; thus, it is $0.1 < \tau < 50$ ps for D^+ and $0.1 < \tau < 25$ ps for D_s^+ . A signal window of invariant mass (1794, 1944) MeV/ c^2 for D^+ and (1894, 2044) MeV/ c^2 for D_s^+ is set for convenience of the mass fit. Due to limited statistics at the high $D_{(s)}^+$ transverse momentum regions, the measurement is performed in the kinematic range of $0 < p_{\text{T}} < 14$ GeV/ c , $2 < |y| < 4.5$.

To reduce the combinatorial background and the $\pi \rightarrow K$ mis-identification fraction in the reconstructed $D_s^+ \rightarrow K^- K^+ \pi^+$ system, the $K^+ K^-$ mass is required to be within a window ± 20 MeV/ c^2 wide centered on the nominal $\phi(1020)$ mass (simply denoted as ϕ). In this thesis, the notation “ $D_s^+ \rightarrow K^- K^+ \pi^+$ ” is interpreted as the decay where the $K^+ K^-$ mass is within ± 20 MeV/ c^2 of the nominal ϕ mass, including the resonant mode $D_s^+ \rightarrow \phi \pi^+$ and non-resonant mode $D_s^+ \rightarrow K^- K^+ \pi^+$. There is no efficiency for D_s^+ associated with the $K^+ K^-$ mass window, as it is included in the definition of the branching fraction.

Different branching fractions of $D_s^+ \rightarrow K^- K^+ \pi^+$ measured by the CLEO collaboration^[159] corresponding to their mass windows are shown in Fig. 4.1. In order to preserve as many signals as possible, the branching fraction ($2.24 \pm 0.13\%$) result measured by the CLEO collaboration in the largest mass window ($\Delta M = 20$ MeV/ c^2) is applied for prompt D_s^+ yield determination. The offline selections are summarized in Table. 4.2.



| Value | This Result | \mathcal{B} (%) |
|--------------------|-----------------|-------------------|
| \mathcal{B}_5 | 1.69 ± 0.08 | ± 0.06 |
| \mathcal{B}_{10} | 1.99 ± 0.10 | ± 0.05 |
| \mathcal{B}_{15} | 2.14 ± 0.10 | ± 0.05 |
| \mathcal{B}_{20} | 2.24 ± 0.11 | ± 0.06 |

Figure 4.1 Definition of the K^-K^+ mass windows ΔM used by the CLEO collaboration (top) and their corresponding branching ratios (bottom). The figure is taken from Ref. [159].

Table 4.2 Offline selections of $D_{(s)}^+$ candidates.

| Quantity | Selections |
|---------------------------------|--|
| p (track) | $3.2 < p < 100 \text{ GeV}/c$ |
| η (track) | $2 < \eta < 5$ |
| ProbNNghost (track) | < 0.3 |
| χ^2/ndf (track) | < 4 |
| χ_{IP}^2 (track) | > 6 |
| $\text{DLL}_{K\pi}(K^-)$ | > 5 |
| $\text{DLL}_{K\pi}(\pi^+)$ | < 0 |
| $m(D^+)$ | $1794 < m(D^+) < 1944 \text{ MeV}/c^2$ |
| $m(D_s^+)$ | $1894 < m(D_s^+) < 2044 \text{ MeV}/c^2$ |
| $ m_{PDG}(\phi) - m(K^+K^-) $ | $< 20 \text{ MeV}/c^2$ |
| Direction angle | $< 0.015 \text{ mrad}$ |
| $\chi^2/\text{ndf}(\text{vtx})$ | < 6 |
| $\chi^2(\text{FD})(D_{(s)}^+)$ | > 50 |
| Lifetime (D^+) | $0.1 < \tau < 50 \text{ ps}$ |
| Lifetime (D_s^+) | $0.1 < \tau < 25 \text{ ps}$ |
| $p_{\text{T}}(D_{(s)}^+)$ | $0 < p_{\text{T}} < 14 \text{ GeV}/c$ |
| $y(D_{(s)}^+)$ | $2 < y < 4.5$ |

4.2 Prompt yield extraction

In order to extract prompt $D_{(s)}^+$ mesons in each kinematics bin, their prompt signal yields should be separated from two different components: the combinatorial background and secondary $D_{(s)}^+$ mesons feed-down from b -hadron decays. A simple one-dimensional fit to just one variable cannot exclude these two components well. Although generally insensitive to discriminate between prompt and secondary signal events, the invariant mass of the decay products can distinguish between inclusive yields and combinatorial backgrounds. The impact parameter and its derivatives, such as the $\log_{10} \chi_{\text{IP}}^2$ (the logarithm of 10 for χ_{IP}^2), are very suitable for distinguishing between the prompt and secondary components; however, isolating the combined background component is difficult because it is hard to describe its $\log_{10} \chi_{\text{IP}}^2$ distribution. Therefore, a multi-step fitting procedure to obtain the signal yields of prompt $D_{(s)}^+$ mesons will be presented below.

4.2.1 Inclusive yield determination

The inclusive yield is determined from an extended unbinned maximum likelihood fit to the $M(K^-\pi^+\pi^+)$ or $M(K^-K^+\pi^+)$ invariant mass distribution. Following previous analyses^[30,78-79], the probability density function (PDF) of signal is described by a Crystal Ball (CB)^[161] plus a Gaussian function (G),

$$F_{\text{sig}} = f \times F_{\text{CB}} + (1 - f) \times G, \quad (4.1)$$

$$F_{\text{CB}}(x; \mathcal{M}, \sigma_{\text{CB}}, \alpha, n) = \begin{cases} \frac{\left(\frac{n}{|\alpha|}\right)^n e^{-\frac{1}{2}\alpha^2}}{\left(\frac{n}{|\alpha|} - |\alpha| - \frac{x-\mathcal{M}}{\sigma_{\text{CB}}}\right)^n}, & \text{if } \frac{x-\mathcal{M}}{\sigma_{\text{CB}}} < -|\alpha|, \\ \exp\left(-\frac{1}{2}\left(\frac{x-\mathcal{M}}{\sigma_{\text{CB}}}\right)^2\right), & \text{if } \frac{x-\mathcal{M}}{\sigma_{\text{CB}}} \geq -|\alpha|, \end{cases} \quad (4.2)$$

$$G(x; \mathcal{M}, \sigma_G) = e^{-\frac{(x-\mathcal{M})^2}{2\sigma_G^2}}. \quad (4.3)$$

Here, the CB function F_{CB} describes the mass peak with a lossy tail on the left. A tail of energy loss caused by photon emission can be well described by the $1/x$ function, which corresponds to $n = 1$ ^[161].

Both the F_{CB} and G components share the same mean value \mathcal{M} . The ratio r of the F_{CB} resolution σ_{CB} to the G resolution σ_G , the fraction of the F_{CB} component f , with the parameter α of F_{CB} are set to the results of the full-interval^① fitting of p Pb MC in

① In this thesis, the full-interval is the kinematic range of $0 < p_{\text{T}} < 14 \text{ GeV}/c$, $1.5 < y^* < 4.0$ in the forward configuration and $0 < p_{\text{T}} < 14 \text{ GeV}/c$, $-5.0 < y^* < -2.5$ in the backward configuration.

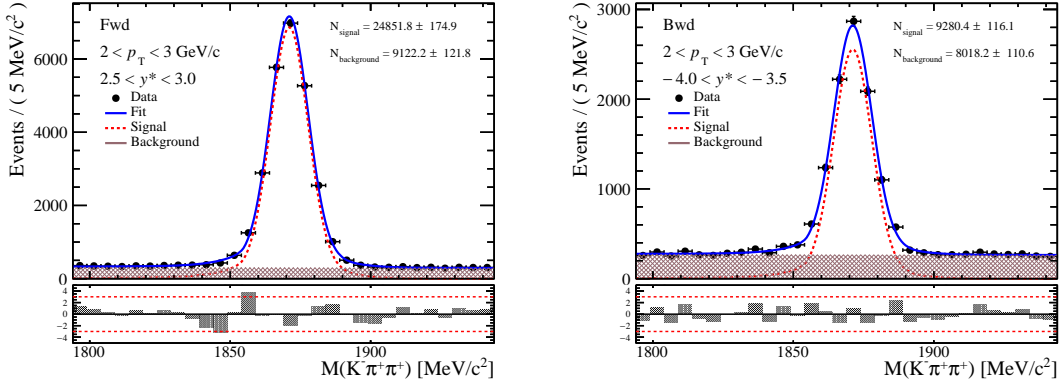


Figure 4.2 $M(K^-\pi^+\pi^+)$ distribution fit results in the kinematic range of $2 < p_T < 3 \text{ GeV}/c$, $2.5 < y^* < 3.0$ for the forward (left) data sample and $2 < p_T < 3 \text{ GeV}/c$, $-4.0 < y^* < -3.5$ for the backward (right) data sample.

Table .3.1 and Table. 3.2. The mass fit studies of simulated samples are displayed in Appendix A.1, and the values of fixed parameters are listed in Table. 4.3.

Table 4.3 Fixed parameter values and their errors when fitting an invariant mass distribution of data sample.

| Source | $D^+ \rightarrow K^-\pi^+\pi^+$ | | $D_s^+ \rightarrow K^-K^+\pi^+$ | |
|-------------------|---------------------------------|-------------------|---------------------------------|-------------------|
| | Forward | Backward | Forward | Backward |
| <i>Parameters</i> | | | | |
| r | 2.36 ± 0.037 | 2.30 ± 0.040 | 2.49 ± 0.090 | 2.46 ± 0.100 |
| f | 0.893 ± 0.005 | 0.895 ± 0.005 | 0.899 ± 0.010 | 0.897 ± 0.011 |
| α | 2.35 ± 0.010 | 2.37 ± 0.010 | 2.60 ± 0.029 | 2.59 ± 0.030 |
| n | 1 | 1 | 1 | 1 |

When fitting MC samples in different (p_T, y^*) bins, it is found that the resolution σ_{CB} and the central value \mathcal{M} of F_{CB} are kinematic dependent. As a result, when the data are finally fitted into kinematic bins independently, only σ_{CB} and \mathcal{M} of F_{CB} are free-floating parameters.

The background is described by a linear function. The invariant mass fit is performed in the range $M \pm |\Delta M|$ around the observed D^+ (D_s^+) mass as $M = 1869 \text{ MeV}/c^2$ ($M = 1969 \text{ MeV}/c^2$), with $|\Delta M| = 75 \text{ MeV}/c^2$. The D^+ (D_s^+) invariant mass spectrum fitting results are shown in Fig. 4.2 (Fig. 4.3) in the forward configuration for $p_T \in (2, 3) \text{ GeV}/c$, $y^* \in (2.5, 3.0)$ and in the backward configuration for $p_T \in (1, 2) \text{ GeV}/c$, $y^* \in (-4.0, -3.5)$.

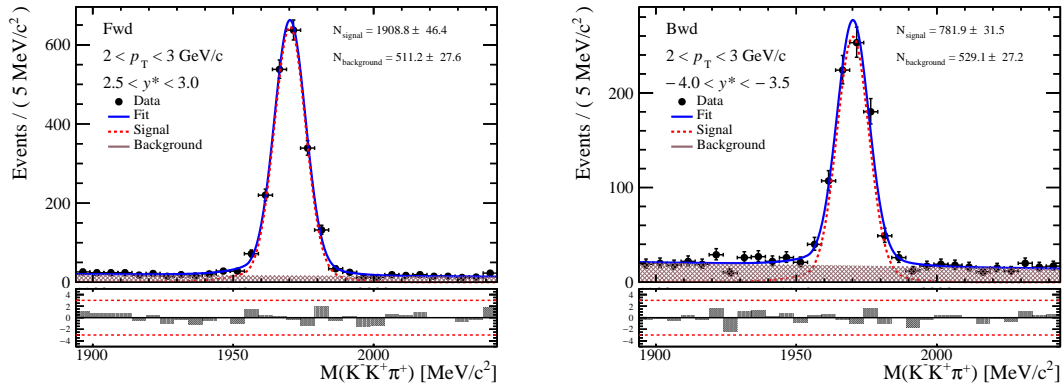


Figure 4.3 $M(K^-K^+\pi^+)$ distribution fit results in the kinematic range of $2 < p_T < 3$ GeV/c, $2.5 < y^* < 3.0$ for the forward (left) data sample and $2 < p_T < 3$ GeV/c, $-4.0 < y^* < -3.5$ for the backward (right) data sample.

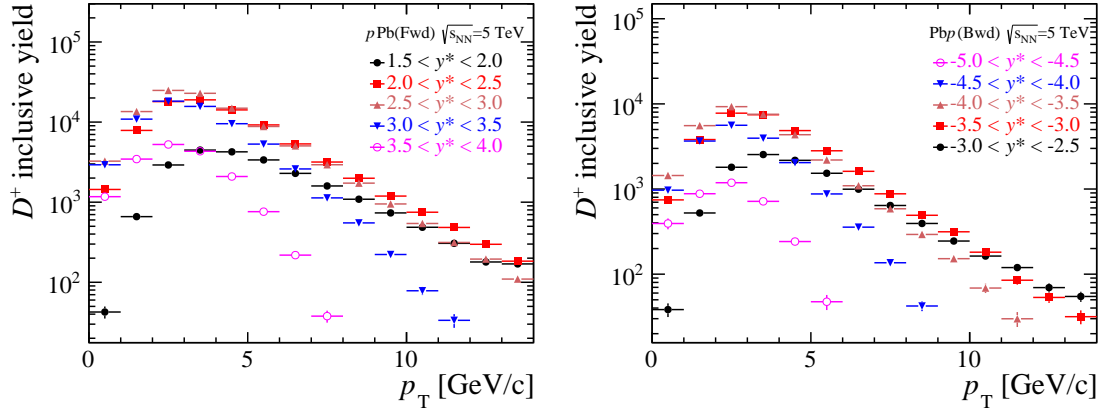


Figure 4.4 Inclusive D^+ signal yields as a function of p_T and y^* in the forward (left) and backward (right) rapidity regions.

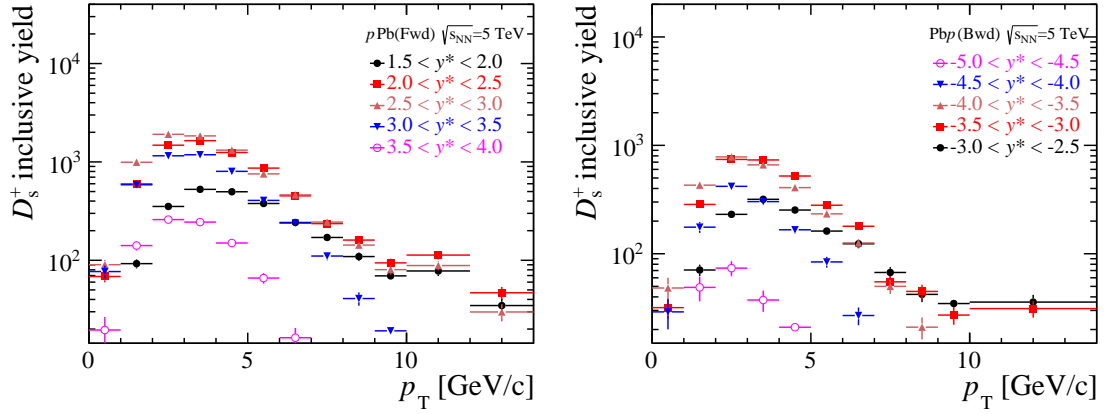
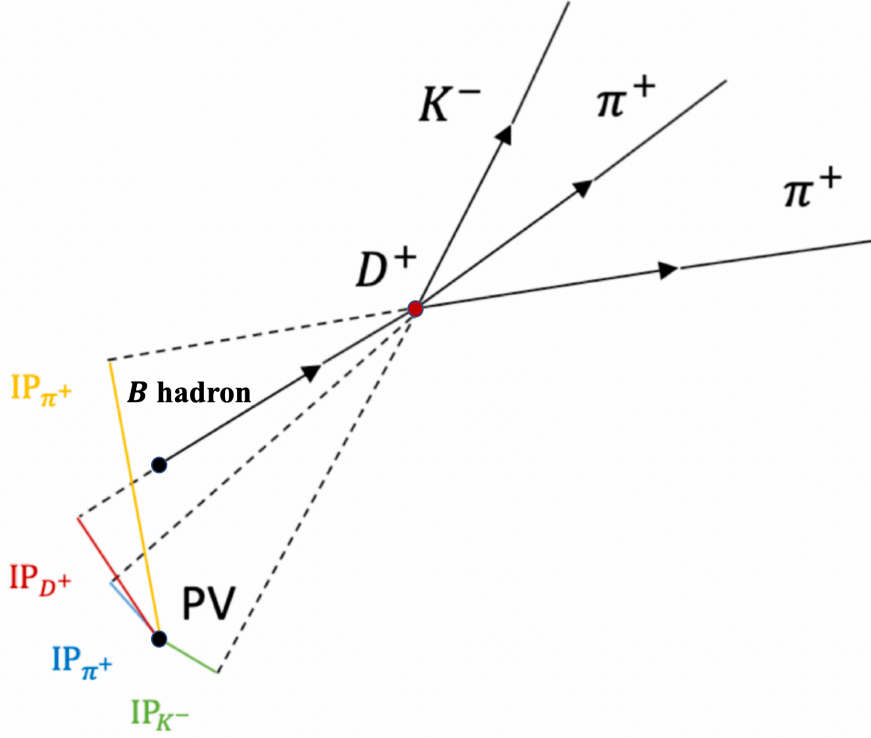


Figure 4.5 Inclusive D_s^+ signal yields as a function of p_T and y^* in the forward (left) and backward (right) rapidity regions.

In Fig. 4.4 and Fig. 4.5, the inclusive signal yields in different (p_T, y^*) bins are given for D^+ and D_s^+ , where the empty bins represent places where the data are insufficient and the fitting processes fail. This fitted inclusive signal yields rise initially, then decrease as the transverse momentum increases.


 Figure 4.6 Topology of the decay $D^+ \rightarrow K^- \pi^+ \pi^+$ from a B hadron.

4.2.2 Prompt yield determination

The IP values of D mesons from PV or excited states are relatively close to zero, while the IP values of D mesons from b -hadron decays are much higher, as shown in Fig. 4.6. In general, the $\log_{10} \chi_{\text{IP}}^2 (D_{(s)}^+)$ has a positive relationship with IP. Therefore, prompt $D_{(s)}^+$ yield can be determined through the following method. To subtract the background component, a *sPlot* technique^[162] is applied to the fit result of the invariant mass spectrum. The $\log_{10} \chi_{\text{IP}}^2 (D_{(s)}^+)$ distribution of background-subtracted data contains the prompt and non-prompt components. The distribution of $\log_{10} \chi_{\text{IP}}^2 (D_{(s)}^+)$ is fitted to discriminate prompt $D_{(s)}^+$ and $D_{(s)}^+$ from b -hadron decays. The shape of the PDFs of the two components can be modeled with a Bukin function:

$$\mathcal{P}(x; \mu, \sigma, \epsilon, \rho_L, \rho_R) = \begin{cases} \exp \left\{ \frac{(x-x_1)\epsilon\sqrt{\epsilon^2+1}\sqrt{2\ln 2}}{\sigma(\sqrt{\epsilon^2+1}-\epsilon)^2 \ln(\sqrt{\epsilon^2+1}+\epsilon)} + \rho_L \left(\frac{x-x_1}{\mu-x_1} \right)^2 - \ln 2 \right\} & x \leq x_1, \\ \exp \left\{ - \left[\frac{\ln \left(1+2\epsilon\sqrt{\epsilon^2+1} - \frac{x-\mu}{\sigma\sqrt{2\ln 2}} \right)}{\ln(1+2\epsilon^2-2\epsilon\sqrt{\epsilon^2+1})} \right]^2 \times \ln 2 \right\} & x_1 < x < x_2, \\ \exp \left\{ \frac{(x-x_2)\epsilon\sqrt{\epsilon^2+1}\sqrt{2\ln 2}}{\sigma(\sqrt{\epsilon^2+1}-\epsilon)^2 \ln(\sqrt{\epsilon^2+1}+\epsilon)} + \rho_R \left(\frac{x-x_2}{\mu-x_2} \right)^2 - \ln 2 \right\} & x \geq x_2, \end{cases} \quad (4.4)$$

where $x_1 = \mu + \sigma \sqrt{2 \ln 2} \left(\frac{\epsilon}{\sqrt{\epsilon^2 + 1}} - 1 \right)$ and $x_2 = \mu + \sigma \sqrt{2 \ln 2} \left(\frac{\epsilon}{\sqrt{\epsilon^2 + 1}} + 1 \right)$. The parameters μ and σ are the average value and width of the Bukin function, ϵ describes the symmetry, while ρ_L and ρ_R characterize the asymmetry of left and right tail. In the forward and backward rapidity regions for both components of $D_{(s)}^+$, parameters σ , ϵ , ρ_L and ρ_R are fixed. The fixed parameters are summarized in Table. 4.4. According to the fit to MC samples within each $D_{(s)}^+$ kinematics bin, it appears that these parameters are not strongly dependent on both p_T and y^* . Within statistical uncertainties, the results using these fixed values are considered nominal, assuming no kinematic dependence on these parameters. The systematic uncertainties are estimated by studying the variation of the nominal results when these parameters are altered, as detailed in Section. 4.7.1 below.

Table 4.4 Fixed parameter values and their errors when fitting a $\log_{10} \chi_{\text{IP}}^2 \left(D_{(s)}^+ \right)$ distribution of background-subtracted data. A parameter with the indicator “1” belongs to the Bukin function of the prompt component; a parameter with the indicator “2” belongs to the Bukin function of the non-prompt component.

| Source | $D^+ \rightarrow K^- \pi^+ \pi^+$ | | $D_s^+ \rightarrow K^- K^+ \pi^+$ | |
|---|-----------------------------------|--------------|-----------------------------------|--------------|
| | Forward | Backward | Forward | Backward |
| <i>Parameters of the prompt component</i> | | | | |
| σ_1 | 0.458±0.001 | 0.461±0.001 | 0.453±0.004 | 0.453±0.004 |
| ϵ_1 | -0.169±0.002 | -0.158±0.003 | -0.150±0.012 | -0.174±0.012 |
| ρ_{L1} | -0.060±0.002 | -0.056±0.003 | -0.048±0.011 | -0.059±0.012 |
| ρ_{R1} | -0.715±0.019 | -0.748±0.023 | 0.900±0.104 | -0.850±0.108 |
| <i>Parameters of the non-prompt component</i> | | | | |
| σ_2 | 0.920±0.001 | 0.920±0.001 | 0.883±0.012 | 0.883±0.012 |
| ϵ_2 | 0.114±0.003 | 0.113±0.001 | 0.060±0.022 | 0.060±0.022 |
| ρ_{L2} | -0.222±0.001 | -0.225±0.014 | -0.295±0.065 | -0.297±0.065 |
| ρ_{R2} | -2.003±0.038 | -1.998±0.001 | -1.644±0.232 | -1.653±0.232 |

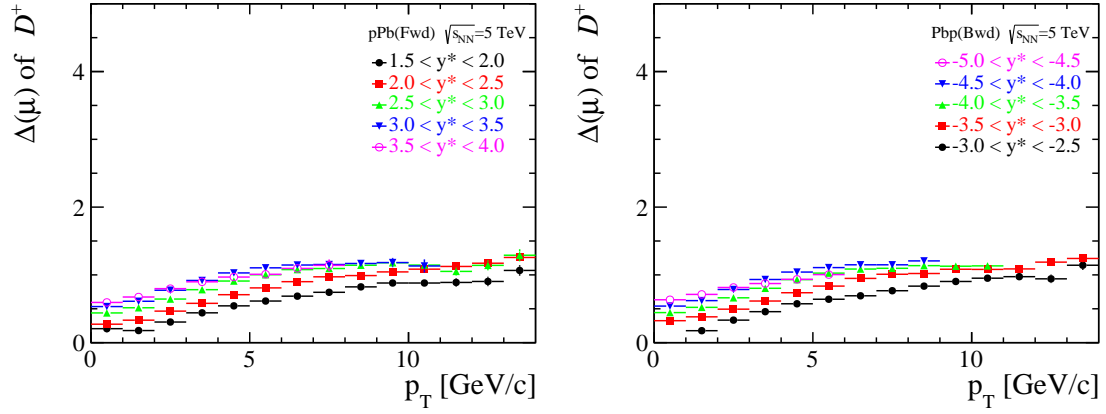


Figure 4.7 Difference of μ between the non-prompt and prompt simulated samples of D^+ in the forward (left) and backward (right) configurations.

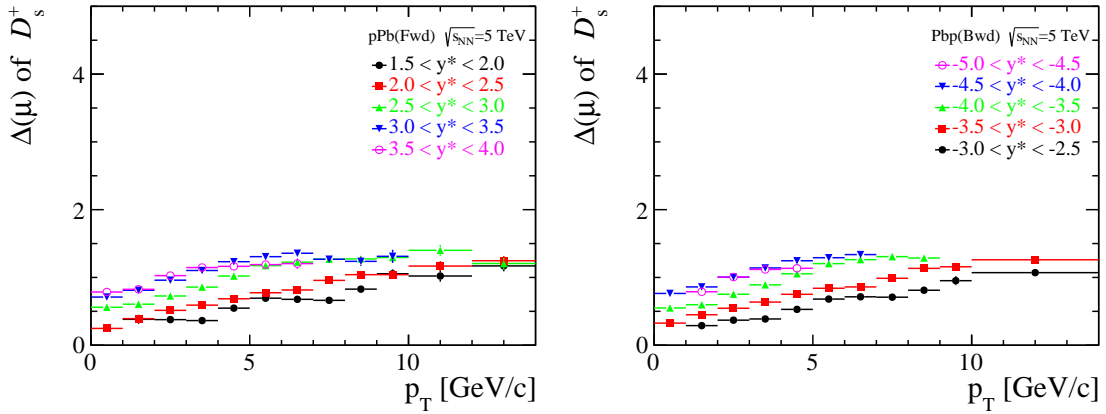


Figure 4.8 Difference of μ between the non-prompt and prompt simulated samples of D_s^+ in the forward (left) and backward (right) configurations.

In the actual fitting process, since the non-prompt component is tiny, it is hard to determine its position accurately. Therefore, the difference of μ between the non-prompt and prompt simulations ($\Delta(\mu)$) for $D_{(s)}^+$ is fixed in each (p_T, y^*) bin, as shown in Fig. 4.7 and Fig. 4.8. In addition, as displayed in Fig. 4.4 and Fig. 4.5, the inclusive event obtained from the invariant mass fit is applied to constrain the total yields with a Gaussian function, with the inclusive yield being the central value and its uncertainty being the resolution of the Gaussian function.

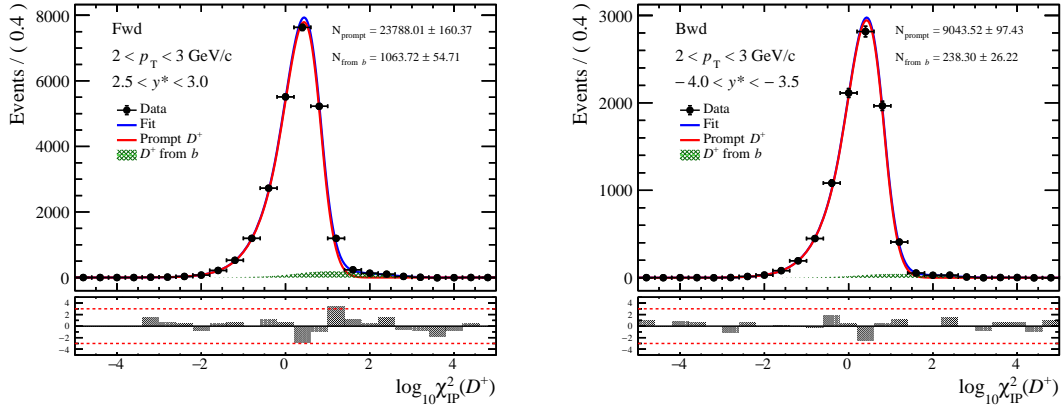


Figure 4.9 The $\log_{10} \chi_{IP}^2(D^+)$ distribution fit results in bin of $2 < p_T < 3$ GeV/c, $2.5 < y^* < 3.0$ in the forward (left) data sample and $2 < p_T < 3$ GeV/c, $-4.0 < y^* < -3.5$ in the backward (right) data sample.

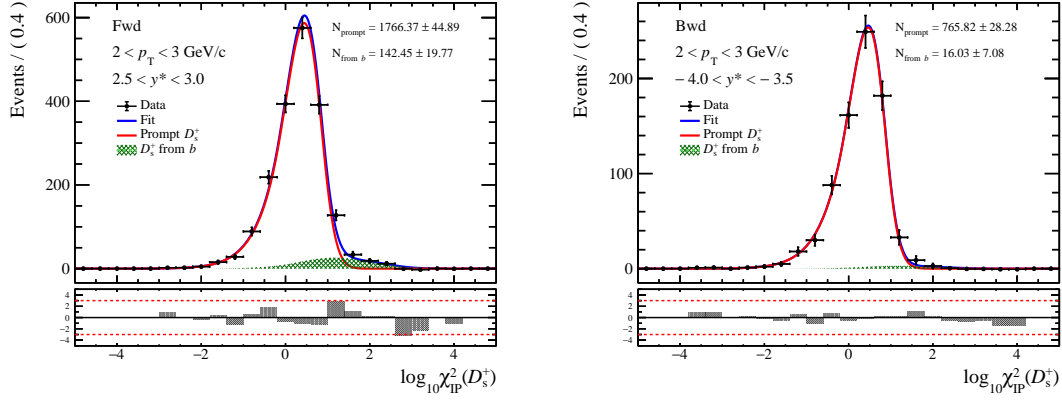


Figure 4.10 The $\log_{10} \chi_{IP}^2(D_s^+)$ distribution fit results in bin of $2 < p_T < 3$ GeV/c, $2.5 < y^* < 3.0$ in the forward (left) data sample and $2 < p_T < 3$ GeV/c, $-4.0 < y^* < -3.5$ in the backward (right) data sample.

The $\log_{10} \chi_{IP}^2(D_{(s)}^+)$ distribution fit results for prompt and non-prompt $D_{(s)}^+$ are given in Fig. 4.9 and Fig. 4.10 in the forward configuration for $p_T \in (2, 3)$ GeV/c, $y^* \in (2.5, 3.0)$ and in the backward configuration for $p_T \in (1, 2)$ GeV/c, $y^* \in (-4.0, -3.5)$, respectively.

The prompt $D_{(s)}^+$ signal yields can be directly obtained from the $\log_{10} \chi_{IP}^2(D_{(s)}^+)$ fit, they first increase and then decrease with p_T , as summarized in Fig. 4.11 and Fig. 4.12. The error in fitting the prompt yield of $D_{(s)}^+$ is taken as the statistical uncertainty of the production cross-section.

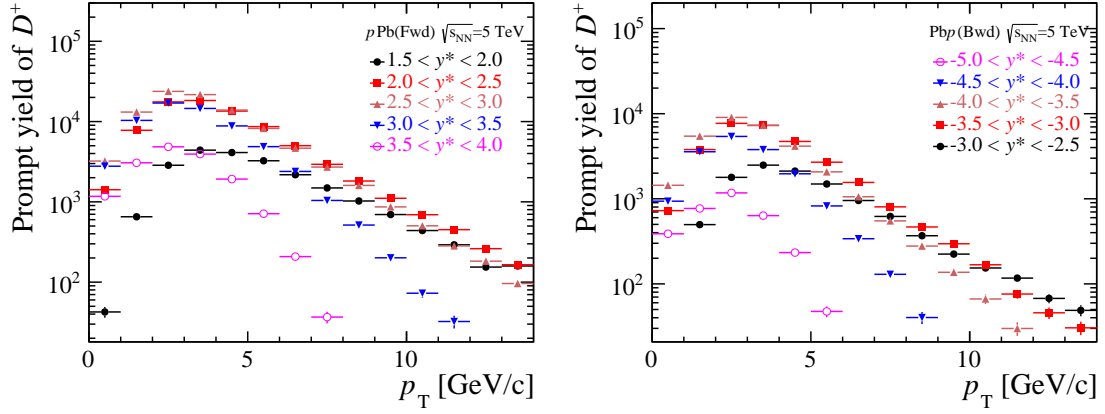


Figure 4.11 Prompt signal yields obtained from the $\log_{10} \chi_{\text{IP}}^2 (D^+)$ fit in the forward (left) and backward (right) rapidity regions. Statistical uncertainties only.

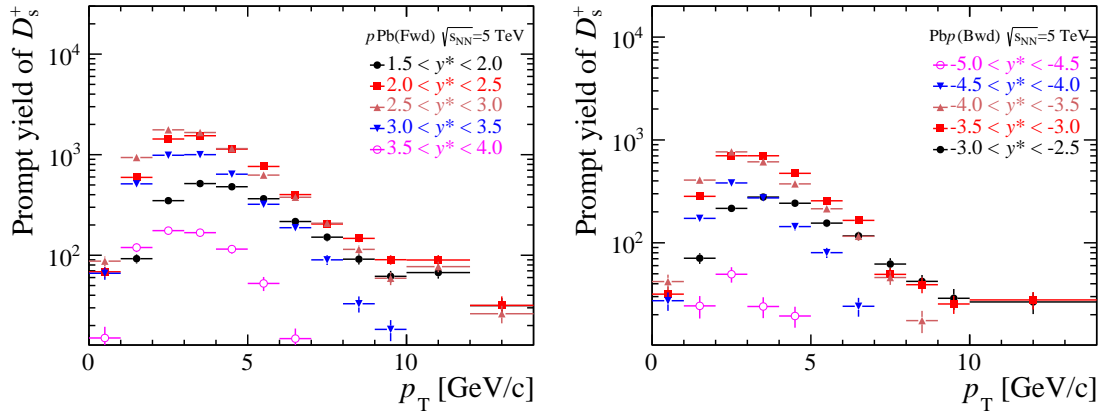


Figure 4.12 Prompt signal yields obtained from the $\log_{10} \chi_{\text{IP}}^2 (D_s^+)$ fit in the forward (left) and backward (right) rapidity regions. Statistical uncertainties only.

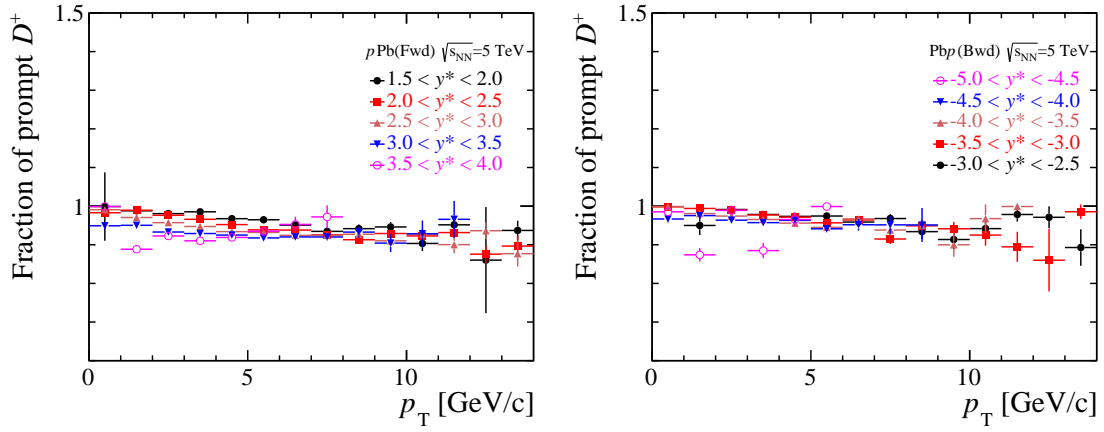


Figure 4.13 Prompt fractions of D^+ as a function of p_T and y^* in the forward (left) and backward (right) configurations.

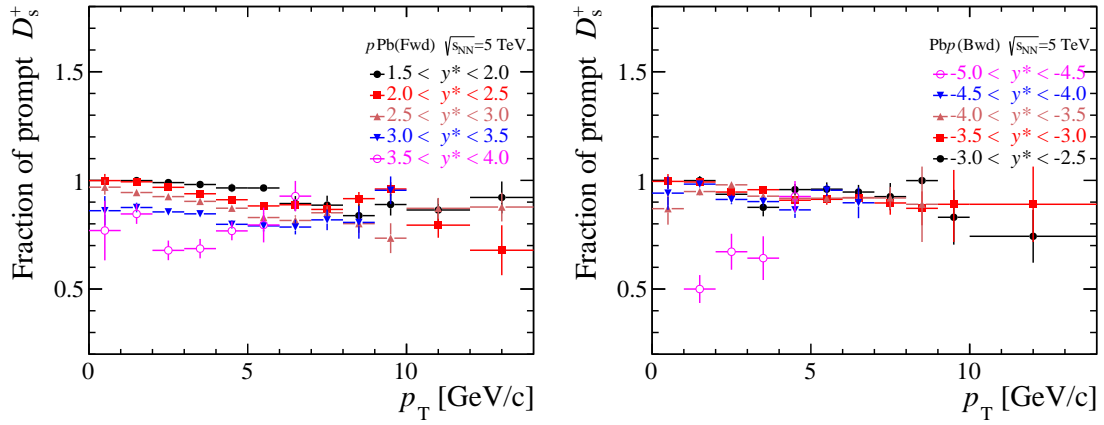


Figure 4.14 Prompt fractions of D_s^+ as a function of p_T and y^* in the forward (left) and backward (right) configurations.

The prompt fractions in different $D_{(s)}^+$ p_T and y^* bins are given in Fig. 4.13 and Fig. 4.14. Overall, there are very few secondary $D_{(s)}^+$ mesons from b -hadron decays, the fractions of prompt D^+ are in the range 80 – 100%, while the fractions of prompt D_s^+ are in the range 50 – 100%.

The last term required for the cross-section calculation in Eq. (3.1) is the total efficiency, which corrects the actual numbers of candidates entering the fitting process in p Pb collisions. The total efficiency ϵ_{tot} is divided into three components: the geometrical acceptance efficiency ϵ_{acc} discussed in Section. 4.3, the reconstruction and selection efficiency $\epsilon_{\text{rec\&sel}}$ (without PID requirements) discussed in Section. 4.4, and the PID efficiency ϵ_{PID} discussed in Section. 4.5. These efficiencies of prompt $D_{(s)}^+$ are determined in each p_T and y^* bin. The determination of each component is discussed separately in the following.

4.3 Acceptance

Since the LHCb detector has a limited spatial acceptance capability, a geometric acceptance efficiency exists. It is impossible to detect a particle that flies outside of the forward region where $2 < \eta < 5$. The effect is estimated by using about 4 million generator-level simulations generated quickly by the Gauss application^[151]. There are no geometrical acceptability requirements for all particles produced at the generator level. The geometrical acceptance efficiency is defined as

$$\epsilon_{\text{acc}} \equiv \frac{N_{\text{all daughters of } D_{(s)}^+ \text{ in LHCb acceptance}}}{N_{\text{Generated } D_{(s)}^+}} \quad (4.5)$$

Ignoring the bending in the magnetic field, “daughters in the LHCb acceptance” requires the decay products must be within the range $10 < \theta < 400$ mrad, where θ represents the polar angle of the momentum vector, defined with respect to the beam direction. The geometrical acceptance efficiency is assumed to be independent of the multiplicity.

In Fig. 4.15 and Fig. 4.16, the geometrical acceptance efficiency in each p_T and y^* bin for prompt $D_{(s)}^+$ meson is given for forward and backward rapidities, respectively. With increasing p_T , the resulting geometrical acceptance efficiency ϵ_{acc} grows until it reaches about 100%.

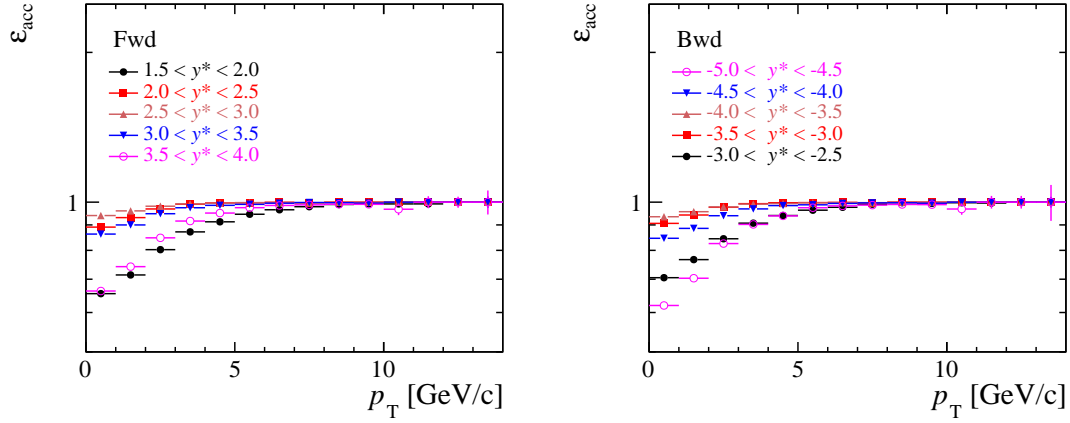


Figure 4.15 Geometrical acceptance efficiency ϵ_{acc} of prompt D^+ as a function of p_T and y^* in the forward (left) and backward (right) configurations. Statistical uncertainties only.

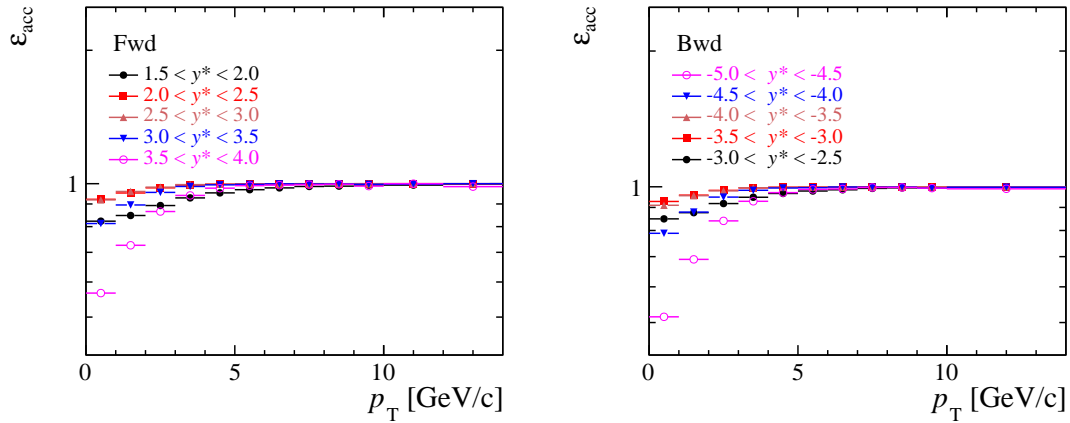


Figure 4.16 Geometrical acceptance efficiency ϵ_{acc} of prompt D_s^+ as a function of p_T and y^* in the forward (left) and backward (right) configurations. Statistical uncertainties only.

4.4 Reconstruction and selection efficiency

The D^+ reconstruction and selection efficiency is defined as

$$\epsilon_{\text{rec\&sel}} = \frac{\sum D^+ \text{in acceptance, reconstructed and selected}}{D^+ \text{with } K^- \pi^+ \pi^+ \text{in LHCb acceptance}}. \quad (4.6)$$

The D_s^+ reconstruction and selection efficiency is defined as

$$\epsilon_{\text{rec\&sel}} = \frac{\sum D_s^+ \text{in acceptance, reconstructed and selected}}{D_s^+ \text{with } K^+ K^- \pi^+ \text{in LHCb acceptance}}. \quad (4.7)$$

Two components are involved: the efficiency of reconstructing the three long tracks (which contain hits from VELO, TT, and tracking stations) and the improvement of the signal purity with requirements in Table. 4.2 (excluding PID selections). As explained below, the efficiency $\epsilon_{\text{rec\&sel}}$ is calculated by utilizing truth matched $D_s^+ \rightarrow K^+ K^- \pi^+$ ($D^+ \rightarrow K^+ K^- \pi^+$) decays in p Pb full simulation samples and modified due to multiplicity effects.

4.4.1 Truth matching efficiency

The LHCb MC truth matching algorithm considers a reconstructed particle to be matched to an simulated particle if the reconstructed particle's hits and the simulated particle's hits overlap by at least 70%. This 70% threshold is somewhat arbitrarily chosen which leads to an inefficiency in truth matching because some reconstructed particles are not tagged as matched when they actually belong to MC particles, resulting in an underestimate of efficiency and an enlargement of the final measurement. This inefficiency (ρ_{truth}) is calculated by the number of truth matched (N_{truth}) and not matched (N_{fail}) signal decays over the matched signal decays,

$$\rho_{\text{truth}} = \frac{N_{\text{truth}} + N_{\text{fail}}}{N_{\text{truth}}}. \quad (4.8)$$

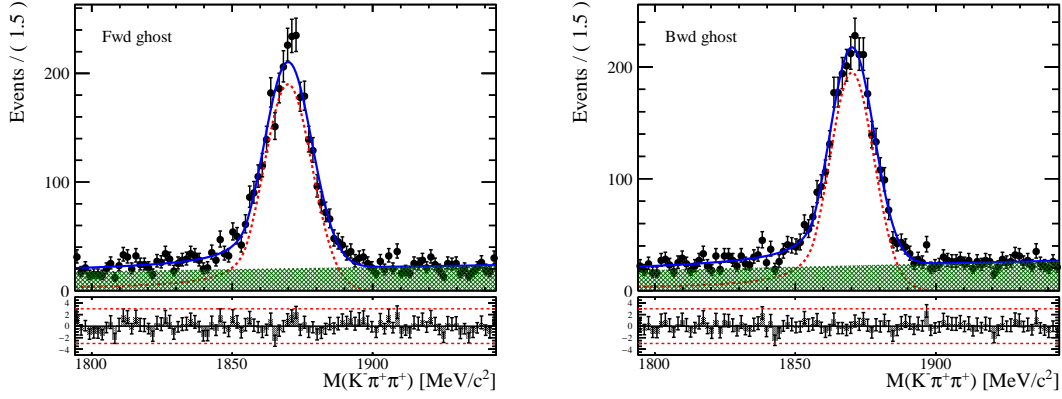


Figure 4.17 Invariant mass distributions of $D^+ \rightarrow K^- \pi^+ \pi^+$ decays that are not truth matched for the forward (left) and backward (right) simulation samples, respectively.

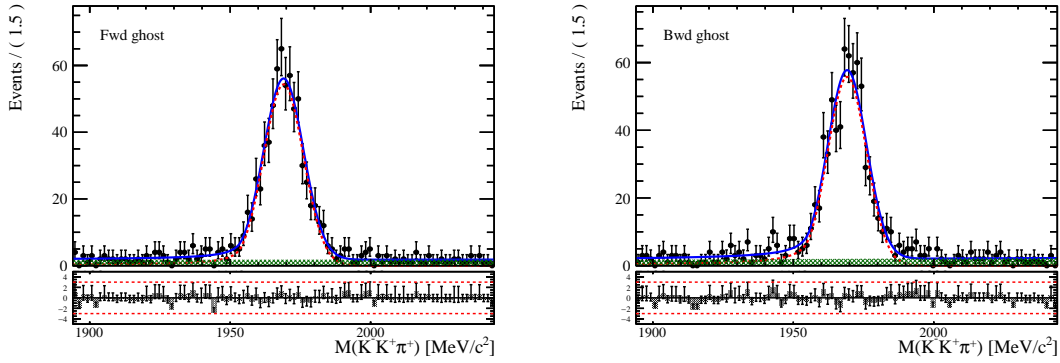


Figure 4.18 Invariant mass distributions of $D_s^+ \rightarrow K^- K^+ \pi^+$ decays that are not truth matched for the forward (left) and backward (right) simulation samples, respectively.

The number of not matched signal decays is determined by fitting the invariant mass distribution of simulation sample. A Crystal Ball signal plus a linear background is used to fit the mass spectrum. The invariant mass distributions of $D^+ \rightarrow K^- \pi^+ \pi^+$ and $D_s^+ \rightarrow K^- K^+ \pi^+$ decays which are not matched for forward and backward rapidities are shown in Fig. 4.17 and Fig. 4.18. Since this effect would result in an underestimate of the reconstruction and selection efficiency, the total efficiency of D^+ (D_s^+) should be multiplied by a truth matching inefficiency correction factor ρ_{truth} of 1.0223 (1.0240) in the forward configuration and 1.0254 (1.0274) in the backward configuration. The truth matching efficiency correction uncertainties of D^+ (D_s^+) are 0.07% (0.12%) in the forward configuration and 0.08% (0.13%) in the backward configuration, which are negligible compared to those of other sources.

4.4.2 Tracking efficiency

Since simulation applications cannot perfectly model the detector response, it is also critical to consider the difference in tracking efficiency between data and simulation. The “tracking group” at LHCb has quantified the difference as the efficiency ratio of the daughter’s track in p and η bins^[163].

By applying a correction factor to each event in simulation, the tracking efficiency is modified by the product of the K and π track efficiency ratios. Taking tracking efficiency correction into account, the reconstruction and selection efficiency is estimated as

$$\epsilon_{\text{rec\&sel}} \equiv \frac{\sum_{D^+ \text{reconstructed and selected}} w_i(p_{K^-}, \eta_{K^-}) \times w_i(p_{\pi^+}, \eta_{\pi^+}) \times w_i(p_{\pi^+}, \eta_{\pi^+})}{D^+ \text{with } K^- \pi^+ \pi^+ \text{ in LHCb acceptance}} \quad (4.9)$$

or

$$\epsilon_{\text{rec\&sel}} \equiv \frac{\sum_{D_s^+ \text{reconstructed and selected}} w_i(p_{K^-}, \eta_{K^-}) \times w_i(p_{K^+}, \eta_{K^+}) \times w_i(p_{\pi^+}, \eta_{\pi^+})}{D_s^+ \text{with } K^+ K^- \pi^+ \text{ in LHCb acceptance}}, \quad (4.10)$$

where ω_i is the tracking efficiency of a K or π track.

In Fig. 4.19, the tracking table (2012) which was released on April 11, 2013, is used to correct the difference between data and MC in (p, η) bins for this analysis. The calibration table is generated in a tag-and-probe approach by calculating the tracking efficiency with $J/\psi \rightarrow \mu^- \mu^+$ decays in 2012 pp data and comparing the same amount in simulation^[163]. The systematic uncertainty associated with the tracking efficiency ratios in Fig. 4.19 is negligible compared with other systematic uncertainties, because the tracking calibration table is measured precisely (the overall uncertainty is less than 0.4%).

4.4.3 Dependence on multiplicity

The variable that could be used to measure the number of particles produced during an event is referred to as detector occupancy or multiplicity. At LHCb, the number of reconstructed charged tracks (nTracks), the number of VELO clusters (nVeloClusters), sum of OT and IT clusters (nTstations), the number of TT clusters (nTTClusters), the number of long tracks (nLongTracks) could be used for this purpose. When calculating the reconstruction and selection efficiency $\epsilon_{\text{rec\&sel}}$ and PID efficiency, the origin and multiplicity-fixed p Pb simulations in Table. 3.1 (Table. 3.2) are merged to increase MC statistics. The multiplicity distributions in p Pb simulations, forward and backward p Pb data samples are different, especially in the case of backward collisions. Fig. 4.20 and Fig. 4.21 show

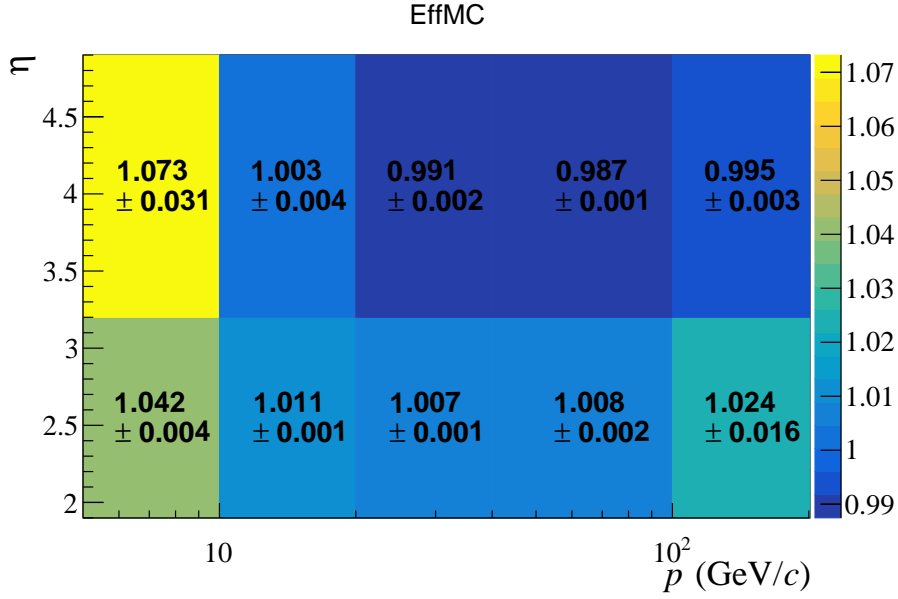


Figure 4.19 Tracking efficiency table (2012) as a function of p and η .

the distributions of nTracks, nVeloClusters, nTstations, nTTClusters and nLongTracks for p Pb, Pb p simulation samples, forward and backward p Pb data of D^+ (D_s^+), respectively. It is found that the multiplicity distributions of detectors are different between data and simulation samples for both forward and backward rapidities, especially in the case of backward, which clearly affect the reconstruction and selection efficiency^[91-92].

The effect of multiplicity should be taken into account when calculating reconstruction and selection efficiency. For example, it is depicted in Fig. 4.22 that the D^+ reconstruction and selection efficiencies $\epsilon_{\text{rec\&sel}}$ vary with the multiplicity x for the backward configuration. As the multiplicity rises, the reconstruction and selection efficiency increases at first, then falls. At low multiplicity, the separation between D^+ quantities and PV is worse due to the poor resolution of PV reconstruction. Meanwhile, the decrease in efficiency at high multiplicities is interpreted as a decrease in tracking capacity. An empirical function can be used to characterize this trend as shown in Fig. 4.22,

$$\epsilon(x) = p_3 \times |s(x - p_0)|^{p_1} \times \exp^{-p_2 s(x - p_0)} \quad (4.11)$$

where the parameter s is a constant scale factor, p_0 indicates the minimum detector occupancy of a given event, p_1 is the rate of increase of efficiency as a function of detector occupancy at a small multiplicity, and p_2 is the rate of decrease of efficiency as the detector occupancy increases, and p_3 is the absolute scale of the efficiency. On average, the reconstruction and selection efficiency increases when the event activity of the data is less than the simulation.

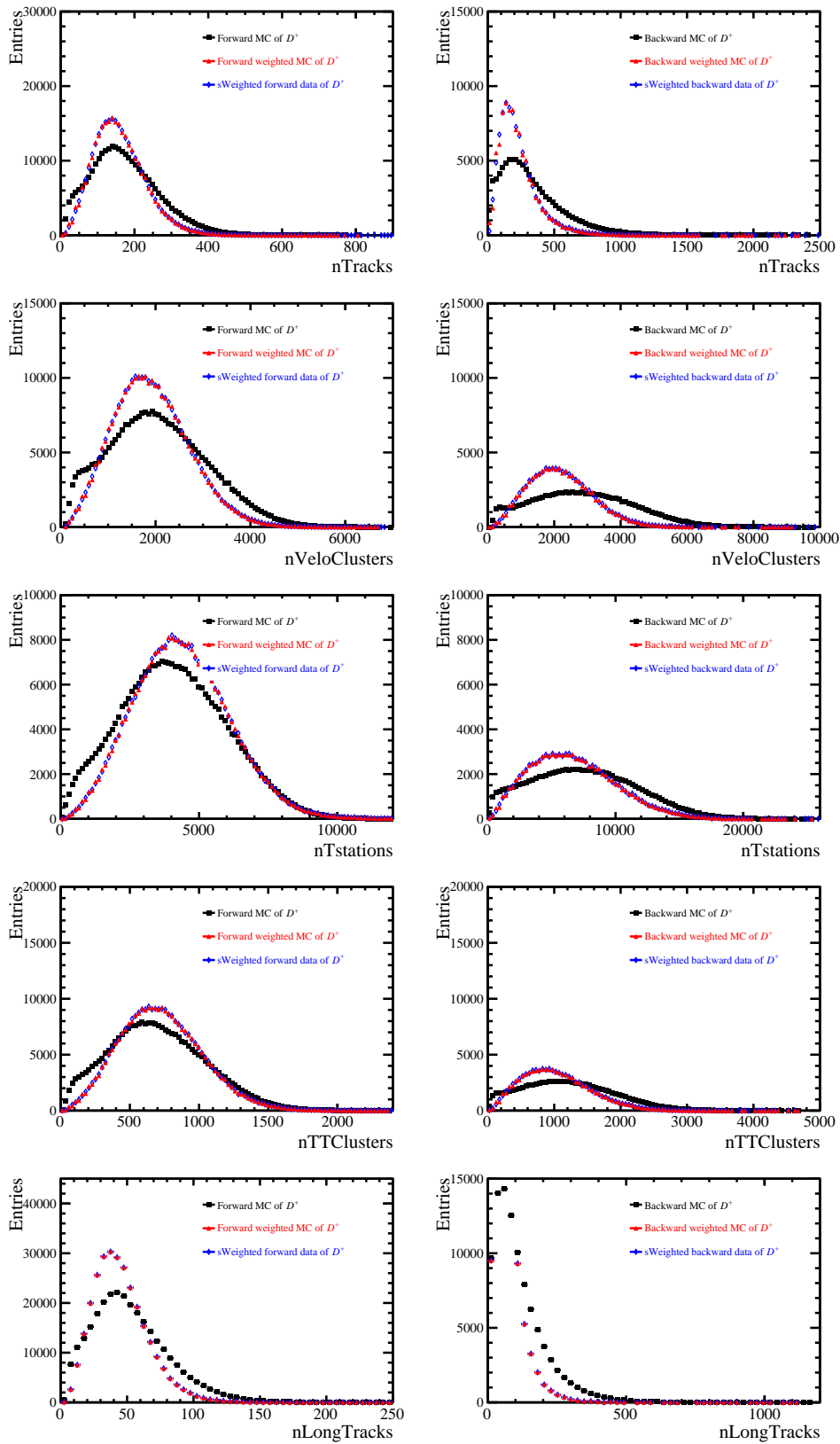


Figure 4.20 Distributions of n Tracks, n VeloClusters, n Tstations, n TTClusters and n LongTracks in forward (left) or backward (right) sWeighted data and simulated samples for D^+ . Both the distributions of sWeighted data and simulated samples are displayed. For simulated events, the raw distributions and reweighted distributions are shown.

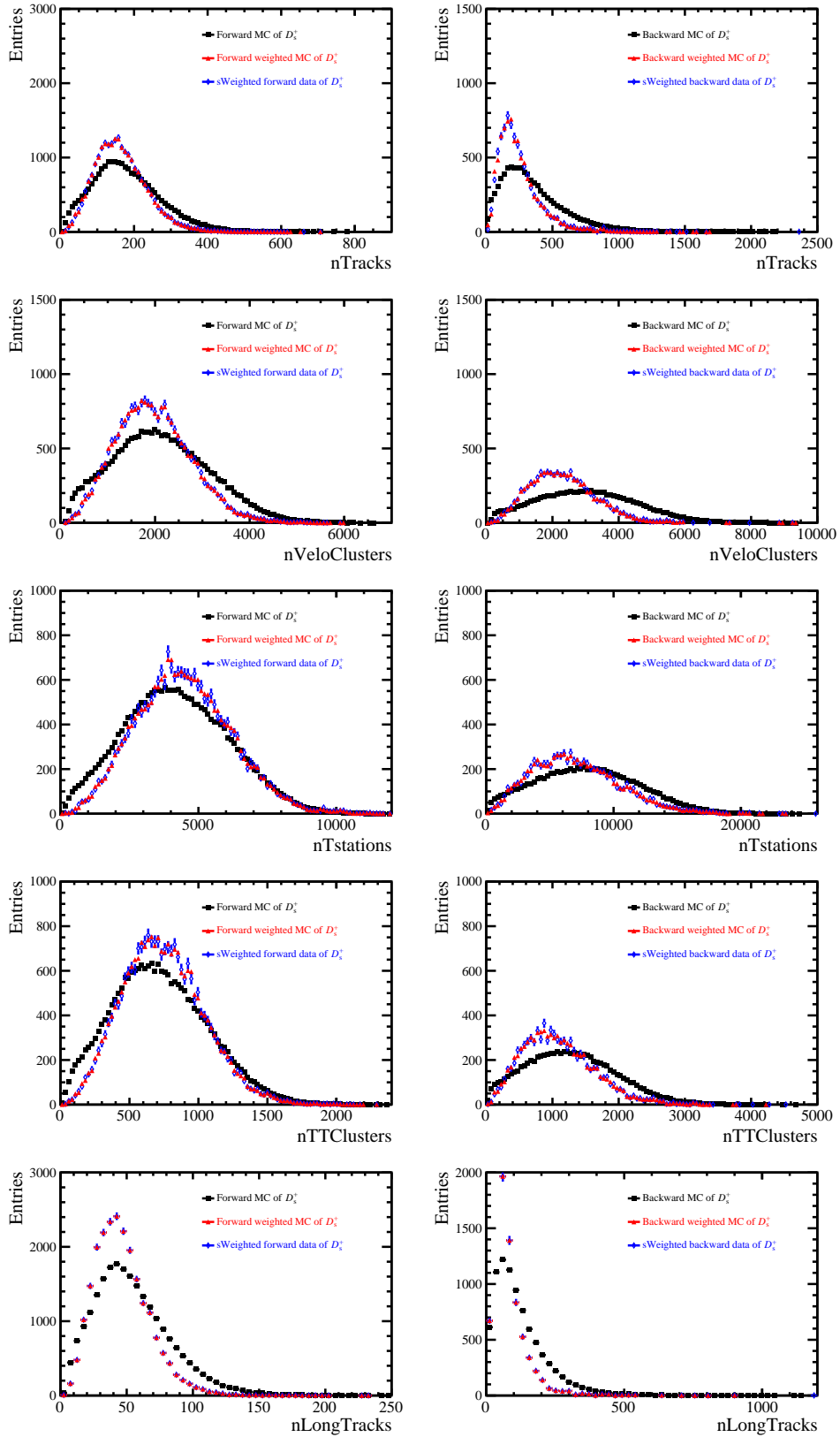


Figure 4.21 Distributions of $nTracks$, $nVeloClusters$, $nTstations$, $nTTClusters$ and $nLongTracks$ in forward (left) or backward (right) $sWeighted$ data and simulated samples for D_s^+ . Both the distributions of $sWeighted$ data and simulated samples are displayed. For simulated events, the raw distributions and reweighted distributions are shown.

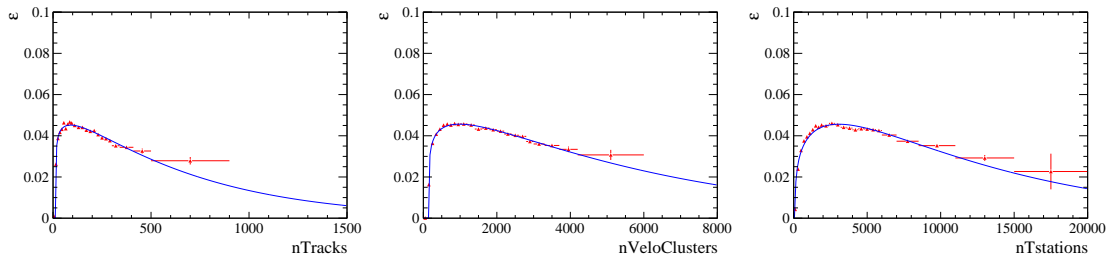


Figure 4.22 The D^+ reconstruction and selection efficiencies $\epsilon(x)$ and their fit results as a function of multiplicity ($nTracks$, $nVeloClusters$ and $nTstations$) for the backward configuration.

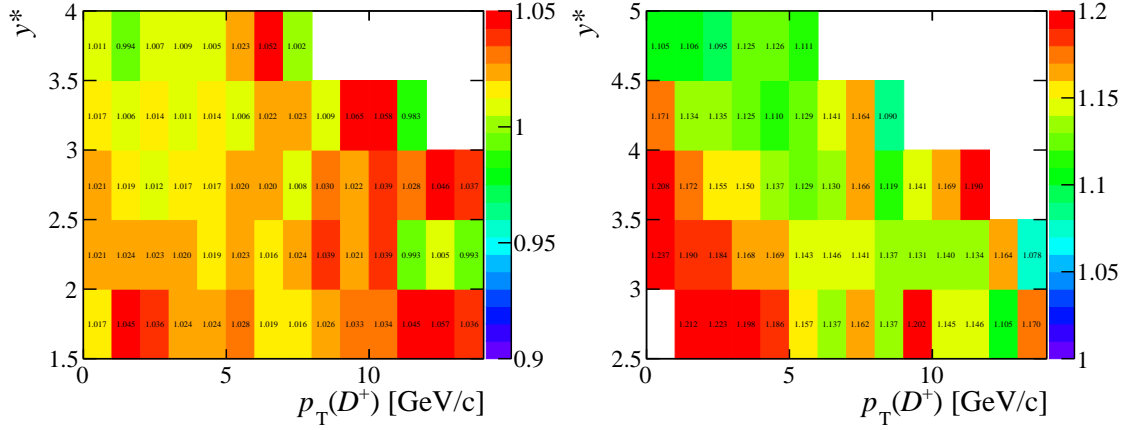


Figure 4.23 Correction factors α_{corr} of D^+ reconstruction and selection efficiencies in each p_T and y^* bin in the forward (left) and backward (right) rapidity regions.

Consequently, the efficiency calculated by the p Pb simulation need to be corrected to account for the fact that efficiency is multiplicity dependent. The method to deal with it is that the detector multiplicity in p Pb simulation is reweighted to match data. When the reconstruction and selection efficiency is calculated based on Eq. (4.9) and Eq. (4.10), while in both numerator and denominator each event is given a one-dimensional weight, which brings the multiplicity distribution of simulation to match data. This weight is determined as the ratio of the histogrammed distribution of nVeloClusters (or any of the remaining four multiplicity variables) in p Pb data over that in simulation.

In order to fully consider the impact of the modification of these five variables on reconstruction and selection efficiency, the average correction factor of not weighted reconstruction and selection efficiency $\epsilon_{\text{rec\&sel}}$ according to Eq. (4.9) and Eq. (4.10) in each p_T and y^* bin is defined as

$$\alpha_{\text{corr}} = \frac{\sum_{i=1}^5 \epsilon_{\text{corr}}(x_i)}{5 \times \epsilon_{\text{rec\&sel}}}, \quad (4.12)$$

where $\epsilon_{\text{corr}}(x_i)$ is the reconstruction and selection efficiency in each p_T and y^* bin corrected by a given multiplicity variable x_i .

The average correction factors for D^+ (D_s^+) α_{corr} in each p_T and y^* bin are shown in Fig. 4.23 and Fig. 4.24. In Fig. 4.25 and Fig. 4.26, the corrected reconstruction and selection efficiency ($\alpha_{\text{corr}} \times \epsilon_{\text{rec\&sel}}$) in each p_T and y^* bin for prompt $D_{(s)}^+$ meson is shown for forward and backward rapidities. As a result of the requirement on momentum of daughters $p < 100 \text{ GeV}/c$ in stripping, the efficiency in high p_T and large y^* bin drops.

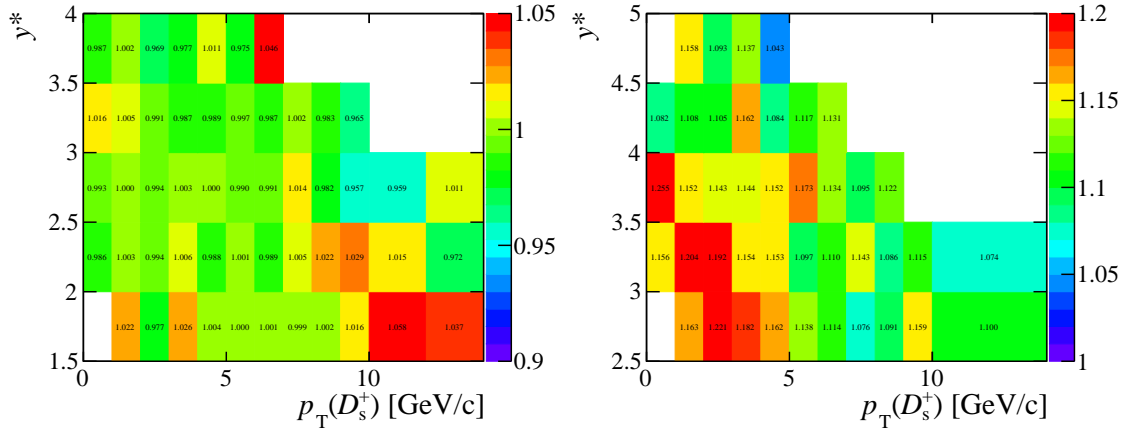


Figure 4.24 Correction factors α_{corr} of D_s^+ reconstruction and selection efficiencies in each p_T and y^* bin in the forward (left) and backward (right) rapidity regions.

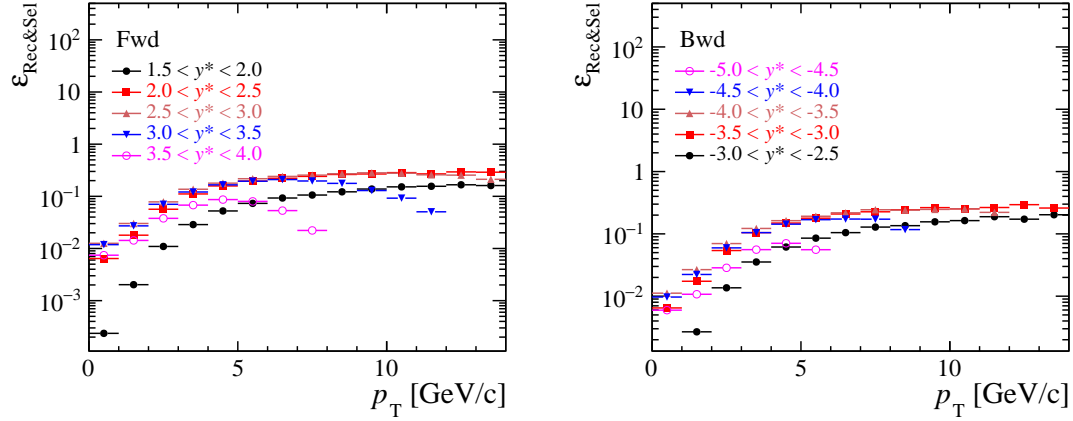


Figure 4.25 Corrected reconstruction and selection efficiency of prompt D^+ as a function of p_T and y^* in forward (left) and backward (right). Only statistical uncertainties are shown.

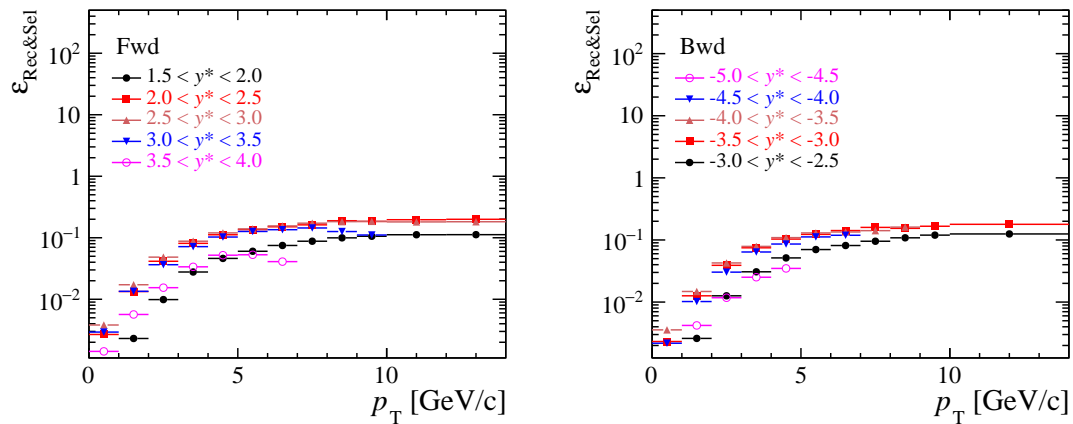


Figure 4.26 Corrected reconstruction and selection efficiency of prompt D_s^+ as a function of p_T and y^* in forward (left) and backward (right) configurations. Only statistical uncertainties are shown.

4.5 Particle identification efficiency

The PID efficiency ϵ_{PID} is defined as the efficiency of the PID requirement on the three tracks of daughters in the $D_{(s)}^+$ selections. With the track calibration method, ϵ_{PID} is evaluated using the single-track efficiency in data convolved with the track kinematic distribution in MC sample as

$$\epsilon_{\text{PID}} = \frac{\sum_i \epsilon_K(p_i^K, \eta_i^K) \epsilon_\pi(p_i^\pi, \eta_i^\pi) \epsilon_\pi(p_i^\pi, \eta_i^\pi)}{N} \quad (4.13)$$

or

$$\epsilon_{\text{PID}} = \frac{\sum_i \epsilon_K(p_i^K, \eta_i^K) \epsilon_K(p_i^K, \eta_i^K) \epsilon_\pi(p_i^\pi, \eta_i^\pi)}{N} \quad (4.14)$$

in each $D_{(s)}^+$ kinematic bin, where N is the sum of the events in MC sample used to estimate the PID efficiency. The single-track efficiency $\epsilon_{K,\pi}(p, \eta)$ is determined using a tag-and-probe method^[91-92]. The D^0 calibration sample is $D^*(2010)^+$ tagged and PID unbiased, which is taken in the same p Pb period as $D_{(s)}^+$ with restripping selections. Detailed stripping selections for this sample can be found in Appendix A.5. The main reason for restripping the calibration sample is to get rid of the p_T threshold, and it retains more low p_T tracks which are essential to calibrate the low p_T bins of $D_{(s)}^+$ mesons. Meanwhile, the calibration line prescale has been raised from 0.89 to 1.

The PID selections are $\text{DLL}_{K\pi}(K^-) > 5$ and $\text{DLL}_{K\pi}(\pi^+) < 0$. With a tag (π) and probe (K) approach, the single-track efficiency of K is defined as

$$\epsilon_K(p_K, \eta_K) = \frac{\# \text{ signal } D^0 \text{ with both } K, \pi \text{ PID applied}}{\# \text{ signal } D^0 \text{ with } \pi \text{ PID applied}}(p_K, \eta_K). \quad (4.15)$$

The efficiency for the π is calculated in the same way, by switching K with π in Eq. (4.15). To subtract the background component, an unbinned maximum likelihood fit to D^0 invariant mass distribution is performed in the same method as the $D_{(s)}^+$ for signal extraction in Section. 4.2.1. In Fig. 4.27, the D^+ (D_s^+) nVeloClusters distributions of simulation, sWeighted data and D^0 calibration sample are different in forward and backward rapidities. Similar to reconstruction and selection efficiency, PID efficiency is also affected by the multiplicity difference between the MC and data.

If the multiplicity dependence of the PID efficiency is considered, the nVeloClusters distributions of both simulation and D^0 calibration sample should be reweighted to be same as sWeighted D^+ (D_s^+) data. For D^0 calibration sample, the weight (wt_1) varies as a function of multiplicity, given by the ratio of nVeloClusters distribution in D^+ (D_s^+) p Pb data over D^0 calibration sample. While for D^+ (D_s^+) simulation sample, the weight

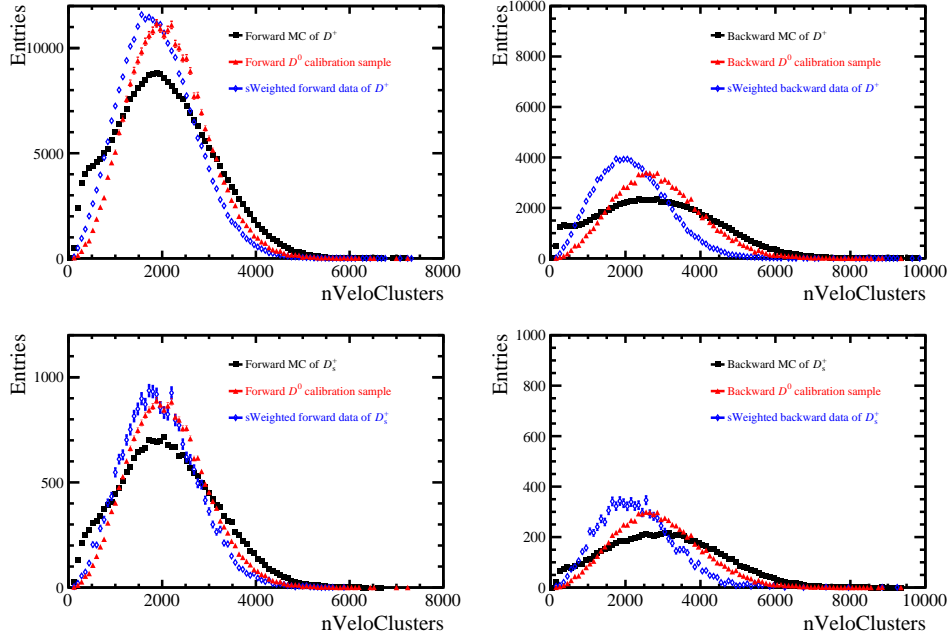


Figure 4.27 The $D_{(s)}^+$ nVeloClusters distributions of simulation, sWeighted data and D^0 calibration sample in the forward (left) and backward (right) rapidity regions.

(wt_2) is defined as a function of detector occupancy, given by the ratio of nVeloClusters distributions in D^+ (D_s^+) p Pb data and simulation. The reweighted nVeloClusters distributions of MC and D^0 calibration sample compared with data are shown in Fig. 4.28 in forward and backward rapidities.

The single-track PID efficiencies are calculated according to Eq. (4.15), in both numerator and denominator each event is given the weight wt_1 . This weight brings the nVeloClusters distribution of the D^0 calibration sample to the same as the corresponding one in D^+ (D_s^+) data. In Fig. 4.29 and Fig. 4.30, the D^+ (D_s^+) single-track PID efficiencies for K and π are shown in bins of (p, η) in both forward and backward rapidities.

- The normal binning scheme of K and π in forward and backward rapidities:
 - p : [3.2, 10, 15, 20, 25, 32, 40, 50, 70, 100];
 - η : [2.0, 2.6, 3.0, 3.4, 3.8, 4.3, 5.0];

Using the simulation kinematics distribution and the single-track efficiencies, the PID efficiency is calculated based on Eq. (4.13) and Eq. (4.14), in which each event is given a weight (wt_2) to make nVeloClusters distribution in simulation to match D^+ (D_s^+) data.

In Fig. 4.31 and Fig. 4.32, the resulting PID efficiency in each p_T and y^* bin for prompt $D_{(s)}^+$ meson is shown for forward and backward rapidities.

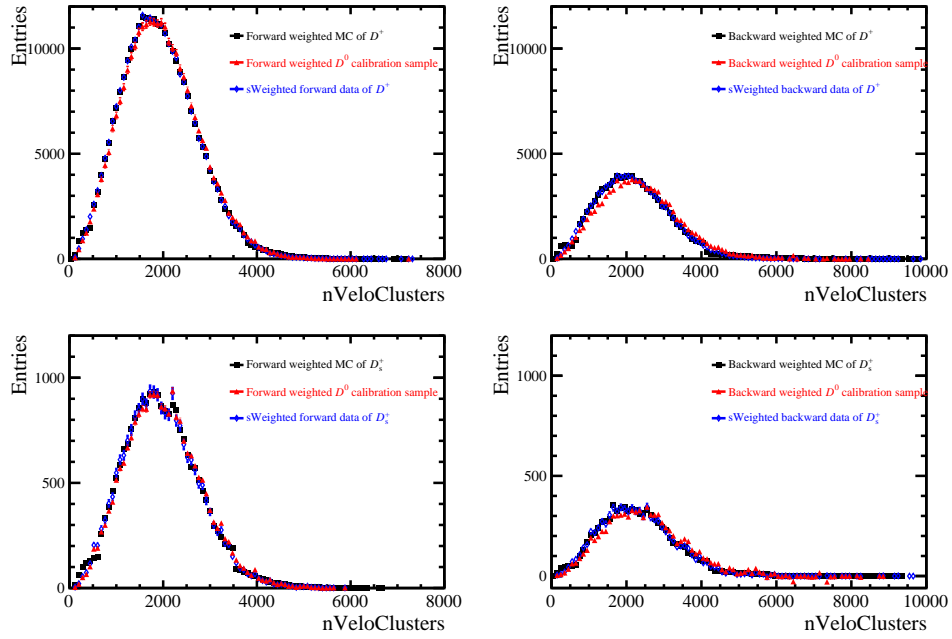


Figure 4.28 The reweighted $D_{(s)}^+$ n VeloClusters distributions of simulation, D^0 calibration sample and sWeighted data in the forward (left) and backward (right) rapidity regions.

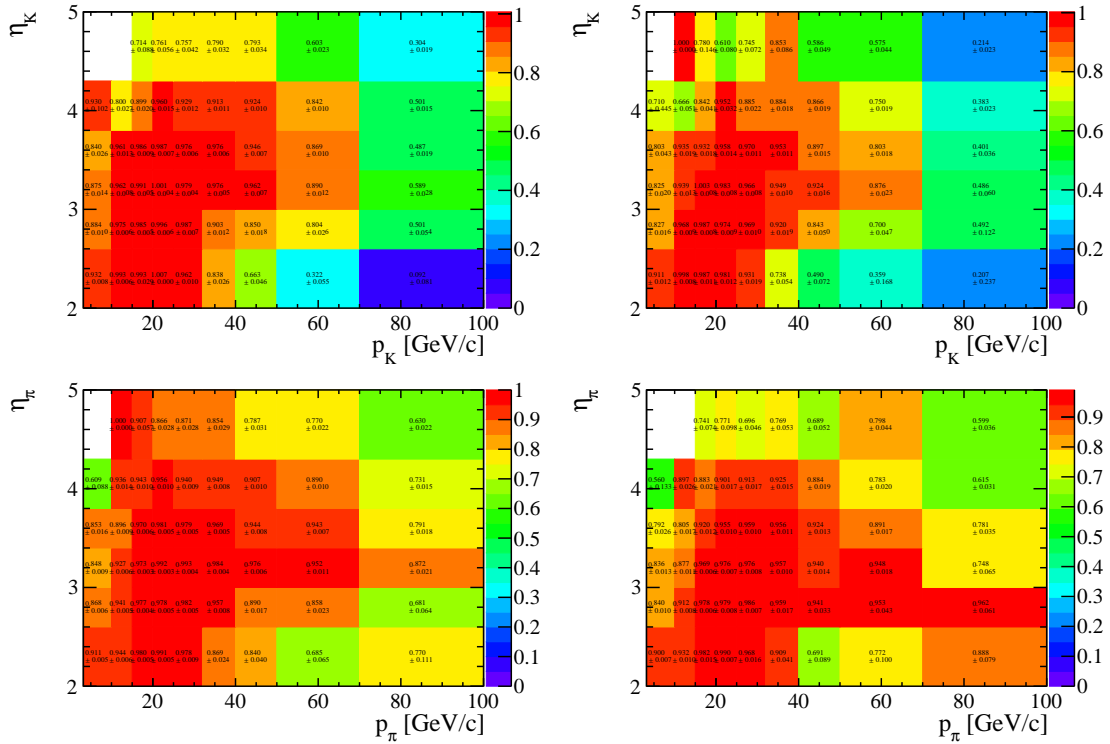


Figure 4.29 The D^+ single-track PID efficiency for K and π in bins of (p, η) for p Pb forward (left) and backward (right) collisions. Statistical uncertainties only.

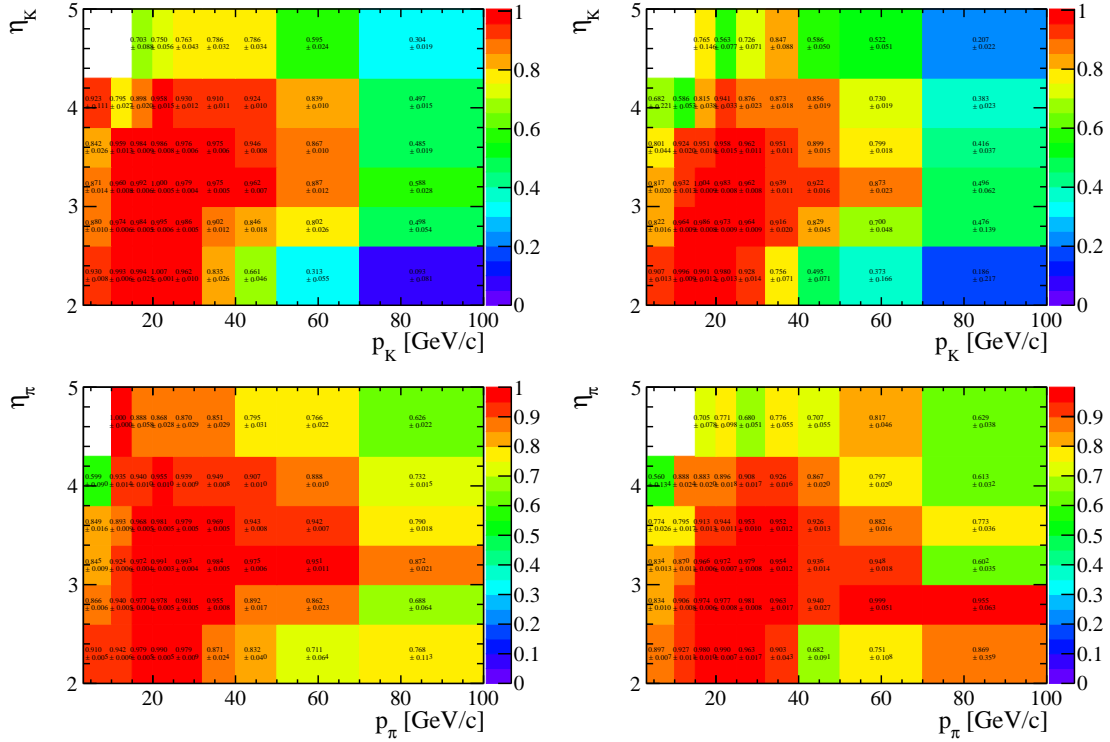


Figure 4.30 The D_s^+ single-track PID efficiency for K and π in bins of (p, η) for p Pb forward (left) and backward (right) collisions. Statistical uncertainties only.

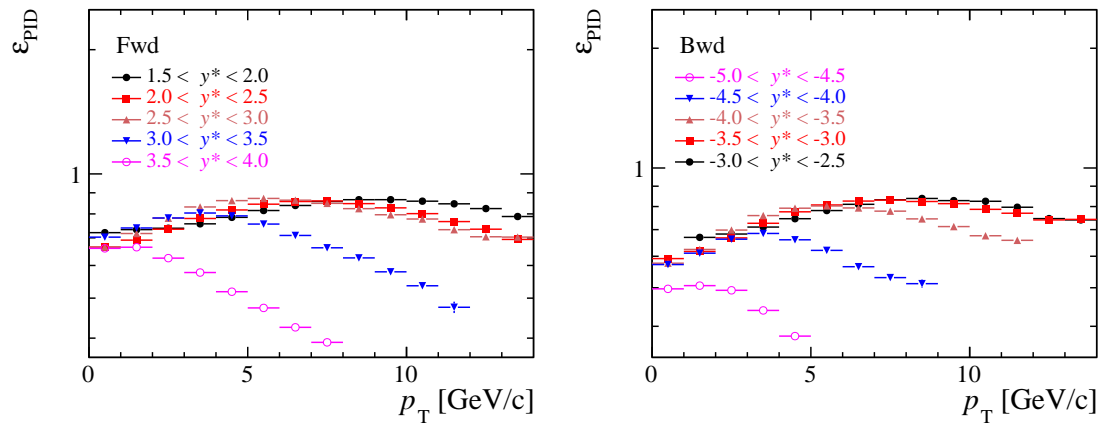


Figure 4.31 Particle identification efficiency ϵ_{PID} of prompt D^+ , as a function of p_T and y^* in the forward (left) and backward (right) collision samples. Statistical uncertainties only.

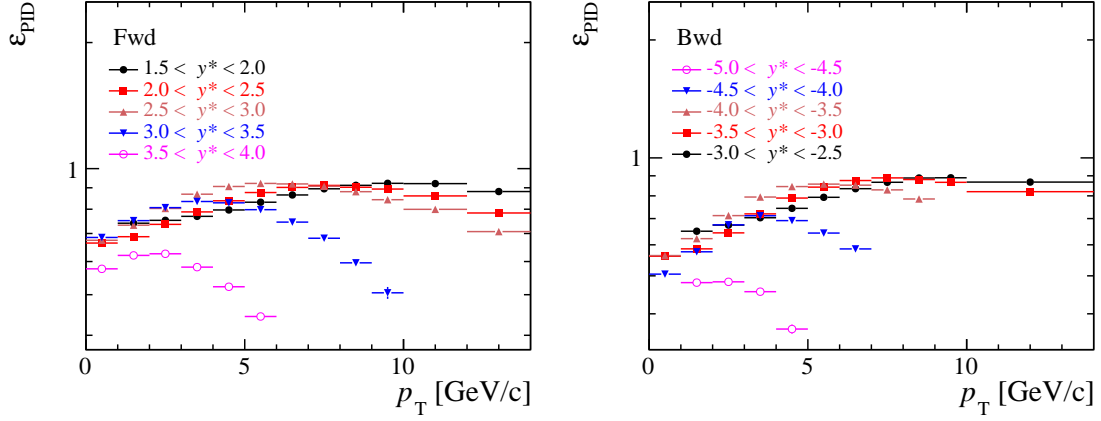


Figure 4.32 Particle identification efficiency ϵ_{PID} of prompt D_s^+ , as a function of p_T and y^* of prompt D_s^+ in the forward (left) and backward (right) collision samples. Statistical uncertainties only.

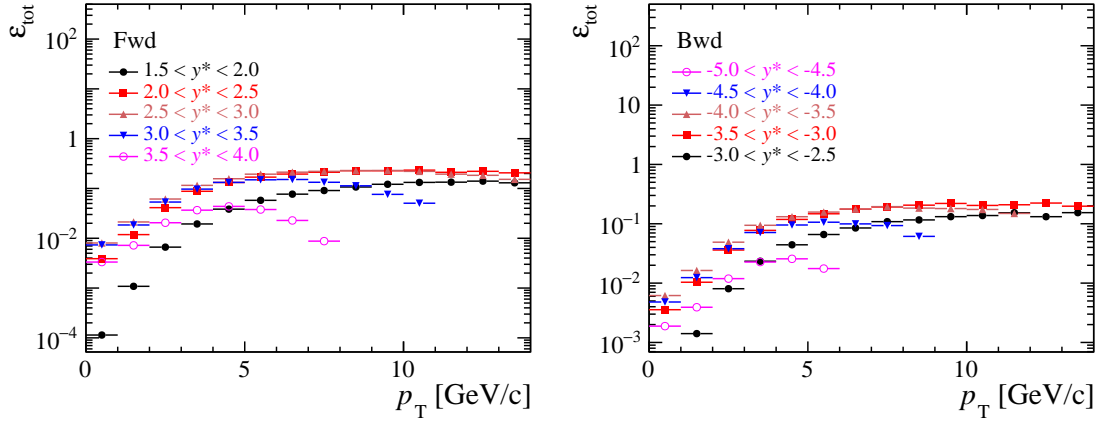


Figure 4.33 Total efficiency ϵ_{tot} of prompt D^+ as a function of p_T and y^* for both forward (left) and backward (right) configurations.

4.6 Total efficiency

Including the corrections from truth matching and multiplicity, the total efficiency ϵ_{tot} of $D_{(s)}^+$, i.e. the product the geometrical acceptance efficiency ϵ_{acc} , the reconstruction and selection efficiency $\epsilon_{\text{rec\&sel}}$ and the PID efficiency ϵ_{PID} , is shown in Fig. 4.33 and Fig. 4.34 and summarized in Appendix A.3. The efficiency ϵ_{tot} in the backward configuration is lower than that in the forward configuration, owing to lower reconstruction efficiency and PID efficiency as a consequence of increased multiplicity.

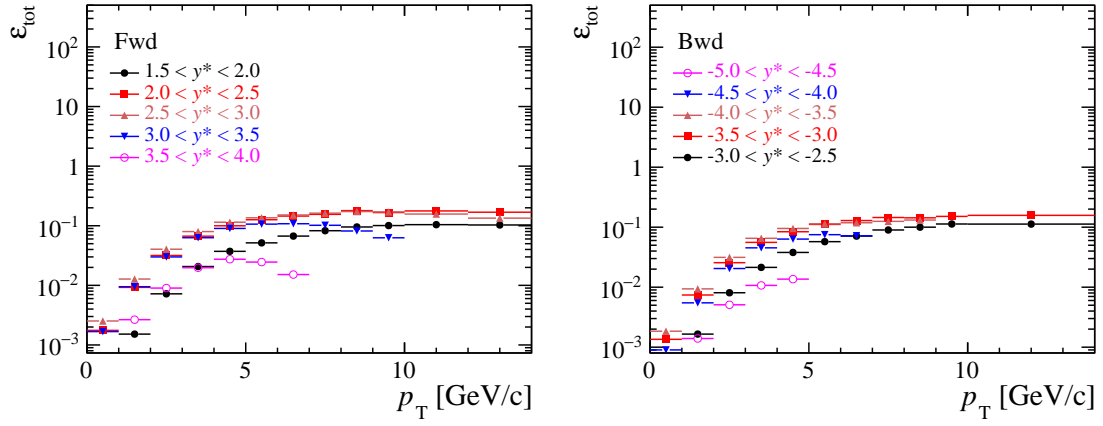


Figure 4.34 Total efficiency ϵ_{tot} of prompt D_s^+ as a function of p_T and y^* for both forward (left) and backward (right) configurations.

4.7 Systematic uncertainties

The following are the sources of systematic uncertainty considered in the measurement of prompt $D_{(s)}^+$ production:

- systematic uncertainty on prompt $D_{(s)}^+$ signal determination including the invariant mass fit and $\log_{10} \chi_{\text{IP}}^2 (D_{(s)}^+)$ fit;
- systematic uncertainty on finite MC sample size;
- systematic uncertainty on the difference in kinematic distributions between data and MC.
- systematic uncertainty on reconstruction and selection efficiency including the correction of tracking and multiplicity.
- systematic uncertainty on PID efficiency;
- systematic uncertainty on luminosity and branching fractions.

Unless otherwise indicated, the systematic uncertainties are calculated independently for the forward and backward configurations due to their highly different environments in $p\text{Pb}$ collisions.

4.7.1 Signal yield systematic uncertainty

The prompt $D_{(s)}^+$ signal yields are determined in this study by fitting two distributions: the invariant mass spectrum and $\log_{10} \chi_{\text{IP}}^2 (D_{(s)}^+)$, whose uncertainties are evaluated independently.

For the invariant mass fit, the fixed parameters during the fit are varied with one sigma away from the mean value. The description of signal model is switched from a Crystal Ball plus a Gaussian function to a Crystal Ball plus another Crystal Ball function, where these two Crystal Ball functions also have the same width σ_{CB} . A linear function describes the form of the background in fitting, while it is swapped to an exponential function for estimating the background shape effect. The largest difference from the default mass fit result is taken as the uncertainty of the invariant mass system. The resulting systematic uncertainty of $D_{(s)}^+$ in different kinematic bins is displayed in Fig. 4.35 and Fig. 4.36. For most of the bins of D^+ (D_s^+), their uncertainties are less than 5% (10%).

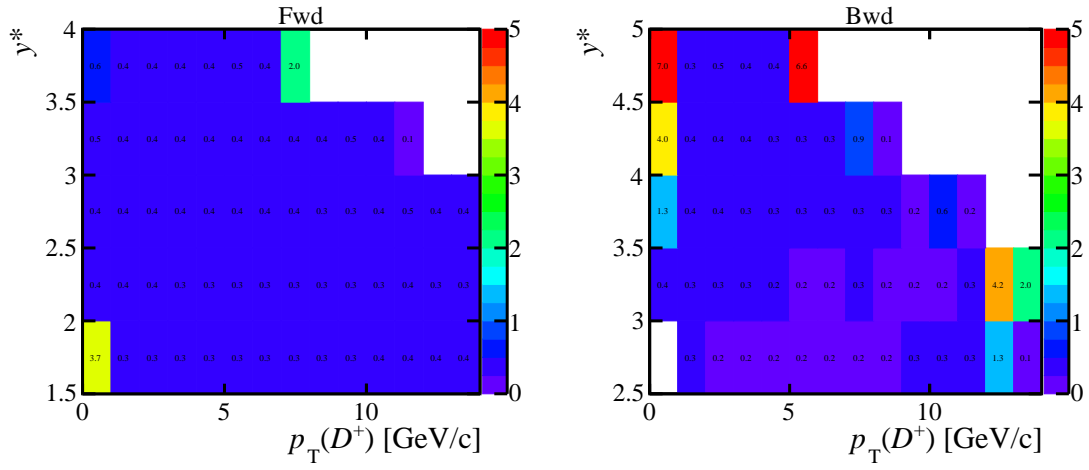


Figure 4.35 Relative systematic uncertainty (%) related to invariant mass fit of D^+ in bins of p_T and y^* in the forward (left) and backward (right) configurations.

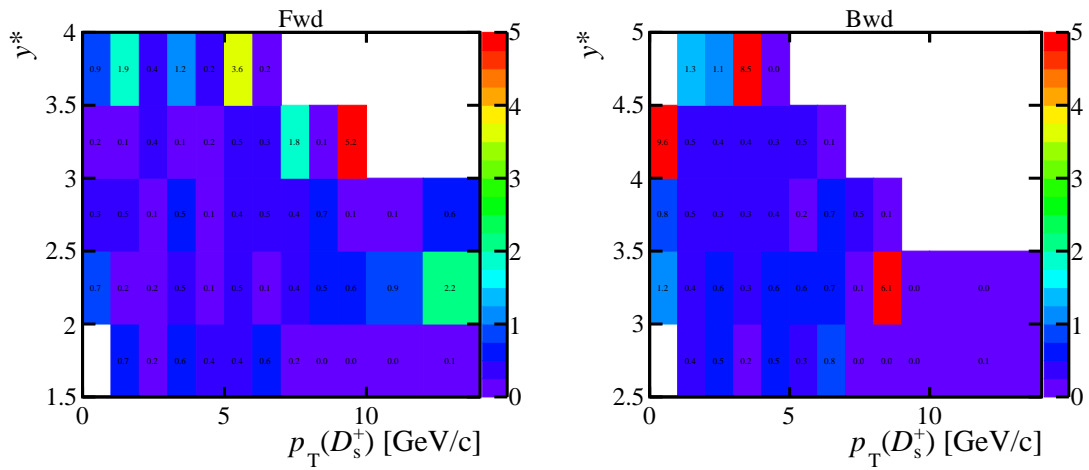


Figure 4.36 Relative systematic uncertainty (%) related to invariant mass fit of D_s^+ in bins of p_T and y^* in the forward (left) and backward (right) configurations.

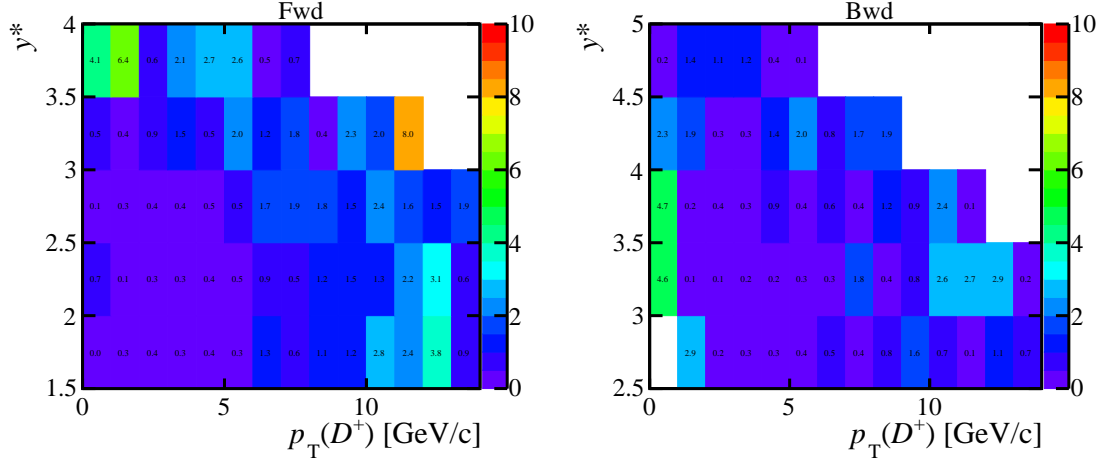


Figure 4.37 Relative systematic uncertainties (%) due to $\log_{10} \chi_{\text{IP}}^2(D^+)$ fit in bins of p_T and y^* in the forward (left) and backward (right) configurations.

For the determination of prompt yield, the data set for $\log_{10} \chi_{\text{IP}}^2(D_{(s)}^+)$ fit with sWeight obtained from the invariant mass fit is described in Section. 4.2.2. In the previous $\log_{10} \chi_{\text{IP}}^2(D_{(s)}^+)$ fit, the parameters σ , ϵ , ρ_L and ρ_R of the prompt and non-prompt components are fixed by fitting simulation sample in the total forward and backward rapidity regions. In addition, the difference of μ between the non-prompt and prompt components for $D_{(s)}^+$ is fixed in each (p_T, y^*) bin. These effects are also considered by shifting the values to one sigma away from the mean value. The shape of non-prompt $\log_{10} \chi_{\text{IP}}^2(D_{(s)}^+)$ is a Bukin function, which is shifted to a Gaussian to evaluate the uncertainty from secondary distribution shape. In the fit, the sum of prompt and non-prompt signal yield are constrained by a Gaussian distribution. Fitting without the inclusive yield constraint is performed to estimate this uncertainty. The differences between the normal result in Section. 4.2.2 and these results are calculated, and the maximum value is considered as the systematic uncertainty from the $\log_{10} \chi_{\text{IP}}^2(D_{(s)}^+)$ fit. The uncertainties in this step are summarized in the Fig. 4.37 and Fig. 4.38 for D^+ and D_s^+ , respectively. For most of the bins, the systematic uncertainty on the $\log_{10} \chi_{\text{IP}}^2$ fit of D^+ (D^+) is less than 5% (10%).

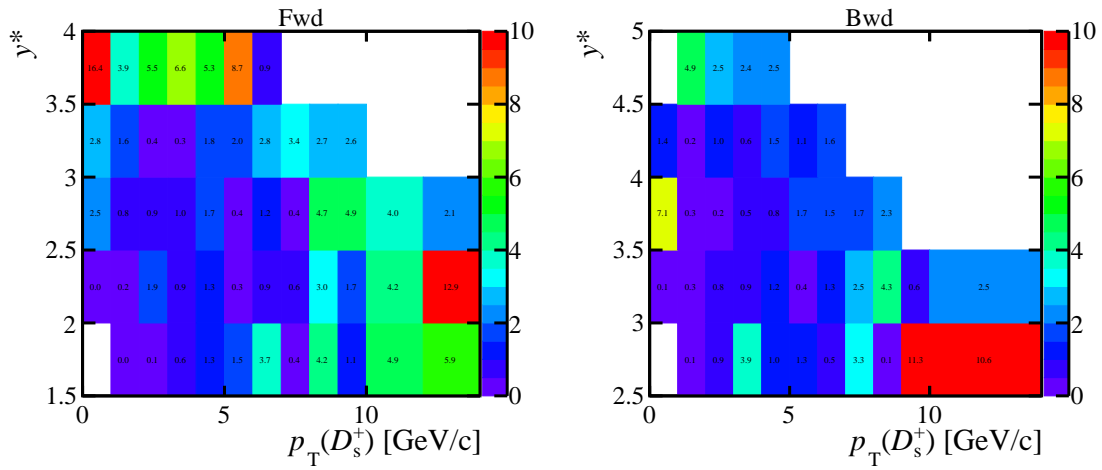


Figure 4.38 Relative systematic uncertainties (%) due to $\log_{10} \chi_{\text{IP}}^2(D_s^+)$ fit in bins of p_T and y^* in the forward (left) and backward (right) configurations.

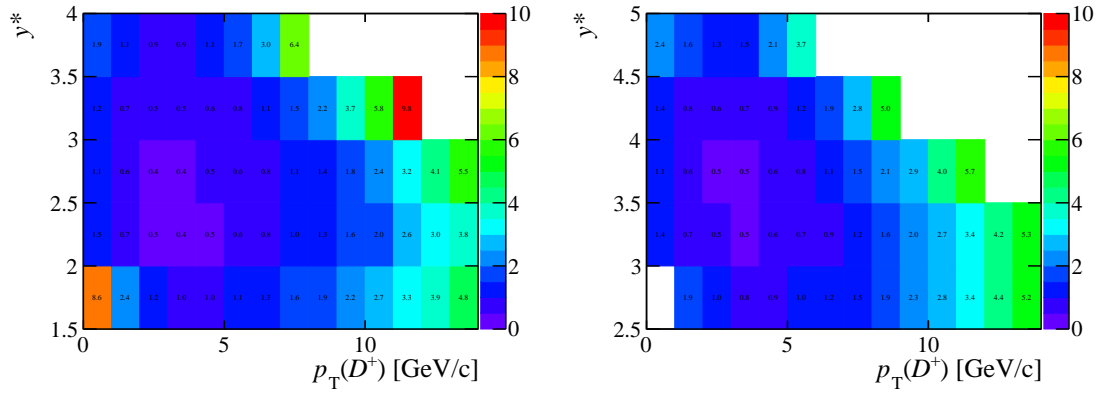


Figure 4.39 Relative systematic uncertainties (%) due to the limited simulation sample size of D^+ as a function of p_T and y^* in the forward (left) and backward (right) configurations.

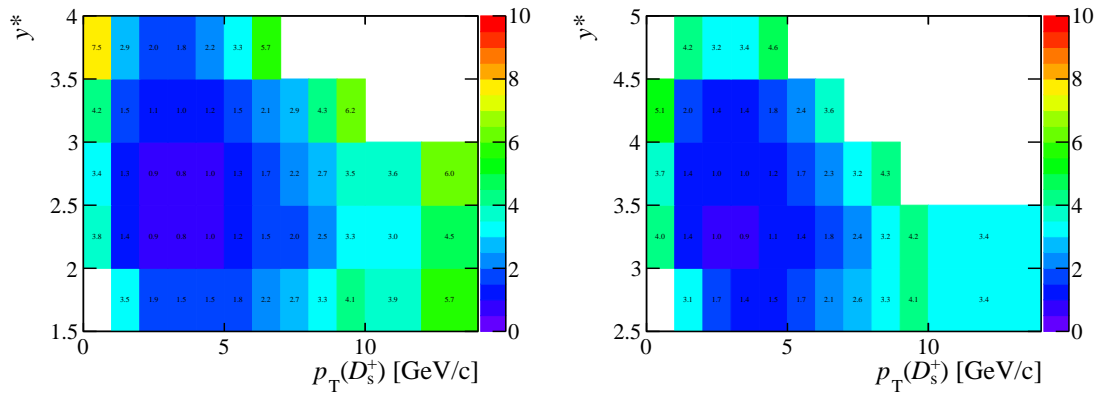


Figure 4.40 Relative systematic uncertainties (%) due to the limited simulation sample size of D_s^+ as a function of p_T and y^* in the forward (left) and backward (right) configurations.

4.7.2 Simulation sample size uncertainty

In the estimation of the efficiency (ϵ_{acc} , $\epsilon_{\text{rec\&sel}}$ and ϵ_{PID}), the results are given with error bars, which are treated as the uncertainties due to limited simulation sample size, shown in Fig. 4.39 and Fig 4.40. Limited statistics in the simulated samples result in uncertainties to efficiency calculation. These uncertainties finally are propagated to the cross-section determination which seems negligible ($\sim 0.4\%$) for mid-kinematic bins, but relatively large ($\sim 10\%$) in acceptance boundary bins.

4.7.3 Kinematic distribution

Since the efficiency (ϵ_{acc} , $\epsilon_{\text{rec\&sel}}$ and ϵ_{PID}) is evaluated as a function of $D_{(s)}^+$ transverse momentum p_T and rapidity y^* , the discrepancy between the p_T or y^* distributions of the data and MC samples will lead to bias in efficiency.

This impact, if any, is significantly reduced because the ‘‘double differential’’ cross-section is measured, which implies all efficiencies are estimated in small (p_T, y^*) bins and

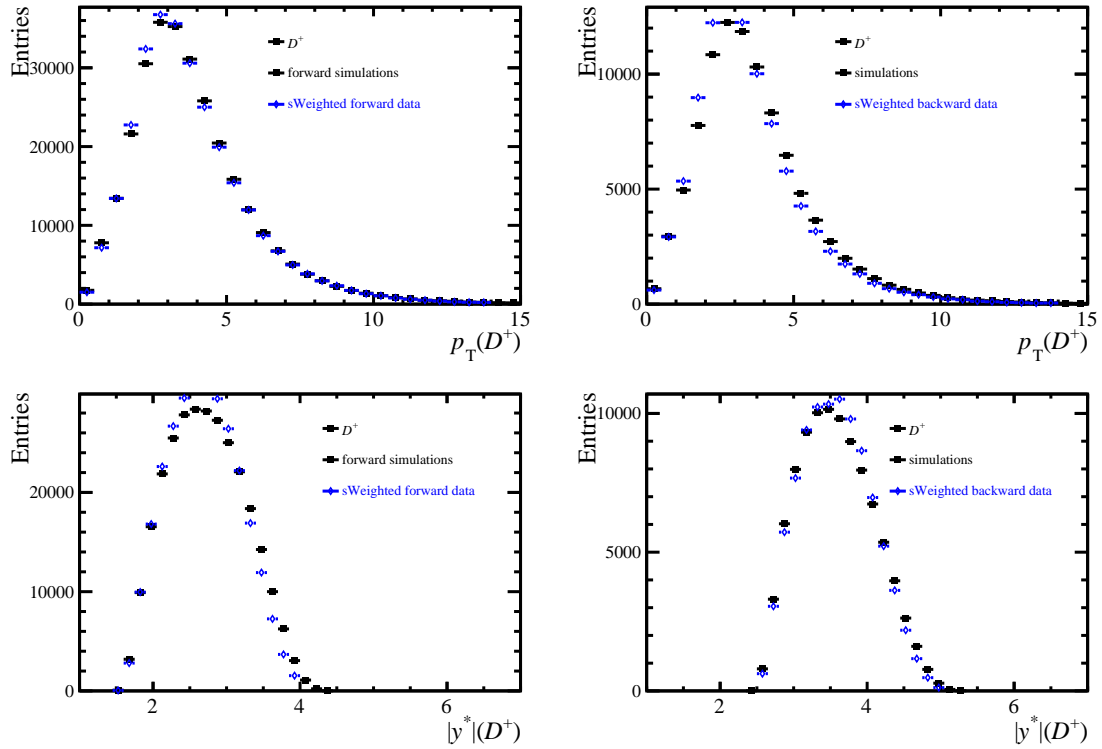


Figure 4.41 Comparisons of p_T and y^* distributions between D^+ data and MC samples in the forward (left) and backward (right) configurations.

the kinematic distribution of the data is almost the same as that of the MC. As can be seen from Fig. 4.41, unlike in the case of multiplicity, the p_T and y^* distributions in the D^+ data are well simulated by the MC sample.

We calculate the $p_T - y^*$ two-dimensional weights, to make p_T and y^* distribution of MC sample almost same as that of data. The $p_T - y^*$ weights are estimated by the ratio of $D_{(s)}^+$ data distribution in (p_T, y^*) bins over the MC distribution in the same bins whose p_T bin width is less than 1 GeV and y^* bin width is less than 0.5. When calculating the acceptance efficiency and PID efficiency, we correct the p_T and y^* distributions of simulation sample with the above weights. There seems no difference between the efficiency (ϵ_{acc} , $\epsilon_{\text{rec\&sel}}$ and ϵ_{PID}) with and without kinematic distribution corrections. It was found that this effect was ultimately negligible ($\ll 1\%$).

4.7.4 Tracking and multiplicity correction

As mentioned in Section. 4.4.2, the tracking efficiency in the simulated samples is corrected by the tracking table (2012), which compensates for the difference in tracking efficiency between the data and MC. The uncertainty arising from the correction factors in this table is negligible. The tracking efficiency difference in data/MC is investigated with

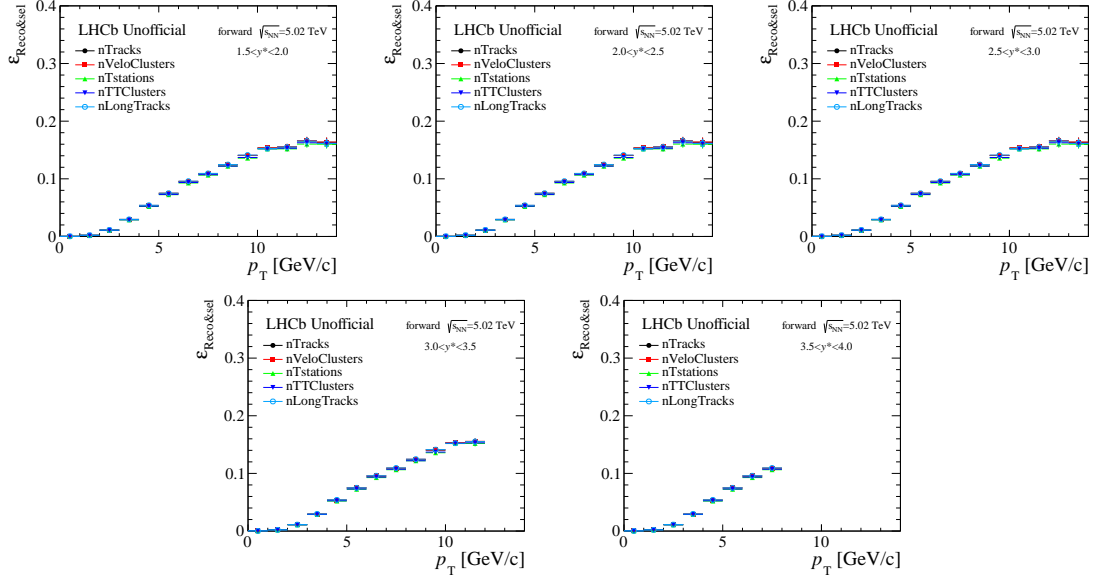


Figure 4.42 The D^+ reconstruction and selection efficiencies in each p_T and y^* bin corrected by five multiplicities (nTracks, nVeloClusters, nTstations, nTTClusters and nLongTracks) in the forward configuration, respectively.

muons from $J/\psi \rightarrow \mu^- \mu^+$ decays. Because of the hadronic interactions of these particles with the detector, an extra uncertainty of 1.1% (1.4%) is attributed to the $K(\pi)$ track. The material budget dominates this uncertainty and a full correlation between the K and π is assumed, providing a total uncertainty of 3.9% (3.6%) for D^+ (D_s^+).

As described in Section. 4.4.3, there are five multiplicity variables (nTracks, nVeloClusters, nTstations, nTTClusters and nLongTracks) that are used to correct for reconstruction and selection efficiency.

Fig. 4.42 and Fig. 4.43 show all results for the reconstruction and selection efficiency of prompt D^+ corrected with one of the multiplicity variables in the forward and backward rapidity regions, respectively. Fig. 4.44 and Fig. 4.45 show all results for the reconstruction and selection efficiency of prompt D_s^+ corrected with one of the multiplicity variables in the forward and backward rapidity regions, respectively. These comparisons of D^+ and D_s^+ demonstrate that the correction factors obtained using different variables are consistent within the uncertainty range. As a result, the final correction factor is the average of the five corrections, and the systematic uncertainty is their standard deviation to fully account for the effects of these variables, as summarized in Appendix A.4. Typically, this systematic uncertainty does not exceed 3% for most bins in the forward rapidity region, and 5% for most bins in the backward rapidity region.

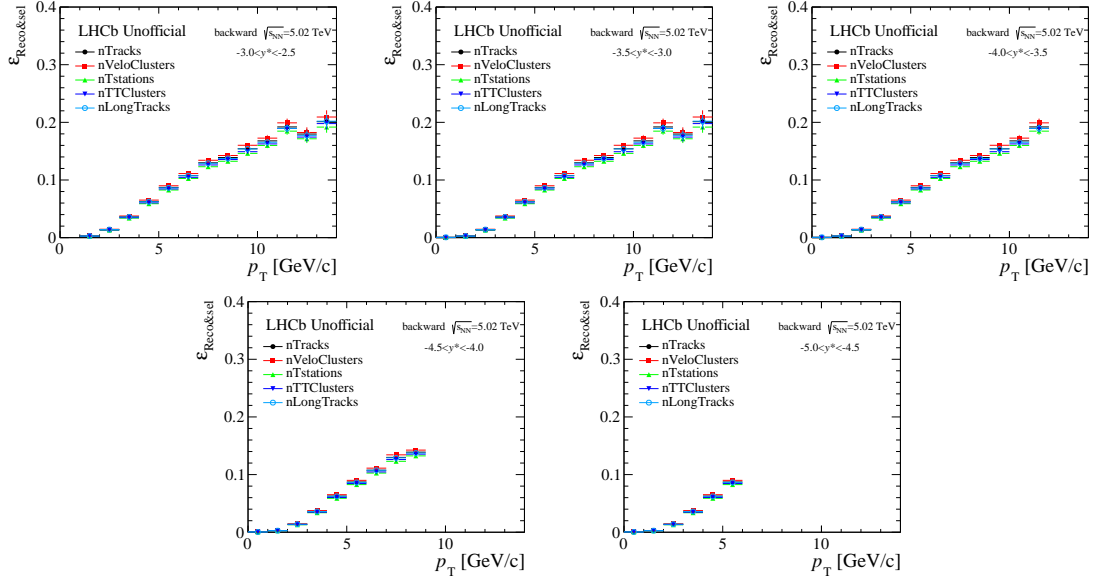


Figure 4.43 The D^+ reconstruction and selection efficiencies in each p_T and y^* bin corrected by five multiplicities (nTracks, nVeloClusters, nTstations, nTTClusters and nLongTracks) in the backward configuration, respectively.

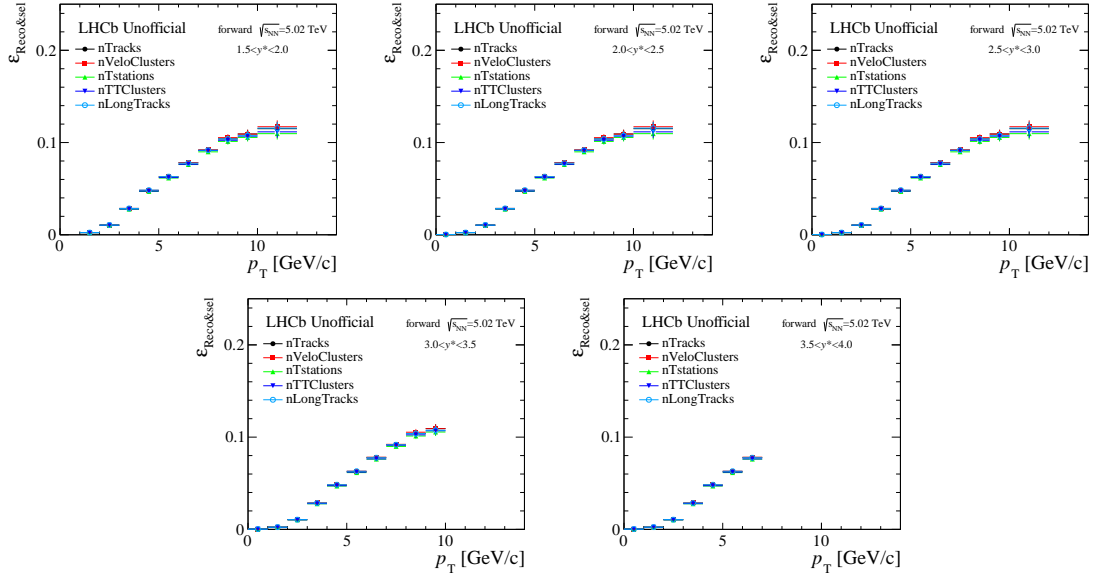


Figure 4.44 The D_s^+ reconstruction and selection efficiencies in each p_T and y^* bin corrected by five multiplicities (nTracks, nVeloClusters, nTstations, nTTClusters and nLongTracks) in the forward configuration, respectively.

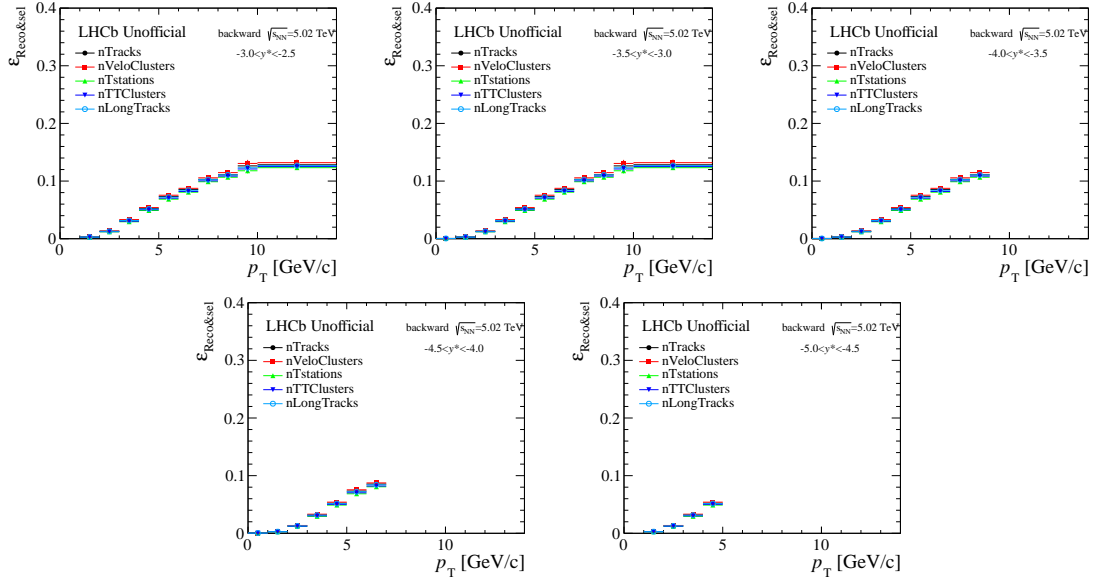


Figure 4.45 The D_s^+ reconstruction and selection efficiencies in each p_T and y^* bin corrected by five multiplicities (nTracks, nVeloClusters, nTstations, nTTClusters and nLongTracks) in the backward configuration, respectively.

4.7.5 PID calibration table

Using the track calibration approach, the PID efficiency is determined by the K and π single-track efficiencies convoluted with the kinematic distributions of simulation in each $D_{(s)}^+ (p_T, y^*)$ bin. The single-track efficiency is calculated with the D^0 calibration sample. With respect to the track calibration method, there are two primary sources of systematic uncertainties: the one caused by limited statistics of the calibration sample and the one caused by the binning scheme used to determine single-track efficiency.

The one resulting from insufficient statistics in the calibration sample is fundamentally connected to the number of calibration tracks and is investigated using a toy MC method. The single-track efficiency in each (p, η) bin is varied individually based on a Gaussian function, whose mean and sigma taken as nominal value and error, and the fluctuation of the consequent PID efficiency is studied. By repeating the procedure 500 times, a collective set of new PID efficiencies is obtained, and the distribution of these new efficiencies is used to estimate this systematic uncertainty. The outcome efficiency distribution is fitted with a Gaussian function for each $D_{(s)}^+ (p_T, y^*)$ bin, and the width of the Gaussian function is taken as the systematic uncertainty from the first source.

The one raised from the binning scheme is investigated by using alternate binning schemes for the single-track efficiency determination. In contrast to the normal binning scheme of 9 p bins and 6 η bins, two alternative binning schemes same as previous D^0 analysis^[91], i.e. more p bins (14) fewer η bins (4), and fewer p bins (6) bins and more η bins (9) are employed.

- The alternative binning scheme of more p bins and fewer η bins for K and π :
 - p [GeV/ c] : [3.2, 7, 12, 15, 18, 22, 25, 29, 34, 40, 46, 53, 71, 84, 100];
 - η : [2.0, 2.8, 3.5, 4.2, 5.0];
- The alternative binning scheme of fewer p bins and more η bins for K and π :
 - p [GeV/ c] : [3.2, 13, 20, 29, 40, 60, 100];
 - η : [2.0, 2.4, 2.7, 3.0, 3.2, 3.5, 3.8, 4.1, 4.5, 5.0];

The new efficiency is determined using these two alternative binning schemes, and the maximum variation from the normal PID efficiency is taken as the system uncertainty from the second source. The total PID systematic uncertainty in the track calibration method is a quadratic sum of the two sources. As p_T decreases or increases, the uncertainty of PID efficiency typically grows, with values ranging from as little as 1% to over 10%.

4.7.6 Other systematic uncertainties

For the forward and backward data samples, the relative uncertainty of luminosity is 1.86% and 2.13%^[93], respectively. The uncertainty of the branching fraction $\mathcal{B}(D^+ \rightarrow K^- \pi^+ \pi^+)$ is 1.7%, obtained from PDG^[8], and the uncertainty of the branching fraction $\mathcal{B}(D_s^+ \rightarrow K^- K^+ \pi^+)$ is 5.8%, obtained from CLEO collaboration^[159]. Both uncertainties from luminosity and branching fractions are fully correlated in all (p_T , y^*) bins.

4.7.7 Summary of systematic uncertainties

The relative systematic uncertainties considered for prompt $D_{(s)}^+$ differential cross-sections are summarized in Table. 4.5. The sources of systematic uncertainty may be divided into two groups: uncertainties from tracking and multiplicity correction, PID efficiency, luminosity and branching fractions are correlated between kinematic bins and are summed linearly; uncertainties from signal determination, MC sample size are uncorrelated between kinematic bins and are summed in quadrature.

Table 4.5 Summary of systematic and statistical uncertainties (%).

| Source | $D^+ \rightarrow K^- \pi^+ \pi^+$ | | $D_s^+ \rightarrow K^- K^+ \pi^+$ | |
|--|-----------------------------------|----------|-----------------------------------|----------|
| | Forward | Backward | Forward | Backward |
| <i>Correlated between bins</i> | | | | |
| Multiplicity correction | 0.4-2.3 | 1.8-4.3 | 0.4-2.4 | 2.1-5.0 |
| Hadronic interactions | 3.9 | 3.9 | 3.6 | 3.6 |
| PID efficiency | 0.3-18.4 | 0.6-9.7 | 0.6-11.8 | 1.1-16.1 |
| Luminosity | 1.9 | 2.1 | 1.9 | 2.1 |
| Branching fraction | 1.7 | 1.7 | 5.8 | 5.8 |
| <i>Uncorrelated between bins</i> | | | | |
| Mass fits | 0.1-3.7 | 0.1-7.0 | 0-5.2 | 0-9.6 |
| $\log_{10} \chi_{\text{IP}}^2(D_{(s)}^+)$ fits | 0-8.0 | 0.1-4.7 | 0-16.4 | 0.1-11.3 |
| MC sample size | 0.4-9.8 | 0.5-5.7 | 0.8-7.5 | 0.9-5.1 |
| Statistical uncertainty | 1-18 | 0-18 | 3-29 | 4-25 |

CHAPTER 5 RESULTS

5.1 Open charm production cross-sections

The double-differential cross-sections of prompt D^+ (D_s^+), as a function of p_T and y^* in proton-lead collisions at $\sqrt{s_{NN}} = 5.02$ TeV for forward and backward rapidities are shown in Fig. 5.1 (Fig. 5.2) and summarized in Tab. 5.1 (Tab. 5.2). There are no measurements in some low p_T or high y^* bins due to the low reconstruction efficiency and lack of statistics.

In 2019, the open charm productions in proton-lead collisions were measured at ALICE in mid-rapidity $-0.96 < y^* < 0.04$ with transverse momentum in the ranges of $1 < p_T < 36$ GeV/c and $2 < p_T < 24$ GeV/c for D^+ and D_s^+ [90], respectively. Compared to the kinematic range measured at ALICE, the double-differential cross-sections of prompt D^+ and D_s^+ are accurately determined at LHCb with a lower transverse momentum and a much wider range of rapidity.

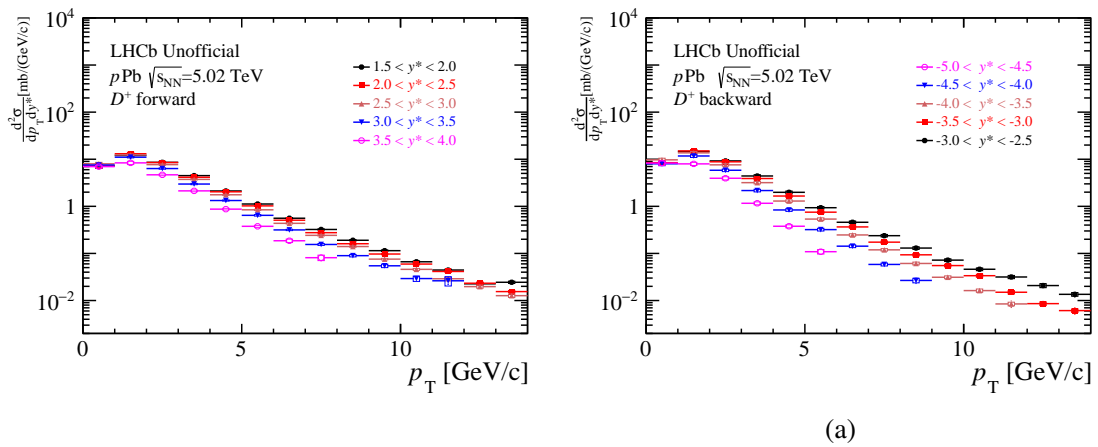


Figure 5.1 Double-differential cross-section of prompt D^+ mesons in proton-lead collisions at $\sqrt{s_{NN}} = 5.02$ TeV for the forward (left) and backward (right) rapidities. The error bar is the statistical uncertainty and the box represents the systematic uncertainty.

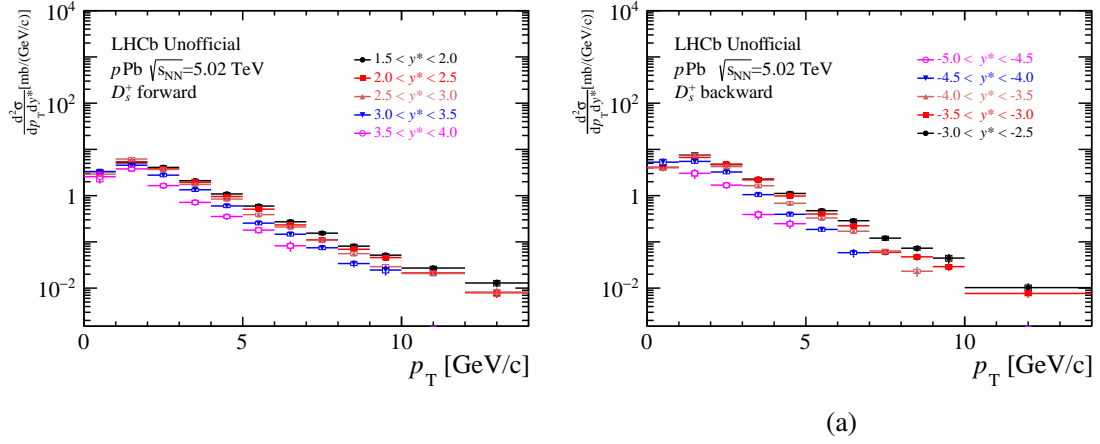


Figure 5.2 Double-differential cross-section of prompt D_s^+ mesons in proton-lead collisions at $\sqrt{s_{\text{NN}}} = 5.02$ TeV for the forward (left) and backward (right) rapidities. The error bar is the statistical uncertainty and the box represents the systematic uncertainty.

Table 5.1 Data values of the double-differential cross-section (mb) of prompt D^+ in proton-lead collisions at $\sqrt{s_{\text{NN}}} = 5.02$ TeV in each (p_T, y^*) bin for forward and backward rapidities. The first uncertainty reflects statistical uncertainty, the second represents uncorrelated systematic uncertainty between bins, and the third represents correlated uncertainty.

| Forward | | | | | |
|---------------|--|--|--|--|---------------------------------------|
| p_T [GeV/c] | $1.5 < y^* < 2.0$ | $2.0 < y^* < 2.5$ | $2.5 < y^* < 3.0$ | $3.0 < y^* < 3.5$ | $3.5 < y^* < 4.0$ |
| [0, 1] | $7.195 \pm 1.100 \pm 0.676 \pm 0.445$ | $7.232 \pm 0.199 \pm 0.122 \pm 0.358$ | $7.986 \pm 0.144 \pm 0.092 \pm 0.409$ | $7.533 \pm 0.152 \pm 0.105 \pm 0.376$ | $6.974 \pm 0.204 \pm 0.316 \pm 0.387$ |
| [1, 2] | $12.016 \pm 0.484 \pm 0.293 \pm 0.617$ | $13.074 \pm 0.152 \pm 0.107 \pm 0.634$ | $12.321 \pm 0.111 \pm 0.093 \pm 0.587$ | $11.051 \pm 0.114 \pm 0.098 \pm 0.556$ | $8.368 \pm 0.165 \pm 0.544 \pm 0.458$ |
| [2, 3] | $8.591 \pm 0.167 \pm 0.113 \pm 0.426$ | $8.509 \pm 0.066 \pm 0.056 \pm 0.405$ | $7.685 \pm 0.052 \pm 0.053 \pm 0.371$ | $6.342 \pm 0.051 \pm 0.072 \pm 0.307$ | $4.669 \pm 0.071 \pm 0.053 \pm 0.237$ |
| [3, 4] | $4.487 \pm 0.070 \pm 0.047 \pm 0.228$ | $4.143 \pm 0.032 \pm 0.027 \pm 0.200$ | $3.733 \pm 0.026 \pm 0.026 \pm 0.177$ | $2.973 \pm 0.026 \pm 0.048 \pm 0.144$ | $2.129 \pm 0.036 \pm 0.049 \pm 0.110$ |
| [4, 5] | $2.119 \pm 0.034 \pm 0.023 \pm 0.107$ | $2.035 \pm 0.018 \pm 0.015 \pm 0.099$ | $1.759 \pm 0.015 \pm 0.014 \pm 0.085$ | $1.328 \pm 0.015 \pm 0.012 \pm 0.062$ | $0.872 \pm 0.021 \pm 0.026 \pm 0.045$ |
| [5, 6] | $1.120 \pm 0.020 \pm 0.013 \pm 0.055$ | $1.022 \pm 0.011 \pm 0.009 \pm 0.048$ | $0.843 \pm 0.010 \pm 0.008 \pm 0.041$ | $0.644 \pm 0.010 \pm 0.014 \pm 0.033$ | $0.376 \pm 0.014 \pm 0.012 \pm 0.019$ |
| [6, 7] | $0.559 \pm 0.012 \pm 0.011 \pm 0.030$ | $0.508 \pm 0.007 \pm 0.006 \pm 0.025$ | $0.436 \pm 0.007 \pm 0.008 \pm 0.021$ | $0.316 \pm 0.007 \pm 0.005 \pm 0.015$ | $0.186 \pm 0.013 \pm 0.006 \pm 0.010$ |
| [7, 8] | $0.323 \pm 0.009 \pm 0.005 \pm 0.016$ | $0.276 \pm 0.005 \pm 0.003 \pm 0.013$ | $0.242 \pm 0.005 \pm 0.005 \pm 0.012$ | $0.155 \pm 0.005 \pm 0.004 \pm 0.008$ | $0.081 \pm 0.013 \pm 0.006 \pm 0.006$ |
| [8, 9] | $0.190 \pm 0.006 \pm 0.004 \pm 0.009$ | $0.161 \pm 0.004 \pm 0.003 \pm 0.007$ | $0.140 \pm 0.004 \pm 0.003 \pm 0.007$ | $0.090 \pm 0.004 \pm 0.002 \pm 0.005$ | – |
| [9, 10] | $0.114 \pm 0.005 \pm 0.003 \pm 0.005$ | $0.097 \pm 0.003 \pm 0.002 \pm 0.005$ | $0.076 \pm 0.003 \pm 0.002 \pm 0.004$ | $0.055 \pm 0.004 \pm 0.002 \pm 0.003$ | – |
| [10, 11] | $0.066 \pm 0.003 \pm 0.003 \pm 0.003$ | $0.059 \pm 0.002 \pm 0.001 \pm 0.003$ | $0.046 \pm 0.002 \pm 0.002 \pm 0.002$ | $0.029 \pm 0.003 \pm 0.002 \pm 0.001$ | – |
| [11, 12] | $0.044 \pm 0.003 \pm 0.002 \pm 0.002$ | $0.041 \pm 0.002 \pm 0.001 \pm 0.002$ | $0.029 \pm 0.002 \pm 0.001 \pm 0.001$ | $0.026 \pm 0.005 \pm 0.003 \pm 0.002$ | – |
| [12, 13] | $0.023 \pm 0.002 \pm 0.001 \pm 0.001$ | $0.023 \pm 0.001 \pm 0.001 \pm 0.001$ | $0.020 \pm 0.001 \pm 0.001 \pm 0.001$ | – | – |
| [13, 14] | $0.024 \pm 0.002 \pm 0.001 \pm 0.001$ | $0.015 \pm 0.001 \pm 0.001 \pm 0.001$ | $0.013 \pm 0.001 \pm 0.001 \pm 0.001$ | – | – |
| Backward | | | | | |
| p_T [GeV/c] | $-3.0 < y^* < -2.5$ | $-3.5 < y^* < -3.0$ | $-4.0 < y^* < -3.5$ | $-4.5 < y^* < -4.0$ | $-5.0 < y^* < -4.5$ |
| [0, 1] | – | $8.264 \pm 0.005 \pm 0.399 \pm 0.538$ | $9.504 \pm 0.250 \pm 0.473 \pm 0.622$ | $7.856 \pm 0.267 \pm 0.377 \pm 0.576$ | $8.146 \pm 0.415 \pm 0.600 \pm 0.660$ |
| [1, 2] | $14.233 \pm 0.726 \pm 0.347 \pm 0.730$ | $14.718 \pm 0.242 \pm 0.121 \pm 0.714$ | $13.407 \pm 0.186 \pm 0.101 \pm 0.639$ | $11.533 \pm 0.200 \pm 0.103 \pm 0.580$ | $7.859 \pm 0.310 \pm 0.511 \pm 0.430$ |
| [2, 3] | $9.003 \pm 0.218 \pm 0.118 \pm 0.446$ | $8.651 \pm 0.100 \pm 0.057 \pm 0.412$ | $7.473 \pm 0.081 \pm 0.051 \pm 0.361$ | $5.742 \pm 0.080 \pm 0.065 \pm 0.278$ | $3.887 \pm 0.121 \pm 0.044 \pm 0.197$ |
| [3, 4] | $4.326 \pm 0.090 \pm 0.045 \pm 0.220$ | $3.830 \pm 0.046 \pm 0.025 \pm 0.185$ | $3.133 \pm 0.038 \pm 0.022 \pm 0.148$ | $2.132 \pm 0.036 \pm 0.035 \pm 0.104$ | $1.146 \pm 0.050 \pm 0.026 \pm 0.059$ |
| [4, 5] | $1.948 \pm 0.044 \pm 0.021 \pm 0.098$ | $1.627 \pm 0.024 \pm 0.012 \pm 0.079$ | $1.275 \pm 0.020 \pm 0.010 \pm 0.062$ | $0.826 \pm 0.019 \pm 0.007 \pm 0.039$ | $0.372 \pm 0.025 \pm 0.011 \pm 0.019$ |
| [5, 6] | $0.920 \pm 0.024 \pm 0.011 \pm 0.045$ | $0.741 \pm 0.015 \pm 0.006 \pm 0.035$ | $0.528 \pm 0.012 \pm 0.005 \pm 0.026$ | $0.316 \pm 0.011 \pm 0.007 \pm 0.016$ | $0.107 \pm 0.016 \pm 0.003 \pm 0.005$ |
| [6, 7] | $0.452 \pm 0.015 \pm 0.008 \pm 0.025$ | $0.360 \pm 0.009 \pm 0.004 \pm 0.018$ | $0.244 \pm 0.008 \pm 0.005 \pm 0.012$ | $0.141 \pm 0.008 \pm 0.002 \pm 0.007$ | – |
| [7, 8] | $0.235 \pm 0.010 \pm 0.004 \pm 0.012$ | $0.171 \pm 0.006 \pm 0.002 \pm 0.008$ | $0.117 \pm 0.005 \pm 0.003 \pm 0.006$ | $0.058 \pm 0.005 \pm 0.001 \pm 0.003$ | – |
| [8, 9] | $0.128 \pm 0.007 \pm 0.003 \pm 0.006$ | $0.092 \pm 0.004 \pm 0.002 \pm 0.004$ | $0.060 \pm 0.004 \pm 0.001 \pm 0.003$ | $0.026 \pm 0.004 \pm 0.001 \pm 0.002$ | – |
| [9, 10] | $0.071 \pm 0.005 \pm 0.002 \pm 0.003$ | $0.054 \pm 0.003 \pm 0.001 \pm 0.003$ | $0.031 \pm 0.003 \pm 0.001 \pm 0.001$ | – | – |
| [10, 11] | $0.045 \pm 0.004 \pm 0.002 \pm 0.002$ | $0.033 \pm 0.003 \pm 0.001 \pm 0.002$ | $0.016 \pm 0.002 \pm 0.001 \pm 0.001$ | – | – |
| [11, 12] | $0.031 \pm 0.003 \pm 0.001 \pm 0.001$ | $0.015 \pm 0.002 \pm 0.000 \pm 0.001$ | $0.008 \pm 0.002 \pm 0.000 \pm 0.000$ | – | – |
| [12, 13] | $0.021 \pm 0.003 \pm 0.001 \pm 0.001$ | $0.008 \pm 0.001 \pm 0.000 \pm 0.000$ | – | – | – |
| [13, 14] | $0.013 \pm 0.002 \pm 0.001 \pm 0.001$ | $0.006 \pm 0.001 \pm 0.000 \pm 0.000$ | – | – | – |

CHAPTER 5 RESULTS

Table 5.2 Data values of the double-differential cross-section (mb) of prompt D_s^+ in proton-lead collisions at $\sqrt{s_{\text{NN}}} = 5.02$ TeV in each (p_T, y^*) bin for forward and backward rapidities. The first uncertainty reflects statistical uncertainty, the second represents uncorrelated systematic uncertainty between bins, and the third represents correlated uncertainty.

| Forward | | | | | |
|---------------|---------------------------------------|---------------------------------------|---------------------------------------|---------------------------------------|---------------------------------------|
| p_T [GeV/c] | $1.5 < y^* < 2.0$ | $2.0 < y^* < 2.5$ | $2.5 < y^* < 3.0$ | $3.0 < y^* < 3.5$ | $3.5 < y^* < 4.0$ |
| [0, 1] | – | $3.283 \pm 0.396 \pm 0.128 \pm 0.267$ | $2.916 \pm 0.324 \pm 0.122 \pm 0.221$ | $3.326 \pm 0.461 \pm 0.167 \pm 0.267$ | $2.564 \pm 0.749 \pm 0.463 \pm 0.356$ |
| [1, 2] | $5.121 \pm 0.532 \pm 0.181 \pm 0.460$ | $5.419 \pm 0.225 \pm 0.076 \pm 0.409$ | $6.188 \pm 0.215 \pm 0.097 \pm 0.454$ | $4.552 \pm 0.220 \pm 0.100 \pm 0.341$ | $3.786 \pm 0.379 \pm 0.195 \pm 0.303$ |
| [2, 3] | $4.079 \pm 0.222 \pm 0.079 \pm 0.346$ | $3.805 \pm 0.106 \pm 0.079 \pm 0.286$ | $3.683 \pm 0.094 \pm 0.045 \pm 0.275$ | $2.774 \pm 0.095 \pm 0.034 \pm 0.209$ | $1.644 \pm 0.150 \pm 0.096 \pm 0.127$ |
| [3, 4] | $2.101 \pm 0.095 \pm 0.036 \pm 0.157$ | $1.945 \pm 0.053 \pm 0.025 \pm 0.142$ | $1.752 \pm 0.046 \pm 0.024 \pm 0.127$ | $1.339 \pm 0.045 \pm 0.014 \pm 0.105$ | $0.715 \pm 0.065 \pm 0.050 \pm 0.054$ |
| [4, 5] | $1.087 \pm 0.053 \pm 0.022 \pm 0.082$ | $0.958 \pm 0.031 \pm 0.015 \pm 0.072$ | $0.844 \pm 0.026 \pm 0.017 \pm 0.065$ | $0.598 \pm 0.026 \pm 0.013 \pm 0.046$ | $0.354 \pm 0.035 \pm 0.021 \pm 0.025$ |
| [5, 6] | $0.595 \pm 0.032 \pm 0.014 \pm 0.046$ | $0.510 \pm 0.020 \pm 0.007 \pm 0.039$ | $0.388 \pm 0.017 \pm 0.005 \pm 0.028$ | $0.254 \pm 0.015 \pm 0.006 \pm 0.020$ | $0.180 \pm 0.029 \pm 0.018 \pm 0.014$ |
| [6, 7] | $0.272 \pm 0.020 \pm 0.012 \pm 0.020$ | $0.232 \pm 0.013 \pm 0.004 \pm 0.018$ | $0.210 \pm 0.012 \pm 0.004 \pm 0.015$ | $0.146 \pm 0.011 \pm 0.005 \pm 0.012$ | $0.082 \pm 0.021 \pm 0.005 \pm 0.008$ |
| [7, 8] | $0.154 \pm 0.014 \pm 0.004 \pm 0.011$ | $0.111 \pm 0.008 \pm 0.002 \pm 0.009$ | $0.108 \pm 0.008 \pm 0.002 \pm 0.008$ | $0.075 \pm 0.008 \pm 0.004 \pm 0.005$ | – |
| [8, 9] | $0.081 \pm 0.009 \pm 0.004 \pm 0.007$ | $0.069 \pm 0.006 \pm 0.003 \pm 0.005$ | $0.056 \pm 0.006 \pm 0.003 \pm 0.004$ | $0.034 \pm 0.006 \pm 0.002 \pm 0.003$ | – |
| [9, 10] | $0.052 \pm 0.007 \pm 0.002 \pm 0.004$ | $0.046 \pm 0.005 \pm 0.002 \pm 0.003$ | $0.029 \pm 0.004 \pm 0.002 \pm 0.003$ | $0.025 \pm 0.006 \pm 0.002 \pm 0.002$ | – |
| [10, 12] | $0.027 \pm 0.004 \pm 0.002 \pm 0.002$ | $0.021 \pm 0.003 \pm 0.001 \pm 0.002$ | $0.021 \pm 0.002 \pm 0.001 \pm 0.002$ | – | – |
| [12, 14] | $0.013 \pm 0.002 \pm 0.001 \pm 0.001$ | $0.008 \pm 0.002 \pm 0.001 \pm 0.001$ | $0.008 \pm 0.002 \pm 0.001 \pm 0.001$ | – | – |
| Backward | | | | | |
| p_T [GeV/c] | $-3.0 < y^* < -2.5$ | $-3.5 < y^* < -3.0$ | $-4.0 < y^* < -3.5$ | $-4.5 < y^* < -4.0$ | $-5.0 < y^* < -4.5$ |
| [0, 1] | – | $4.027 \pm 0.716 \pm 0.168 \pm 0.406$ | $3.906 \pm 0.653 \pm 0.313 \pm 0.355$ | $5.218 \pm 1.059 \pm 0.572 \pm 0.559$ | – |
| [1, 2] | $7.360 \pm 0.873 \pm 0.227 \pm 0.885$ | $6.558 \pm 0.400 \pm 0.099 \pm 0.589$ | $7.463 \pm 0.388 \pm 0.113 \pm 0.658$ | $5.414 \pm 0.414 \pm 0.110 \pm 0.479$ | $2.998 \pm 0.738 \pm 0.198 \pm 0.340$ |
| [2, 3] | $4.595 \pm 0.343 \pm 0.092 \pm 0.389$ | $4.708 \pm 0.190 \pm 0.065 \pm 0.388$ | $4.187 \pm 0.155 \pm 0.045 \pm 0.366$ | $3.204 \pm 0.175 \pm 0.057 \pm 0.272$ | $1.670 \pm 0.285 \pm 0.069 \pm 0.178$ |
| [3, 4] | $2.236 \pm 0.164 \pm 0.093 \pm 0.186$ | $2.158 \pm 0.084 \pm 0.029 \pm 0.184$ | $1.612 \pm 0.068 \pm 0.019 \pm 0.132$ | $1.036 \pm 0.064 \pm 0.016 \pm 0.086$ | $0.386 \pm 0.089 \pm 0.036 \pm 0.040$ |
| [4, 5] | $1.098 \pm 0.075 \pm 0.020 \pm 0.090$ | $0.969 \pm 0.048 \pm 0.017 \pm 0.078$ | $0.674 \pm 0.036 \pm 0.010 \pm 0.055$ | $0.390 \pm 0.034 \pm 0.009 \pm 0.032$ | $0.245 \pm 0.056 \pm 0.013 \pm 0.026$ |
| [5, 6] | $0.465 \pm 0.040 \pm 0.010 \pm 0.038$ | $0.395 \pm 0.026 \pm 0.006 \pm 0.037$ | $0.323 \pm 0.023 \pm 0.008 \pm 0.026$ | $0.184 \pm 0.021 \pm 0.005 \pm 0.015$ | – |
| [6, 7] | $0.283 \pm 0.027 \pm 0.007 \pm 0.023$ | $0.220 \pm 0.018 \pm 0.005 \pm 0.019$ | $0.168 \pm 0.016 \pm 0.005 \pm 0.013$ | $0.058 \pm 0.012 \pm 0.002 \pm 0.005$ | – |
| [7, 8] | $0.119 \pm 0.017 \pm 0.005 \pm 0.011$ | $0.058 \pm 0.009 \pm 0.002 \pm 0.005$ | $0.063 \pm 0.010 \pm 0.002 \pm 0.005$ | – | – |
| [8, 9] | $0.072 \pm 0.011 \pm 0.002 \pm 0.006$ | $0.047 \pm 0.008 \pm 0.004 \pm 0.004$ | $0.023 \pm 0.006 \pm 0.001 \pm 0.002$ | – | – |
| [9, 10] | $0.044 \pm 0.010 \pm 0.005 \pm 0.004$ | $0.029 \pm 0.006 \pm 0.001 \pm 0.003$ | – | – | – |
| [10, 14] | $0.010 \pm 0.002 \pm 0.001 \pm 0.001$ | $0.008 \pm 0.001 \pm 0.000 \pm 0.001$ | – | – | – |

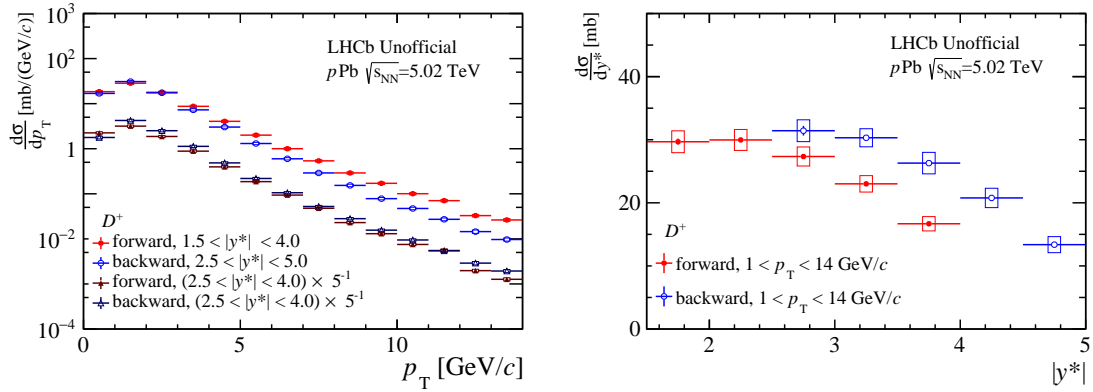


Figure 5.3 One-dimensional cross-section of prompt D^+ as a function of p_T (left) or y^* (right) in the forward and backward configurations.

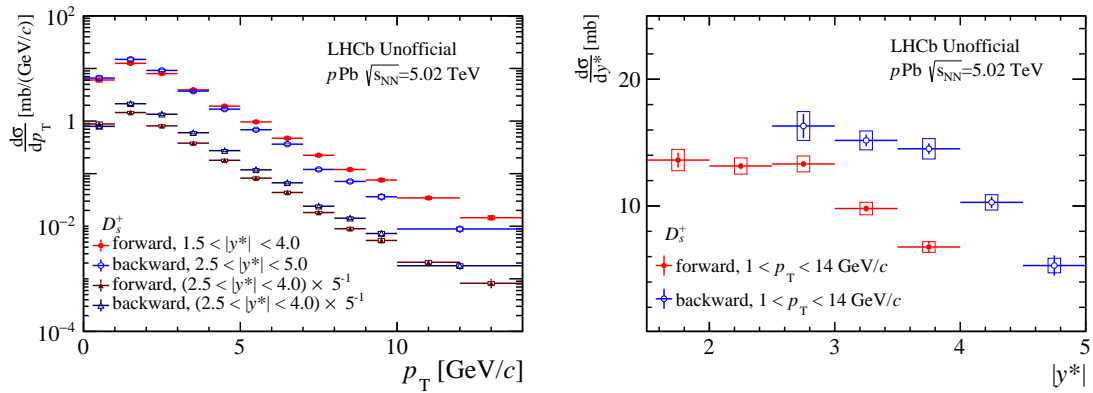


Figure 5.4 One-dimensional cross-section of prompt D_s^+ as a function of p_T (left) or y^* (right) in the forward and backward configurations.

As shown in Fig. 5.3 (Fig. 5.4) and summarized in Appendix A.6, the one-dimensional prompt D^+ (D_s^+) cross-sections are measured as a function of p_T or y^* in the full forward rapidity range ($1.5 < y^* < 4.0$) and backward range ($-5.0 < y^* < -2.5$)^① (^②), as well as in the common rapidity range ($2.5 < |y^*| < 4.0$). As shown in these figures, the cross-section first rises and subsequently falls with the increasing p_T , peaking roughly in the range of $1 < p_T < 2$ GeV/c, and it almost stays constant for $|y^*| < 3$ and drops quickly at larger $|y^*|$.

① The integrated regions of D^+ are $1.5 < y^* < 3.5$ for $8 < p_T < 12$ GeV/c, and $1.5 < y^* < 3.0$ for $12 < p_T < 14$ GeV/c in forward configurations; the integrated regions of D^+ are $-5.0 < y^* < -3.0$ for $0 < p_T < 1$ GeV/c, $-4.5 < y^* < -2.5$ for $6 < p_T < 9$ GeV/c, $-4.0 < y^* < -2.5$ for $9 < p_T < 12$ GeV/c, $-3.5 < y^* < -2.5$ for $12 < p_T < 14$ GeV/c in backward configurations. This applied for all the one-dimensional integrated cross-sections in Section. 5.1.

② The integrated regions of D_s^+ are $2.0 < y^* < 4.0$ for $0 < p_T < 1$ GeV/c, $1.5 < y^* < 3.5$ for $7 < p_T < 10$ GeV/c, $1.5 < y^* < 3.0$ for $10 < p_T < 14$ GeV/c in forward configurations; the integrated regions of D_s^+ are $-4.5 < y^* < -2.5$ for $0 < p_T < 1$ GeV/c, $-4.5 < y^* < -2.5$ for $5 < p_T < 7$ GeV/c, $-4.0 < y^* < -2.0$ for $7 < p_T < 9$ GeV/c, $-3.5 < y^* < -2.5$ for $9 < p_T < 14$ GeV/c in backward configurations. This applied for all the one-dimensional integrated cross-sections in Section. 5.1.

The integrated cross-sections of prompt $D_{(s)}^+$ in $p\text{Pb}$ forward configuration in the defined fiducial region, summing over the bins in this analysis, are

$$\sigma(D^+)_{\text{Fwd}}(1 < p_{\text{T}} < 10 \text{ GeV}/c, 1.5 < y^* < 4.0) = 63.1 \pm 0.3(\text{stat.}) \pm 3.6(\text{syst.}) \text{ mb},$$

$$\sigma(D^+)_{\text{Fwd}}(1 < p_{\text{T}} < 10 \text{ GeV}/c, 2.5 < y^* < 4.0) = 33.5 \pm 0.1(\text{stat.}) \pm 1.9(\text{syst.}) \text{ mb},$$

$$\sigma(D_s^+)_{\text{Fwd}}(1 < p_{\text{T}} < 10 \text{ GeV}/c, 1.5 < y^* < 4.0) = 28.2 \pm 0.4(\text{stat.}) \pm 1.5(\text{syst.}) \text{ mb},$$

$$\sigma(D_s^+)_{\text{Fwd}}(1 < p_{\text{T}} < 10 \text{ GeV}/c, 2.5 < y^* < 4.0) = 14.9 \pm 0.3(\text{stat.}) \pm 0.7(\text{syst.}) \text{ mb}.$$

The first error is statistical, whereas the second is systematic.

The integrated cross-sections of prompt $D_{(s)}^+$ in $p\text{Pb}$ backward data in the defined fiducial region, summing over the bins in this analysis, are

$$\sigma(D^+)_{\text{Bwd}}(1 < p_{\text{T}} < 10 \text{ GeV}/c, -5.0 < y^* < -2.5) = 60.8 \pm 0.5(\text{stat.}) \pm 3.8(\text{syst.}) \text{ mb},$$

$$\sigma(D^+)_{\text{Bwd}}(1 < p_{\text{T}} < 10 \text{ GeV}/c, -4.0 < y^* < -2.5) = 44.0 \pm 0.4(\text{stat.}) \pm 2.7(\text{syst.}) \text{ mb},$$

$$\sigma(D_s^+)_{\text{Bwd}}(1 < p_{\text{T}} < 10 \text{ GeV}/c, -5.0 < y^* < -2.5) = 30.8 \pm 0.7(\text{stat.}) \pm 1.8(\text{syst.}) \text{ mb},$$

$$\sigma(D_s^+)_{\text{Bwd}}(1 < p_{\text{T}} < 10 \text{ GeV}/c, -4.0 < y^* < -2.5) = 23.0 \pm 0.6(\text{stat.}) \pm 1.4(\text{syst.}) \text{ mb}.$$

The first error is statistical, whereas the second is systematic.

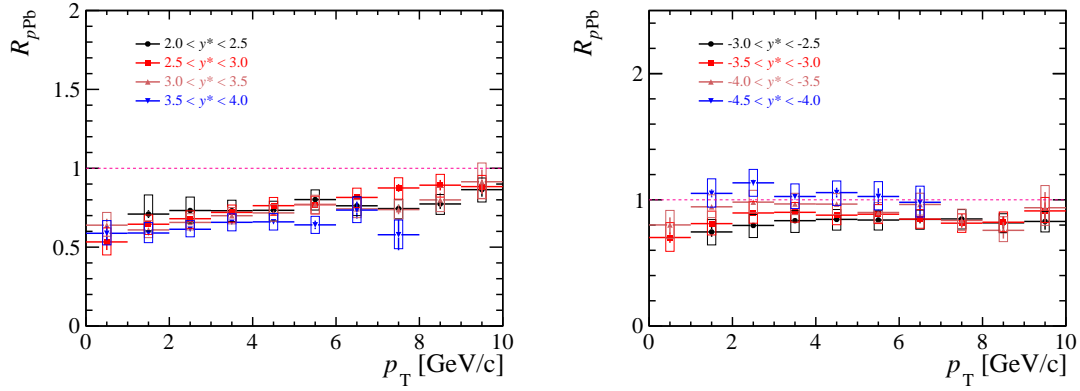


Figure 5.5 Prompt D^+ nuclear modification factors as a function of p_T in the forward (left) and backward (right) rapidity bins. The error bar on each data point denotes the statistical uncertainty, whereas the box represents the systematic uncertainty.

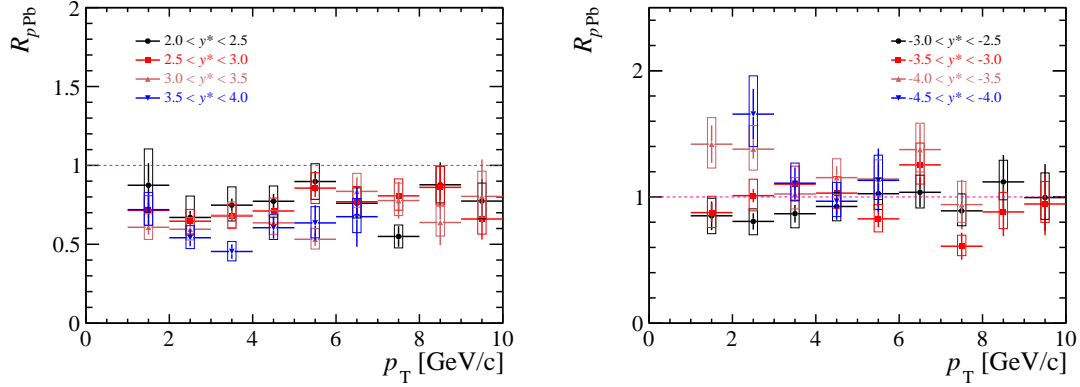


Figure 5.6 Prompt D_s^+ nuclear modification factors as a function of p_T in the forward (left) and backward (right) rapidity bins. The error bar on each data point denotes the statistical uncertainty, whereas the box represents the systematic uncertainty.

5.2 Nuclear modification factors

The calculations of the nuclear modification factors, R_{pPb} , for D^+ and D_s^+ needs the corresponding production cross-sections in pp collisions at $\sqrt{s} = 5.02$ TeV, which have been measured previously by LHCb^[30] within a rapidity range of $2.0 < y$ (or y^*) < 4.5 . The correlations between the uncertainties of pp and pPb measurements should be considered in the estimations of R_{pPb} uncertainties. In this analysis, the uncertainties originating from branching fractions and hadronic interactions with detector materials are fully correlated, whereas the rest uncertainties are uncorrelated. The uncertainty propagation formula for the numerator-denominator correlation components of the ratios (R_{pPb} , R_{FB} , R_{D^+/D^0} , $R_{D_s^+/D^0}$ and $R_{D_s^+/D^+}$) are discussed specifically in Appendix A.7.

The nuclear modification factors as a function of p_T in different y^* bins for prompt D^+ (D_s^+) are presented in Fig. 5.5 (Fig. 5.6). After integrating over the common rapidity ranges of $2.0 < y^* < 4.0$ and $-4.5 < y^* < -2.5$, the nuclear modification factors as

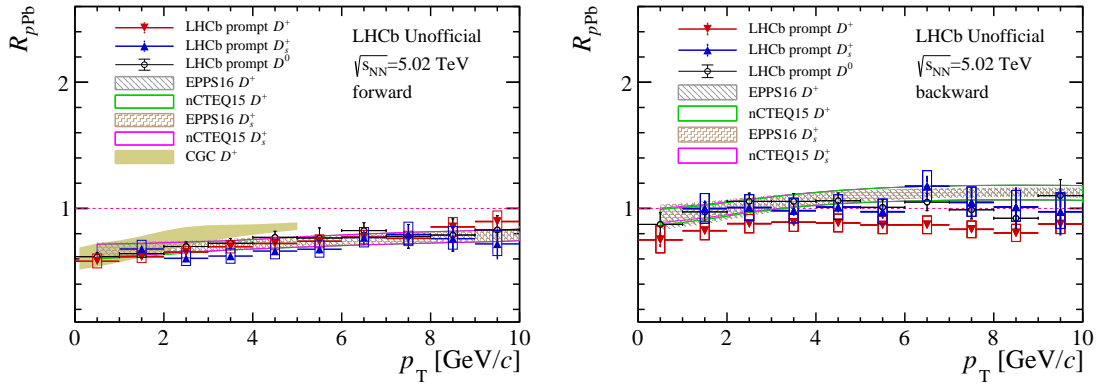


Figure 5.7 Nuclear modification factor R_{pPb} for prompt D^+ and D_s^+ as a function of p_T for the forward (left) and backward (right) data samples, integrated over the common rapidity range of $2.0 < y^* < 4.0$ (left) and $-4.5 < y^* < -2.5$ (right), respectively. Previous LHCb D^0 results and various model calculations are shown for comparison.

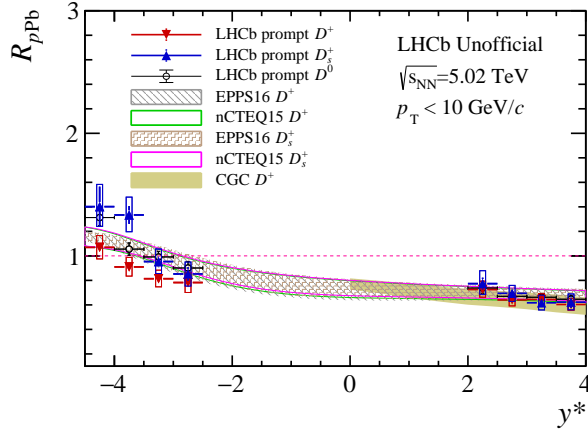


Figure 5.8 Nuclear modification factor R_{pPb} for prompt D^+ and D_s^+ as a function of y^* , integrated over the p_T range of $p_T < 10 \text{ GeV}/c$. Previous LHCb D^0 results and various model calculations are shown for comparison.

a function of p_T for prompt D^+ and D_s^+ in the forward and backward configurations are shown in Fig. 5.7. The corresponding data values for D^+ and D_s^+ are listed in Table 5.3 and Table 5.4, respectively. The nuclear modification factors as a function of y^* for prompt D^+ and D_s^+ , integrated over the p_T range of $p_T < 10 \text{ GeV}/c$, are shown in Fig. 5.8. The forward R_{pPb} results in these figures show a clear suppression at lower p_T for both D^+ and D_s^+ , similar to the previous D^0 results, confirming the existence of CNM effects in open charm production in pPb collisions. In backward rapidities, the D^+ R_{pPb} gradually decreases with the increasing y^* from the value of slightly above unity at $y^* > -4.0$ to about 0.8 at $y^* = -2.5$ across the whole measured p_T range; while the D_s^+ R_{pPb} gradually decreases with the increasing y^* from the value of slightly above 1.4 at $y^* > -3.5$ to about 0.9 at $y^* = -2.5$ across the whole measured p_T range.

In Figs. 5.7 and 5.8 the measured nuclear modification factors of D^+ and D_s^+ are compared with the previous LHCb D^0 data and the theoretical predictions on D^+ and D_s^+ using the HELAC-Onia generator^[109-110], incorporating the nPDFs of EPPS16^[59] and nCTEQ15^[58]. Both EPPS16 and nCTEQ15 nPDFs are already reweighted by the D^0 production at $\sqrt{s_{NN}} = 5.02$ TeV from LHCb. Thus the predicted R_{pPb} of D^+ and D_s^+ by these two models are very close and have less uncertainty compared to the calculations without D^0 constraint in Fig. 1.20. At forward rapidities, the new D^+ and D_s^+ results agree very well with the D^0 results and the nPDF calculations within uncertainties. At backward rapidities, the D_s^+ results are still consistent with the D^0 data and the nPDF calculations within uncertainties. However, the D^+ R_{pPb} seem to be systematically lower than D^0 and D_s^+ across the whole p_T range. The D^+ R_{pPb} results are slightly lower than nPDF calculations for $0 < p_T < 6$ GeV/c, indicating the potential changes in charm hadronization at backward rapidities where the event multiplicity are much larger; while they are significant lower than the nPDF predictions for high p_T , suggesting the possible additional final-state energy loss, which may not exist at forward rapidity^[164].

The D^+ R_{pPb} values at forward rapidities are also compared with the calculations of CGC^[72-73] effective field theory, as shown in Figs. 5.7 and 5.8. The charm quark mass, the initial saturation scales for proton and lead nucleus, and the fragmentation scale are main inputs of this CGC model. The uncertainties originating from the charm quark mass and fragmentation scale are negligible in the deep saturation regime. The uncertainty due to saturation scales does not change much when adjusting the charm quark mass and fragmentation scale in the p_T range of $0 < p_T < 5$ GeV/c. As a result, the R_{pPb} of D^+ is computed till $p_T = 5$ GeV/c in this CGC calculations. Since the process of c quark fragmentation to strange D_s^+ meson is more complicated than non-strange D mesons, this CGC model cannot deliver the R_{pPb} predictions for D_s^+ . In general, there is good agreement between the CGC calculations and the LHCb D^+ R_{pPb} data within uncertainties.

Table 5.3 Nuclear modification factor of D^+ in different p_T range, integrated over the rapidity range of $2.0 < y^* < 4.0$ in the forward (left) configuration and $-4.5 < y^* < -2.5$ in the backward (right) configuration. The first and second uncertainties are statistical and systematic, respectively.

| p_T [GeV/c] | Forward | Backward |
|----------------|---------------------------------------|---------------------------------------|
| [0, 1] | $0.582^{+0.028+0.057}_{-0.028-0.053}$ | $0.751^{+0.058+0.112}_{-0.058-0.103}$ |
| [1, 2] | $0.617^{+0.006+0.047}_{-0.006-0.046}$ | $0.824^{+0.016+0.073}_{-0.016-0.072}$ |
| [2, 3] | $0.654^{+0.004+0.046}_{-0.004-0.046}$ | $0.880^{+0.010+0.072}_{-0.010-0.073}$ |
| [3, 4] | $0.697^{+0.005+0.047}_{-0.005-0.050}$ | $0.891^{+0.009+0.069}_{-0.009-0.073}$ |
| [4, 5] | $0.723^{+0.007+0.049}_{-0.007-0.050}$ | $0.885^{+0.011+0.069}_{-0.011-0.071}$ |
| [5, 6] | $0.740^{+0.010+0.051}_{-0.010-0.052}$ | $0.869^{+0.014+0.068}_{-0.014-0.069}$ |
| [6, 7] | $0.773^{+0.015+0.054}_{-0.015-0.054}$ | $0.870^{+0.018+0.070}_{-0.018-0.070}$ |
| [7, 8] | $0.763^{+0.027+0.057}_{-0.027-0.057}$ | $0.835^{+0.024+0.066}_{-0.024-0.066}$ |
| [8, 9] | $0.854^{+0.031+0.075}_{-0.031-0.073}$ | $0.806^{+0.031+0.068}_{-0.031-0.067}$ |
| [9, 10] | $0.896^{+0.046+0.084}_{-0.046-0.079}$ | $0.877^{+0.045+0.079}_{-0.045-0.076}$ |

Table 5.4 Nuclear modification factor of D_s^+ in different p_T range, integrated over the rapidity range of $2.0 < y^* < 4.0$ in the forward (left) configuration and $-4.5 < y^* < -2.5$ in the backward (right) configuration. The first and second uncertainties are statistical and systematic, respectively.

| p_T [GeV/c] | Forward | Backward |
|----------------|---------------------------------------|---------------------------------------|
| [1, 2] | $0.679^{+0.035+0.069}_{-0.035-0.067}$ | $0.999^{+0.062+0.119}_{-0.062-0.117}$ |
| [2, 3] | $0.605^{+0.019+0.057}_{-0.019-0.057}$ | $1.007^{+0.037+0.102}_{-0.037-0.102}$ |
| [3, 4] | $0.623^{+0.020+0.058}_{-0.020-0.057}$ | $0.983^{+0.038+0.098}_{-0.038-0.097}$ |
| [4, 5] | $0.662^{+0.022+0.062}_{-0.022-0.061}$ | $1.010^{+0.040+0.099}_{-0.040-0.098}$ |
| [5, 6] | $0.677^{+0.037+0.066}_{-0.037-0.063}$ | $0.974^{+0.053+0.100}_{-0.053-0.096}$ |
| [6, 7] | $0.770^{+0.058+0.080}_{-0.058-0.075}$ | $1.176^{+0.082+0.124}_{-0.082-0.116}$ |
| [7, 8] | $0.794^{+0.077+0.097}_{-0.077-0.082}$ | $1.048^{+0.120+0.122}_{-0.120-0.110}$ |
| [8, 9] | $0.760^{+0.096+0.096}_{-0.096-0.083}$ | $1.012^{+0.153+0.130}_{-0.153-0.114}$ |
| [9, 10] | $0.719^{+0.122+0.105}_{-0.122-0.092}$ | $0.974^{+0.187+0.149}_{-0.187-0.133}$ |

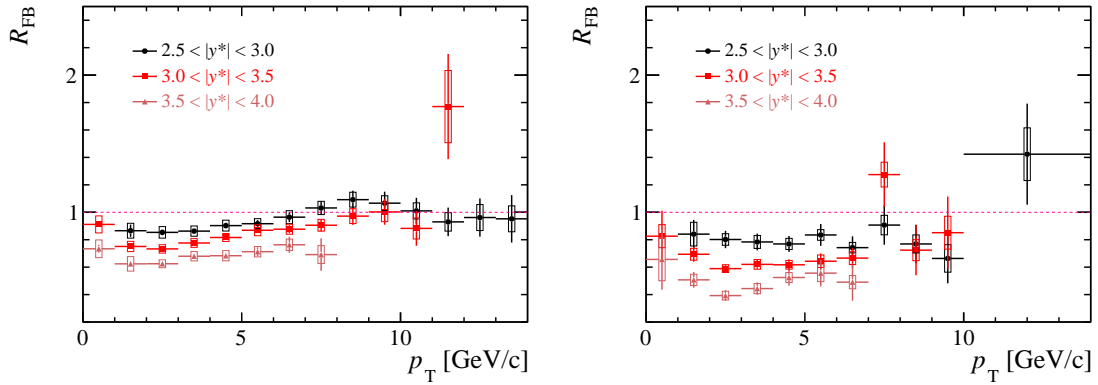


Figure 5.9 Forward-backward production ratios for prompt D^+ (left) and D_s^+ (right) as a function of p_T in different $|y^*|$ bins in $p\text{Pb}$ collisions.

5.3 Forward-backward ratio

Cold nuclear matter effects can also be studied with the forward-backward production asymmetry in $p\text{Pb}$ collisions. The corresponding forward-backward production ratio, R_{FB} , is independent of the cross-section in pp collisions. And in this observable, the common uncertainties between the forward and backward measurements largely cancel. The uncertainties originating from the branching fractions and the K (π) hadronic interactions with detector materials can be considered as fully correlated. All the rest uncertainties are considered as uncorrelated, for example, the forward and backward luminosities were measured independently, and the correlation in their uncertainties is negligible.

The forward-backward ratios R_{FB} of D^+ and D_s^+ as a function of p_T in different $|y^*|$ bins are shown in Fig. 5.9. The data show that the R_{FB} for both hadrons are less than unity for most $|y^*|$ and p_T bins, consistent with the existence of CNM effects on charm productions in $p\text{Pb}$ collisions. In general, R_{FB} decreases as $|y^*|$ increases, which is also consistent with the expectations of nPDFs calculations. However, the R_{FB} of D^+ , which has much smaller uncertainty, shows a clear p_T dependence for $|y^*| < 3.5$ bins. It shows a minimum value (less than unity) at $p_T \sim 2 - 3$ GeV/c, then increases towards higher p_T and reaches unity at $p_T \sim 8 - 9$ GeV/c, finally stays around unity towards higher p_T .

After integrating over the rapidity range of $2.5 < |y^*| < 4.0$, the R_{FB} for prompt D^+ and D_s^+ as a function of p_T are shown in Fig. 5.10 (left) and listed in Tables 5.5 and 5.6. The R_{FB} for prompt D^+ and D_s^+ as a function of $|y^*|$, integrated over $0 < p_T < 14$ GeV/c, are shown in Fig. 5.10 (right) and listed in Tables 5.5 and 5.6 as well. These data are compared with the previous D^0 and Λ_c^+ results^[91-92] and theory calculations.

R_{FB} of all charm hadrons decrease as $|y^*|$ increases, suggesting that the asymmetry becomes more pronounced in large rapidity region. The R_{FB} of D_s^+ as a function of

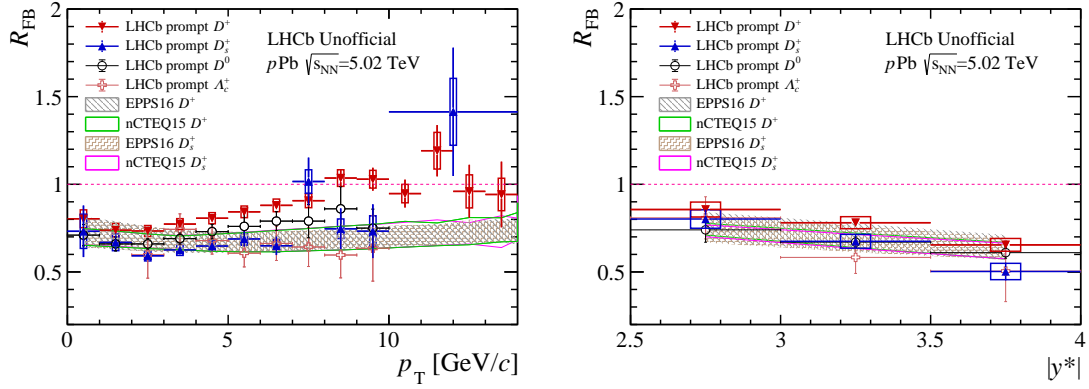


Figure 5.10 Forward-backward production ratio R_{FB} of $D_{(s)}^+$ as a function of (left) p_{T} integrated over $2.5 < y^* < 4.0$, (right) as a function of $|y^*|$ integrated over $0 < p_{\text{T}} < 14 \text{ GeV}/c$. Previous D^0 and Λ_c^+ results and various model calculations are shown for comparison.

Table 5.5 Forward-backward production ratio R_{FB} for D^+ in different p_{T} range (top), integrated over the common rapidity range of $2.5 < y^* < 4.0$; in different $|y^*|$ range (bottom) integrated over $0 < p_{\text{T}} < 14 \text{ GeV}/c$. The first error is statistical, while the second is systematic.

| p_{T} [GeV/c] | R_{FB} |
|--------------------------|-----------------------------|
| [0, 1] | $0.816 \pm 0.020 \pm 0.051$ |
| [1, 2] | $0.749 \pm 0.015 \pm 0.040$ |
| [2, 3] | $0.744 \pm 0.009 \pm 0.032$ |
| [3, 4] | $0.783 \pm 0.009 \pm 0.032$ |
| [4, 5] | $0.816 \pm 0.011 \pm 0.032$ |
| [5, 6] | $0.851 \pm 0.015 \pm 0.034$ |
| [6, 7] | $0.888 \pm 0.022 \pm 0.036$ |
| [7, 8] | $0.914 \pm 0.036 \pm 0.040$ |
| [8, 9] | $1.042 \pm 0.049 \pm 0.048$ |
| [9, 10] | $1.039 \pm 0.066 \pm 0.051$ |
| [10, 11] | $0.956 \pm 0.080 \pm 0.053$ |
| [11, 12] | $1.201 \pm 0.147 \pm 0.105$ |
| [12, 13] | $0.962 \pm 0.152 \pm 0.094$ |
| [13, 14] | $0.952 \pm 0.190 \pm 0.093$ |
| $ y^* $ | R_{FB} |
| [2.5, 3.0] | $0.870 \pm 0.022 \pm 0.043$ |
| [3.0, 3.5] | $0.792 \pm 0.008 \pm 0.035$ |
| [3.5, 4.0] | $0.663 \pm 0.010 \pm 0.037$ |

CHAPTER 5 RESULTS

Table 5.6 Forward-backward production ratio R_{FB} for D_s^+ in different p_{T} range (top), integrated over the common rapidity range of $2.5 < y^* < 4.0$; in different $|y^*|$ range (bottom) integrated over $0 < p_{\text{T}} < 14 \text{ GeV}/c$. The first error is statistical, while the second is systematic.

| p_{T} [GeV/c] | R_{FB} |
|--------------------------|-----------------------------|
| [0, 1] | $0.742 \pm 0.149 \pm 0.099$ |
| [1, 2] | $0.679 \pm 0.040 \pm 0.048$ |
| [2, 3] | $0.601 \pm 0.024 \pm 0.030$ |
| [3, 4] | $0.634 \pm 0.026 \pm 0.032$ |
| [4, 5] | $0.655 \pm 0.030 \pm 0.030$ |
| [5, 6] | $0.695 \pm 0.044 \pm 0.036$ |
| [6, 7] | $0.654 \pm 0.053 \pm 0.036$ |
| [7, 8] | $1.028 \pm 0.138 \pm 0.068$ |
| [8, 9] | $0.751 \pm 0.117 \pm 0.056$ |
| [9, 10] | $0.738 \pm 0.154 \pm 0.089$ |
| [10, 14] | $1.424 \pm 0.369 \pm 0.192$ |
| $ y^* $ | R_{FB} |
| [2.5, 3.0] | $0.815 \pm 0.054 \pm 0.053$ |
| [3.0, 3.5] | $0.684 \pm 0.041 \pm 0.040$ |
| [3.5, 4.0] | $0.509 \pm 0.052 \pm 0.047$ |

$|y^*|$ shows reasonable agreements with D^0 and Λ_c^+ results and with the EPPS16^[59] and nCTEQ15^[58] predictions within uncertainties. The D^+ R_{FB} is slightly larger than other charm hadrons and model predictions, due to the overall suppression of D^+ production at backward rapidities. The R_{FB} of D^+ and D_s^+ are consistent with D^0 and Λ_c^+ and nPDFs calculations at low p_{T} , but the most precise D^+ data shows a clear increasing trend with increasing p_{T} and saturates at unity at high p_{T} ($> 10 \text{ GeV}/c$) within uncertainties, which deviates from the almost p_{T} independent nPDF calculations. This discrepancy derives from the suppression of the high p_{T} D^+ production in the backward configuration^[164], which is also pronounced in Fig. 5.7.

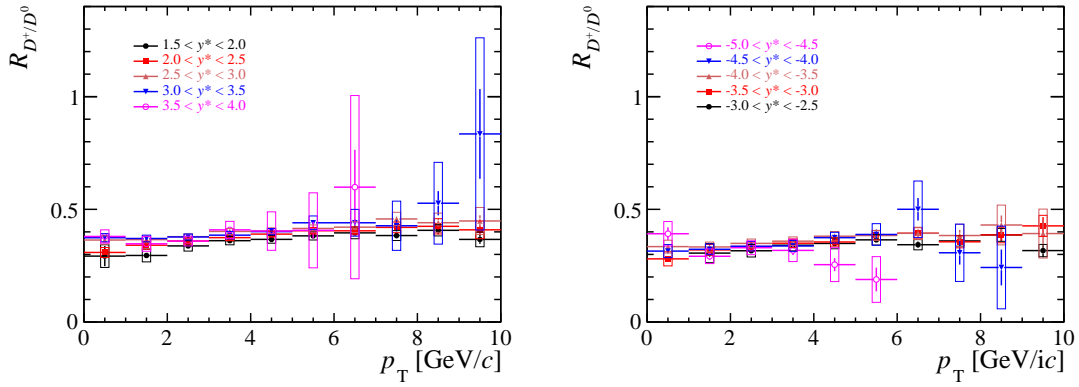


Figure 5.11 Cross-section ratio of D^+ to D^0 , R_{D^+/D^0} , as a function of p_T in different y^* bins for the forward (left) and backward (right) p Pb configurations at 5.02 TeV.

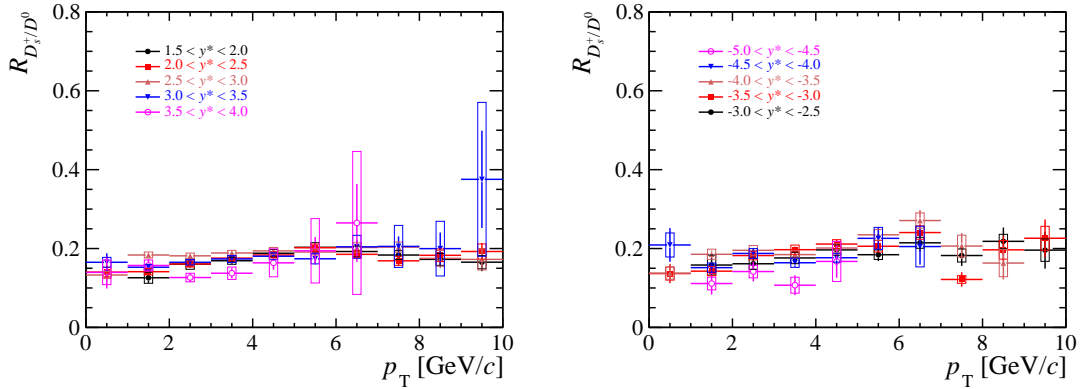


Figure 5.12 Cross-section ratio of D_s^+ to D^0 , $R_{D_s^+/D^0}$, as a function of p_T in different y^* bins for the forward (left) and backward (right) p Pb configurations at 5.02 TeV.

5.4 Cross-section ratios between D mesons

The measurements of D^+ and D_s^+ cross-sections in p Pb collisions at 5.02 TeV, together with the previous D^0 results from LHCb, enable the calculation of cross-section ratios of D^+ to D^0 , D_s^+ to D^0 and D_s^+ to D^+ . In these calculations, the uncertainties of branching fraction are not considered, as it only provides a global offset independent of p_T and y^* . The uncertainty due to K (π) hadronic interactions with the detector are considered as partially correlated, due to different numbers of K (π) tracks between the numerators and denominators of R_{D^+/D^0} , $R_{D_s^+/D^0}$ or $R_{D_s^+/D^+}$. The uncertainty from luminosity cancels out in these ratios, whereas the rest uncertainties are considered as uncorrelated. The cross-section ratios R_{D^+/D^0} , $R_{D_s^+/D^0}$ and $R_{D_s^+/D^+}$ as a function of p_T in different y^* bins are shown in Fig. 5.11, Fig. 5.12 and Fig. 5.13, respectively. These cross-section ratios do not show a significant rapidity dependence within current experimental precision.

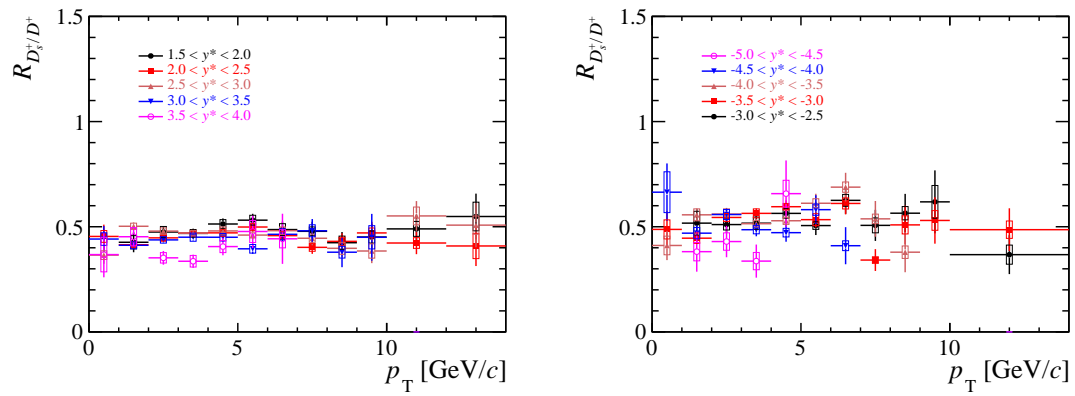


Figure 5.13 Cross-section ratio of D_s^+ to D^+ , $R_{D_s^+/D^+}$, as a function of p_T in different y^* bins for the forward (left) and backward (right) p Pb configurations at 5.02 TeV.

Fig. 5.14 shows the ratios of R_{D^+/D^0} , $R_{D_s^+/D^0}$ and $R_{D_s^+/D^+}$ as a function of p_T , integrated over the total rapidity range of $1.5 < y^* < 4.0$ for the forward and $-5.0 < y^* < -2.5$ for the backward $p\text{Pb}$ configurations. The corresponding results in pp collisions at 5.02 TeV from LHCb and in $p\text{Pb}$ collisions at 5.02 TeV from ALICE are shown as well for comparisons. Figure 5.15 shows the R_{D^+/D^0} , $R_{D_s^+/D^0}$ and $R_{D_s^+/D^+}$ ratios as a function of $|y^*|$, integrated over the p_T range of $p_T < 10 \text{ GeV}/c$ for the forward and backward $p\text{Pb}$ configurations. The LHCb pp results are also shown for comparisons. These one-dimensional production ratios in $p\text{Pb}$ collisions are also listed in Appendix A.8. In general, the LHCb ratio measurements are consistent with those in $p\text{Pb}^{[90]}$ and $pp^{[31]}$ collisions from ALICE in mid-rapidity at 5.02 TeV within uncertainties. The higher precision LHCb data allows more detailed studies on charm hadronization in $p\text{Pb}$ collisions. Figure 5.14 shows a slight p_T dependence of these ratios. This p_T dependence is potentially interpreted as the heavier particles with a harder p_T spectrum^[30,79]. Both Figures 5.14 and 5.15 show that the $R_{D_s^+/D^0}$ ratios from the forward and backward $p\text{Pb}$ configurations and the pp collisions are consistent within uncertainties. In other words, there is no evidence for strangeness enhancement in minimum bias $p\text{Pb}$ collisions, at both forward and backward rapidities. However, the R_{D^+/D^0} ratios from pp collisions and the forward $p\text{Pb}$ collisions are consistent with each other, but both of them are slightly larger than in the backward $p\text{Pb}$ data, implying the possible change of charm fragmentation in higher multiplicity circumstances. As a result, the $R_{D_s^+/D^+}$ ratios are a bit larger in the backward $p\text{Pb}$ data than in the forward $p\text{Pb}$ data and in pp collisions.

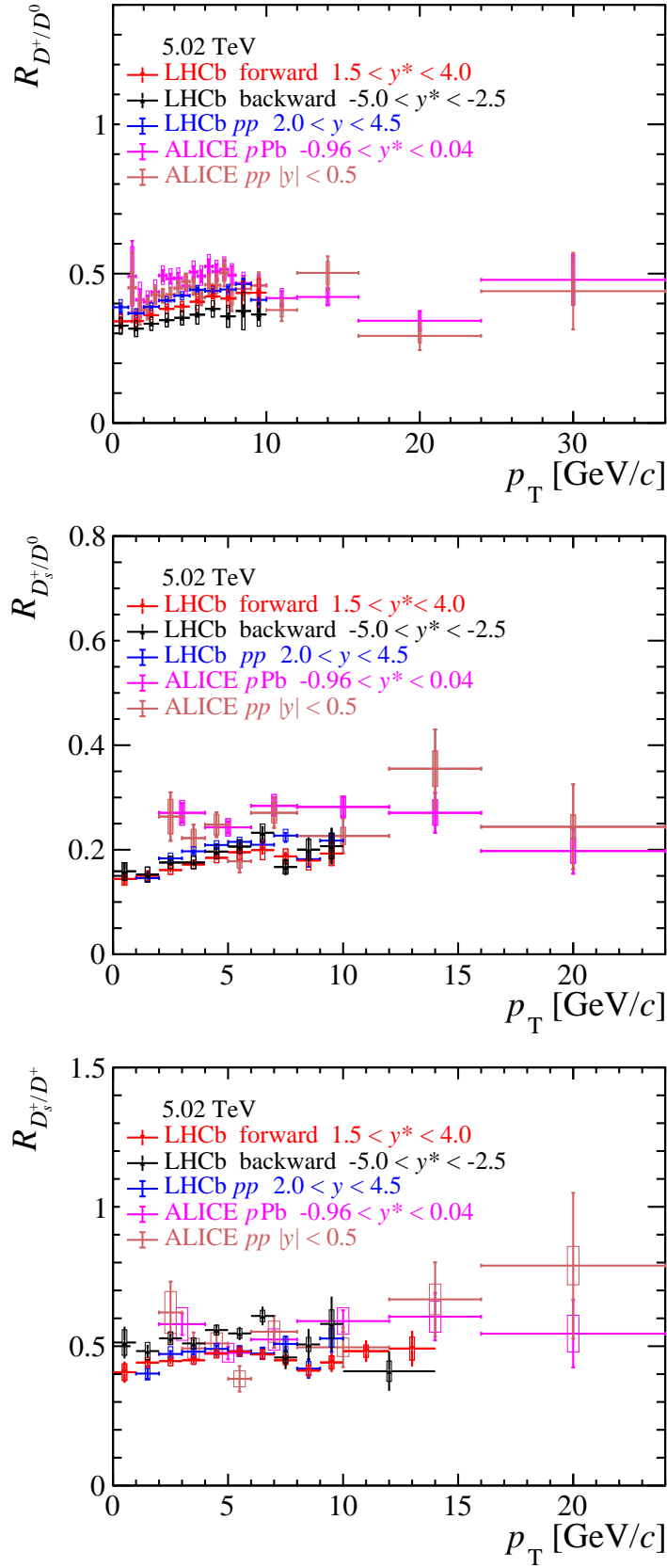


Figure 5.14 R_{D^+/D^0} , $R_{D_s^+/D^0}$ and $R_{D_s^+/D^+}$ ratio as a function of p_T , integrated over the full measured rapidity range in the forward and backward pPb configurations. The previous measurements in pp collisions from LHCb^[30] and in pp and pPb collisions from ALICE^[31,90] at 5.02 TeV are also shown for comparisons.

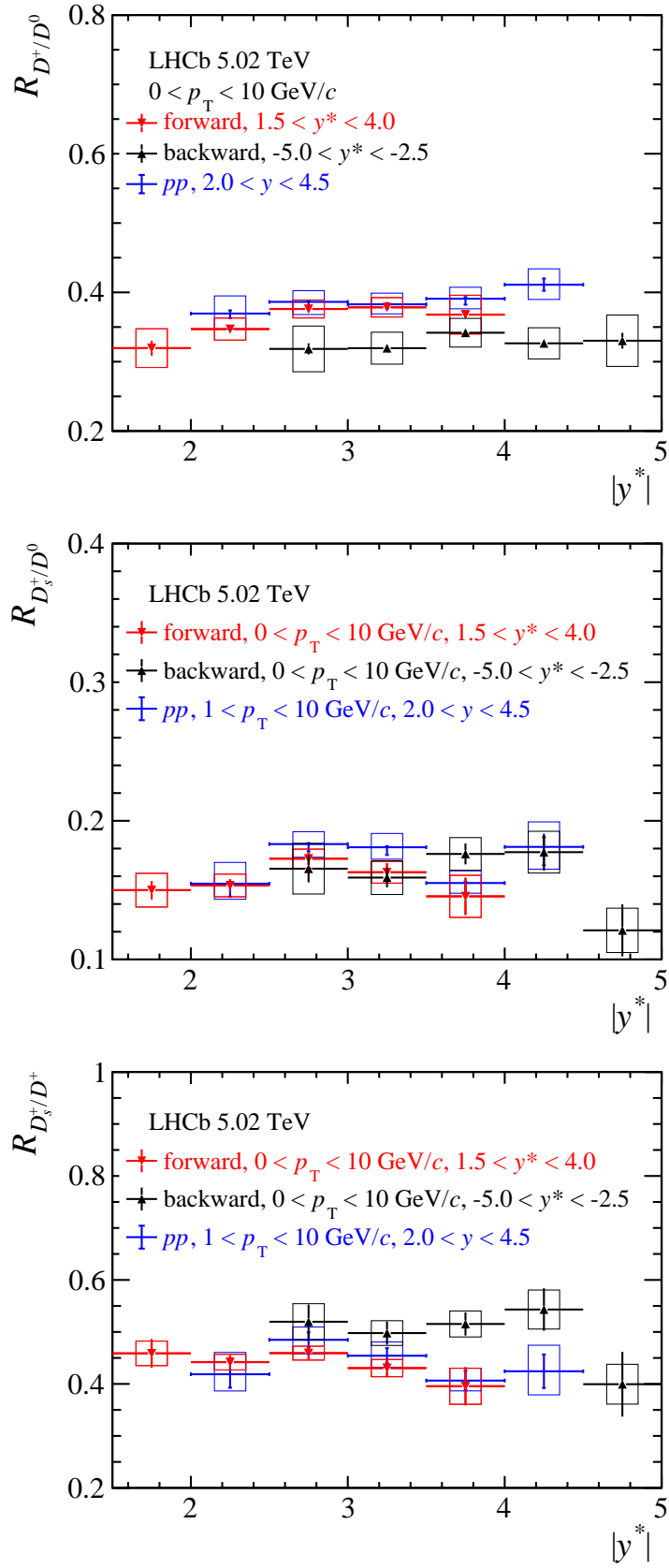


Figure 5.15 R_{D^+/D^0} , $R_{D_s^+/D^0}$ and $R_{D_s^+/D^+}$ ratio as a function of $|y^*|$, integrated over the measured p_T ranges in the forward and backward pPb configurations. The previous measurements in pp collisions from LHCb^[30] at 5.02 TeV are also shown for comparisons.

CHAPTER 6 SUMMARY AND OUTLOOK

6.1 Summary

The main goal of relativistic heavy-ion collisions is to produce quark-gluon plasma (QGP) and study its properties. In these experiments, proton-nucleus collisions, where QGP is not expected to exist, provide essential reference for quantitatively constraining the cold nuclear matter effects, which is needed for extracting the QGP-induced hot nuclear matter effects in nucleus-nucleus collisions. In recent years, many signatures of QGP formation have also been observed in high multiplicity pp or $p\text{Pb}$ collisions at LHC, for example, the strangeness enhancement and large collective flow, challenging the assumption of no-QGP production in $p\text{Pb}$ collisions. Experimentally, it will be very helpful to explore as many QGP signatures as possible to fully understand the nature of small systems created in, for example, $p\text{Pb}$ collisions. The charm quark has a mass much larger than the QCD energy scale ($m_c \gg \Lambda_{QCD}$) and is produced in the initial stage hard scatterings. The measurements of open charm hadrons (D^+ , D_s^+) production in nucleus-nucleus and proton-nucleus collisions can provide valuable information about the properties of nuclear matter created in these collisions.

As the unique detector fully instrumented in the forward region at LHC, LHCb has excellent particle identification, precise vertex reconstruction and tracking. It can measure particle productions in a phase-space region inaccessible to other detectors with exceptional precision, especially for heavy flavor hadrons. LHCb took the data of $p\text{Pb}$ collisions at $\sqrt{s_{NN}} = 5.02$ TeV in early 2013. The integrated luminosity is 1.1 nb^{-1} for the forward configuration and 0.5 nb^{-1} for the backward configuration. One of the primary goals of the LHCb $p\text{Pb}$ data-taking is to accurately measure the prompt open charm (D^+ and D_s^+) productions down to very low p_T in a wide rapidity range. These results can be compared with the previous LHCb open charm results in pp collisions at 5.02 TeV to study the nuclear matter effects. The cold nuclear matter effects can be quantitatively constrained in a wide x and Q^2 region by the deviation from unity of the nuclear modification factor, $R_{p\text{Pb}}$ and the forward-backward cross-section ratio, R_{FB} . While the hot nuclear matter effect in $p\text{Pb}$ small system can be studied through the cross-section ratios between different open charm hadrons. For example, possible strangeness enhancement in charm hadronization can be studied by comparing the $R_{D_s^+/D^0}$ cross-section ratio in $p\text{Pb}$ to that in pp .

This thesis presents the first measurement of prompt open charm hadrons, D^+ and D_s^+ , production cross-sections in $p\text{Pb}$ collisions at $\sqrt{s_{NN}} = 5.02$ TeV with the LHCb detector at the LHC. The total number of D^+ and D_s^+ signals are obtained by fitting the $K\pi\pi$ and $KK\pi$ invariant mass distributions. The prompt signal yields are further extracted by fitting their $\log_{10} \chi_{\text{IP}}^2$ distributions in each (p_{T}, y^*) bin. The measurements of D^+ and D_s^+ double-differential cross-sections are performed in the forward ($1.5 < y^* < 4.0$) and backward ($-5.0 < y^* < -2.5$) rapidity regions with the transverse momentum p_{T} down to zero. In the forward and backward regions, the integrated production cross-sections for prompt D^+ and D_s^+ mesons with $p_{\text{T}} < 10$ GeV/ c are determined to be

$$\sigma(D^+)_{\text{Fwd}}(1 < p_{\text{T}} < 10 \text{ GeV}/c, 1.5 < y^* < 4.0) = 63.1 \pm 0.3(\text{stat.}) \pm 3.6(\text{syst.}) \text{ mb},$$

$$\sigma(D_s^+)_{\text{Fwd}}(1 < p_{\text{T}} < 10 \text{ GeV}/c, 1.5 < y^* < 4.0) = 28.2 \pm 0.4(\text{stat.}) \pm 1.5(\text{syst.}) \text{ mb},$$

$$\sigma(D^+)_{\text{Bwd}}(1 < p_{\text{T}} < 10 \text{ GeV}/c, -5.0 < y^* < -2.5) = 60.8 \pm 0.5(\text{stat.}) \pm 3.8(\text{syst.}) \text{ mb},$$

$$\sigma(D_s^+)_{\text{Bwd}}(1 < p_{\text{T}} < 10 \text{ GeV}/c, -5.0 < y^* < -2.5) = 30.8 \pm 0.7(\text{stat.}) \pm 1.8(\text{syst.}) \text{ mb},$$

where the first uncertainties are statistical, and the second are systematic. In forward and backward configurations, the nuclear modification factors are measured, with the pp references taken from the previous LHCb D^+ and D_s^+ measurements in pp collisions at 5.02 TeV^[30]. The forward-backward ratios of D^+ and D_s^+ are determined in the common rapidity region of $2.5 < |y^*| < 4.0$. The $R_{p\text{Pb}}$ and R_{FB} results show an apparent suppression of prompt D^+ and D_s^+ productions in the forward region, suggesting the presence of could nuclear matter effects in $p\text{Pb}$ collisions. In forward rapidities, the $R_{p\text{Pb}}$ values of D^+ and D_s^+ agree with the previous D^0 ^[91] results and are consistent with the pQCD calculations based on the latest nPDFs^[58-59] and the CGC models^[72-73]. In backward rapidities, the $R_{p\text{Pb}}$ values of D_s^+ is still consistent with D^0 and nPDF calculations, while that of D^+ seems to be systematically lower across the whole measure p_{T} range. The R_{FB} values of D^+ and D_s^+ are clearly less than unity and consistent with the nPDF predictions and the previous measurements of D^0 ^[91] and Λ_c^+ ^[92] at low p_{T} . However, the R_{FB} of D^+ shows a clear increase towards higher p_{T} , and reaches a saturation around unity for p_{T} above 8 GeV/ c . Within experimental uncertainties, the cross-section ratios R_{D^+/D^0} , $R_{D_s^+/D^0}$ and $R_{D_s^+/D^+}$ are consistent with the measurements in pp collisions from LHCb^[30] and in pp and $p\text{Pb}$ collisions from ALICE^[31,31] at 5.02 TeV. With much higher precision, the new LHCb $R_{D_s^+/D^0}$ results show no evidence for strangeness enhancement in minimum bias

Table 6.1 Integrated luminosities in $p\text{Pb}$ collisions and the corresponding pp reference at LHCb from Run 2 to Run 4.

| Period | Run 2 | | Run 3 | | | Run 4 | | |
|------------------------|-----------------------|-----------------------|----------------------|----------------------|----------------------|----------------------|----------------------|----------------------|
| $\sqrt{s_{\text{NN}}}$ | 8.16 TeV | | 8.8 TeV | | | 8.8 TeV | | |
| Configuration | forward | backward | pp | forward | backward | pp | forward | backward |
| \mathcal{L} | 12.5 nb ⁻¹ | 17.4 nb ⁻¹ | 104 pb ⁻¹ | 250 nb ⁻¹ | 250 nb ⁻¹ | 104 pb ⁻¹ | 250 nb ⁻¹ | 250 nb ⁻¹ |

$p\text{Pb}$ collisions. The R_{D^+/D^0} in the backward $p\text{Pb}$ data is slightly lower than in pp and in the forward $p\text{Pb}$ data, indicating the possible change of charm fragmentation in higher multiplicity circumstances.

6.2 Outlook

As summarized in Table 6.1, during LHCb Run 2, nearly 12.5 nb⁻¹ (17.4 nb⁻¹) of $p\text{Pb}$ forward (backward) data have been collected at $\sqrt{s_{\text{NN}}} = 8.16$ TeV, which are 20 times larger statistics than Run 1. In Run 3 and Run 4, the upgraded LHCb detector will collect about 500 nb⁻¹ $p\text{Pb}$ collisions data and about 104 pb⁻¹ pp collisions data at $\sqrt{s_{\text{NN}}} = 8.8$ TeV. The major LHCb upgrade in Run3 are as the following: to remove the L0 hardware trigger and replace the HLT with a full software trigger capable of handling a 40 MHz events readout rate; to install a new vertex silicon pixel detector, three scintillating fiber (SciFi) trackers, a new upstream tracker (UT), and new fast photodetectors of the RICH; to improve readout electronics for calorimeter and muon systems^[165].

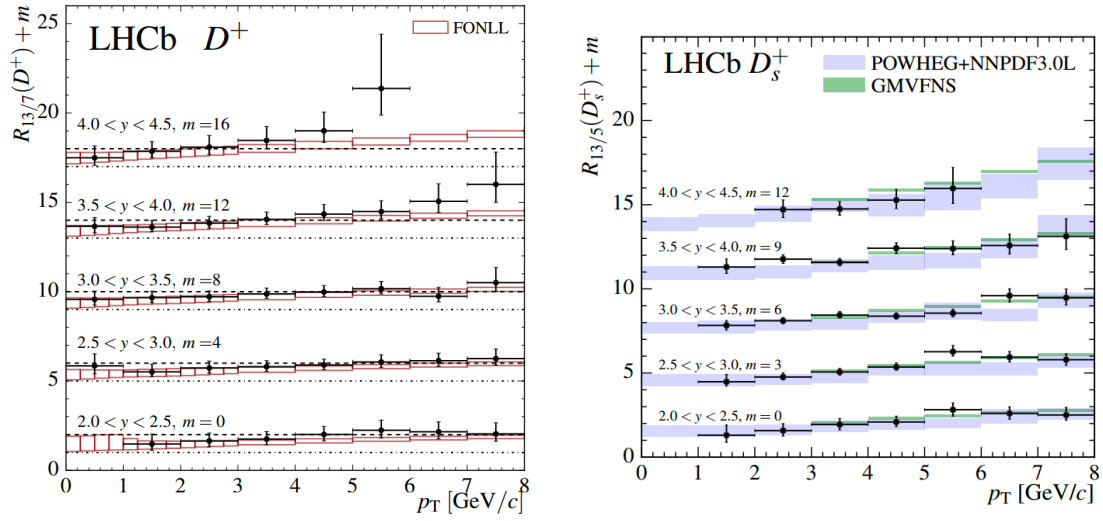


Figure 6.1 Open charm cross-section ratios of $R_{13/7}(D^+) + m$ and $R_{13/5}(D_s^+) + m$ in 5 TeV pp collisions at LHCb, where m represents a 10^{-m} scaling of the result. Then figures are taken from Ref. [30] and Ref. [79], respectively.

Based on the higher luminosity pp and pPb collisions data collected at higher nucleon-nucleon centre-of-mass energies from LHCb Run 2 to Run 4 periods, we present the following prospects for the open charm production measurements:

- The total $c\bar{c}$ cross-section is dominated by the values in low p_T bins. With more statistics, the open charm production down to $p_T = 0$ GeV/ c will be more accurately measured, which is essential to calculate the total $c\bar{c}$ cross-section in pPb collisions and hence to constrain the nPDFs precisely. Multiplicity-dependent D meson productions can explore the correlation between soft and hard process mechanisms in heavy-ion collisions, as well as the multiple partons interactions (MPI) in charm production at high event activities^[166]. Since there are not enough high-multiplicity events in pPb collisions at $\sqrt{s_{NN}} = 5.02$ TeV, multiplicity-dependent D meson productions are not measured in this thesis. We expect to conduct this measurement using the Run 2 to Run 4 pPb data which has higher multiplicity on average.
- Fig. 6.1 shows the cross-section ratios between 5.02, 7 and 13 TeV in pp collision at LHCb. The correlated systematic uncertainties (the luminosity, the branching and the tracking calibration) of these ratios are largely canceled relative to the double-differential cross-section measurements. Additionally, some theoretical uncertainties (e.g. the PDF, the mass dependence, the scale and fragmentation fractions) of the ratios between different centre-of-mass energies predicted by pQCD have been reduced^[167]. Therefore, open charm cross-section ratios between 5, 8.16 and 8.8 TeV in pPb collisions at LHCb are supposed to provide a more accurate constrain

to the nPDF predictions than the double-differential cross-sections.

- At high p_T , the statistical uncertainty of R_{FB} dominates. In the future, R_{FB} and $R_{p\text{Pb}}$ can be obtained with smaller statistical and systematic uncertainties than at 5.02 TeV by measuring the charm cross-section at 8.16 and 8.8 TeV in Run 2-Run 4. Those measurements will play an important role in the study of CNM effects and put more stringent constraint on nPDF or CGC theories.
- Although the $R_{D_s^+/D^0}$ and $R_{D_s^+/D^+}$ ratios were not found to be enhanced in minimum bias $p\text{Pb}$ collisions at $\sqrt{s_{NN}} = 5.02$ TeV. As shown in Fig. 1.12, in high multiplicity events, the yield ratios between strange and non-strange hadrons in pp and $p\text{Pb}$ collisions are comparable to PbPb. The production ratios R_{D^+/D^0} , $R_{D_s^+/D^0}$ and $R_{D_s^+/D^+}$ as a function of event multiplicity are not investigated in this thesis due to the lack of high-multiplicity events. One of the major goals for an expanded $p\text{Pb}$ data collection in LHCb Run 3-Run 4 is to understand the similarities of high-multiplicity events between the small systems and PbPb collisions^[165]. Utilizing data of Run 2-Run 4, the yield ratios between strange D_s^+ and non-strange D^0 , D^+ and D^{*+} as a function of multiplicity can be measured at 8.16 and 8.8 TeV, providing new opportunities to study the strangeness enhancement in charm hadronization in small systems.

Furthermore, LHCb is the unique detector at LHC which can operate in both collider ($pp/p\text{Pb}/\text{PbPb}$) and fixed-target (SMOG^[168]) modes. The upgraded internal gas target (SMOG2) is planned to be installed upstream of the VELO in Run 3. Inside the LHCb vacuum pipe, hydrogen, deuterium or noble gases can be injected close to the collision point with an integrated luminosity up to 150 pb^{-1} at a centre-of-mass energy up to $\sqrt{s_{NN}} = 115 \text{ GeV}$ ^[168]. Shown in Fig. 6.2 (left), the measurement in fixed-target mode is an effective tool for constraining nPDFs at large Bjorken x and low Q^2 , which is a vital input for not only heavy-ion but also cosmic ray physics. The AFTER Group has made several predictions of nPDFs such as nCTEQ15 with simulations in a fixed-target configuration at the LHCb^[170]. As shown in Fig. 6.2 (right), with expected fixed-target input of open charm productions, the accuracy of nPDFs calculations will be significantly improved.

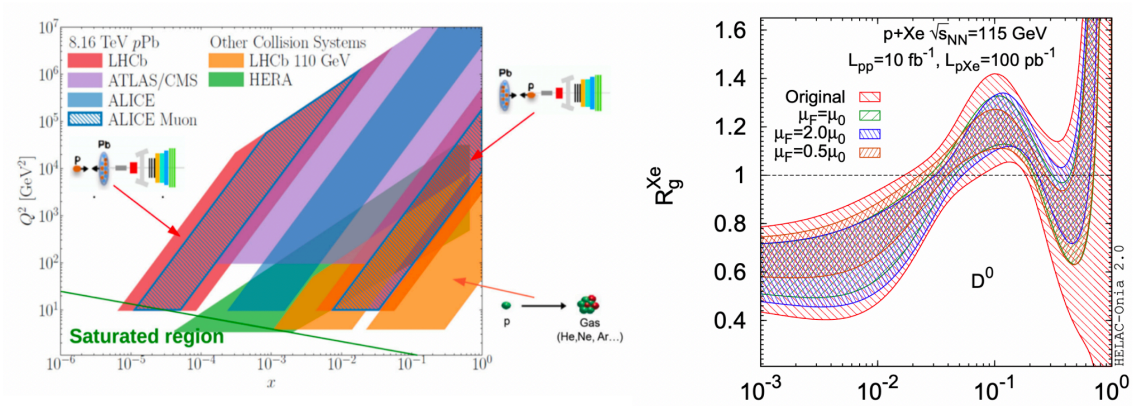


Figure 6.2 Phase space range covered by fixed-target experiments (left); the nCTEQ15 nPDFs before (red) and after (green, blue and yellow) the reweighting are predicted by AFTER Group using D^0 production with different factorization scales μ_F (right). These figures are taken from Ref. [169] and Ref. [170], respectively.

REFERENCES

- [1] Skalský V. The quantum-relativistic dynamics of the universe[J]. arXiv: General Physics, 2014.
- [2] Higgs P W. Broken Symmetries and the Masses of Gauge Bosons[J/OL]. Phys. Rev. Lett., 1964, 13: 508-509. DOI: 10.1103/PhysRevLett.13.508.
- [3] Aad G, et al. Observation of a new particle in the search for the Standard Model Higgs boson with the ATLAS detector at the LHC[J/OL]. Phys. Lett. B, 2012, 716: 1-29. DOI: 10.1016/j.physletb.2012.08.020.
- [4] Mariotti C. Observation of a new Boson at a Mass of 125 gev With the CMS Experiment at the LHC[C/OL]//13th Marcel Grossmann Meeting on Recent Developments in Theoretical and Experimental General Relativity, Astrophysics, and Relativistic Field Theories. 2015: 352-372. DOI: 10.1142/9789814623995_0019.
- [5] Wikipedia contributors. Standard model — Wikipedia, the free encyclopedia[EB/OL]. 2022. https://en.wikipedia.org/w/index.php?title=Standard_Model&oldid=1070462393.
- [6] Glashow S L. Partial symmetries of weak interactions[J]. Nuclear Physics, 1961, 22: 579-588.
- [7] Skands P. Introduction to QCD[C/OL]//Theoretical Advanced Study Institute in Elementary Particle Physics: Searching for New Physics at Small and Large Scales. 2013: 341-420. DOI: 10.1142/9789814525220_0008.
- [8] Zyla P A, et al. Review of Particle Physics[J/OL]. PTEP, 2020, 2020(8): 083C01. DOI: 10.1093/ptep/ptaa104.
- [9] Gross D J, Wilczek F. Ultraviolet Behavior of Nonabelian Gauge Theories[J/OL]. Phys. Rev. Lett., 1973, 30: 1343-1346. DOI: 10.1103/PhysRevLett.30.1343.
- [10] Politzer H D. Reliable perturbative results for strong interactions?[J/OL]. Phys. Rev. Lett., 1973, 30: 1346-1349. <https://link.aps.org/doi/10.1103/PhysRevLett.30.1346>.
- [11] Wilson K G. Confinement of Quarks[J/OL]. Phys. Rev. D, 1974, 10: 2445-2459. DOI: 10.1103/PhysRevD.10.2445.
- [12] Gao F, Chen C, xin Liu Y. Colour confinement: a dynamical phenomenon of qcd[J]. arXiv: High Energy Physics - Phenomenology, 2018.
- [13] Fodor Z, Katz S. Critical point of QCD at finite t and μ , lattice results for physical quark masses [J/OL]. Journal of High Energy Physics, 2004, 2004(04): 050-050. <https://doi.org/10.1088/1126-6708/2004/04/050>.
- [14] Kharzeev D E, Liao J. Chiral magnetic effect reveals the topology of gauge fields in heavy-ion collisions[J]. Nature Reviews Physics, 2020, 3: 55-63.
- [15] Brown F R, Butler F P, Chen H, et al. On the existence of a phase transition for qcd with three light quarks[J/OL]. Phys. Rev. Lett., 1990, 65: 2491-2494. <https://link.aps.org/doi/10.1103/PhysRevLett.65.2491>.
- [16] Karsch F. Lattice results on QCD thermodynamics[J/OL]. Nucl. Phys. A, 2002, 698: 199-208. DOI: 10.1016/S0375-9474(01)01365-3.

REFERENCES

- [17] Philipsen O. Lattice QCD at finite temperature and density[J/OL]. *Eur. Phys. J. ST*, 2007, 152: 29-60. DOI: 10.1140/epjst/e2007-00376-3.
- [18] de Forcrand P, Philipsen O. The QCD phase diagram for small densities from imaginary chemical potential[J/OL]. *Nucl. Phys. B*, 2002, 642: 290-306. DOI: 10.1016/S0550-3213(02)00626-0.
- [19] Aoki Y, Endrodi G, Fodor Z, et al. The Order of the quantum chromodynamics transition predicted by the standard model of particle physics[J/OL]. *Nature*, 2006, 443: 675-678. DOI: 10.1038/nature05120.
- [20] Miller M L, Reygers K, Sanders S J, et al. Glauber modeling in high energy nuclear collisions [J/OL]. *Ann. Rev. Nucl. Part. Sci.*, 2007, 57: 205-243. DOI: 10.1146/annurev.nucl.57.090506.123020.
- [21] Acharya S, et al. *D*-meson azimuthal anisotropy in midcentral Pb-Pb collisions at $\sqrt{s_{NN}} = 5.02$ TeV[J/OL]. *Phys. Rev. Lett.*, 2018, 120(10): 102301. DOI: 10.1103/PhysRevLett.120.102301.
- [22] Zhao J, Zhou K, Chen S, et al. Heavy flavors under extreme conditions in high energy nuclear collisions[J/OL]. *Progress in Particle and Nuclear Physics*, 2020, 114: 103801. <https://www.sciencedirect.com/science/article/pii/S014664102030048X>. DOI: <https://doi.org/10.1016/j.pnpnp.2020.103801>.
- [23] Catani S, Ciafaloni M, Hautmann F. High-energy factorization and small x heavy flavor production[J/OL]. *Nucl. Phys. B*, 1991, 366: 135-188. DOI: 10.1016/0550-3213(91)90055-3.
- [24] Collins J C, Soper D E, Sterman G F. Factorization of Hard Processes in QCD[J/OL]. *Adv. Ser. Direct. High Energy Phys.*, 1989, 5: 1-91. DOI: 10.1142/9789814503266_0001.
- [25] Kramer G, Spiesberger H. Inclusive d production in photon-photon collisions at next-to-leading order qcd[J/OL]. *European Physical Journal C*, 2001, 22(2): 289-301. <https://www.scopus.com/inward/record.uri?eid=2-s2.0-0012687906&doi=10.1007%2fs100520100805&partnerID=40&md5=2485bcfaa7f5fceeef7b4b2036342949>. DOI: 10.1007/s100520100805.
- [26] Kniehl B A, Kramer G, Schienbein I, et al. Collinear subtractions in hadroproduction of heavy quarks[J/OL]. *Eur. Phys. J. C*, 2005, 41: 199-212. DOI: 10.1140/epjc/s2005-02200-7.
- [27] Alioli S, Nason P, Oleari C, et al. A general framework for implementing nlo calculations in shower monte carlo programs: the powheg box[J/OL]. *Journal of High Energy Physics*, 2010, 2010(6). [http://dx.doi.org/10.1007/JHEP06\(2010\)043](http://dx.doi.org/10.1007/JHEP06(2010)043). DOI: 10.1007/jhep06(2010)043.
- [28] Cacciari M, Frixione S, Nason P. The pT spectrum in heavy-flavour photoproduction[J/OL]. *Journal of High Energy Physics*, 2001, 2001(03): 006-006. <https://doi.org/10.1088/1126-6708/2001/03/006>.
- [29] Abelev B, et al. Heavy flavour decay muon production at forward rapidity in proton-proton collisions at $\sqrt{s} = 7$ TeV[J/OL]. *Phys. Lett. B*, 2012, 708: 265-275. DOI: 10.1016/j.physletb.2012.01.063.
- [30] Aaij R, et al. Measurements of prompt charm production cross-sections in pp collisions at $\sqrt{s} = 5$ TeV[J/OL]. *JHEP*, 2017, 06: 147. DOI: 10.1007/JHEP06(2017)147.
- [31] Acharya S, et al. Measurement of D^0 , D^+ , D^{*+} and D_s^+ production in pp collisions at $\sqrt{s} = 5.02$ TeV with ALICE[J/OL]. *Eur. Phys. J. C*, 2019, 79(5): 388. DOI: 10.1140/epjc/s10052-019-6873-6.

REFERENCES

- [32] d’Enterria D. 6.4 jet quenching: Datasheet from landolt-börnstein - group i elementary particles, nuclei and atoms · volume 23: “relativistic heavy ion physics” in springermaterials (https://doi.org/10.1007/978-3-642-01539-7_16)[M/OL]. Springer-Verlag Berlin Heidelberg. https://materials.springer.com/lb/docs/sm_lbs_978-3-642-01539-7_16. DOI: 10.1007/978-3-642-01539-7_16.
- [33] Martin A D, Stirling W J, Thorne R S, et al. Parton distributions for the LHC[J/OL]. Eur. Phys. J. C, 2009, 63: 189-285. DOI: 10.1140/epjc/s10052-009-1072-5.
- [34] Abt I, et al. Impact of jet-production data on the next-to-next-to-leading-order determination of HERAPDF2.0 parton distributions[J]. 2021.
- [35] Binnewies J, Kniehl B A, Kramer G. Inclusive B meson production in e^+e^- and $p\bar{p}$ collisions [J/OL]. Phys. Rev. D, 1998, 58: 034016. DOI: 10.1103/PhysRevD.58.034016.
- [36] Bertone V, Prestel S. Combining N3LO QCD calculations and parton showers for hadronic collision events[J]. 2022.
- [37] Peterson C, Schlatter D, Schmitt I, et al. Scaling violations in inclusive e^+e^- annihilation spectra [J/OL]. Physical Review D, 1983, 27(1): 105-111. <https://www.scopus.com/inward/record.uri?eid=2-s2.0-0001727414&doi=10.1103%2fPhysRevD.27.105&partnerID=40&md5=d68c8516cc024574f0f7988d0b69971f>. DOI: 10.1103/PhysRevD.27.105.
- [38] Bowler M. e^+e^- production of heavy quarks in the string model[J/OL]. Zeitschrift für Physik C Particles and Fields, 1981, 11(2): 169-174. <https://www.scopus.com/inward/record.uri?eid=2-s2.0-0000579473&doi=10.1007%2fBF01574001&partnerID=40&md5=f88820ee42a6bc57efb09ba5f4b2cb39>. DOI: 10.1007/BF01574001.
- [39] Andersson B, Gustafson G, Ingelman G, et al. Parton fragmentation and string dynamics[J/OL]. Physics Reports, 1983, 97(2): 31-145. <https://www.sciencedirect.com/science/article/pii/0370157383900807>. DOI: [https://doi.org/10.1016/0370-1573\(83\)90080-7](https://doi.org/10.1016/0370-1573(83)90080-7).
- [40] Sirunyan A M, et al. Search for resonant and nonresonant new phenomena in high-mass dilepton final states at $\sqrt{s} = 13$ TeV[J/OL]. JHEP, 2021, 07: 208. DOI: 10.1007/JHEP07(2021)208.
- [41] Schwierz N, Wiedenhover I, Volya A. Parameterization of the Woods-Saxon Potential for Shell-Model Calculations[J]. 2007.
- [42] Mohanty A. Heavy-Flavour Jet Production and Charm Fragmentation with ALICE at LHC [J/OL]. Springer Proc. Phys., 2020, 250: 153-157. DOI: 10.1007/978-3-030-53448-6_22.
- [43] Antinori F, et al. Enhancement of hyperon production at central rapidity in 158-A-GeV/c Pb-Pb collisions[J/OL]. J. Phys. G, 2006, 32: 427-442. DOI: 10.1088/0954-3899/32/4/003.
- [44] Adam J, et al. Enhanced production of multi-strange hadrons in high-multiplicity proton-proton collisions[J/OL]. Nature Phys., 2017, 13: 535-539. DOI: 10.1038/nphys4111.
- [45] Abelev B B, et al. Multiplicity Dependence of Pion, Kaon, Proton and Lambda Production in p-Pb Collisions at $\sqrt{s_{NN}} = 5.02$ TeV[J/OL]. Phys. Lett. B, 2014, 728: 25-38. DOI: 10.1016/j.physletb.2013.11.020.
- [46] Abelev B B, et al. Multi-strange baryon production at mid-rapidity in Pb-Pb collisions at $\sqrt{s_{NN}} = 2.76$ TeV[J/OL]. Phys. Lett. B, 2014, 728: 216-227. DOI: 10.1016/j.physletb.2014.05.052.

REFERENCES

- [47] Adam J, et al. Observation of D_s^\pm/D^0 enhancement in Au+Au collisions at $\sqrt{s_{NN}} = 200$ GeV [J/OL]. Phys. Rev. Lett., 2021, 127: 092301. DOI: 10.1103/PhysRevLett.127.092301.
- [48] Paukkunen H. Global analysis of nuclear parton distribution functions at leading and next-to-leading order perturbative QCD[D]. 2009.
- [49] Kharzeev D, Tuchin K. Signatures of the color glass condensate in J/psi production off nuclear targets[J/OL]. Nucl. Phys. A, 2006, 770: 40-56. DOI: 10.1016/j.nuclphysa.2006.01.017.
- [50] Trombetta G. New results on initial state and quarkonia with alice[Z]. 2017.
- [51] Cronin J W, Frisch H J, Shochet M J, et al. Production of hadrons at large transverse momentum at 200, 300, and 400 gev[J/OL]. Phys. Rev. D, 1975, 11: 3105-3123. <https://link.aps.org/doi/10.1103/PhysRevD.11.3105>.
- [52] Arleo F, Tram V N. A Systematic study of J/psi suppression in cold nuclear matter[J/OL]. Eur. Phys. J. C, 2008, 55: 449-461. DOI: 10.1140/epjc/s10052-008-0604-8.
- [53] Arleo F, Peigne S. J/ψ suppression in p-A collisions from parton energy loss in cold QCD matter [J/OL]. Phys. Rev. Lett., 2012, 109: 122301. DOI: 10.1103/PhysRevLett.109.122301.
- [54] Eskola K J, Paukkunen H, Salgado C A. EPS09: A New Generation of NLO and LO Nuclear Parton Distribution Functions[J/OL]. JHEP, 2009, 04: 065. DOI: 10.1088/1126-6708/2009/04/065.
- [55] Eskola K J, Kolhinen V J, Salgado C A. The Scale dependent nuclear effects in parton distributions for practical applications[J/OL]. Eur. Phys. J. C, 1999, 9: 61-68. DOI: 10.1007/s100520050513.
- [56] Hirai M, Kumano S, Nagai T H. Determination of nuclear parton distribution functions and their uncertainties in next-to-leading order[J/OL]. Phys. Rev. C, 2007, 76: 065207. DOI: 10.1103/PhysRevC.76.065207.
- [57] de Florian D, Sassot R, Zurita P, et al. Global Analysis of Nuclear Parton Distributions[J/OL]. Phys. Rev. D, 2012, 85: 074028. DOI: 10.1103/PhysRevD.85.074028.
- [58] Kovarik K, et al. nCTEQ15 - Global analysis of nuclear parton distributions with uncertainties in the CTEQ framework[J/OL]. Phys. Rev. D, 2016, 93(8): 085037. DOI: 10.1103/PhysRevD.93.085037.
- [59] Eskola K J, Paakkinen P, Paukkunen H, et al. EPPS16: Nuclear parton distributions with LHC data[J/OL]. Eur. Phys. J. C, 2017, 77(3): 163. DOI: 10.1140/epjc/s10052-017-4725-9.
- [60] Brodsky S J, Lu H J. Shadowing and Antishadowing of Nuclear Structure Functions[J/OL]. Phys. Rev. Lett., 1990, 64: 1342. DOI: 10.1103/PhysRevLett.64.1342.
- [61] Norton P R. The EMC effect[J/OL]. Rept. Prog. Phys., 2003, 66: 1253-1297. DOI: 10.1088/0034-4885/66/8/201.
- [62] Wikipedia contributors. Emc effect — Wikipedia, the free encyclopedia[EB/OL]. 2022. https://en.wikipedia.org/w/index.php?title=EMC_effect&oldid=1064796335.
- [63] Bodek A, Ritchie J L. Fermi Motion Effects in Deep Inelastic Lepton Scattering from Nuclear Targets[J/OL]. Phys. Rev. D, 1981, 23: 1070. DOI: 10.1103/PhysRevD.23.1070.
- [64] Saito K, Uchiyama T. Effect of the Fermi Motion on Nuclear Structure Functions and the Emc Effect[J/OL]. Z. Phys. A, 1985, 322: 299. DOI: 10.1007/BF01411895.

REFERENCES

- [65] Caporale F, Chachamis G, Murdaca B, et al. Balitsky-Fadin-Kuraev-Lipatov Predictions for Inclusive Three Jet Production at the LHC[J/OL]. *Phys. Rev. Lett.*, 2016, 116(1): 012001. DOI: 10.1103/PhysRevLett.116.012001.
- [66] Kovchegov Y V. Unitarization of the BFKL pomeron on a nucleus[J/OL]. *Phys. Rev. D*, 2000, 61: 074018. DOI: 10.1103/PhysRevD.61.074018.
- [67] Bondarenko S, Pozdnyakov S, Prygarin A. Unifying approaches: derivation of Balitsky hierarchy from the Lipatov effective action[J/OL]. *Eur. Phys. J. C*, 2021, 81(9): 793. DOI: 10.1140/epjc/s10052-021-09572-0.
- [68] Kovner A, Lublinsky M, Mulian Y. Jalilian-Marian, Iancu, McLerran, Weigert, Leonidov, Kovner evolution at next to leading order[J/OL]. *Phys. Rev. D*, 2014, 89(6): 061704. DOI: 10.1103/PhysRevD.89.061704.
- [69] Gelis F, Iancu E, Jalilian-Marian J, et al. The Color Glass Condensate[J/OL]. *Ann. Rev. Nucl. Part. Sci.*, 2010, 60: 463-489. DOI: 10.1146/annurev.nucl.010909.083629.
- [70] Gelis F. The initial stages of heavy-ion collisions in the colour glass condensate framework [J/OL]. *Pramana*, 2015, 84(5): 685-701. DOI: 10.1007/s12043-015-0974-z.
- [71] Wang H, Xu Y, Sun X, 等. Lhc 能量下 d 介子的核修正因子[J/OL]. *Nucl. Phys. Rev.*, 2021, 38(1): 24-29. DOI: 10.11804/NuclPhysRev.38.2020056.
- [72] Fujii H, Watanabe K. Heavy quark pair production in high energy pA collisions: Open heavy flavors[J/OL]. *Nucl. Phys. A*, 2013, 920: 78-93. DOI: 10.1016/j.nuclphysa.2013.10.006.
- [73] Fujii H, Watanabe K. Heavy quark pair production in high energy pA collisions: Quarkonium [J/OL]. *Nucl. Phys. A*, 2013, 915: 1-23. DOI: 10.1016/j.nuclphysa.2013.06.011.
- [74] Vitev I, Goldman J T, Johnson M B, et al. Open charm tomography of cold nuclear matter [J/OL]. *Phys. Rev. D*, 2006, 74: 054010. DOI: 10.1103/PhysRevD.74.054010.
- [75] Neufeld R B, Vitev I, Zhang B W. A possible determination of the quark radiation length in cold nuclear matter[J/OL]. *Phys. Lett. B*, 2011, 704: 590-595. DOI: 10.1016/j.physletb.2011.09.045.
- [76] Cronin J W, Frisch H J, Shochet M J, et al. Production of hadrons with large transverse momentum at 200, 300, and 400 GeV[J/OL]. *Phys. Rev. D*, 1975, 11: 3105-3123. DOI: 10.1103/PhysRevD.11.3105.
- [77] Sharma R, Vitev I. High transverse momentum quarkonium production and dissociation in heavy ion collisions[J/OL]. *Phys. Rev. C*, 2013, 87(4): 044905. DOI: 10.1103/PhysRevC.87.044905.
- [78] Aaij R, et al. Prompt charm production in pp collisions at $\sqrt{s}=7$ TeV[J/OL]. *Nucl. Phys. B*, 2013, 871: 1-20. DOI: 10.1016/j.nuclphysb.2013.02.010.
- [79] Aaij R, et al. Measurements of prompt charm production cross-sections in pp collisions at $\sqrt{s} = 13$ TeV[J/OL]. *JHEP*, 2016, 03: 159. DOI: 10.1007/JHEP03(2016)159.
- [80] Abelev B, et al. Measurement of charm production at central rapidity in proton-proton collisions at $\sqrt{s} = 2.76$ TeV[J/OL]. *JHEP*, 2012, 07: 191. DOI: 10.1007/JHEP07(2012)191.
- [81] Abelev B, et al. D_s^+ meson production at central rapidity in proton-proton collisions at $\sqrt{s} = 7$ TeV[J/OL]. *Phys. Lett. B*, 2012, 718: 279-294. DOI: 10.1016/j.physletb.2012.10.049.

REFERENCES

- [82] Abelev B, et al. Measurement of charm production at central rapidity in proton-proton collisions at $\sqrt{s} = 7$ TeV[J/OL]. JHEP, 2012, 01: 128. DOI: 10.1007/JHEP01(2012)128.
- [83] Adam J, et al. D -meson production in p -Pb collisions at $\sqrt{s_{NN}} = 5.02$ TeV and in pp collisions at $\sqrt{s} = 7$ TeV[J/OL]. Phys. Rev. C, 2016, 94(5): 054908. DOI: 10.1103/PhysRevC.94.054908.
- [84] Aad G, et al. Measurement of $D^{*\pm}$, D^\pm and D_s^\pm meson production cross sections in pp collisions at $\sqrt{s} = 7$ TeV with the ATLAS detector[J/OL]. Nucl. Phys. B, 2016, 907: 717-763. DOI: 10.1016/j.nuclphysb.2016.04.032.
- [85] Andronic A, et al. Heavy-flavour and quarkonium production in the LHC era: from proton-proton to heavy-ion collisions[J/OL]. Eur. Phys. J. C, 2016, 76(3): 107. DOI: 10.1140/epjc/s10052-015-3819-5.
- [86] Adare A, et al. Cold-nuclear-matter effects on heavy-quark production in d +Au collisions at $\sqrt{s_{NN}} = 200$ GeV[J/OL]. Phys. Rev. Lett., 2012, 109(24): 242301. DOI: 10.1103/PhysRevLett.109.242301.
- [87] Adams J, et al. Open charm yields in $d + Au$ collisions at $s(NN)^{1/2} = 200$ -GeV[J/OL]. Phys. Rev. Lett., 2005, 94: 062301. DOI: 10.1103/PhysRevLett.94.062301.
- [88] Sirunyan A M, et al. Elliptic flow of charm and strange hadrons in high-multiplicity pPb collisions at $\sqrt{s_{NN}} = 8.16$ TeV[J/OL]. Phys. Rev. Lett., 2018, 121(8): 082301. DOI: 10.1103/PhysRevLett.121.082301.
- [89] Sirunyan A M, et al. Measurements of the charm jet cross section and nuclear modification factor in pPb collisions at $\sqrt{s_{NN}} = 5.02$ TeV[J/OL]. Phys. Lett. B, 2017, 772: 306-329. DOI: 10.1016/j.physletb.2017.06.053.
- [90] Acharya S, et al. Measurement of prompt D^0 , D^+ , D^{*+} , and D_s^+ production in p-Pb collisions at $\sqrt{s_{NN}} = 5.02$ TeV[J/OL]. JHEP, 2019, 12: 092. DOI: 10.1007/JHEP12(2019)092.
- [91] Aaij R, et al. Study of prompt D^0 meson production in pPb collisions at $\sqrt{s_{NN}} = 5$ TeV[J/OL]. JHEP, 2017, 10: 090. DOI: 10.1007/JHEP10(2017)090.
- [92] Aaij R, et al. Prompt Λ_c^+ production in pPb collisions at $\sqrt{s_{NN}} = 5.02$ TeV[J/OL]. JHEP, 2019, 02: 102. DOI: 10.1007/JHEP02(2019)102.
- [93] Aaij R, et al. Study of J/ψ production and cold nuclear matter effects in pPb collisions at $\sqrt{s_{NN}} = 5$ TeV[J/OL]. JHEP, 2014, 02: 072. DOI: 10.1007/JHEP02(2014)072.
- [94] Aaij R, et al. Study of $\psi(2S)$ production and cold nuclear matter effects in pPb collisions at $\sqrt{s_{NN}} = 5$ TeV[J/OL]. JHEP, 2016, 03: 133. DOI: 10.1007/JHEP03(2016)133.
- [95] Aaij R, et al. Prompt and nonprompt J/ψ production and nuclear modification in pPb collisions at $\sqrt{s_{NN}} = 8.16$ TeV[J/OL]. Phys. Lett. B, 2017, 774: 159-178. DOI: 10.1016/j.physletb.2017.09.058.
- [96] Aaij R, et al. Measurement of prompt-production cross-section ratio $\sigma(\chi_{c2})/\sigma(\chi_{c1})$ in pPb collisions at $\sqrt{s_{NN}} = 8.16$ TeV[J/OL]. Phys. Rev. C, 2021, 103: 064905. DOI: 10.1103/PhysRevC.103.064905.
- [97] Study of prompt D^0 meson production in pPb at $\sqrt{s_{NN}} = 8.16$ TeV at LHCb[J]. 2019.

REFERENCES

- [98] Adam J, et al. Measurement of electrons from heavy-flavour hadron decays in p-Pb collisions at $\sqrt{s_{NN}} = 5.02$ TeV[J/OL]. Phys. Lett. B, 2016, 754: 81-93. DOI: 10.1016/j.physletb.2015.12.067.
- [99] Acharya S, et al. Production of muons from heavy-flavour hadron decays in p-Pb collisions at $\sqrt{s_{NN}} = 5.02$ TeV[J/OL]. Phys. Lett. B, 2017, 770: 459-472. DOI: 10.1016/j.physletb.2017.03.049.
- [100] Adam J, et al. Rapidity and transverse-momentum dependence of the inclusive J/ψ nuclear modification factor in p-Pb collisions at $\sqrt{s_{NN}} = 5.02$ TeV[J/OL]. JHEP, 2015, 06: 055. DOI: 10.1007/JHEP06(2015)055.
- [101] Adam J, et al. Centrality dependence of inclusive J/ψ production in p-Pb collisions at $\sqrt{s_{NN}} = 5.02$ TeV[J/OL]. JHEP, 2015, 11: 127. DOI: 10.1007/JHEP11(2015)127.
- [102] Acharya S, et al. Inclusive J/ψ production at forward and backward rapidity in p-Pb collisions at $\sqrt{s_{NN}} = 8.16$ TeV[J/OL]. JHEP, 2018, 07: 160. DOI: 10.1007/JHEP07(2018)160.
- [103] Abelev B B, et al. Suppression of $\psi(2S)$ production in p-Pb collisions at $\sqrt{s_{NN}} = 5.02$ TeV [J/OL]. JHEP, 2014, 12: 073. DOI: 10.1007/JHEP12(2014)073.
- [104] Adam J, et al. Centrality dependence of $\psi(2S)$ suppression in p-Pb collisions at $\sqrt{s_{NN}} = 5.02$ TeV[J/OL]. JHEP, 2016, 06: 050. DOI: 10.1007/JHEP06(2016)050.
- [105] Aaboud M, et al. Measurement of quarkonium production in proton–lead and proton–proton collisions at 5.02 TeV with the ATLAS detector[J/OL]. Eur. Phys. J. C, 2018, 78(3): 171. DOI: 10.1140/epjc/s10052-018-5624-4.
- [106] Khachatryan V, et al. Suppression and azimuthal anisotropy of prompt and nonprompt J/ψ production in PbPb collisions at $\sqrt{s_{NN}} = 2.76$ TeV[J/OL]. Eur. Phys. J. C, 2017, 77(4): 252. DOI: 10.1140/epjc/s10052-017-4781-1.
- [107] Sirunyan A M, et al. Measurement of prompt $\psi(2S)$ production cross sections in proton-lead and proton-proton collisions at $\sqrt{s_{NN}} = 5.02$ TeV[J/OL]. Phys. Lett. B, 2019, 790: 509-532. DOI: 10.1016/j.physletb.2019.01.058.
- [108] Lansberg J P, Shao H S. Towards an automated tool to evaluate the impact of the nuclear modification of the gluon density on quarkonium, D and B meson production in proton–nucleus collisions[J/OL]. Eur. Phys. J. C, 2017, 77(1): 1. DOI: 10.1140/epjc/s10052-016-4575-x.
- [109] Shao H S. HELAC-Onia: An automatic matrix element generator for heavy quarkonium physics [J/OL]. Comput. Phys. Commun., 2013, 184: 2562-2570. DOI: 10.1016/j.cpc.2013.05.023.
- [110] Shao H S. HELAC-Onia 2.0: an upgraded matrix-element and event generator for heavy quarkonium physics[J/OL]. Comput. Phys. Commun., 2016, 198: 238-259. DOI: 10.1016/j.cpc.2015.09.011.
- [111] Ni H. Nuclear modification factors of strange and multi-strange particles in pPb collisions with the CMS experiment[J/OL]. J. Phys. Conf. Ser., 2018, 1070(1): 012009. DOI: 10.1088/1742-6596/1070/1/012009.
- [112] Aad G, et al. Transverse momentum, rapidity, and centrality dependence of inclusive charged-particle production in $\sqrt{s_{NN}} = 5.02$ TeV p + Pb collisions measured by the ATLAS experiment [J/OL]. Phys. Lett. B, 2016, 763: 313-336. DOI: 10.1016/j.physletb.2016.10.053.

REFERENCES

- [113] Abelev B, et al. Transverse momentum distribution and nuclear modification factor of charged particles in p -Pb collisions at $\sqrt{s_{NN}} = 5.02$ TeV[J/OL]. Phys. Rev. Lett., 2013, 110(8): 082302. DOI: 10.1103/PhysRevLett.110.082302.
- [114] Aidala C, et al. Nuclear-modification factor of charged hadrons at forward and backward rapidity in p +Al and p +Au collisions at $\sqrt{s_{NN}} = 200$ GeV[J/OL]. Phys. Rev. C, 2020, 101(3): 034910. DOI: 10.1103/PhysRevC.101.034910.
- [115] Back B B, et al. Pseudorapidity dependence of charged hadron transverse momentum spectra in d+Au collisions at $s(NN)^{1/2} = 200$ GeV[J/OL]. Phys. Rev. C, 2004, 70: 061901. DOI: 10.1103/PhysRevC.70.061901.
- [116] Golec-Biernat K J, Wusthoff M. Saturation effects in deep inelastic scattering at low Q^2 and its implications on diffraction[J/OL]. Phys. Rev. D, 1998, 59: 014017. DOI: 10.1103/PhysRevD.59.014017.
- [117] Kowalski H, Lappi T, Venugopalan R. Nuclear enhancement of universal dynamics of high parton densities[J/OL]. Phys. Rev. Lett., 2008, 100: 022303. DOI: 10.1103/PhysRevLett.100.022303.
- [118] Aaij R, et al. Measurement of the nuclear modification factor and prompt charged particle production in p Pb and pp collisions at $\sqrt{s_{NN}} = 5$ TeV[J]. 2021.
- [119] Abt I, et al. Kinematic distributions and nuclear effects of J/ψ production in 920-GeV fixed-target proton-nucleus collisions[J/OL]. Eur. Phys. J. C, 2009, 60: 525-542. DOI: 10.1140/epjc/s10052-009-0965-7.
- [120] Leitch M J, et al. Measurement of J/ψ and ψ' suppression in p-A collisions at 800-GeV/c[J/OL]. Phys. Rev. Lett., 2000, 84: 3256-3260. DOI: 10.1103/PhysRevLett.84.3256.
- [121] Alessandro B, et al. Charmonium production and nuclear absorption in p A interactions at 450-GeV[J/OL]. Eur. Phys. J. C, 2004, 33: 31-40. DOI: 10.1140/epjc/s2003-01539-y.
- [122] Alessandro B, et al. J/ψ and ψ' production and their normal nuclear absorption in proton-nucleus collisions at 400-GeV[J/OL]. Eur. Phys. J. C, 2006, 48: 329. DOI: 10.1140/epjc/s10052-006-0079-4.
- [123] Scomparin E. J/ψ production in p-A collisions at 158-GeV and 400-GeV: Recent results from the NA60 experiment[J/OL]. Nucl. Phys. A, 2009, 830: 239C-242C. DOI: 10.1016/j.nuclphysa.2009.10.020.
- [124] Badier J, et al. Experimental J/ψ Hadronic Production from 150-GeV/c to 280-GeV/c[J/OL]. Z. Phys. C, 1983, 20: 101. DOI: 10.1007/BF01573213.
- [125] Khalek R A, Gauld R, Giani T, et al. nNNPDF3.0: Evidence for a modified partonic structure in heavy nuclei[J]. 2022.
- [126] Alves A A, Jr., et al. The LHCb Detector at the LHC[J/OL]. JINST, 2008, 3: S08005. DOI: 10.1088/1748-0221/3/08/S08005.
- [127] LHC Machine[J/OL]. JINST, 2008, 3: S08001. DOI: 10.1088/1748-0221/3/08/S08001.
- [128] Aad G, et al. The ATLAS Experiment at the CERN Large Hadron Collider[J/OL]. JINST, 2008, 3: S08003. DOI: 10.1088/1748-0221/3/08/S08003.

REFERENCES

- [129] Chatrchyan S, et al. The CMS Experiment at the CERN LHC[J/OL]. JINST, 2008, 3: S08004. DOI: 10.1088/1748-0221/3/08/S08004.
- [130] Aamodt K, et al. The ALICE experiment at the CERN LHC[J/OL]. JINST, 2008, 3: S08002. DOI: 10.1088/1748-0221/3/08/S08002.
- [131] Jing F. Study of Cold Nuclear Matter Effects on Heavy Quarkonia in Proton-Lead Collisions at LHCb[D]. Tsinghua U., Beijing, 2014.
- [132] LHCb VELO TDR: Vertex locator. Technical design report[J]. 2001.
- [133] Gassner J, Lehner F, Steiner F. The mechanical design of the LHCb silicon trigger tracker[J]. 2005.
- [134] LHCb: Inner tracker technical design report[J]. 2002.
- [135] LHCb: Outer tracker technical design report[J]. 2001.
- [136] LHCb technical design report: Reoptimized detector design and performance[J]. 2003.
- [137] Aaij R, et al. LHCb Detector Performance[J/OL]. Int. J. Mod. Phys. A, 2015, 30(07): 1530022. DOI: 10.1142/S0217751X15300227.
- [138] Brook N H, et al. LHCb RICH 1 engineering design review report[J]. 2004.
- [139] Belyaev I, Carboni G, Harnew N, et al. The history of LHCb[J/OL]. Eur. Phys. J. H, 2021, 46 (1): 3. DOI: 10.1140/epjh/s13129-021-00002-z.
- [140] Adinolfi M, et al. LHCb RICH 2 engineering design review report[J]. 2002.
- [141] LHCb calorimeters: Technical design report[J]. 2000.
- [142] LHCb muon system technical design report[J]. 2001.
- [143] Archilli F, et al. Performance of the Muon Identification at LHCb[J/OL]. JINST, 2013, 8: P10020. DOI: 10.1088/1748-0221/8/10/P10020.
- [144] Aaij R, et al. The LHCb Trigger and its Performance in 2011[J/OL]. JINST, 2013, 8: P04022. DOI: 10.1088/1748-0221/8/04/P04022.
- [145] Dziurda A. The LHCb trigger and its upgrade[J/OL]. Nucl. Instrum. Meth. A, 2016, 824: 277-279. DOI: 10.1016/j.nima.2015.10.041.
- [146] Albrecht J, Gligorov V V, Raven G, et al. Performance of the LHCb High Level Trigger in 2012 [J/OL]. J. Phys. Conf. Ser., 2014, 513: 012001. DOI: 10.1088/1742-6596/513/1/012001.
- [147] Corti G, Cattaneo M, Charpentier P, et al. Software for the LHCb experiment[J/OL]. IEEE Trans. Nucl. Sci., 2006, 53: 1323-1328. DOI: 10.1109/TNS.2006.872627.
- [148] Barrand G, et al. GAUDI - A software architecture and framework for building HEP data processing applications[J/OL]. Comput. Phys. Commun., 2001, 140: 45-55. DOI: 10.1016/S0010-4655(01)00254-5.
- [149] Corti G, Cattaneo M, Charpentier P, et al. Software for the LHCb experiment[C/OL]//2004 IEEE Nuclear Science Symposium and Medical Imaging Conference: number 4. 2004: 2048-2052. DOI: 10.1109/NSSMIC.2004.1462666.
- [150] Benson S, Gligorov V V, Vesterinen M A, et al. The LHCb Turbo Stream[J/OL]. J. Phys. Conf. Ser., 2015, 664(8): 082004. DOI: 10.1088/1742-6596/664/8/082004.

REFERENCES

- [151] Belyaev I, et al. Handling of the generation of primary events in Gauss, the LHCb simulation framework[J/OL]. J. Phys. Conf. Ser., 2011, 331: 032047. DOI: 10.1088/1742-6596/331/3/032047.
- [152] Gandelman M, Van Herwijnen E. Data quality check procedures and tools for Monte Carlo production[J]. 2003.
- [153] Sjostrand T, Mrenna S, Skands P Z. PYTHIA 6.4 Physics and Manual[J/OL]. JHEP, 2006, 05: 026. DOI: 10.1088/1126-6708/2006/05/026.
- [154] Ferrario Ravasio S, Ježo T. State of the art POWHEG generators for top mass measurements at the LHC[J/OL]. PoS, 2018, DIS2018: 137. DOI: 10.22323/1.316.0137.
- [155] Pierog T, Karpenko I, Katzy J M, et al. EPOS LHC: Test of collective hadronization with data measured at the CERN Large Hadron Collider[J/OL]. Phys. Rev. C, 2015, 92(3): 034906. DOI: 10.1103/PhysRevC.92.034906.
- [156] Lange D J. The EvtGen particle decay simulation package[J/OL]. Nucl. Instrum. Meth. A, 2001, 462: 152-155. DOI: 10.1016/S0168-9002(01)00089-4.
- [157] Golonka P, Was Z. PHOTOS Monte Carlo: A Precision tool for QED corrections in Z and W decays[J/OL]. Eur. Phys. J. C, 2006, 45: 97-107. DOI: 10.1140/epjc/s2005-02396-4.
- [158] Agostinelli S, et al. GEANT4—a simulation toolkit[J/OL]. Nucl. Instrum. Meth. A, 2003, 506: 250-303. DOI: 10.1016/S0168-9002(03)01368-8.
- [159] Alexander J P, et al. Absolute Measurement of Hadronic Branching Fractions of the $D(s)+$ Meson[J/OL]. Phys. Rev. Lett., 2008, 100: 161804. DOI: 10.1103/PhysRevLett.100.161804.
- [160] Acharya S, et al. Measurement of D^0 , D^+ , D^{*+} and D_s^+ production in Pb-Pb collisions at $\sqrt{s_{NN}} = 5.02$ TeV[J/OL]. JHEP, 2018, 10: 174. DOI: 10.1007/JHEP10(2018)174.
- [161] Skwarnicki T. A study of the radiative CASCADE transitions between the Upsilon-Prime and Upsilon resonances[D]. Cracow, INP, 1986.
- [162] Pivk M, Le Diberder F R. SPlot: A Statistical tool to unfold data distributions[J/OL]. Nucl. Instrum. Meth. A, 2005, 555: 356-369. DOI: 10.1016/j.nima.2005.08.106.
- [163] Aaij R, et al. Measurement of the track reconstruction efficiency at LHCb[J/OL]. JINST, 2015, 10(02): P02007. DOI: 10.1088/1748-0221/10/02/P02007.
- [164] Aaij R, et al. Measurement of the prompt D^0 nuclear modification factor in p Pb collisions at $\sqrt{s_{NN}} = 8.16$ TeV[J]. 2022.
- [165] Di Nezza P. LHC Run 3 and Run 4 prospects for heavy-ion physics with LHCb[J/OL]. Nucl. Phys. A, 2021, 1005: 121872. DOI: 10.1016/j.nuclphysa.2020.121872.
- [166] Adam J, et al. Measurement of D-meson production versus multiplicity in p-Pb collisions at $\sqrt{s_{NN}} = 5.02$ TeV[J/OL]. JHEP, 2016, 08: 078. DOI: 10.1007/JHEP08(2016)078.
- [167] Gauld R, Rojo J, Rottoli L, et al. Charm production in the forward region: constraints on the small-x gluon and backgrounds for neutrino astronomy[J/OL]. JHEP, 2015, 11: 009. DOI: 10.1007/JHEP11(2015)009.
- [168] Bursche A, et al. Physics opportunities with the fixed-target program of the LHCb experiment using an unpolarized gas target[J]. 2018.

REFERENCES

- [169] Nezza P D. Lhc run 3 and run 4 prospects for heavy-ion physics with lhcb[J]. Nuclear Physics, 2021, 1005: 121872.
- [170] Hadjidakis C, Kikoła D, Lansberg J, et al. A fixed-target programme at the LHC: Physics case and projected performances for heavy-ion, hadron, spin and astroparticle studies[J/OL]. Physics Reports, 2021, 911: 1-83. <https://doi.org/10.1016%2Fj.physrep.2021.01.002>. DOI: 10.1016/j.physrep.2021.01.002.

APPENDIX A SUPPLEMENTARY MATERIAL

A.1 Invariant mass fit results of simulation

The invariant mass distributions for prompt D^+ in $p\text{Pb}$ simulation are given in Figs. A.1. The invariant mass distributions for prompt D_s^+ in $p\text{Pb}$ simulation are given in Figs. A.2.

A.2 The IP fit results of simulation

The $\log_{10} \chi_{\text{IP}}^2(D^+)$ distributions for the prompt D^+ and D^+ -from- b in simulation are given in Figs. A.3, A.4 for forward and backward rapidities, respectively. The $\log_{10} \chi_{\text{IP}}^2(D_s^+)$ distributions for the prompt D_s^+ and D_s^+ -from- b in simulation are given in Figs. A.5, A.6 for forward and backward rapidities, respectively.

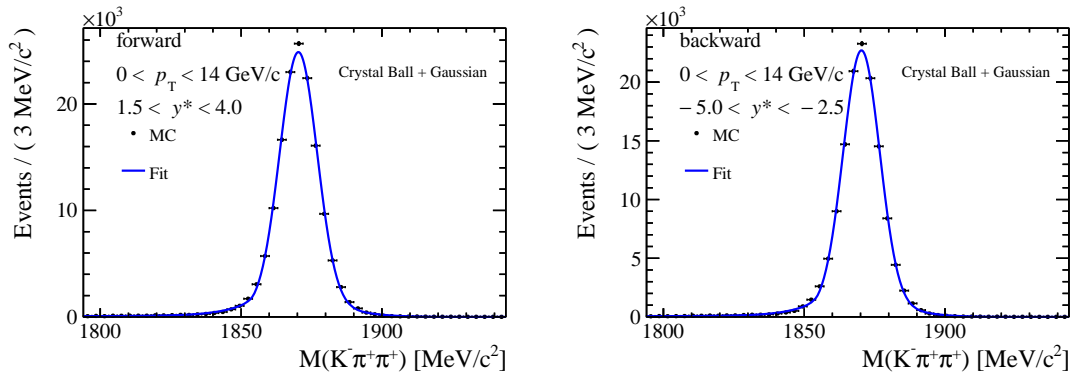


Figure A.1 Invariant mass distributions for prompt D^+ , determined from simulation. The left plot is in total kinematic region of $0 < p_T < 14 \text{ GeV}/c$, $1.5 < y^* < 4.0$ (forward region) and the right one is in bin of $0 < p_T < 14 \text{ GeV}/c$, $-5.0 < y^* < -2.5$ (backward region).

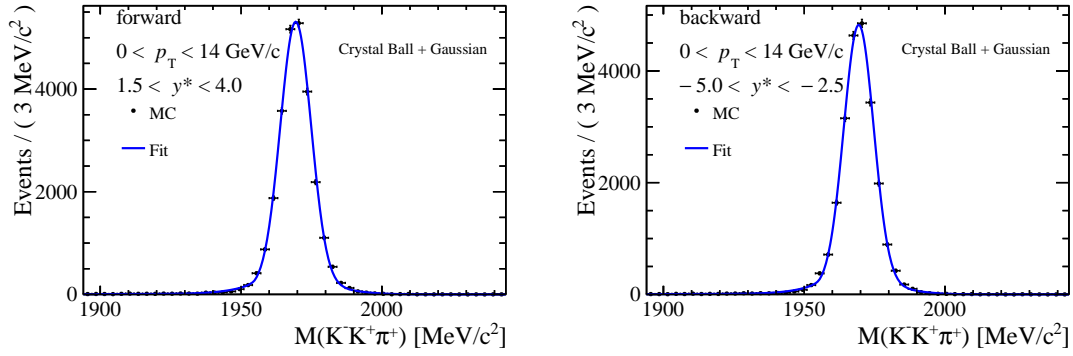


Figure A.2 Invariant mass distributions for prompt D_s^+ , determined from simulation. The left plot is in total kinematic region of $0 < p_T < 14 \text{ GeV}/c$, $1.5 < y^* < 4.0$ (forward region) and the right one is in bin of $p_T < 14 \text{ GeV}/c$, $-5.0 < y^* < -2.5$ (backward region).

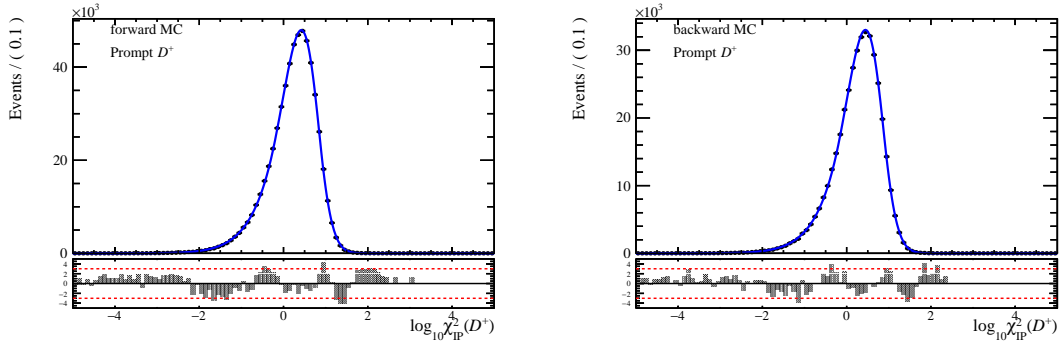


Figure A.3 The $\log_{10} \chi_{\text{IP}}^2(D^+)$ distributions for prompt D^+ , determined from simulation. The left plot is in total kinematic region of $0 < p_T < 14 \text{ GeV}/c$, $1.5 < y^* < 4.0$ (forward region) and the right one is in bin of $0 < p_T < 14 \text{ GeV}/c$, $-5.0 < y^* < -2.5$ (backward region).

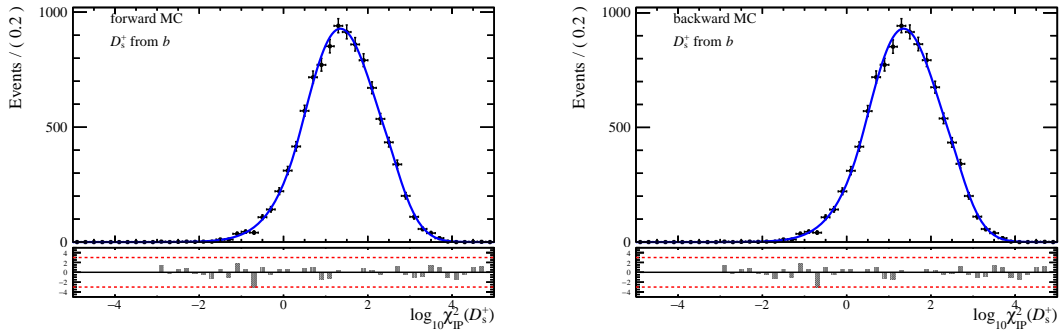


Figure A.4 The $\log_{10} \chi_{\text{IP}}^2(D^+)$ distributions for D^+ -from- b , determined from simulation. The left plot is in total kinematic region of $0 < p_T < 14 \text{ GeV}/c$, $1.5 < y^* < 4.0$ (forward region) and the right one is in bin of $0 < p_T < 14 \text{ GeV}/c$, $-5.0 < y^* < -2.5$ (backward region).

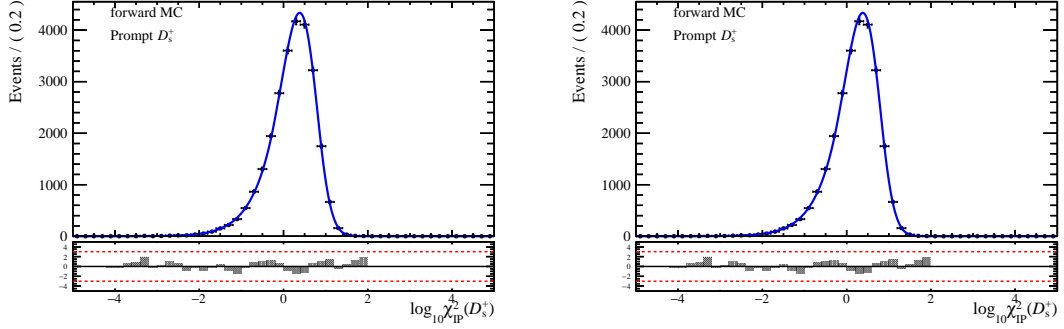


Figure A.5 The $\log_{10} \chi_{\text{IP}}^2(D_s^+)$ distributions for prompt D_s^+ , determined from simulation. The left plot is in total kinematic region of $0 < p_{\text{T}} < 14 \text{ GeV}/c$, $1.5 < y^* < 4.0$ (forward region) and the right one is in bin of $0 < p_{\text{T}} < 14 \text{ GeV}/c$, $-5.0 < y^* < -2.5$ (backward region).

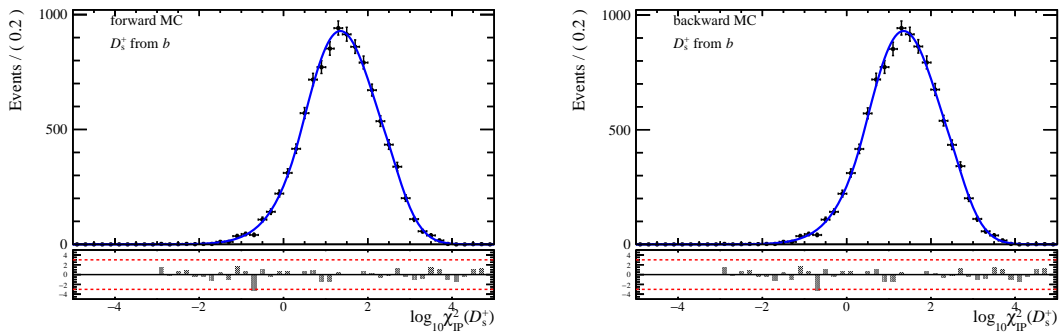


Figure A.6 The $\log_{10} \chi_{\text{IP}}^2(D_s^+)$ distributions for D_s^+ -from- b , determined from simulation. The left plot is in total kinematic region of $0 < p_{\text{T}} < 14 \text{ GeV}/c$, $1.5 < y^* < 4.0$ (forward region) and the right one is in bin of $0 < p_{\text{T}} < 14 \text{ GeV}/c$, $-5.0 < y^* < -2.5$ (backward region).

APPENDIX A SUPPLEMENTARY MATERIAL

Table A.1 Total efficiency ϵ_{tot} in bins of D^+ p_T and y^* in the forward configuration.

| $p_T[\text{ GeV}/c]\backslash y^*$ | (1.5, 2] | (2, 2.5] | (2.5, 3] | (3, 3.5] | (3.5, 4] |
|------------------------------------|-------------------|-------------------|-------------------|-------------------|-------------------|
| [0, 1] | 0.000 ± 0.000 | 0.004 ± 0.000 | 0.008 ± 0.000 | 0.007 ± 0.000 | 0.003 ± 0.000 |
| [1, 2] | 0.001 ± 0.000 | 0.012 ± 0.000 | 0.021 ± 0.000 | 0.019 ± 0.000 | 0.007 ± 0.000 |
| [2, 3] | 0.007 ± 0.000 | 0.042 ± 0.000 | 0.062 ± 0.000 | 0.054 ± 0.000 | 0.021 ± 0.000 |
| [3, 4] | 0.020 ± 0.000 | 0.089 ± 0.000 | 0.117 ± 0.000 | 0.099 ± 0.001 | 0.037 ± 0.000 |
| [4, 5] | 0.039 ± 0.000 | 0.134 ± 0.001 | 0.159 ± 0.001 | 0.134 ± 0.001 | 0.044 ± 0.000 |
| [5, 6] | 0.058 ± 0.001 | 0.170 ± 0.001 | 0.196 ± 0.001 | 0.152 ± 0.001 | 0.038 ± 0.001 |
| [6, 7] | 0.078 ± 0.001 | 0.198 ± 0.002 | 0.215 ± 0.002 | 0.152 ± 0.002 | 0.023 ± 0.001 |
| [7, 8] | 0.093 ± 0.001 | 0.214 ± 0.002 | 0.225 ± 0.002 | 0.135 ± 0.002 | 0.009 ± 0.001 |
| [8, 9] | 0.108 ± 0.002 | 0.228 ± 0.003 | 0.230 ± 0.003 | 0.115 ± 0.003 | – |
| [9, 10] | 0.122 ± 0.003 | 0.229 ± 0.004 | 0.230 ± 0.004 | 0.074 ± 0.003 | – |
| [10, 11] | 0.133 ± 0.004 | 0.234 ± 0.005 | 0.220 ± 0.005 | 0.050 ± 0.003 | – |
| [11, 12] | 0.132 ± 0.004 | 0.219 ± 0.006 | 0.196 ± 0.006 | 0.025 ± 0.002 | – |
| [12, 13] | 0.137 ± 0.005 | 0.225 ± 0.007 | 0.186 ± 0.008 | – | – |
| [13, 14] | 0.131 ± 0.006 | 0.214 ± 0.008 | 0.152 ± 0.008 | – | – |

A.3 Total efficiency tables

The efficiency ϵ_{tot} tables of prompt D^+ (D_s^+) are Table. A.1 (Table .A.3) in the forward and Table. A.2 (Table. A.4) in the backward rapidity regions.

APPENDIX A SUPPLEMENTARY MATERIAL

Table A.2 Total efficiency ϵ_{tot} in bins of D^+ p_T and y^* in the backward configuration.

| $p_T[\text{ GeV}/c]\backslash y^*$ | (2.5, 3] | (3, 3.5] | (3.5, 4] | (4, 4.5] | (4.5, 5] |
|------------------------------------|-------------------|-------------------|-------------------|-------------------|-------------------|
| [0, 1] | – | 0.004 ± 0.000 | 0.006 ± 0.000 | 0.005 ± 0.000 | 0.002 ± 0.000 |
| [1, 2] | 0.001 ± 0.000 | 0.011 ± 0.000 | 0.017 ± 0.000 | 0.013 ± 0.000 | 0.004 ± 0.000 |
| [2, 3] | 0.008 ± 0.000 | 0.036 ± 0.000 | 0.050 ± 0.000 | 0.039 ± 0.000 | 0.012 ± 0.000 |
| [3, 4] | 0.024 ± 0.000 | 0.078 ± 0.000 | 0.095 ± 0.000 | 0.073 ± 0.000 | 0.023 ± 0.000 |
| [4, 5] | 0.045 ± 0.000 | 0.119 ± 0.001 | 0.134 ± 0.001 | 0.098 ± 0.001 | 0.026 ± 0.001 |
| [5, 6] | 0.067 ± 0.001 | 0.149 ± 0.001 | 0.161 ± 0.001 | 0.107 ± 0.001 | 0.018 ± 0.001 |
| [6, 7] | 0.087 ± 0.001 | 0.177 ± 0.002 | 0.178 ± 0.002 | 0.099 ± 0.002 | – |
| [7, 8] | 0.108 ± 0.002 | 0.193 ± 0.002 | 0.192 ± 0.003 | 0.092 ± 0.003 | – |
| [8, 9] | 0.118 ± 0.002 | 0.207 ± 0.003 | 0.189 ± 0.004 | 0.063 ± 0.003 | – |
| [9, 10] | 0.129 ± 0.003 | 0.223 ± 0.004 | 0.183 ± 0.005 | – | – |
| [10, 11] | 0.139 ± 0.004 | 0.207 ± 0.006 | 0.171 ± 0.007 | – | – |
| [11, 12] | 0.154 ± 0.005 | 0.210 ± 0.007 | 0.147 ± 0.008 | – | – |
| [12, 13] | 0.135 ± 0.006 | 0.221 ± 0.009 | – | – | – |
| [13, 14] | 0.150 ± 0.008 | 0.207 ± 0.011 | – | – | – |

Table A.3 Total efficiency ϵ_{tot} in bins of D_s^+ p_T and y^* in the forward configuration.

| $p_T[\text{ GeV}/c]\backslash y^*$ | (1.5, 2] | (2, 2.5] | (2.5, 3] | (3, 3.5] | (3.5, 4] |
|------------------------------------|-------------------|-------------------|-------------------|-------------------|-------------------|
| [0, 1] | – | 0.002 ± 0.000 | 0.003 ± 0.000 | 0.002 ± 0.000 | 0.000 ± 0.000 |
| [1, 2] | 0.002 ± 0.000 | 0.009 ± 0.000 | 0.013 ± 0.000 | 0.009 ± 0.000 | 0.003 ± 0.000 |
| [2, 3] | 0.007 ± 0.000 | 0.032 ± 0.000 | 0.040 ± 0.000 | 0.030 ± 0.000 | 0.009 ± 0.000 |
| [3, 4] | 0.021 ± 0.000 | 0.067 ± 0.001 | 0.080 ± 0.001 | 0.063 ± 0.001 | 0.020 ± 0.000 |
| [4, 5] | 0.037 ± 0.001 | 0.100 ± 0.001 | 0.115 ± 0.001 | 0.090 ± 0.001 | 0.027 ± 0.001 |
| [5, 6] | 0.052 ± 0.001 | 0.126 ± 0.002 | 0.136 ± 0.002 | 0.106 ± 0.002 | 0.025 ± 0.001 |
| [6, 7] | 0.067 ± 0.001 | 0.145 ± 0.002 | 0.151 ± 0.003 | 0.108 ± 0.002 | 0.015 ± 0.001 |
| [7, 8] | 0.083 ± 0.002 | 0.155 ± 0.003 | 0.163 ± 0.004 | 0.102 ± 0.003 | – |
| [8, 9] | 0.095 ± 0.003 | 0.179 ± 0.004 | 0.173 ± 0.005 | 0.082 ± 0.004 | – |
| [9, 10] | 0.101 ± 0.004 | 0.166 ± 0.005 | 0.171 ± 0.006 | 0.063 ± 0.004 | – |
| [10, 12] | 0.104 ± 0.004 | 0.177 ± 0.005 | 0.157 ± 0.006 | – | – |
| [12, 14] | 0.103 ± 0.006 | 0.169 ± 0.008 | 0.134 ± 0.008 | – | – |

Table A.4 Total efficiency ϵ_{tot} in bins of D_s^+ p_T and y^* in the backward configuration.

| p_T [GeV/c]\y* | (2.5, 3] | (3, 3.5] | (3.5, 4] | (4, 4.5] | (4.5, 5] |
|-------------------|-------------------|-------------------|-------------------|-------------------|-------------------|
| [0, 1] | – | 0.001 ± 0.000 | 0.002 ± 0.000 | 0.001 ± 0.000 | – |
| [1, 2] | 0.002 ± 0.000 | 0.007 ± 0.000 | 0.009 ± 0.000 | 0.005 ± 0.000 | 0.001 ± 0.000 |
| [2, 3] | 0.008 ± 0.000 | 0.026 ± 0.000 | 0.031 ± 0.000 | 0.020 ± 0.000 | 0.005 ± 0.000 |
| [3, 4] | 0.021 ± 0.000 | 0.056 ± 0.001 | 0.065 ± 0.001 | 0.045 ± 0.001 | 0.011 ± 0.000 |
| [4, 5] | 0.038 ± 0.001 | 0.084 ± 0.001 | 0.095 ± 0.001 | 0.063 ± 0.001 | 0.014 ± 0.001 |
| [5, 6] | 0.057 ± 0.001 | 0.111 ± 0.002 | 0.114 ± 0.002 | 0.075 ± 0.002 | – |
| [6, 7] | 0.071 ± 0.002 | 0.129 ± 0.002 | 0.119 ± 0.003 | 0.072 ± 0.003 | – |
| [7, 8] | 0.090 ± 0.002 | 0.145 ± 0.003 | 0.125 ± 0.004 | – | – |
| [8, 9] | 0.100 ± 0.003 | 0.143 ± 0.005 | 0.132 ± 0.006 | – | – |
| [9, 10] | 0.113 ± 0.005 | 0.151 ± 0.006 | – | – | – |
| [10, 14] | 0.113 ± 0.004 | 0.157 ± 0.005 | – | – | – |

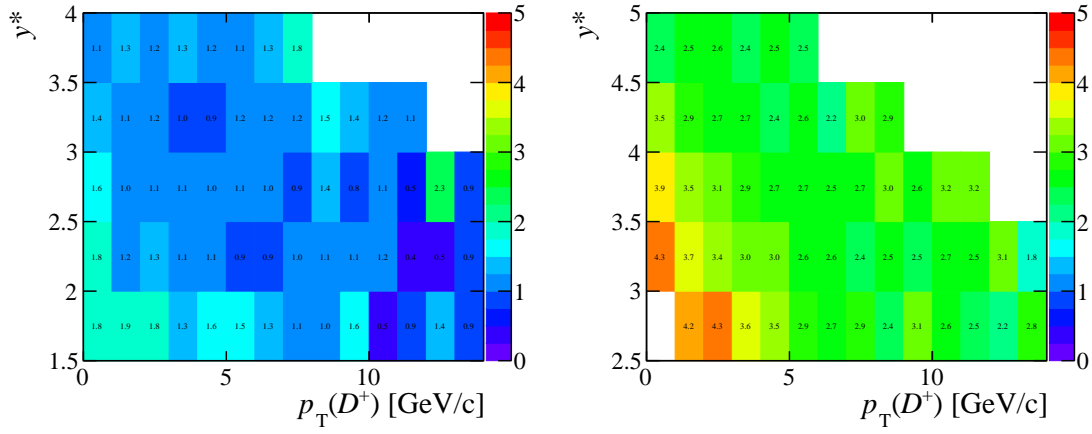


Figure A.7 The relative systematic uncertainty (%) of α_{corr} , in each (p_T, y^*) bin for D^+ in forward (left) and backward (right) rapidities.

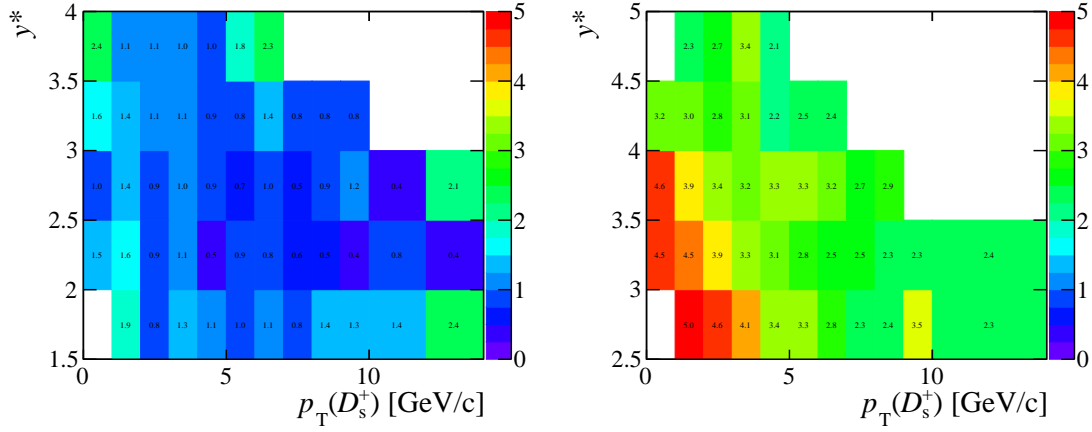


Figure A.8 The relative systematic uncertainty (%) of α_{corr} , in each (p_T, y^*) bin for D_s^+ in forward (left) and backward (right) rapidities.

A.4 Systematic uncertainty of α_{corr}

The relative systematic uncertainty of α_{corr} from multiplicity correction is summarized in Fig. A.7 and Fig. A.8 for D^+ and D_s^+ , respectively.

Table A.5 Stripping selections for D^0 calibration sample.

| Quantity | Selections |
|---------------------------------|--------------------------|
| p_T (track) | $> 250 \text{ MeV}/c$ |
| p (track) | $> 2000 \text{ MeV}/c$ |
| χ_{IP}^2 (track) | > 16 |
| DIRA | > 0.9999 |
| $\chi^2/\text{ndf}(\text{vtx})$ | < 13 |
| Vertex Displacement χ^2 | $\chi^2(\text{VD}) > 49$ |
| $p_T(D^0)$ | $> 1.5 \text{ GeV}/c$ |

A.5 Selections of the PID calibration sample

The stripping line for the PID calibration sample of D^0 is NoPIDDstar-WithD02RSKPiLine. The reconstructed D^0 begins with the standard kaon and pion containers (StdAllNoPIDsKaons and StdAllNoPIDsPions), without PID requirements. The stripping selections are listed in Table. A.5.

The mis-identification background events of $D^0 \rightarrow \pi^- K^+, K^+ K^-, \pi^+ \pi^-$ are reduced by applying vetoing the $\pm 25 \text{ MeV}/c^2$ mass window in the corresponding mass hypotheses. The background is further reduced by tagging the $D^{*+}(2010)$, requiring the invariant mass of the D^0 with a soft pion in $\pm 75 \text{ MeV}/c^2$ of the $D^{*+}(2010)$ mass. The soft pion is required to have $p_T > 150 \text{ MeV}/c$. The sum of the transverse momenta of the D^0 and the soft pion is required to larger than $2200 \text{ MeV}/c$. The $D^{*+}(2010)$ is also required to have good vertex fit quality.

A.6 One-dimensional production cross-sections

The one-dimensional production cross-sections as a function of p_T in $p\text{Pb}$ forward and backward configurations, are listed in Table. A.6 for D^+ and in Table. A.7 for D_s^+ .

The one-dimensional production cross-sections as a function of y^* in $p\text{Pb}$ forward and backward configurations, are listed in Table. A.8 for D^+ and in Table. A.9 for D_s^+ .

APPENDIX A SUPPLEMENTARY MATERIAL

Table A.6 Measured one-dimensional cross-section (mb) for prompt D^+ as a function of p_T in p Pb forward (top) and backward (bottom) configurations, respectively. The first component of uncertainty is statistical, the second is the uncorrelated component of systematic uncertainty, and the third is the correlated component.

| Forward | | |
|---------------|--------------|--|
| p_T [GeV/c] | y^* | $\frac{d\sigma}{dp_T}$ [mb/(GeV/c)] |
| [0, 1] | [1.5, 4.0] | $18.460 \pm 0.578 \pm 0.384 \pm 1.102$ |
| [1, 2] | [1.5, 4.0] | $28.415 \pm 0.278 \pm 0.321 \pm 1.619$ |
| [2, 3] | [1.5, 4.0] | $17.898 \pm 0.103 \pm 0.082 \pm 0.997$ |
| [3, 4] | [1.5, 4.0] | $8.732 \pm 0.046 \pm 0.046 \pm 0.490$ |
| [4, 5] | [1.5, 4.0] | $4.056 \pm 0.024 \pm 0.021 \pm 0.227$ |
| [5, 6] | [1.5, 4.0] | $2.003 \pm 0.015 \pm 0.013 \pm 0.111$ |
| [6, 7] | [1.5, 4.0] | $1.002 \pm 0.011 \pm 0.008 \pm 0.057$ |
| [7, 8] | [1.5, 4.0] | $0.538 \pm 0.009 \pm 0.005 \pm 0.031$ |
| [8, 9] | [1.5, 3.5] | $0.290 \pm 0.005 \pm 0.003 \pm 0.016$ |
| [9, 10] | [1.5, 3.5] | $0.171 \pm 0.004 \pm 0.002 \pm 0.010$ |
| [10, 11] | [1.5, 3.5] | $0.101 \pm 0.003 \pm 0.002 \pm 0.006$ |
| [11, 12] | [1.5, 3.5] | $0.071 \pm 0.003 \pm 0.002 \pm 0.004$ |
| [12, 13] | [1.5, 3.0] | $0.033 \pm 0.001 \pm 0.001 \pm 0.002$ |
| [13, 14] | [1.5, 3.0] | $0.026 \pm 0.001 \pm 0.001 \pm 0.002$ |
| Backward | | |
| p_T [GeV/c] | y^* | $\frac{d\sigma}{dp_T}$ [mb/(GeV/c)] |
| [0, 1] | [-5.0, -3.0] | $16.885 \pm 0.276 \pm 0.470 \pm 1.115$ |
| [1, 2] | [-5.0, -2.5] | $30.875 \pm 0.435 \pm 0.299 \pm 1.974$ |
| [2, 3] | [-5.0, -2.5] | $17.378 \pm 0.146 \pm 0.074 \pm 1.068$ |
| [3, 4] | [-5.0, -2.5] | $7.283 \pm 0.062 \pm 0.029 \pm 0.431$ |
| [4, 5] | [-5.0, -2.5] | $3.025 \pm 0.031 \pm 0.015 \pm 0.178$ |
| [5, 6] | [-5.0, -2.5] | $1.306 \pm 0.018 \pm 0.009 \pm 0.075$ |
| [6, 7] | [-4.5, -2.5] | $0.598 \pm 0.010 \pm 0.004 \pm 0.035$ |
| [7, 8] | [-4.5, -2.5] | $0.290 \pm 0.007 \pm 0.003 \pm 0.016$ |
| [8, 9] | [-4.5, -2.5] | $0.154 \pm 0.005 \pm 0.002 \pm 0.009$ |
| [9, 10] | [-4.0, -2.5] | $0.078 \pm 0.003 \pm 0.001 \pm 0.004$ |
| [10, 11] | [-4.0, -2.5] | $0.047 \pm 0.003 \pm 0.001 \pm 0.003$ |
| [11, 12] | [-4.0, -2.5] | $0.027 \pm 0.002 \pm 0.001 \pm 0.002$ |
| [12, 13] | [-3.5, -2.5] | $0.014 \pm 0.001 \pm 0.001 \pm 0.001$ |
| [13, 14] | [-3.5, -2.5] | $0.010 \pm 0.001 \pm 0.000 \pm 0.001$ |

Table A.7 Measured one-dimensional cross-section (mb) for prompt D_s^+ as a function of p_T in p Pb forward (top) and backward (bottom) configurations, respectively. The first component of uncertainty is statistical, the second is the uncorrelated component of systematic uncertainty, and the third is the correlated component.

| Forward | | |
|---------------|--------------|--|
| p_T [GeV/c] | y^* | $\frac{d\sigma}{dp_T}$ [mb/(GeV/c)] |
| [0, 1] | [2.0, 4.0] | $6.044 \pm 0.509 \pm 0.262 \pm 0.418$ |
| [1, 2] | [1.5, 4.0] | $12.533 \pm 0.378 \pm 0.155 \pm 0.658$ |
| [2, 3] | [1.5, 4.0] | $7.993 \pm 0.159 \pm 0.079 \pm 0.416$ |
| [3, 4] | [1.5, 4.0] | $3.926 \pm 0.071 \pm 0.036 \pm 0.186$ |
| [4, 5] | [1.5, 4.0] | $1.920 \pm 0.040 \pm 0.020 \pm 0.093$ |
| [5, 6] | [1.5, 4.0] | $0.964 \pm 0.026 \pm 0.013 \pm 0.048$ |
| [6, 7] | [1.5, 4.0] | $0.471 \pm 0.018 \pm 0.008 \pm 0.024$ |
| [7, 8] | [1.5, 3.5] | $0.224 \pm 0.010 \pm 0.003 \pm 0.011$ |
| [8, 9] | [1.5, 3.5] | $0.120 \pm 0.007 \pm 0.003 \pm 0.006$ |
| [9, 10] | [1.5, 3.5] | $0.076 \pm 0.006 \pm 0.002 \pm 0.004$ |
| [10, 12] | [1.5, 3.0] | $0.035 \pm 0.002 \pm 0.001 \pm 0.002$ |
| [12, 14] | [1.5, 3.0] | $0.015 \pm 0.002 \pm 0.001 \pm 0.001$ |
| Backward | | |
| p_T [GeV/c] | y^* | $\frac{d\sigma}{dp_T}$ [mb/(GeV/c)] |
| [0, 1] | [-4.5, -3.0] | $6.576 \pm 0.718 \pm 0.337 \pm 0.481$ |
| [1, 2] | [-5.0, -2.5] | $14.897 \pm 0.669 \pm 0.177 \pm 1.029$ |
| [2, 3] | [-5.0, -2.5] | $9.182 \pm 0.269 \pm 0.076 \pm 0.487$ |
| [3, 4] | [-5.0, -2.5] | $3.714 \pm 0.113 \pm 0.054 \pm 0.186$ |
| [4, 5] | [-5.0, -2.5] | $1.688 \pm 0.058 \pm 0.016 \pm 0.079$ |
| [5, 6] | [-4.5, -2.5] | $0.684 \pm 0.028 \pm 0.007 \pm 0.034$ |
| [6, 7] | [-4.5, -2.5] | $0.364 \pm 0.019 \pm 0.005 \pm 0.017$ |
| [7, 8] | [-4.0, -2.5] | $0.120 \pm 0.011 \pm 0.003 \pm 0.007$ |
| [8, 9] | [-4.0, -2.5] | $0.071 \pm 0.007 \pm 0.002 \pm 0.004$ |
| [9, 10] | [-3.5, -2.5] | $0.036 \pm 0.006 \pm 0.003 \pm 0.002$ |
| [10, 14] | [-3.5, -2.5] | $0.009 \pm 0.001 \pm 0.001 \pm 0.001$ |

Table A.8 One-dimensional cross-section (mb) for prompt D^+ as a function of y^* in p Pb forward (top) and backward (bottom) configurations, respectively. The first uncertainty is statistical, and the second is a result of systematic uncertainty.

| Forward [mb] | |
|-----------------|-----------------------------------|
| y^* | $p_T \in [1, 14][\text{GeV}/c]$ |
| [1.5, 2.0] | $29.68 \pm 0.52 \pm 1.73$ |
| [2.0, 2.5] | $29.96 \pm 0.17 \pm 1.66$ |
| [2.5, 3.0] | $27.34 \pm 0.13 \pm 1.51$ |
| [3.0, 3.5] | $23.01 \pm 0.13 \pm 1.30$ |
| [3.5, 4.0] | $16.68 \pm 0.19 \pm 1.13$ |
| Backward [mb] | |
| y^* | $p_T \in [1, 14][\text{GeV}/c]$ |
| [-3.0, -2.5] | $31.43 \pm 0.77 \pm 1.73$ |
| [-3.5, -3.0] | $30.31 \pm 0.27 \pm 1.43$ |
| [-4.0, -3.5] | $26.29 \pm 0.21 \pm 1.70$ |
| [-4.5, -4.0] | $20.77 \pm 0.22 \pm 1.53$ |
| [-5.0, -4.5] | $13.37 \pm 0.34 \pm 1.27$ |

Table A.9 One-dimensional cross-section (mb) for prompt D_s^+ as a function of y^* in p Pb forward (top) and backward (bottom) configurations, respectively. The first uncertainty is statistical, and the second is a result of systematic uncertainty.

| Forward [mb] | |
|-----------------|-----------------------------------|
| y^* | $p_T \in [1, 14][\text{GeV}/c]$ |
| [1.5, 2.0] | $13.62 \pm 0.59 \pm 0.84$ |
| [2.0, 2.5] | $13.15 \pm 0.26 \pm 0.64$ |
| [2.5, 3.0] | $13.32 \pm 0.24 \pm 0.62$ |
| [3.0, 3.5] | $9.80 \pm 0.25 \pm 0.50$ |
| [3.5, 4.0] | $6.76 \pm 0.42 \pm 0.42$ |
| Backward [mb] | |
| y^* | $p_T \in [1, 14][\text{GeV}/c]$ |
| [-3.0, -2.5] | $16.31 \pm 0.96 \pm 1.14$ |
| [-3.5, -3.0] | $15.17 \pm 0.45 \pm 0.74$ |
| [-4.0, -3.5] | $14.51 \pm 0.43 \pm 0.80$ |
| [-4.5, -4.0] | $10.29 \pm 0.46 \pm 0.60$ |
| [-5.0, -4.5] | $5.30 \pm 0.80 \pm 0.58$ |

A.7 Uncertainty propagation

Suppose there are two variables v_1 , and v_2 , and their relative uncertainties $[x_i, y_j]$, $[X_m, z_n]$, respectively. There are no correlations among different sources of uncertainties. $x_i, X_m, i = m$ are totally correlated, and while y_j, Z_n are not correlated with each other and with other uncertainties. Let $r = v_1/v_2$, then we have $\log r = \log v_1 - \log v_2$, and $\delta r/r = \sqrt{(\delta v_1/v_1)^2 + (\delta v_2/v_2)^2 - 2\rho * (\delta v_1/v_1) * (\delta v_2/v_2)}$. The total relative uncertainty $\delta v_1/v_1 = \sqrt{\sum x_i^2 + \sum y_j^2}$, and $\delta v_2/v_2 = \sqrt{\sum X_m^2 + \sum z_n^2}$. The correlation between the total uncertainties of δv_1 and δv_2 is

$$\rho = \frac{\sum(x_i * v_1) * (X_i * v_2)}{\delta v_1 * \delta v_2} = \frac{\sum x_i * X_i}{(\delta v_1/v_1) * (\delta v_2/v_2)}.$$

That is

$$\rho * (\delta v_1/v_1) * (\delta v_2/v_2) \equiv 2 * \sum x_i * X_i.$$

Then we have

$$\delta r/r = \sqrt{(\delta v_1/v_1)^2 + (\delta v_2/v_2)^2 - 2 * \sum x_i * X_i}.$$

This is the final equation, which allows us calculate simply the uncertainties of the ratios, without the need of investigating the details of each component. For example, suppose the cross-section in the forward configuration at 8.16 TeV is $1000 \mu\text{b} \pm 50 \mu\text{b}$, and the one in the forward configuration at 5.02 TeV is $400 \mu\text{b} \pm 30 \mu\text{b}$, and the correlated uncertainty between the two is $20 \mu\text{b}$ in the first number and $5 \mu\text{b}$ in the second number. The uncertainty of the ratio is thus calculated as $\sqrt{(50/1000)^2 + (30/400)^2 - 2 * 20/1000 * 5/400} = 8.7\%$.

A.8 One-dimensional cross-section ratios

The one-dimensional cross-section ratios R_{D^+/D^0} , $R_{D_s^+/D^0}$ and $R_{D_s^+/D^+}$, as a function of p_T are summarized in Table. A.10, Table A.11. and Table. A.12, respectively.

The one-dimensional cross-section ratios R_{D^+/D^0} , $R_{D_s^+/D^0}$ and $R_{D_s^+/D^+}$, as a function of y^* are summarized in Table. A.13, Table A.14. and Table. A.15, respectively.

Table A.10 R_{D^+/D^0} ratio as a function of p_T in LHCb p Pb collisions at 5.02 TeV for forward (left) and backward (right) rapidities.

| p_T [GeV/c] | Forward $2.5 < y^* < 4.0$ | Backward $-4.0 < y^* < -2.5$ |
|-----------------|-----------------------------|------------------------------|
| [0, 1] | $0.340 \pm 0.011 \pm 0.025$ | $0.326 \pm 0.007 \pm 0.028$ |
| [1, 2] | $0.341 \pm 0.004 \pm 0.019$ | $0.316 \pm 0.005 \pm 0.027$ |
| [2, 3] | $0.361 \pm 0.002 \pm 0.015$ | $0.332 \pm 0.003 \pm 0.022$ |
| [3, 4] | $0.382 \pm 0.002 \pm 0.015$ | $0.344 \pm 0.004 \pm 0.022$ |
| [4, 5] | $0.390 \pm 0.003 \pm 0.017$ | $0.352 \pm 0.005 \pm 0.024$ |
| [5, 6] | $0.406 \pm 0.005 \pm 0.027$ | $0.363 \pm 0.009 \pm 0.031$ |
| [6, 7] | $0.424 \pm 0.009 \pm 0.037$ | $0.382 \pm 0.009 \pm 0.027$ |
| [7, 8] | $0.417 \pm 0.009 \pm 0.029$ | $0.357 \pm 0.012 \pm 0.037$ |
| [8, 9] | $0.435 \pm 0.011 \pm 0.040$ | $0.375 \pm 0.021 \pm 0.063$ |
| [9, 10] | $0.436 \pm 0.015 \pm 0.047$ | $0.363 \pm 0.022 \pm 0.039$ |

Table A.11 $R_{D_s^+/D^0}$ ratio as a function of p_T in p Pb collisions at 5.02 TeV from LHCb for forward (left) and backward (right) rapidities.

| p_T [GeV/c] | Forward $2.5 < y^* < 4.0$ | Backward $-4.0 < y^* < -2.5$ |
|-----------------|-----------------------------|------------------------------|
| [0, 1] | $0.156 \pm 0.013 \pm 0.013$ | $0.174 \pm 0.018 \pm 0.019$ |
| [1, 2] | $0.159 \pm 0.004 \pm 0.010$ | $0.167 \pm 0.008 \pm 0.015$ |
| [2, 3] | $0.174 \pm 0.003 \pm 0.010$ | $0.199 \pm 0.005 \pm 0.017$ |
| [3, 4] | $0.183 \pm 0.003 \pm 0.010$ | $0.195 \pm 0.005 \pm 0.017$ |
| [4, 5] | $0.196 \pm 0.004 \pm 0.011$ | $0.220 \pm 0.008 \pm 0.020$ |
| [5, 6] | $0.206 \pm 0.006 \pm 0.015$ | $0.224 \pm 0.011 \pm 0.019$ |
| [6, 7] | $0.203 \pm 0.009 \pm 0.019$ | $0.254 \pm 0.014 \pm 0.024$ |
| [7, 8] | $0.199 \pm 0.009 \pm 0.017$ | $0.189 \pm 0.017 \pm 0.019$ |
| [8, 9] | $0.198 \pm 0.012 \pm 0.021$ | $0.204 \pm 0.025 \pm 0.024$ |
| [9, 10] | $0.183 \pm 0.015 \pm 0.022$ | $0.242 \pm 0.039 \pm 0.030$ |

Table A.12 $R_{D_s^+/D^+}$ ratio as a function of p_T in pPb collisions at 5.02 TeV from LHCb for forward (left) and backward (right) rapidities.

| p_T [GeV/c] | Forward $2.5 < y^* < 4.0$ | Backward $-4.0 < y^* < -2.5$ |
|-----------------|-----------------------------|------------------------------|
| [0, 1] | $0.407 \pm 0.038 \pm 0.030$ | $0.513 \pm 0.057 \pm 0.046$ |
| [1, 2] | $0.441 \pm 0.014 \pm 0.018$ | $0.482 \pm 0.023 \pm 0.031$ |
| [2, 3] | $0.447 \pm 0.009 \pm 0.017$ | $0.528 \pm 0.016 \pm 0.023$ |
| [3, 4] | $0.450 \pm 0.009 \pm 0.014$ | $0.510 \pm 0.016 \pm 0.020$ |
| [4, 5] | $0.473 \pm 0.010 \pm 0.015$ | $0.558 \pm 0.020 \pm 0.018$ |
| [5, 6] | $0.481 \pm 0.014 \pm 0.017$ | $0.546 \pm 0.024 \pm 0.018$ |
| [6, 7] | $0.470 \pm 0.019 \pm 0.018$ | $0.608 \pm 0.034 \pm 0.021$ |
| [7, 8] | $0.450 \pm 0.022 \pm 0.016$ | $0.460 \pm 0.042 \pm 0.020$ |
| [8, 9] | $0.412 \pm 0.025 \pm 0.018$ | $0.506 \pm 0.056 \pm 0.025$ |
| [9, 10] | $0.442 \pm 0.034 \pm 0.023$ | $0.580 \pm 0.098 \pm 0.050$ |
| [10, 12] | $0.482 \pm 0.038 \pm 0.022$ | – |
| [12, 14] | $0.491 \pm 0.064 \pm 0.041$ | – |
| [10, 14] | – | $0.410 \pm 0.070 \pm 0.037$ |

Table A.13 R_{D^+/D^0} ratio as a function of $|y^*|$ in pPb collisions at 5.02 TeV from LHCb for forward (left) and backward (right) rapidities.

| $ y^* $ | Forward $0 < p_T < 10$ [GeV/c] | Backward $0 < p_T < 10$ [GeV/c] |
|------------|----------------------------------|-----------------------------------|
| [1.5, 2.0] | $0.320 \pm 0.011 \pm 0.028$ | – |
| [2.0, 2.5] | $0.347 \pm 0.003 \pm 0.016$ | – |
| [2.5, 3.0] | $0.376 \pm 0.002 \pm 0.013$ | $0.318 \pm 0.008 \pm 0.033$ |
| [3.0, 3.5] | $0.378 \pm 0.003 \pm 0.014$ | $0.320 \pm 0.003 \pm 0.023$ |
| [3.5, 4.0] | $0.368 \pm 0.005 \pm 0.028$ | $0.342 \pm 0.004 \pm 0.021$ |
| [4.0, 4.5] | – | $0.326 \pm 0.005 \pm 0.022$ |
| [4.5, 5.0] | – | $0.330 \pm 0.011 \pm 0.037$ |

Table A.14 $R_{D_s^+/D^0}$ ratio as a function of $|y^*|$ in p Pb collisions at 5.02 TeV from LHCb for forward (left) and backward (right) rapidities.

| $ y^* $ | Forward $0 < p_T < 10$ [GeV/c] | Backward $0 < p_T < 10$ [GeV/c] |
|------------|----------------------------------|-----------------------------------|
| [1.5, 2.0] | $0.150 \pm 0.007 \pm 0.012$ | – |
| [2.0, 2.5] | $0.153 \pm 0.004 \pm 0.008$ | – |
| [2.5, 3.0] | $0.173 \pm 0.004 \pm 0.007$ | $0.165 \pm 0.010 \pm 0.018$ |
| [3.0, 3.5] | $0.163 \pm 0.007 \pm 0.008$ | $0.159 \pm 0.007 \pm 0.012$ |
| [3.5, 4.0] | $0.146 \pm 0.013 \pm 0.015$ | $0.176 \pm 0.008 \pm 0.012$ |
| [4.0, 4.5] | – | $0.177 \pm 0.013 \pm 0.015$ |
| [4.5, 5.0] | – | $0.121 \pm 0.019 \pm 0.016$ |

Table A.15 $R_{D_s^+/D^+}$ ratio as a function of $|y^*|$ in p Pb collisions at 5.02 TeV from LHCb for forward (left) and backward (right) rapidities.

| $ y^* $ | Forward $0 < p_T < 10$ [GeV/c] | Backward $0 < p_T < 10$ [GeV/c] |
|------------|----------------------------------|-----------------------------------|
| [1.5, 2.0] | $0.459 \pm 0.027 \pm 0.024$ | – |
| [2.0, 2.5] | $0.442 \pm 0.013 \pm 0.015$ | – |
| [2.5, 3.0] | $0.459 \pm 0.012 \pm 0.013$ | $0.520 \pm 0.033 \pm 0.035$ |
| [3.0, 3.5] | $0.430 \pm 0.017 \pm 0.017$ | $0.498 \pm 0.022 \pm 0.024$ |
| [3.5, 4.0] | $0.396 \pm 0.037 \pm 0.035$ | $0.515 \pm 0.022 \pm 0.025$ |
| [4.0, 4.5] | – | $0.543 \pm 0.041 \pm 0.038$ |
| [4.5, 5.0] | – | $0.399 \pm 0.062 \pm 0.038$ |

ACKNOWLEDGEMENTS

衷心感谢导师朱相雷副教授在我读博士期间在学业的精心指导,以及在平时生活上对我的关心与帮助,不胜感激。同时也衷心感谢工程物理系的张黎明副教授,北京大学的高原宁教授、杨振伟教授和张艳席研究员,老师们都学识渊博,平易近人,对我的指导使我终生受益。

感谢王梦臻,许泽华和杨迪师兄,孙佳音师姐在平时学习对我帮助。感谢和我同一级的陈晨、任赞、辜晨曦和许傲同学,以及实验室的王剑桥、许立、牟宏杰等同学,这几年大家常常一起探讨学术问题、打球吃饭,相处得非常愉快。很荣幸能认识这么多集身高、颜值、才华与幽默于一身的的朋友。

最后感谢我的父亲母亲对我的鼓励与与开导。

祝大家身心健康,心想事成,万事如意,为祖国至少健康工作 50 年!

声 明

本人郑重声明：所提交的学位论文，是本人在导师指导下，独立进行研究工作所取得的成果。尽我所知，除文中已经注明引用的内容外，本学位论文的研究成果不包含任何他人享有著作权的内容。对本论文所涉及的研究工作做出贡献的其他个人和集体，均已在文中以明确方式标明。

签 名： 罗毅恒 日 期： 2022年5月11日

RESUME

个人简历

1994年11月18日出生于四川南充市。

2013年9月考入华中师范大学大学数学与统计学院数学物理专业，2017年7月本科毕业并获得理学学士学位。

2017年9月免试进入清华大学工程物理系攻读物理学博士至今。

在学期间完成的相关学术成果

无

COMMENTS FROM THESIS SUPERVISOR

显粲强子产生是高能重离子碰撞中产生的退禁闭物态性质的重要实验探针。而在高能质子-核碰撞中精确测量瞬发显粲强子产生是定量限定重离子碰撞中影响粲强子产生的冷核物质效应的重要实验手段。罗毅恒基于 LHCb Run1 的核子-核子质心系能量为 5.02TeV 的质子-铅核碰撞数据系统测量 D_s^+ 和 D^0 这两种显粲强子在前向和后向快度区的产生。该论文的实验数据分析工作，包括两种显粲强子的信号拟合、瞬发信号提取、探测器接受度和重建效率估计、截面计算、系统误差分析、核修正因子和截面比的计算等都由罗毅恒独立完成。该实验结果相比 ALICE 的相应数据显著提高了测量精度，并且覆盖了对冷核物质效应更敏感的前向和后向快度区，为限定冷核物质效应提供了重要实验参考。尤其是高横动量下 D^+ 的前向后向比或者后向快度区的核修正因子测量也对基于核部分子分布函数的理论模型计算提出了挑战。此外 D_s^+ 和 D^0 截面比值的测量还为研究 LHC 能量下铅核-铅核碰撞中的粲强子化中的奇异性增强提供了基准。论文表述清晰准确，内容详实完整，是一篇优秀的博士论文。

RESOLUTION OF THESIS DEFENSE COMMITTEE